A STUDY OF ELECTRON PAIR PRODUCTION IN 16 GeV/C PI-MINUS PROTON COLLISIONS

Thesis by

Max Marshall

In Partial Fulfillment of the Requirements

for the Degree of

Doctor of Philosophy

California Institute of Technology

Pasadena, California

1980

(Submitted December 20, 1979)

Acknowledgements

I acknowledge the U.S. Dept. of Energy and Caltech for financial support, both personal and for this research. I acknowledge and thank the following people: Jerry Pine, my thesis adviser, for patient guidance and instruction; David Blockus, Bill Dunwoodie, Ryszard Stroynowski, and Craig Woody, who worked on the data analysis, for contributions and companionship during difficult work; Bill Walsh, Dick Bierce, and Bill Johnson, for assistance at SLAC; Hans Jensen, Jerry Pine, John Scheid, Ricardo Gomez, Tom Himel, and Bill Friedler, for their contributions and companionship over various time periods while building the cylindrical chambers; David Leith and the others of SLAC Group B, past and present, for their contributions to planning and running the experiment; Laura Peirce for personal support and help with the text; and the staff of the accelerator, computer, and technical drawing groups at SLAC for making it a pleasant and productive environment.

Abstract

Inclusive electron-pair production in pi-minus proton collisions at 16 GeV/c was studied using a large-acceptance spectrometer equipped with Cerenkov and shower counters. A two standard-deviation signal was observed in a region of invariant pair mass greater than 140 MeV/c^2 and Feynman X between 0.15 and 0.4. The cross section, extrapolated to the full range of X, for masses greater than 140 MeV/c^2, is estimated to be less than 2.5 microbarns, and the corresponding single electron to pion ratio to be less than $2.6 \cdot 10^{-5}$. The observed electron pairs occurred mainly in the mass region 200 to 600 MeV/c^2 and are believed to have originated in the primary hadronic interaction rather than the decay of secondary particles.

Table of Contents

CHAPTER 1 -- Introduction

1.A -- Motivation

Science is a process of observation and systematization. In physics, systematization often takes the form of fundamental laws of nature that are much simpler than the observed phenomena. Once the fundamental principles are known, understanding complex phenomena is straightforward, but recognizing a new principle is difficult unless the observed phenomenon depends on it in a particularly simple way.

In the area of so-called elementary particle physics, the interactions of hadrons display complex and multi-faceted behavior. This behavior seems to arise from a compound nature where different combinations of more elementary constituents are bound in a dynamic structure. It has been difficult to study these constituents because the binding force seems not to allow them to be isolated.

Electron scattering has been particularly useful for studying the inner structure of hadrons because electrons are not affected by the strong-interaction binding forces and because they exhibit no inner structure of their own. The interaction occurs by the well understood electromagnetic process, and when the energy is high enough, large angle scattering involves the constituents

individually.

Electron-positron annihilation into hadrons is closely related to electron-hadron scattering. The electromagnetic coupling between a charged particle and a virtual photon is the same whether the charged particle is scattered or is annihilated (or created) with its antiparticle. A collision between an electron and positron has a certain probability of producing a virtual photon which may return to a pair of electrons, create a pair of muons, or create a pair of any of the constituents of hadrons. (The number of constituents has been inferred from the ratio of hadron production to muon pair production in electron annihilations.) The constituent pair can exist as a single hadron (a vector meson), or produce several hadrons, where the additional constituents are created in pairs from kinetic energy.

The third related process, the annihilation of hadron constituents into a pair of leptons, occurs occasionally in the collision of two hadrons. The aim of this experiment was to detect electron pairs produced in hadron collisions and to determine if they occurred as the result of a constituent annihilation process.

In this experiment, electrons were identified with Cerenkov counters and shower counters. Cerenkov counters tag particles having a velocity greater than a constant

determined by the material in the counter. Electrons, having a very small mass, needed little momentum to exceed the critical velocity, while hadrons needed more momentum than was generally imparted to outgoing particles. Since the Cerenkov medium was a gas, the particle trajectories usually were not disturbed. Shower counters contain a large amount of dense material with which incoming electrons interact, their energy being converted into a detectible shower of electron-positron pairs. Again it is the low mass that distinguishes the electrons from other types of particles. Since the shower counters absorbed the particles, they were placed last in the line of detectors.

The major challenge in this experiment was to distinguish "direct" electrons produced in the hadronic interaction from hadrons and from secondary electrons created by hadrons made in the interaction. Electron pairs are produced in hadron collisions with a probability approximately equal to the ratio of the strengths of the electromagnetic to strong interactions squared, about 1/20,000. The probability of misidentifying two hadrons needed to be less than one in 20,000 in order that the real signal was larger than the misidentified hadron background.

Secondary electrons can be produced when a hadron decays and produces either a lepton (electron or muon) pair via the electromagnetic interaction or a single charged lepton via

the weak interaction. Such decays are greatly enhanced when the intermediate particle cannot decay by the strong interaction. (Lack of a strong decay mode results in a much increased lifetime and thus a greater opportunity to decay into leptons.) Weak decays are often so slow that there is a discernible path length before the decay, in which case they were ignored. This was the case for the long-lived strange baryons, kaons, and charged pions. Weak decays of the D mesons, heavy leptons, and the W-boson, however, would produce leptons coming apparently from the primary interaction. The pi-zero and eta mesons are stable with respect to strong interactions and decay into electron pairs on the order of one percent of the time by the Dalitz decay mode (electron pair plus a photon). Other mesons may also decay this way but with less probability because they are short-lived.

The most serious source of background was electron pairs from the Bethe-Heitler process (photon conversion) where photons from the decay of pi-zeros interacted with matter too close to the primary interaction to be resolved. These could usually be recognized and eliminated because the electron pair invariant mass was less than 150 MeV/c^2. However, the detector failed to find one of the tracks in 10-20% of the pairs, in which case the other track could not be eliminated on the basis of pair mass. Photon conversion pairs were produced at an average rate of about 0.1 per

hadronic interaction, so that a simultaneous occurrence of this phenomenon for two pi-zeros, which mimicked direct high mass electron pairs, occurred at a rate several times higher than the direct process.

A source of direct lepton pairs was the decay of vector mesons. These give rise to pairs at particular masses, and can be recognized in that way. (Vector mesons may be considered resonance effects that modify the amplitude for the constituent annihilation at certain masses, or they may be considered particles that decay into lepton pairs). The lepton production rate due to vector meson decays is calculable from fairly well measured inclusive cross sections and branching ratios. Thus, they provide a useful calibration signal in the lepton pair mass spectrum.

The original motivation for observing direct leptons was the search for the W-boson through its weak decay, starting in 1965. Once direct leptons were observed, curiosity was aroused about their source, which is only now being determined. By 1974, more than ten experiments reported direct muons or electrons, detected singly and in pairs. The most interesting feature of these experiments was that the ratio of leptons to pions was about 10^{-4} over a wide range of center of mass energy and transverse momentum of the outgoing lepton/pion. More recent measurements of this ratio have all been 2 to 3 $\cdot 10^{-5}$.

The Drell-Yan model for the annihilation of constituents into lepton pairs was proposed in 1970. This model predicted a scaling law for a fixed ratio of pair mass to center of mass energy and a relationship between the cross section and the quark (constituent) momentum distributions inside hadrons (which were measured in electron-hadron and neutrino-hadron scattering). The assumptions are valid only in the limit of large center of mass energy and lepton pair mass (relative to the masses of hadrons). This experiment is compared with a modified Drell-Yan model in which meson constituents annihilate rather than quarks. The unmodified model agrees poorly with measurements at the energy of this experiment. Feynman diagrams are shown for the original and modified models in fig. 1.A.

The lepton to pion ratio was considered anomalously large in 1976 when this experiment was proposed. The source of the extra leptons was not known, nor was the fraction originating as pairs. The recent experiments indicate that most of the leptons occur as pairs, and that the extra pairs are created by constituent annihilations at a rate more than an order of magnitude larger than predicted by the Drell-Yan model. A thorough history of direct lepton physics is given in the thesis of Woody(1), and the models and experiments are described in several review articles(2).

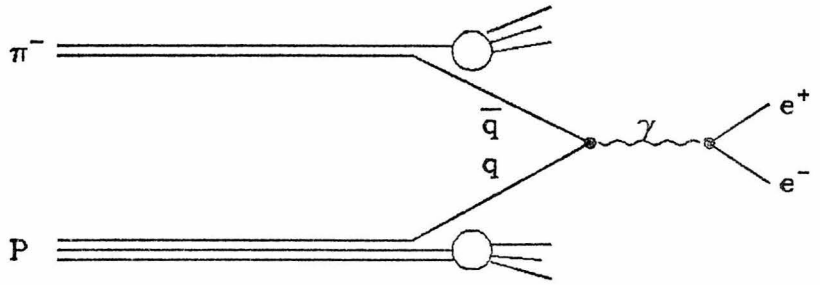

a) Drell-Yan model

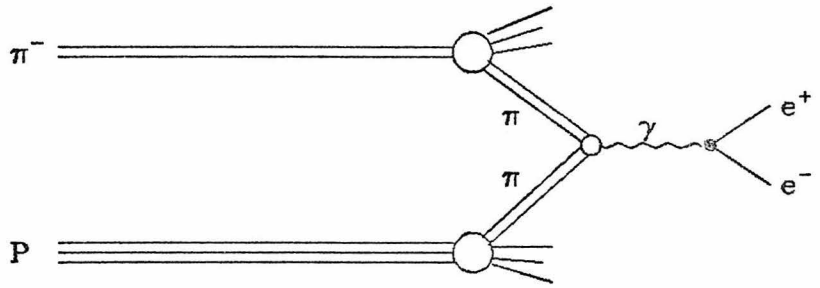

b) Pion annihilation model

Figure 1.A: Feynman diagrams for lepton pair production

This experiment complements a recent high statistics muon pair experiment at the same energy, by observing electron pairs at a lower value of X and at masses below the two muon threshold.

1.B -- This Experiment

This experiment (SLAC E-127) triggered on single electrons produced in the interactions of 16 GeV/c pi-minuses with protons in a one meter liquid hydrogen target. Only events with electron-positron pairs were studied.

The experiment was the first use of most of the components of the LASS facility and was chosen because of its modest trackfinding and resolution requirements in addition to its intrinsic interest. The electron pair requirement was well suited to LASS because of its ability to handle the large data rates due to the relatively loose trigger, and because air had the right Cerenkov threshold for electron identification. (The large segmented Cerenkov counter was not yet gas-tight.) Because of the full solid angle acceptance, LASS had the capacity to observe a large fraction of the kinematic region of pair production and to study the accompanying hadrons. A small, but potentially interesting, acceptance in the region of X below 0.15 and above 0.4 was lost because the downstream detectors were not used in the data analysis.

Electron identification was accomplished using the 38-segment Cerenkov counter and 13 off-axis shower counters which identified only high transverse momentum tracks. A count in at least one of the Cerenkov cells (pulse height corresponding to a single photo-electron) and a pulse height in at least one shower counter corresponding to an energy deposition of 750 MeV was the trigger requirement. Events with single electrons were recorded in the hope that hadron misidentification would be low enough to allow a comparison of single electrons and pairs. It was later clear that adequate hadron rejection was possible only for pairs in which both tracks were identified in the Cerenkov counter and at least one identified also in a shower counter.

The experiment was run in Nov.-Dec. 1976 and Feb.-Apr. 1977. The first computer track reconstruction program was run in Dec.-Jan. 1977-1978. A new, improved version was written and run in Jul.-Aug. 1978 on half the data and was rerun with further improvements on the full sample in Apr.-Jul. 1979.

Approximately 10^9 pions were received giving sensitivity before acceptance losses of 4 events per nanobarn. Five million triggers were recorded on tape from which one million were preselected and processed by the trackfinding program. One hundred thousand were selected as possibly

containing an electron pair. About two hundred were finally accepted, of which one-third was estimated to be genuine. The overall acceptance was 1.2%, and the corrected inclusive electron pair cross section for pairs with mass above 140 MeV/c^2 was 1.1±0.7 microbarns. This corresponds to an electron to pion ratio of $2.6 \pm 1.6 \cdot 10^{-5}$.

The observed number of events whose mass was consistent with the rho and omega vector mesons was smaller than the number predicted from the measured cross sections and branching ratios. Due to the small number of events and the relatively large background estimate, the measurement was consistent both with zero and the prediction. The signal between the pi-zero and rho in mass, which is attributed to constituent annihilation, was greater than zero with a significance of two standard deviations, and in agreement with other experiments and the predictions of the constituent-annihilation model discussed in the results section. The lowest mass data point was not in agreement with the steep rise in cross section at low masses predicted by the model.

Chapters 2 and 3 discuss the physical layout of the experiment and the data-acquisition system respectively, and for the most part need not be read to understand the following more interesting chapters. Sections 2.A and 2.B give an overview of the layout and should be read. Chapter

4 describes the track reconstruction procedure which is quite interesting, but need not be read. The selection of real electron pair events and estimation of the losses and backgrounds are described in chapter 5, and the results are discussed in chapter 6. The appendix describes the building and testing of the cylindrical spark chamber package and the associated electronics.

The event selection procedure described in chapter 5 was developed independently of the main group effort. The final results of E-127 may use different cuts and therefore may have a different statistical significance than those reported here.

References for chapter 1

1. C. L. Woody, A Study of Electron Pair Production in 16.1 GeV/c pi-minus proton Collisions Using a Large Aperture Solenoid Spectrometer, Ph.D. Thesis, Johns Hopkins University (1978).

2. N. S. Craigie, Lepton and Photon Production in Hadron collisions, Phys. Rep. 47, 1 (1978); L. M. Lederman, Lepton Production in Hadronic Collisions, Phys. Rep. 26, 149 (1976)

CHAPTER 2 -- The Experimental Apparatus

2.A -- Introduction

This chapter describes the apparatus used in this experiment. LASS, the Large Aperture Solenoid Spectrometer facility at SLAC, was the framework, consisting of a large superconducting solenoid magnet surrounding the hydrogen target, several sets of spark and proportional chambers, a multi-cell Cerenkov counter, and a large dipole spectrometer magnet preceded and followed by spark and proportional chambers(1). LASS was modified for electron identification by lengthening the Cerenkov counter and adding a wall of shower counters. The following sections describe the beam line, the numerous and diverse detectors, and their layout in LASS.

2.B -- Overview of LASS

Fig. 2.B.1 shows a cross section of the whole apparatus viewed from above. The solenoid magnet was 4 meters long and 1 meter in radius. The upstream end was a solid iron disk with a hole for the beam to enter. The superconducting windings were divided into four coils, each inside a separate cryostat ring. Plane chamber packages fit in the narrow spaces between the rings, covering the entire solenoid bore. A solid iron ring after the last coil acted

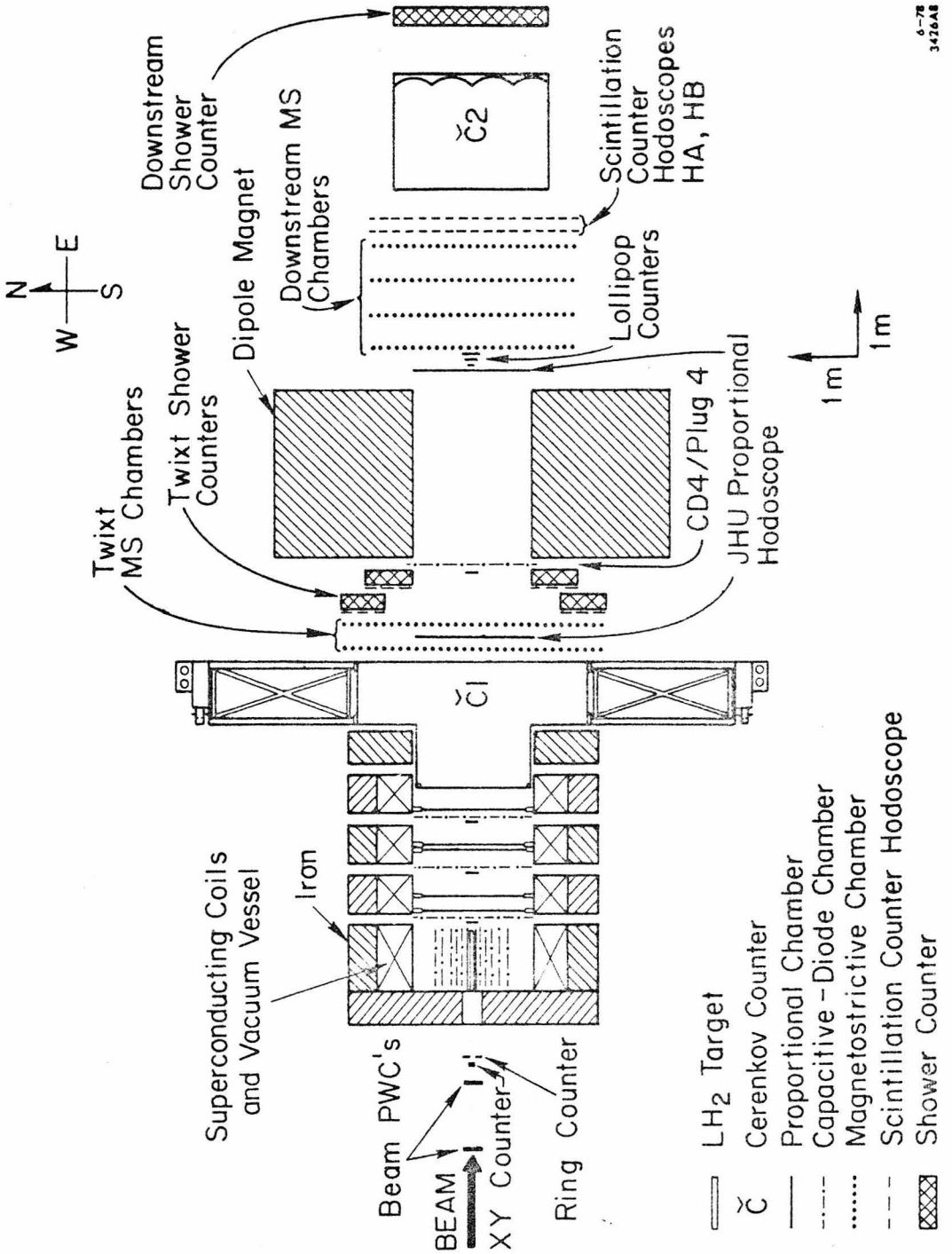

Figure 2.B.1: LASS Spectrometer

as magnetic flux return path.

Beam entered the solenoid magnet parallel to its axis and along the 22.4 kilogauss field. Charged particles produced in the target followed a helical path forward (or backward) through the magnet. The radius of the helix was proportional to the transverse momentum (P_t) of the particle. A 350 MeV/c P_t particle just skimmed the inside of the magnet (a helix with a radius of 0.5 meter). The pitch of the helix (meters/turn) was proportional to the longitudinal momentum (P_l). A 500 MeV/c P_l particle rotated through one radian in 70 cm., about the distance between plane chambers.

Particles with large transverse momentum hit the inside wall of the solenoid unless a correspondingly large longitudinal momentum (1 GeV/c P_l was needed for a P_t of 350 MeV/c, 4 Gev/c P_l for 1 GeV/c P_t) carried them out the end soon enough. Those with low forward momentum hit the wall without intersecting any plane chambers. Cylindrical chambers surrounding the target measured these. For very forward particles, the solenoid package did not accurately determine the momentum. These particles passed through the dipole magnet. The chambers before and after it were intended to determine the momentum from the bend in the horizontal plane. (The dipole had a field integral of 20 kG•m, and an aperture of about 2 m. horizontally by 1 m.

vertically.) Fig. 2.B.2 shows the magnetic field due to the solenoid and dipole.

The field near the solenoid made conventional magnetostrictive readout of spark chambers impractical. The spark chambers (called the CD chambers) in the solenoid used a capacitor-diode readout method. The center of these chambers was deadened because of their long memory time and the high particle multiplicity near the beam path. The dead spot in each was covered by a small area proportional wire chamber ("plug" chambers). Three of these chamber packages (plug1/CD1, plug2/CD2, plug3/CD3) slid between the coils. Two large active area proportional chambers (called 1.5 and 2.5) were installed inside coils 2 and 3. (More chambers have since been added.) The path of a forward particle intersected five measuring planes. Three induced charge readout proportional chambers (trigger chambers TA,TB,TC) with rings of wedge shaped pads (polar coordinate readout) were also mounted inside the coils. (It was once intended that fast logic make these signals into a selectable $P_1 - P_2$ trigger.)

The cylindrical chamber package surrounded the target inside coil 1. It consisted of a cylindrical proportional chamber and ten concentric spark chambers with capacitor-diode readout.

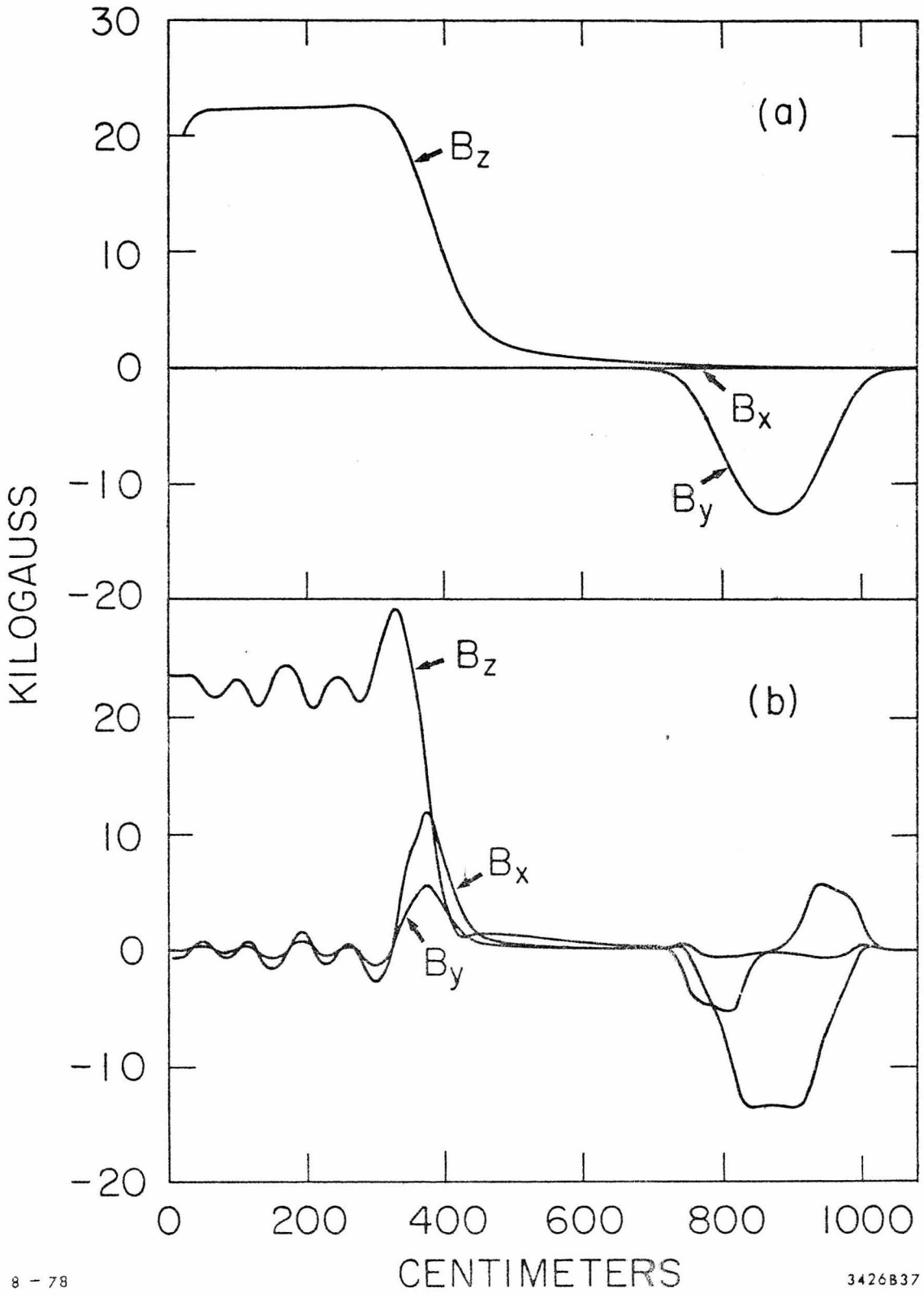

Figure 2.B.2: Magnetic field components as a function of Z: a) along X=0, Y=0; b) along X=75 cm., Y=35 cm.

The region between the end of the solenoid and the dipole is called the twixt-region. The solenoid field develops a large radial component here, which complicates track reconstruction. Particles entering this region pass through the 38 cell atmospheric pressure Cerenkov counter (C1) and several spark chambers. Some pass through the aperture of the dipole magnet and some hit its front face. The main shower counter wall was mounted on the front face of the dipole.

A relatively low refractive index gas was needed to identify electrons in C1. Air was used, giving a pion threshold of 5.8 GeV/c. The light output was small, necessitating the extension of the beginning of C1 from the last iron ring to the middle of coil 4. CD4-plug4 was displaced and used in front of the shower counter wall and dipole. The other twixt-region chambers were two large magnetostrictive readout spark chambers (MS1T and MS2T) and a vertical wire proportional hodoscope (JH-UP) between the MS chambers.

Four MS chambers (MS1D through MS4D) measured tracks behind the dipole. Another proportional hodoscope (JH-DN) just in front of MS1D provided timing information. Behind the last chamber were two scintillation counter hodoscopes (HA and HB), a large Cerenkov counter (C2) and a large shower counter (Group B SC), not used in this experiment. The 40 inch bubble chamber stored behind the shower counter was

also not used in this experiment. Other detectors not mentioned here are discussed in the next sections (mostly scintillators associated with the beam system).

The gas systems, power supplies, magnetic field shielding systems, and readout electronics associated with the spectrometer detectors are not described. An exception is the cylindrical chamber system which is described in greater detail in Appendix 1. The data acquisition system is described in chapter 3.

2.C -- Beam System

SLAC beamline 20-21 (shown in fig. 2.C) transported to LASS particles produced by the interaction of the 20 GeV/c, 1.5 mA., primary electron beam with a beryllium target. The beam spill lasted 1.6 microsec., repeated up to 180 times per second.

Collimators in the beam line were adjusted to allow about 4 pions to reach the target per pulse. (The usable rate was limited to 10 particles per spill in order to aviod multiple interactions. In practice, the long lifetime of residual ions from old tracks in the spark chambers necessitated a lower trigger rate, which was accomplished by reducing the number of pions per spill.) The beam was focused by alternating horizontally and vertically focusing quadrapole

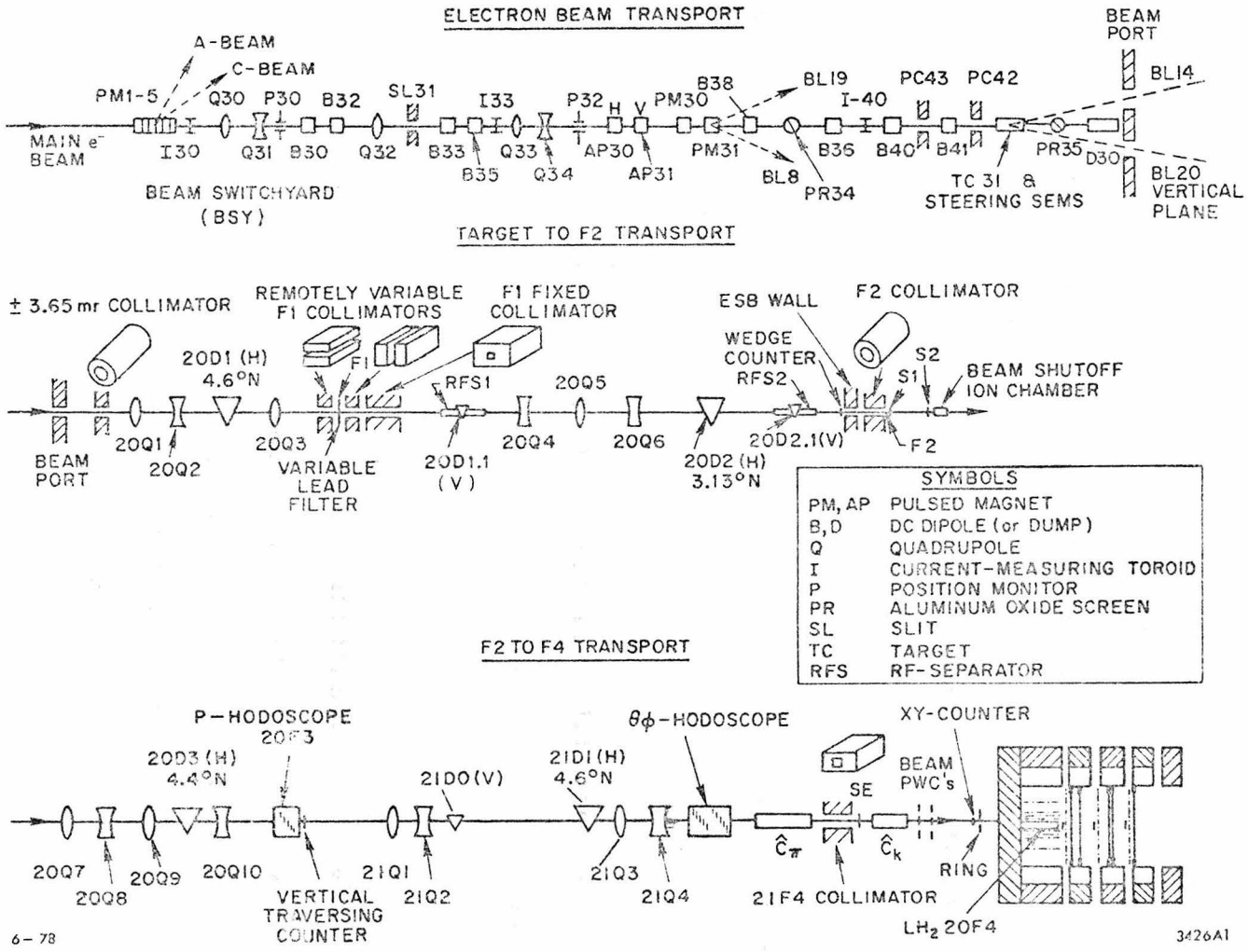

Figure 2.C: SLAC Beamline 21

magnets, and the position of a particle at the first focus (F1) depended on its momentum. A variable slit lead collimator passed only particles with momentum of 16 GeV/c ±2%. A thin lead filter at F1 removed electrons from the beam. The magnets after F1 brought the beam to a second achromatic focus (F2). The beamline has been described in detail elsewhere(2).

Particle-type separation was possible using the RF separators between F1 and F2. (The separation was based on the dispersion in space of particles from the same accelerator bunch due to velocity differences.) The separators were not used since 94% of the particles produced were pions.

Like F1 and F2, F3 was a momentum dispersed focus and F4 was achromatic. The P-hodoscope located at F3, with six scintillation counter fingers overlapping to form 11 bins, tagged the momentum of each particle to ±.25%. F4 was located at the far end of the hydrogen target.

Two threshold Cerenkov counters checked the mass of the beam particles. C-pi tagged pions, and C-k tagged pions and kaons. They were located near the end of the beam line, just outside and inside the LASS building respectively. These counters did not differentiate pions from muons, and 2.3% of the accepted beam particles were muons.

The theta-phi (named for pinning down the track angle) hodoscope located in front of C-pi tagged the position of the particles with 0.127 cm. scintillation counter fingers in x and y. Downstream, near the target, were two sets of proportional wire chambers one meter apart. Beam position and direction were calculated from the theta-phi hodoscope and these chambers. The main computer provided online histograms of the beam position which was adjusted manually when necessary.

Scintillation counter SE, just inside the building before C-k, generated a narrow (2 nsec.) pulse, the master timing pulse in the trigger logic circuit. A final check of the beam position was made by the XY and RING scintillation counter assembly. The XY was a square divided into four quadrants (each 1.91 cm. square, 0.64 cm. thick) which counted equally if the beam was centered. The RING counter, also with four sections, surrounded the XY and was used to veto particles outside the main beam spot.

2.D -- Liquid Hydrogen Target

The target assembly was separate from the solenoid magnet. It was mounted on rails so that the hydrogen vessel slid into position inside the solenoid through the hole in the iron end plate. Fig. 2.D shows the target construction.

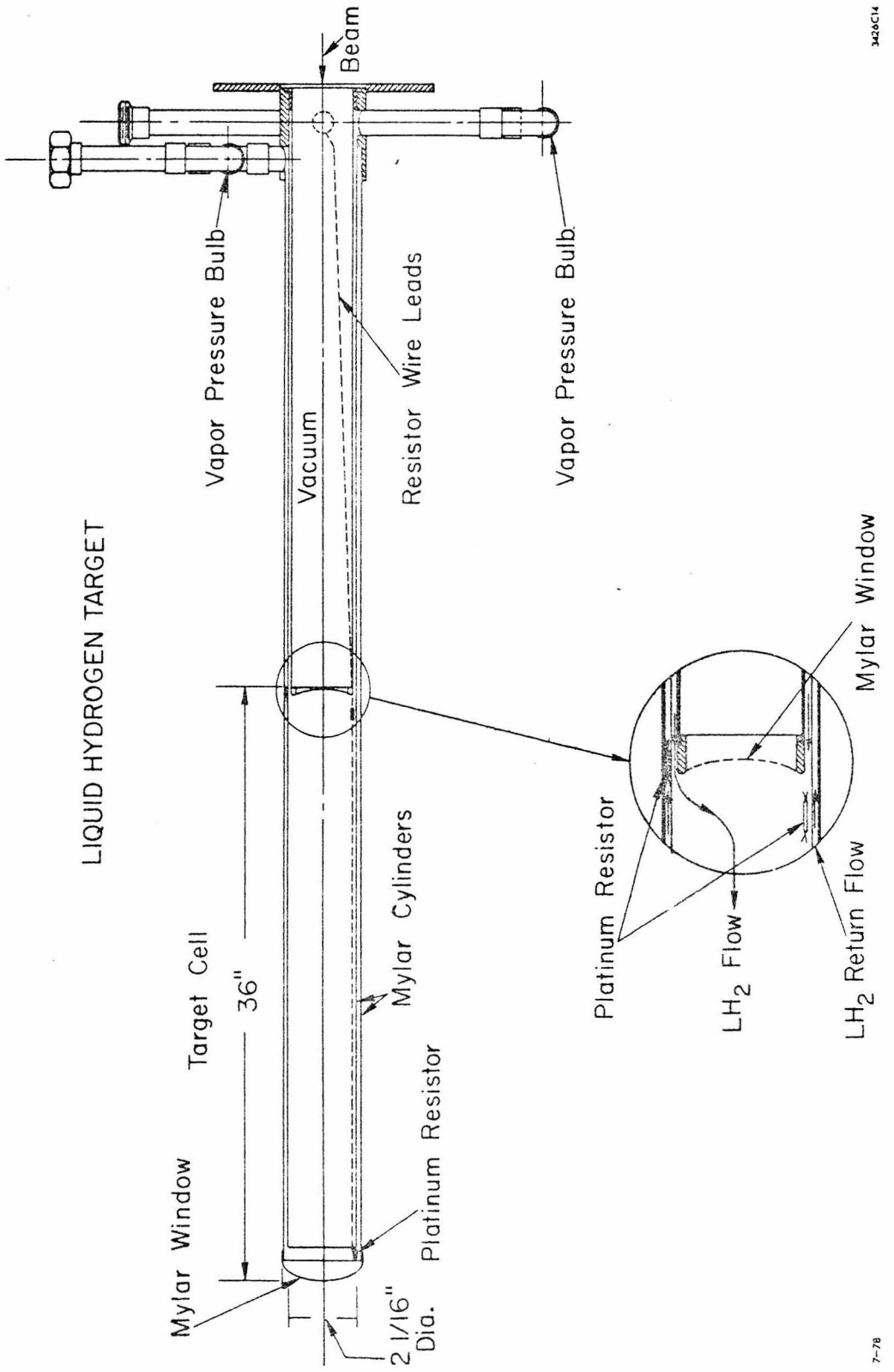

Figure 2.D: Liquid hydrogen target

The hydrogen vessel was a cylinder 91.4 cm. long and 52.4 mm. in diameter, with end windows 0.13 mm. thick. The hydrogen vessel was enclosed in an evacuated aluminum tube .71 mm. thick with a 0.13 mm. mylar window at downstream end.

2.E -- Proportional Wire Chambers

All the proportional chambers in LASS used the same electronics. The electronics were unusual in that they recorded in a memory the time when a signal occurred on a wire in 25 nsec. bins(3). The low duty cycle of SLAC necessitated a high instantaneous particle flux which led to the need for the precise time resolution. This memory feature also avoided the need for delaying the signals with a cable to await a final trigger. In this experiment, wrong time tracks and tracks without proportional chamber points were rejected.

The planar proportional chambers had a central wire plane surrounded by two cathode planes for each coordinate measured. The chambers measured the X and Y coordinates, and another coordinate (called E) at an angle between X and Y. This measurement was necessary to resolve ambiguities in matching up the X and Y coordinates. In track fitting it was used with the same weight as X and Y. The wire planes consisted of gold plated tungsten wires stretched on an

aluminum frame. The cathodes were aluminized mylar sheets etched to prevent operation outside the active area. The cathodes were connected to negative high voltage with the sense wires at ground. The sandwich of three planes was enclosed between two aluminized mylar sheets which served as a gas bag and blocked light.

In the plug chambers, each plane has 256 wires spaced at 1.016 mm. The E plane wires are at 35 degrees to the horizontal. The frames are large so as not to obstruct the solenoid bore, so that the wires are 2 meters long. The cathodes are etched away outside the 33 cm. square region where sensitivity is desired. The X and Y wires are supported with mylar strips perpendicular to them, limiting the active length to ±14 cm. The mylar strips for the E wires are placed the same as for the Y wires.

The 1.5 and 2.5 chambers have planes with 640 wires each, 2.032 mm. apart. The wires are supported at two places inside the active area. The E plane wires run at 45 degrees.

The beam chambers have four planes each. The first (BM-UP) has an X plane, a Y plane, and an E and a P plane at ±45 degrees. The second (BM-DN) has an X, a Y, and an X' and a Y' displaced half a wire spacing from X and Y to double the resolution. There are 64 wires per plane spaced at 1.016

mm.

JH-UP and JH-DN have only one plane with vertical wires. The active area covers the aperture of the dipole. There are 512 wires in each, spaced at 4.064 mm.

The trigger chambers cathodes were divided into three concentric rings, each divided into 128 wedge shaped segments. The approximate radii of the boundaries of the rings (in cm.) were: 3, 7, 23, 59 for TA; (no inner ring), 32, 48, 71 for TB; 17, 25, 38, 55 for TC. They were used for track verification only because the resolution was so poor.

The cylindrical proportional chamber construction was different due to the requirement of low density of matter in the path of scattered particles. It is shown in fig. 2.E. The basic structural support was the inner styrofoam tube 3.5 mm. thick bonded to a layers of 0.005 inch aluminized mylar on the inside and outside. The 160 anode wires were stretched between two plexiglas rings glued to the mylar. Wire spacing was 2.037 mm., at a radius of 5.188 cm. An outer mylar-styrofoam tube served as the other cathode and gas seal. There is a plexiglas ring in the center of the active length to stabilize the wires which caused a 15 mm. dead area.

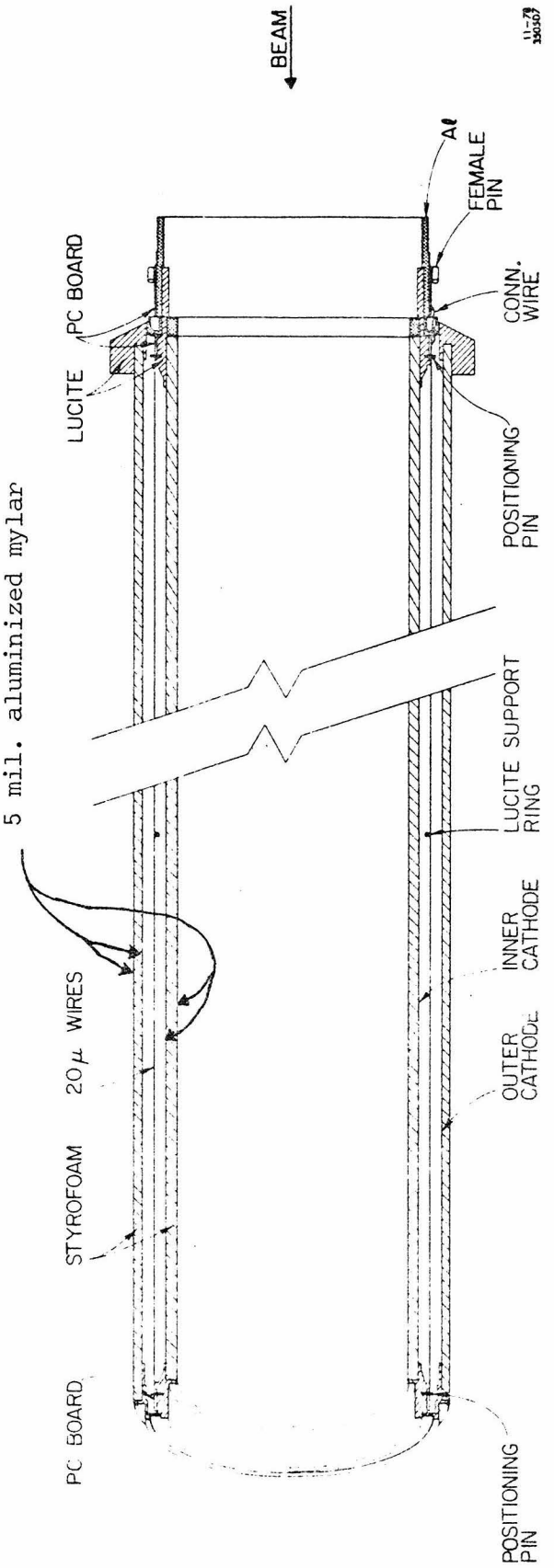

Figure 2.E: Cylindrical proportional chamber

2.F -- Spark Chambers

Four different kinds of spark chambers were used: cylindrical capacitor-diode, plane capacitor-diode, and two sizes of magnetostrictive chambers.

All the plane chambers had four readout planes: X, Y, E, and P. The X and Y were one spark gap, the E and P another. The E and P wires were ±30 degrees from vertical in the MS-downstream and CD chambers, 25 degrees in the MS-twixt. The planes were a woven mesh of nylon filaments and aluminum wires. The wire spacing was about 1 mm, which varied over the wire cloth. It was mapped and corrected in software. All the plane chambers were deadened in the region of the beam by the insertion of a polyurethane disk into the gap (radius 10.8 cm. for CD's, 3.68 cm. for MS's).

The twixt MS chambers were 4 m. wide by 2 m. high, and the downstream chambers were 3 by 1.5 m. The following scheme was devised to cancel the relatively large field for the twixt chamber wands: The wands were wrapped with fine enameled wire which carried a large current (10 amps, at a voltage drop of several hundred volts). This created a field that opposed the longitudinal component of the spectrometer field. This field, arising from the solenoid, was radially symmetric; the component along the wand was zero in the center and in opposite directions at the ends.

The canceling coil winding direction reversed in the center. The spectrometer field was somewhat overcompensated near the center and very undercompensated near the ends. The efficiency near the ends was therefore poor. (A varying pitch winding would have properly solved the problem.)

In the capacitor diode chambers, each wire was connected to its own small readout circuit. Spark current in the wire charged a capacitor which remained charged and was read electronically long after the spark was over. In the plane CD chambers, a network of diodes and data busses allowed the capacitors to be interrogated serially by a small number of discriminators. This had the advantage of a low cost per wire and small size. The disadvantage was the rectification of inductive voltage drops along the busses caused by enormous rates of change of current in the spark circuit. This problem has been solved over a period of several years. When this experiment ran, the efficiency was still in the 60-80% range, and crosstalk between wires where the currents were large led to sparks apparently spanning many wires and a distortion of the apparent position of the spark.

The cylindrical CD chamber readout was more straightforward and also more bulky and expensive. There was a discriminator for each wire and no circuitry was shared. The worst feature of this system was that each capacitor and its discriminator were separated by 25 feet of wire. The

only problems with the readout circuitry have been failures of capacitors or diodes associated with 2% of the wires (after 10**7 pulses, about 10^5 sparks per wire).

The cylindrical chambers were made of concentric mylar cylinders with wires glued to their surfaces, shown in fig. 2.F. The cylinders are supported only by spacer rings at the ends. There were problems with the straightness of the cylinders and consequently with variations in their spacing. This led to regions of low efficiency and regions of breakdown. It was found that a large concentration of alcohol in the gas mixture allowed the chambers to operate over the wide range of electric field strength that occurred with the nonuniform gap spacing. The breakdown problem increased with use (possibly because of roughening of the surface of the wires, especially in the inner chambers where the spark rate per wire was high). Several wires were cut before the chambers were installed, because of breakdown, and one chamber was shut off during the running because a breakdown in it was shunting current away from the adjacent chamber. The efficiency of these chambers ranged from 60 to 98%.

There were two types of chambers in the cylindrical package. In one the wires were glued at a slight angle so that the azimuthal angle varied along the length of the cylinder. The wires on the two sides of the gap pitched in opposite

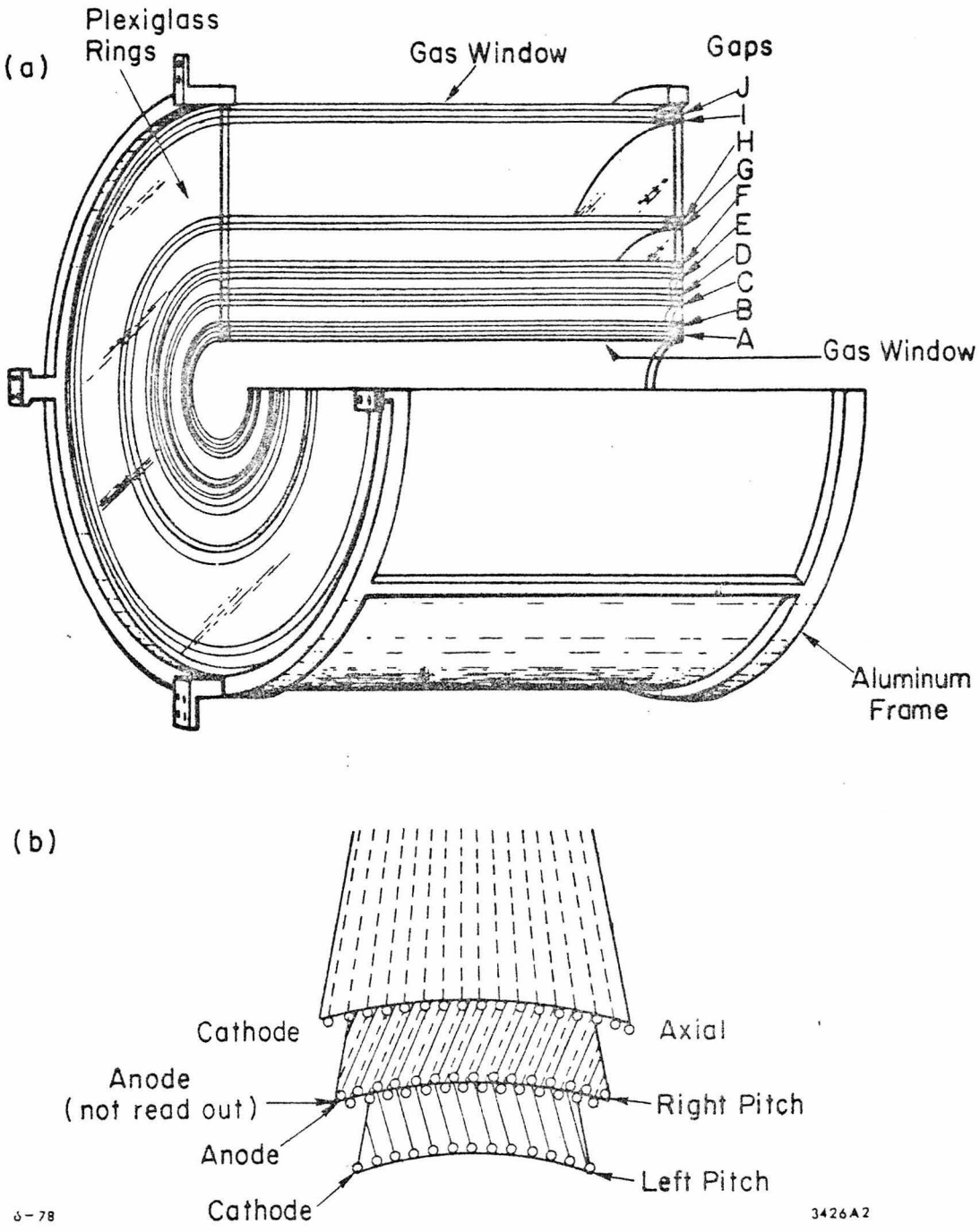

Figure 2.F: Cylindrical spark chamber:
a) package b) detail of gap

directions so that looking at both sides gave the lengthwise position as well as the azimuthal angle. In the other type, the wires were parallel to the axis and only one side was read out. The chamber package consisted of five of the first type alternating with five of the second. The radii varied from 10 cm. to 60 cm., and the length was 1 meter.

The cylindrical spark chamber package was the major piece of experimental apparatus for which the author was responsible, and is described more fully in Appendix 1. The supporting electronics and gas system are described as well as results of performance tests.

The gas for all the spark chambers was standard neon-helium, purified and recirculated. Alcohol was added separately to the gas for the cylinders and the (plane) CD chambers. The MS chambers ran without alcohol. The high voltage pulse for all the chambers (300 nsec. long, about 4 kV depending on the chamber) was formed by switching a charged coaxial cable by means of a thyratron tube. All chambers had a d.c. clearing field of about 40 volts to remove the ions left over from the spark. There was also a pulsed clearing field of 250 volts applied to the MS and cylinder chambers for extra clearing after the sparking. The recovery time for the cylinder and CD chambers was 50 msec. Running faster produced an increased spark multiplicity. This effect is not understood. The experiment was run with a compromise

deadtime of 25 msec. between events.

2.G -- Cerenkov Counters

Four Cerenkov counters were used in the experiment. Two were used for tagging the beam particles. The other two were large and complex, with large angular acceptance, to tag scattered particles. All were threshold counters, accepting all angles of Cerenkov light.

The beam Cerenkovs were simple pressurized pipes in the beam line. C-pi was 5 m. long and 20 cm. in diameter, filled with hydrogen at 25 psig. (Threshold gamma 37; 5.2 GeV/c for pions.) C-k was 1 meter by 20 cm. diameter filled with carbon dioxide at 35 psig. (Threshold gamma 18; 9.1 GeV/c for kaons.)

The multicell Cerenkov counter, C1, was originally designed to identify pions using a high refractive index gas at atmospheric pressure. In this experiment, air had the right index for separating electrons and hadrons below 5 GeV/c (threshold for electrons, 20 MeV; for pions, 5.8 GeV). Because of the low refractive index of air an insufficient amount of light was radiated. The efficiency was therefore increased by moving the upstream window 60 cm. farther upstream and sealing it to the inner surface of the solenoid. The cell partitions were not extended since the

Cerenkov cone was narrow (maximum 24 milliradians) and generally illuminated only one cell at a time). The counter is drawn in fig. 2.G.

The counter was divided into four radial regions. The innermost region was split into two cells and the outer three annular regions were divided into twelve cells each. The radial distance from axis of the inner and outer walls of the cells increased with distance from the target so that stiff tracks tend to stay in one cell. A thin mylar mirror at the end of each cell (just past the end of the solenoid) reflected the light outward, through a long extension arm, where it was focused by an ultraviolet-transmitting fresnel lens onto a 2 inch photomultiplier tube. Even at the end of the extension arm, the tube required heavy shielding from the magnetic field. The extension arms for the inner cells ran out behind those of the outer cells so that the inner cells were longer. Not counting the upstream extension, the outer cells were 1.25 m. and the inner two 2 m. long. The bottom three cells of each of the outer three rings were not installed when the experiment was run. These 9 cells are referred to as the "unequipped region".

Cerenkov C2 was an eight segment pressurized counter with several centimeters of material in the path of tracks. It was filled with freon-12 at a pressure of 44 psig., making it useful only for separating protons from kaons. It was

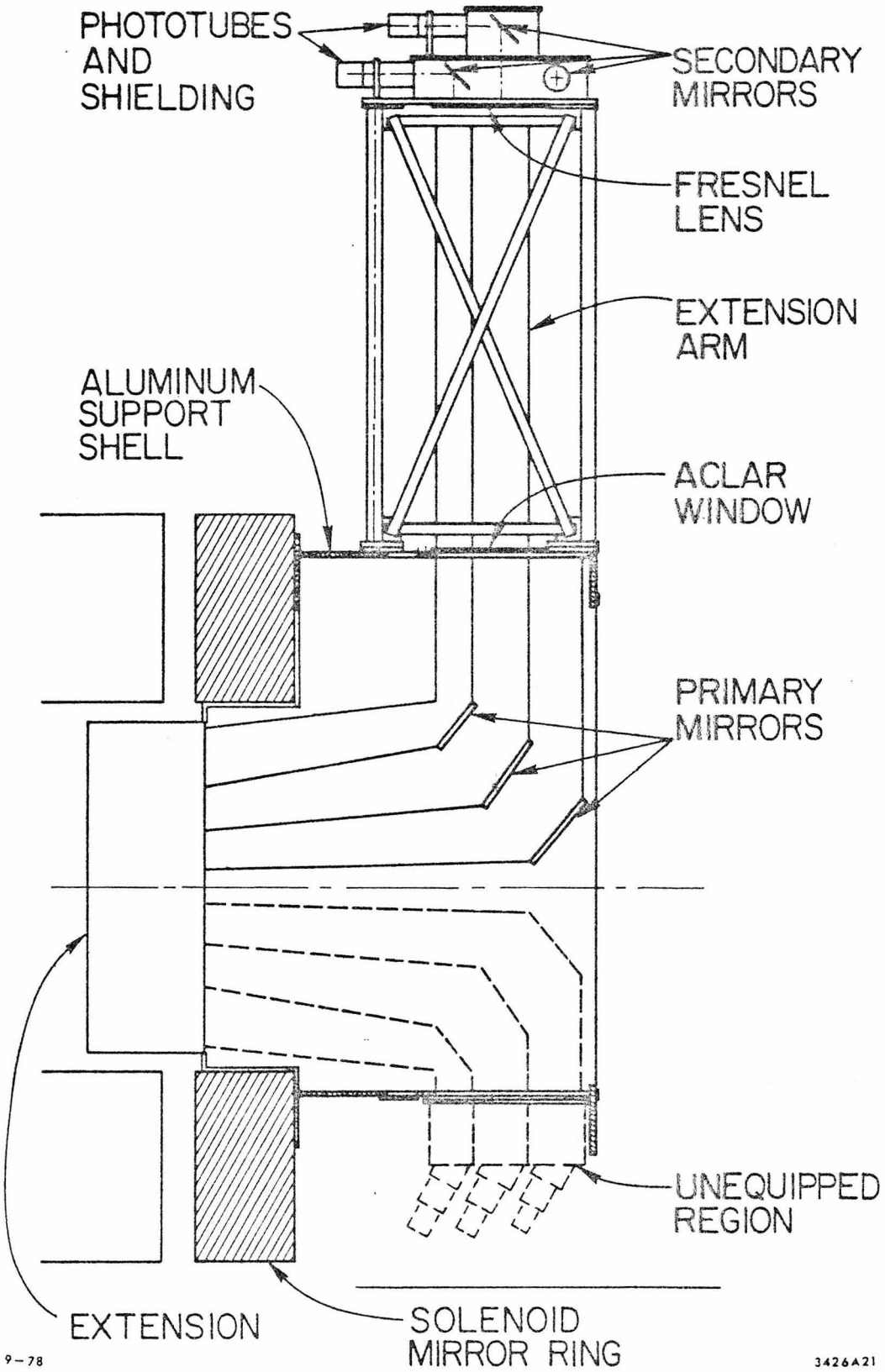

Figure 2.G: C1 Cherenkov counter, side view

not studied or calibrated in this analysis.

2.H -- Shower Counters

Three types of shower counters, built earlier for other experiments, were used. They were named after their owners, SLAC Group B, SLAC Group E, and Cal Tech. Ten Group E counters and three Cal Tech counter pairs were mounted on the front face of the dipole magnet as shown in fig. 2.H. Along with C1, these counters recognized the electrons. The Group B shower counter at the downstream end of the experiment tagged some of the high energy tracks passing through the dipole. (A track straight down the solenoid center needed 5 Gev/c to hit this counter.) It has not been studied or used in this analysis.

The Group E counters were designed to give uniform light output over the entire active area (18 by 25 inches). They consisted of 16 0.25 in. sheets of wavelength-shifter-doped lucite with interspersed lead (type-metal) sheets, and five 2 inch phototubes along one edge. The lead sheets were tapered to absorb less energy near the far end where the light acceptance was lower. The average pulse height (from the five tubes summed) varied only 10% over the face.

The Cal Tech counters consist of two 80 x 9 x 0.5 inch lead sheets interspersed with three 1.125 in. sheets of lucite.

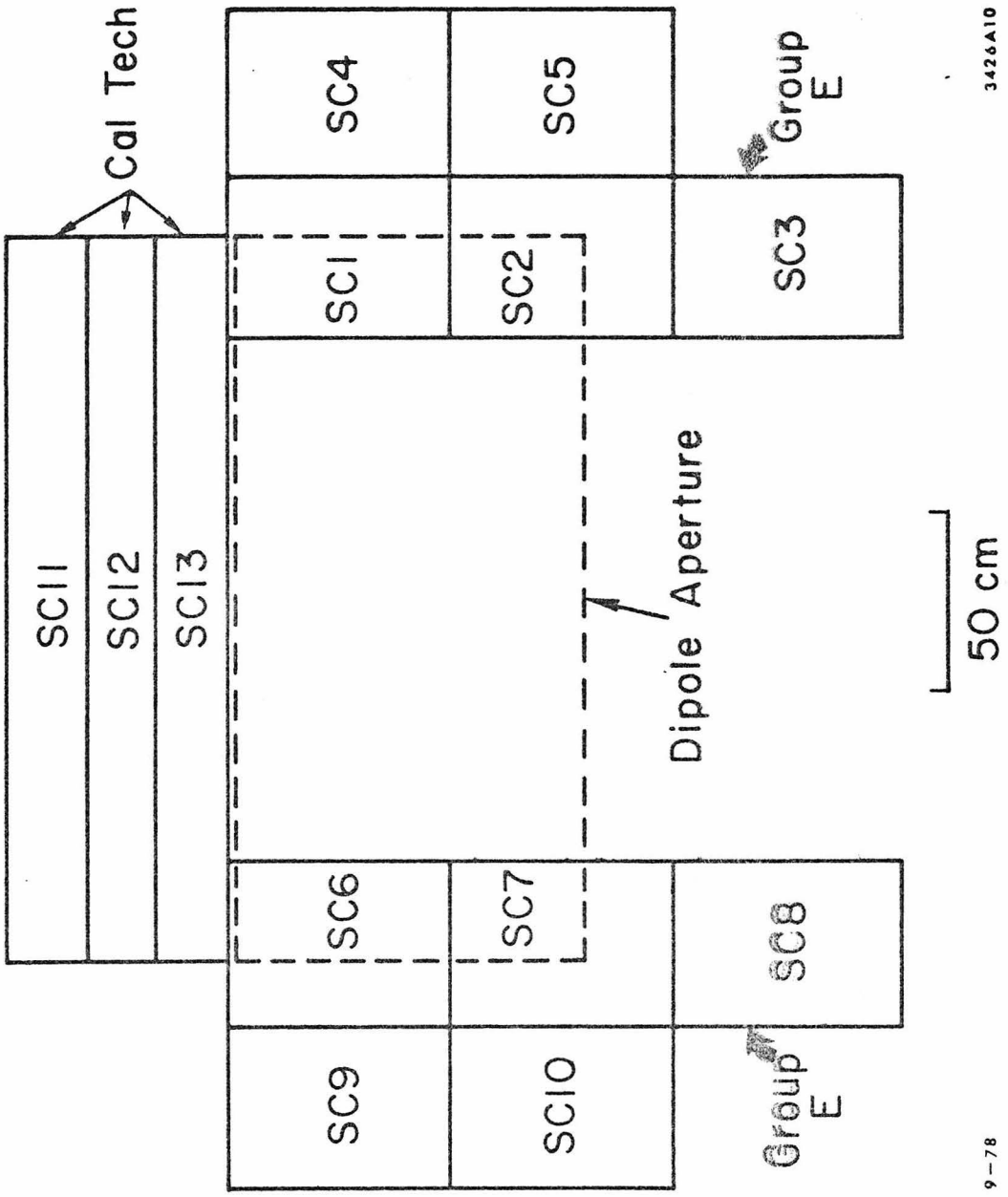

Figure 2.H: Dipole-face shower counters

The light pipes at each of the long ends, meant for five inch tubes were adapted to two inch tubes with reflective mylar shaped into a truncated cone (shielding the large tubes from the magnet was not practical). Two such counters with 0.25 in. lead in front of the first and between the two gave acceptable energy resolution when the signals from all four tubes were summed. In spite of the lucite being very yellow, the light output varied less than 20% from the ends to the middle.

Both types of counters were preceded by 0.25 in. scintillation counters (called "gamma-veto" counters) to differentiate electrons from photons. The signals from these were used in the trigger as well as in the analysis. The phototube signals from each counter of both types were treated as follows: The signal from the last dynode was inverted and summed for all tubes in the counter (five for GPB, four for CIT). The sum was discriminated for use in the trigger and its presence recorded. The anode signals were separately digitized and recorded. In the analysis the individual phototube pulse heights are weighted according to the known position of a hit to get better energy resolution.

The Group B and CIT counters were calibrated at several positions over their faces with electrons and pions at three beam energies. This information was used in the analysis to convert from pulse height to energy as a function of the

position of a track. Several counters were calibrated again, as a check, after the experiment was dismantled(4).

2.I -- Photomultipliers and Downstream Scintillators

Those phototubes giving analog information, in C1 and the three types of shower counters, were outfitted with light emitting diodes for gain calibration. The calibration was done automatically before each run by pulsing the LED's 2048 times and recording the pulse heights from the tubes. The tube high voltage was manually adjusted when the pulse height drifted too far (20%). When the shower counters were recalibrated at the end of the experiment the light output from the LED's was found to have drifted in some cases by as much as a factor of two. The response of the shower counters was therefore not constant over the experiment. No attempt was made to treat differently pulse height data recorded at different times. The electron detection efficiency used to correct the result was obtained from electron trigger events recorded over the whole run, and therefore, to first order, took these variations into account.

The phototube high voltage was supplied from adjustable resistor and gas tube voltage divider boxes. The voltage to each tube was monitored by a multiplexed digital voltmeter which was read by the computer every 256 events.

All tubes were shielded from the magnetic field of the solenoid by a layer of mu-metal inside a thick steel tube extending well past the photocathode region. The tubes in the twixt-region (C1, GpB and CIT shower counters and gamma-vetos) required another steel tube and a so called "bucking coil" which carried a current adjusted to cancel the field.

There were three areas where simple scintillation counters were used in the experiment: in the beam system; the gamma-veto counters; and the downstream arrays, HA and HB hodoscopes and the lollipop counters. The downstream counters are described below. These arrays were used in some of the triggers (although not in the main electron trigger).

Hodoscope HA consisted of 42 rectangular paddles 8 by 33 inches, arranged side by side, 21 above and below center, without spaces. The center counters on the top and bottom were only 4 inches wide. They were raised and lowered to leave a 4 by 4 inch hole for the undeflected beam. Hodoscope HB was similar, having ten 4 inch counters surrounded by seven 6 inch counters on each side. One counter top and bottom just off center were displaced to make the 4 by 4 hole. These hodoscopes were used to corroborate the timing of downstream tracks.

The lollipop counters were a set of three concentric circular counters of radii 8.6, 11.4, and 19.7 cm., stacked back to back. The array was hung between the dipole and JH-DN centered on the beam spot. They were used to define two of the auxiliary triggers.

References for chapter 2

1. The detector components are described in more detail in C. L. Woody, A Study of Electron Pair Production in 16.1 GeV/c pi-minus proton Collisions Using a Large Aperture Solenoid Spectrometer, Ph.D. Thesis, Johns Hopkins University (1978).

2. Design and Operation of SLAC Beamline 20-21-22, F. C. Winkleman, SLAC Report 160 (1973).

3. Shapiro, S. L. et. al., IEEE Trans. Nucl. Sci., NS-23, No.1, 264 (1976).
Shapiro, S. L. et. al., IEEE Trans. Nucl. Sci., NS-23, No. 1, 269 (1976).

4. op. cit., C. L. Woody, Thesis, Appendix B.

CHAPTER 3 -- Electronics: Trigger and Data Acquisition

3.A -- Introduction

Five separate triggers were generated and or-ed together to form the master trigger which caused the spark chambers to fire, the proportional chamber system to hold its memory of the preceeding 500 nsec., and the digitizers and binary latches to record the phototube information. The trigger pulse also started the digital controllers which transferred the data into the memory of a PDP-11 computer.

When the data transfer was completed, the computer was signaled. The PDP-11 then reset the controllers to read the next event, compressed the data, and initiated the transfer to two other computers. These computers recorded the event data on magnetic tape, and analyzed some of the events to produce visual displays (showing chamber and scintillator hits and reconstructed tracks) and to monitor the performance of some detectors.

One of the destination computers was the SLAC triplex (two IBM 370/168s and a IBM 360/91) which did most of the computing for SLAC. The other was an IBM 1800 which was used only to record data when the triplex was not operating. The program on the triplex resided in the memory of one of the 168s along with several other jobs. The "LASS" job was

different in that it needed to be executed soon after data were presented by the PDP-11 or the experiment would stop. The PDP-11 was able to store two completed events and still read in a third. The LASS program was built in the framework of a program called REALTIME which could demand execution with a higher priority than normal computation jobs. The REALTIME program transferred data between subtasks, for example from the subtask that received data from the PDP-11 to one that wrote it onto tape.

3.B -- PDP-11 System

Almost no data processing was done by the PDP-11 which functioned as a controller. It was connected to the other computers and the detector controllers by direct memory access (DMA). There were DMA input ports for: CAMAC which read binary latches (phototube discriminators and complex logic signals), pulse height digitizers, fast time digitizers, scalers and the multiplexed digital voltmeter; the proportional chamber system; the cylindrical spark chambers; the CD spark chambers (two DMA ports); and the MS chamber system. There were two DMA output ports, one for the IBM 1800 and one which connected to an IBM SYSTEM/7, a minicomputer extension of the triplex system. The PDP-11 assigned to each detector DMA controller before each event an area in memory to be filled. It also assigned an area for messages coming in from the triplex computer. When it

finished formatting a data buffer it could instruct the SYS7 or 1800 DMA to transmit it directly from memory. The DMAs signaled the PDP-11 with an interrupt when the data transmission was complete. The detector DMAs each received a done signal from their respective device controllers and did not signal the PDP-11 until all were finished.

The data acquisition was controlled using the PDP-11 control panel. It consisted of many switches for entering information like date and run number, and for choosing a configuration of detectors and computers. There were pushbuttons for starting and ending runs, and indicators used to display the state of the PDP-11 program. It also produced logic levels used to control the fast logic and test devices for the detectors. It controlled a "self scan" panel which displayed data logging information: tape i.d., file number, and run number.

Besides administering data collection the PDP-11 calculated the size and layout of data buffers depending on which detectors were requested. It sent begin-run and end-run messages to the data logging computers and waited for confirmation. It read and transmitted the scaler and voltmeter data every 256 events and at end of run. It summed internally a beam-counting scaler that was reset every event, and it ran the LED phototube calibration at the beginning of each run. The LED test was similar to normal

data taking with the following exceptions: The PDP-11 enabled the LED pulser which flashed the LED's 20 times per second. Only the CAMAC DMA was enabled (it was triggered by the LED pulse instead of a beam particle). The pulse height values were summed over 64 repititions, before being transmitted to avoid the speed limitation of the intercomputer link. The only data processing done by the PDP-11 was the summing of the software scaler (BTEZ) and the LED pulse height records.

3.C -- Fast Logic: Triggers, Gating and Scalers

The fast logic generated the master trigger signal which started the recording of the event. The trigger was a coincidence of a pion entering the target, an enable signal called the event gate, and a trigger signal formed out of signals from Cerenkov C1, shower counters, and scintillation counters. This trigger signal was the logical sum ("or") of five separate triggers, each selecting a particular kind of event.

The event gate was a coincidence of the run gate, the PDP-11 OK flip flop, spark chamber deadtime, and clearing field OK. The 11 OK flip flop was turned off by the master trigger and on by the PDP-11 when it was ready for the next event (less than 10 msec. except when data buffers backed up). The spark chamber deadtime was a simple 25 msec. delay to give

the spark chambers time to clear out old ions. The clearing field OK signal stopped the experiment when the pulsed clearing field power supply for the MS chambers latched up. The event gated scalers counted only when the experiment was ready to be triggered. The numbers they showed corresponded to the events actually recorded. They were reset at the beginning of each run.

Counters SE, XY, Ring, C-k, C-pi defined the beam signal (BEAMTRIG). The logic is shown in fig. 3.C.1. The four segment XY counter produced signals XYGE1 when any segment fired, and XYGE2 when two were hit within 20 nsec. XYGE2 was used as a veto to avoid events too close in time. Two particles passing through the same segment were not vetoed. The ring counter tagged particles which could hit the target wall or the support structure and produce a splash. A hit in it vetoed the beam signal if it occurred within 150 nsec. (before or after). The final pion trigger required C-k and C-pi to fire as well. Signals were generated also for kaons, protons, and "junkons" (C-k fired without C-pi). The master trigger came about 500 nsec. after the particle entered the target.

Five kinds of triggers were generated, named T0,T1,T2,T3, and T4. T0 was the electron trigger. It required at least one of the cells in C1 to fire and at least one of the dipole face shower counters, plus its gamma-veto counter, to

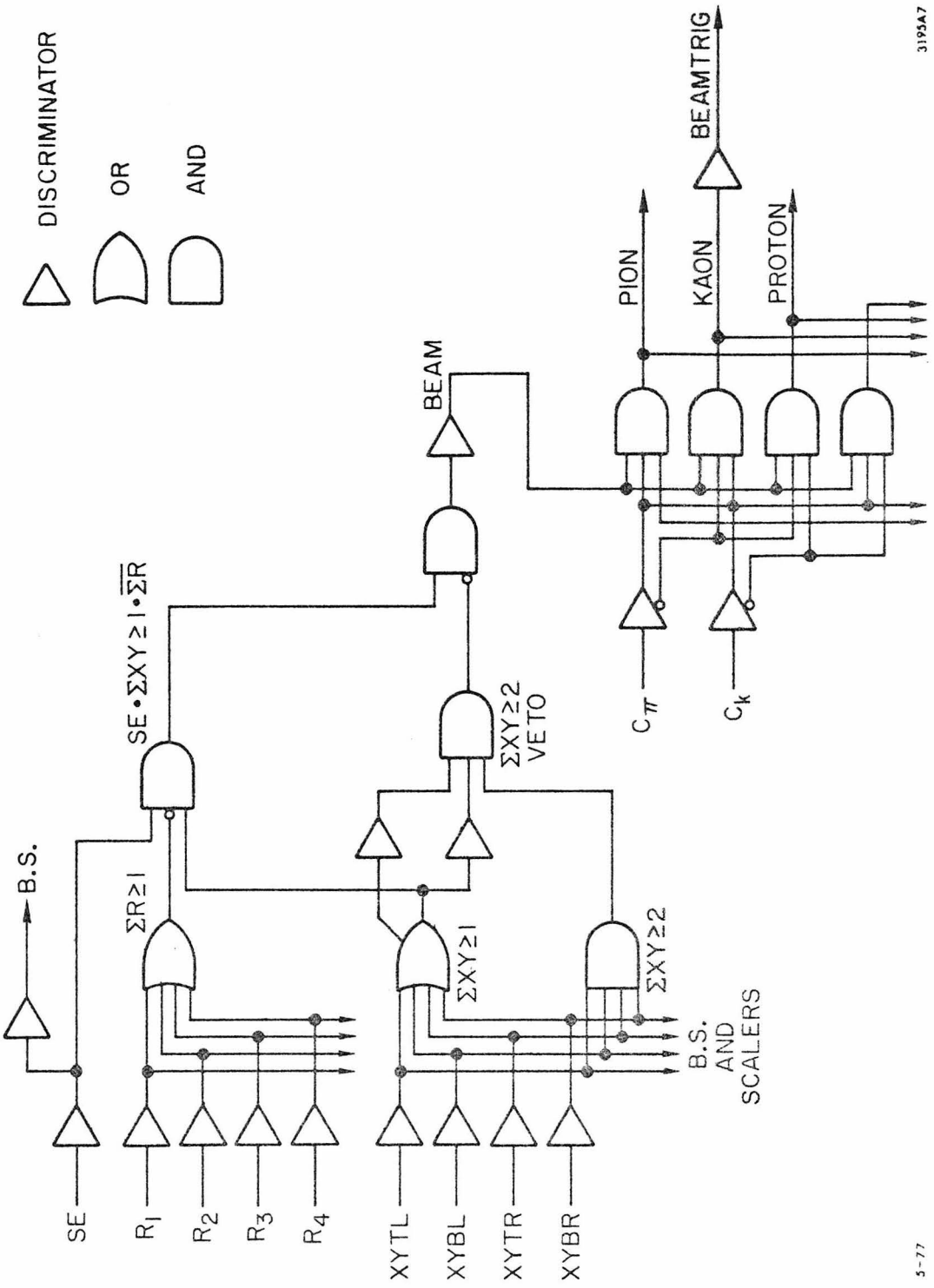

Figure 3.C.1: Beam logic

fire. The logic is shown in fig. 3.C.2. The threshold in C1 corresponded to 1 ADC count above threshold, in the shower counters, about 600 ADC counts above threshold.

T1 was the total interaction trigger, requiring only the absence of a signal from the 8 inch lollipop counter (LP3) in the undeflected beam path. The data from this trigger were compared to a total cross section bubble chamber experiment to check the normalization and the track finding efficiency. The T1 data were used also to estimate the probability of C1 and shower counter "cell sharing" preventing electron identification in electron pair events ("cell sharing" cuts are described in sections 5.B.2 and 5.B.3).

T2 was the elastic trigger, requiring one and only one element of HA and one and only one of HB firing (undeflected beam went through the central hole). The elastic data were intended to check the accuracy of momentum and angle measurement, of the proton at large angle and of the pion in the downstream (dipole) system. (This check was not completed.)

T3 was the beam straight through trigger, requiring the 4 inch lollipop (LP1). T3 was used online as a trigger for measuring proportional chamber efficiencies since one and only one hit should be seen in each. The recorded data were

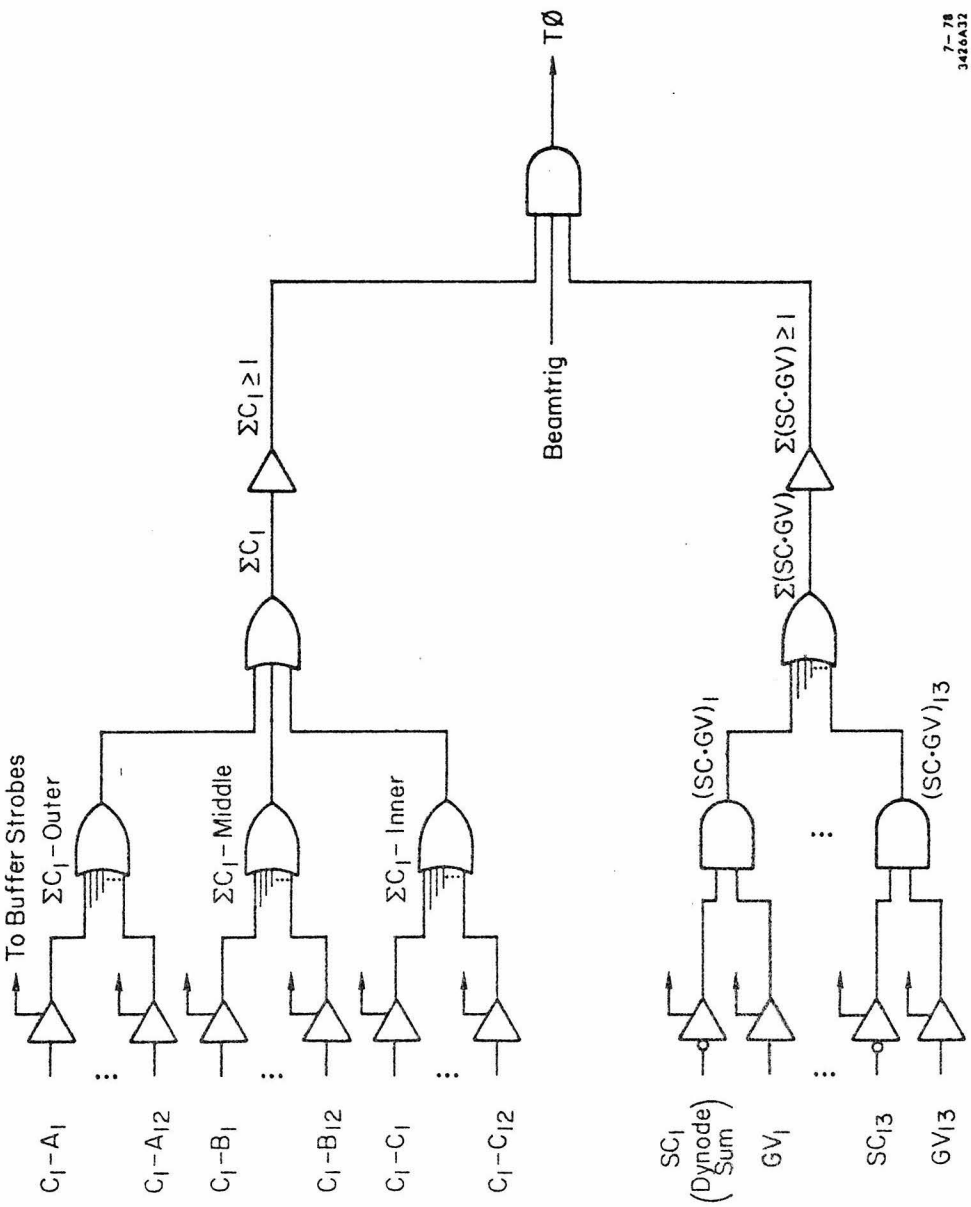

Figure 3.C.2: Electron (TO) trigger

used to align the chambers.

T4, the gamma-veto trigger, required one or more gamma-veto counters to fire. These events were topologically similar to the T0 trigger, but accepted all charged tracks. It was intended to provide large angle tracks to estimate hadron punch-through. Lacking computer time to process these data, the T1 data sufficed for that purpose.

Triggers T1-T4 occurred more frequently than T0. They were "scaled down" by counting each and passing it on to the master trigger only once in a preset number of occurrences. They were each divided by a factor of 20 to 40 (these numbers were not kept fixed) with the result that they made up about half the triggers.

3.D -- CAMAC and Chamber Readout

The phototube signal latches (buffer strobes), the pulse digitizers (ADC's), the time digitizers (TDC's), the scalers, and the multichannel digital voltmeter (DVM) were all controlled and read by CAMAC. There were two CAMAC controllers. The one that read the buffer strobes, ADC's, and TDC's (and also one scaler), operated every event, writing pulse height values and bits indicating which counters fired as part of the event record. The other branch controlled the scalers and DVM modules. It was read

by the PDP-11 every 256 events. This branch was also read by a versatile scaler display system which connected to many identical display units with thumb switches. The scaler count corresponding to the channel number on the switch was continuously fetched and displayed on each, so that any scaler could be dialed in and displayed.

The controllers for the proportional chamber, the CD spark chambers, and the cylindrical spark chambers were similar to each other. Each represented hits in the chamber as an address of the first wire on and a "width" giving the number of adjacent wires. This method reduced the number of data entries for hits which were more than one wire wide. The proportional chamber hits were grouped this way for each memory time slot. The analysis program expanded the clusters, grouped the time slots for the same wire, and regrouped the wires into clusters. The proportional chamber system was read out in an expandable chain so that chambers could be added without rewiring. The cylindrical system had fixed "fiducial" simulated hits which gave immediate warning if it miscounted. The MS chamber system had a set of timers for each wand, which were stopped one at a time as spark pulses were received, up to a total of 16 hits. Additional hits were not recorded.

3.E -- Realtime Network

The "realtime" program made it possible to use the triplex computer system for realtime data acquisition and control. It ran as a batch job and controlled the execution of and communication between various tasks contained in the job. The REALTIME job was composed of the following "tasks": a task that controlled the SYS7 data channel, a task that wrote the data tapes, a task that contained the trackfinding program and analyzed a sample of the incoming events, a task that controlled the graphics display scope (located in the control room), and several tasks concerned with the realtime management. Tasks which could not wait for their turn in the normal time sharing sequence were executed at high priority(1).

Realtime differed from a dedicated minicomputer system in the greater speed and memory space of the IBM 370 and the availability of peripheral devices (which would be too expensive to buy and maintain if they were not shared by all users at SLAC). The high density tape drives (6250 bits per inch, four times normal high density) were crucial to managing the data. Even with the high density, tapes were filled every hour, and a total of 185 were written. Another advantage was the existing software for the triplex: a good text editing and file storage system; an optimizing fortran compiler; and a graphics display system.

The disadvantage was that the triplex system was out of the hands of the experimenters. The triplex often went down, the operating system being so complicated that its detailed operation was not understood. But for the cost of a tape drive, writing tape with the PDP-11 would have been ideal.

References for chapter 3

1. Introduction to SLAC's Real-Time System, I. Denecke, Stanford Center for Information Processing at SLAC (SCSSCIP) (1974).

CHAPTER 4 -- Trackfinding Program

4.A -- Introduction

This chapter describes the computer program which read the raw data tapes and produced data summary tapes of the parameters of reconstructed tracks. Section 4.B describes the mathematical conventions, coordinate systems and the parameterization of the tracks as helices. Sections 4.C through 4.E describe the steps by which the raw coordinates of hits in the chambers were combined into match-points, match-points into track candidates, and the candidates checked for plausibility and fitted to nearby coordinates. The final chamber alignment procedure using the tracks is described in section 4.F. Section 4.G describes a comparison of tracks found in interaction trigger data with tracks produced in a bubble chamber experiment using the same beam. Section 4.H describes a pre-trackfinding filter that quickly determined that a large number of events could not contain an electron and removed them. Several other cuts are described also.

Making a good trackfinding program was a difficult task. The mathematical complexity of helical tracks, and of the irregularity of the chamber types conspired with low chamber efficiency, spurious hits, and a trigger that selected "dirty" events (i.e. containing electron showers). It was

necessary to include approximately 20% spurious tracks in order not to reject the real tracks. The most important trade-off was computer time versus the examination of a maximum number of track candidates. Most of the complicated procedures described below were intended to eliminate implausible combinations at an early stage.

4.B -- Mathematical Conventions

Two coordinate systems were used to represent tracks and points in the computer program. An orthonormal system took Z as the direction of the beam (increasing downbeam), Y as up, and X to complete the system in the right-handed sense (North). The origin was taken at the center of the solenoid for X and Y, and the inside face of the upbeam solenoid end-plate for Z. The other useful system was a cylindrical system (R, φ, and Z) centered at X=0 and Y=0 when referring to the cylindrical chambers, or, when referring to the helical tracks, concentric with the helix. The momentum of the track (discussed in Chapter 5) is expressed in spherical coordinates, P, Θ and φ.) and P were constant for the length of the helix.

The magnetic field was treated as constant, uniform, and parallel to the Z axis, in the region of Z from 0 to 285 cm. (up to Plug3/CD3). Beyond 285 cm., the path was calculated by numerically integrating the equations of motion, using a

representation of the field interpolated between measured values with a polynomial.

Inside the uniform field region, the track was a helix characterized by five parameters: X_o and Y_o, the coordinates of the axis; R_o, the radius; B_o, the inverse pitch, $B_o = d\varphi/dZ = -CH \cdot R_o / TAN(\theta)$; and a starting φ value, φ_o, at a given Z position Z_o. (Charge, CH, was +1 or -1 for positive and negative tracks respectively.) Rather than taking Z at a fixed place, it was used to denote the beginning of the track, and recorded as a sixth quantity. CH and were recorded also, either one determining the direction of motion of the particle along the helix. Using the parameterization, the X and Y position at a given Z was given by:

$$\varphi = \varphi_o + B_o \cdot (Z - Z_o),$$

$$X = X_o + R_o \cdot COS(\varphi),$$

$$Y = Y_o + R_o \cdot SIN(\varphi).$$

The momentum was related to the helix by

$$P = a \cdot \sqrt{(R_o^2 + 1/B_o^2)},$$

$$P_t = a \cdot R_o = P \cdot SIN(\theta),$$

$$P_l = -a \cdot CH/B_o = P \cdot COS(\theta),$$

$$P_x = -CH \cdot P_t \cdot SIN(\varphi),$$

$$P_y = CH \cdot P_t \cdot COS(\varphi),$$

where a = (magnetic field) $\cdot$ 0.000300 = .006735 for 22.4 kG.

4.C -- Match Point Making

Making "match-points" was the first step in reducing the number of track candidates searched. When N tracks hit a chamber that measures only X and Y coordinates, there are N^2 X-Y pairs to choose from. By measuring the hits along a redundant (linearly dependent) direction, and requiring the projection of the X-Y point in the extra direction to be corroborated by a measured hit, most false pairs are eliminated. The corroborated pairs are called match-points. The plane proportional chambers (3 plugs, and the 1.5 and 2.5 PWC's) measured X, Y, and "E" in separate gaps about 1 cm. apart. The CD plane chambers measured X and Y in the same gap, and the two redundant coordinates, "E" and "P", in another gap, about 5 cm. away. The separation in Z necessitated a large corroboration window, because the slope of the track was not known at that stage. In the cylindrical CD chambers, all L-R (left and right pitched wires) combinations were taken. This was possible because of the small angle between the L and R directions. False combinations represented a point outside the physical Z limits of the chambers unless the two hits were close together in ϕ.)

The raw data blocks from the chamber readout controllers were converted into lists of physical coordinates, using previously determined alignment constants. Adjacent hits

were combined into clusters. (In the case of the CD planes in which the readout of every second wire was less sensitive, single wire gaps were permitted within a cluster.) The raw data were occasionally garbled, due usually to noise in the readout logic or a larger amount of data than fitted in the fixed PDP-11 buffer space. Processing was terminated for such events.

Match-points were reviewed after each new track was accepted. Those coordinates used in good quality tracks were "poisoned", that is, flagged and ignored in the process of subsequent trackfinding. In a region of 20 cm. radius in chambers 1 and 1.5, hits were sometimes coincident, so that poisoning was not done in that region.

In the CD planes, X-Y combinations were corroborated by a hit in either the E or P plane (or both) within 2 cm. of a point projected from the X-Y plane along a line from the middle of the target. These match-points were recorded at the X, Y, and Z of the X-Y chamber hit. E-P pairs were corroborated by an X or a Y coordinate, and recorded at the X and Y calculated from the E and P, and at the Z of the E-P gap. E-P match-points were not recorded when they coincided with an X-Y match-points.

The proportional chamber match-point criteria were more complex. The corroboration distance was taken as the

minimum of the discrepancies formed by projecting the three coordinates to a common Z along several lines, having various slopes and directions. The distance was converted into a quality value (standard error) by dividing by an estimate of the chamber resolutions. Match-points which shared coordinates with more than 4 match-points of better quality were dropped. For good quality match-points, the number of shared coordinates was allowed to be higher, up to 7. Finally, all pairs of unused coordinates were recorded also (as "two-way",i.e. uncorroborated, match-points).

The match-points were stored in order of decreasing quality, with the two-ways last. This caused those most likely to be real to be tried first for trackfinding. Many of the less likely points were thereby poisoned before being tried.

Certain events had large numbers of hits inside small areas in the chambers, leading to large numbers of match-points, large numbers of apparently good trial helices, and execution times up to 100 times the average. An empirical test for such events was more than 50 match-points in two of the three CD chambers, or a product of the number of match-points in the three plug chambers greater than 1500. Processing was terminated for these events (called "overflows" in section 5.G.3).

4.D -- Trackfinding Algorithm

Track candidates were defined by match-points in three so-called "pivotal planes". If the intersections with chambers were corroborated by nearby hits, the candidate was fitted by minimizing the CHI-squared of the agreement between the helix and the nearby chamber hits. The program looped over different sets of pivotal planes, starting with those that were likely to produce the largest number of tracks per unit time. (This minimized the computer time because extra match-points were eliminated early.) The difference in the geometry of the plane and cylindrical chambers dictated that all pivotal "planes" (plane or cylindrical detector surfaces) were of one type or the other. So-called "beam calls" consisted of only two pivotal planes, where the helix was constrained to intersect the beam track inside the target volume.

For a given set of pivotal planes, all triplets of match-points were examined. Most were rejected quickly because the change in φ divided by the change in Z, was different between the first and second planes, than between the second and third. The change in φ was evaluated without calculating the helix center by using the fact that the angle between two points on a circle measured from the center is twice the angle measured from the third point on the circumference. The ratio of $d\varphi/dZ$ (between 1 and 2, and

2 and 3) was required to be within a window around 1.0 whose width increased empirically for points defining small radii. This increase allowed for the greater relative importance of resolution errors and scattering for small radii. In the case of the beam calls, the constancy of d /dZ was assumed and used to calculate the point of intersection with the beam track. This point was required to be not more than 10 cm. outside the target.

For candidates passing the initial cuts, the helix was refitted using the previously determined slope to correctly project the pivotal coordinates to a common Z position. The corrected CD match-points were required to have a corroboration distance less than 5 mm. and the CHI-squared of the helix fit was cut above 25. If the candidate survived, the other chambers were examined for corroborating coordinates within a distance of 2.5 wire spacings (4.0 if the chamber was not between the pivotal chambers). Coordinates poisoned for match-point making were acceptable for corroboration. The trigger chambers which resolved position very poorly were nonetheless gainfully used to corroborate the track candidates. The number of corroborated coordinates (out of the possible number where the track intersected a chamber) was required to be greater than 65% when a large number of chambers were traversed, and ranging up to 100% for a small number of possible coordinates. Corroborated tracks were passed to the fitting

subroutine.

4.E -- Fitting Procedure: Tracks and Vertices

This section describes the algorithm for finding the best helix fit to a set of chamber coordinates. The procedure for fitting a best vertex to a set of tracks was quite similar and is therefore described here also. The basic procedure in both cases was to minimize the value of CHI-squared by varying the parameters to be fitted.

For track fitting, CHI-squared was the sum of the squares of the distances between the hypothetical helix and the measured coordinates, normalized by the expected chamber resolution. The uncertainty of the final helix was expressed in an "error matrix" giving the coefficients of the second degree terms in the Taylor series expansion of the CHI-squared function centered at the best fit.

In order to fit a vertex, the CHI-squared was the sum of the squares of the distances from the hypothetical vertex point to each of the tracks, normalized according to the track error matrices. When making a vertex for two tracks that were parallel at some point (as described in section 4.E.1), there were often two points of closest approach. When this occurred, the vertex was fitted at both points, and the one with the lower CHI-squared was used.

The minimization algorithm was Newton's method generalized to 5 dimensions (3 for vertex fitting). If a new trial point gave a higher CHI-squared, another point was tried half as far away. (This usually solved the problem of large corrections in cases when the gradient was anomalously small.) After the first adjustment, coordinates which made a major contribution to the CHI-squared were dropped. The procedure was iterated until the change in CHI-squared was small, or for a maximum number of steps. The confidence level of the fit was computed from the CHI-squared and the number of degrees of freedom.

Fitted tracks with confidence levels below 10^{-8} were rejected. Tracks with less than 15 coordinates were cut at 10^{-2} because of the increased probability of spurious combinations of coordinates. If a new track had many coordinates in common with a previously accepted track, only the one with the higher confidence level was retained.

A large number of candidates were produced and subjected to various trials, many being rejected at each stage. As elsewhere in nature, only the fitted survived.

4.F -- Chamber Alignment.

The approximate position of the chambers was determined by

optical surveying. The positions were fine-tuned by measuring straight (field off) tracks with them.

The plane chambers were aligned in X and Y using beam tracks (T3 trigger) measured in the beam PWC's and the - scintillation hodoscope.

The Z position discrepancies of the plane chambers (plug, CD, and trigger) were checked by comparing the discrepancies in the X-Y position with the slope using wide angle (T4) field-off tracks. The slope was determined assuming the Z positions of chambers 1.5 and 2.5. The apparent position of the two sides of the CD chamber gaps coincided approximately at the middle of the physical gap. Discrepancies of several millimeters in the spacing between the X, Y, and E planes of all the proportional chambers were observed and have not been understood.

The cylindrical chambers were aligned in two steps. The package was first made self-consistent by centering the residual distributions for straight tracks. This left four degrees of freedom to be fixed: Z and (the longitudinal position and azimuthal rotation) of the package as a whole, and possible shifts in Z and that varied linearly with the radius of the chambers. The varying Z displacement appeared as an error in the of the track, and the varying rotation caused the track not to coincide with the beam

track at the center. A large set of straight tracks found in the cylindrical chambers transformed according to four parameters that mimicked these shifts and another four that mimicked a slope and displacement of the axis of the package. These eight parameters were adjusted to minimize the CHI-squared of the agreement (summed over all tracks) of the tracks with the beam track and the plane chamber hits. The four and Z parameters specified adjustments to the alignment constants. The effects of the slope and displacement of the axis were compensated at the trackfitting stage.

In the cylindrical spark chambers, the spark position displaced about 4 mm. in the azimuthal direction when the solenoid was magnetized. The direction of the change corresponded to the electric field of the high voltage pulse rather than the reverse clearing field. The displacement appeared only at the anode end. (The cathode displacements were less than 1 mm.) The shifts were compensated in the alignment constants.

4.G -- Bubble Chamber Comparison

This section summarizes the results of a comparison(1) between interaction trigger (T1) events analyzed by the trackfinding program and total cross section data from a bubble chamber experiment(2), pi-minus proton interactions at

16 GeV/c. The study checked trackfinding efficiency as a function of P and P and the absolute normalization.

The T1 trigger cross section was 42.2 millibarns. After correcting for empty target interactions, 22.2 millibarns were left. (Most of the empty target events came from upstream interactions where no tracks were found.) The bubble chamber cross section was 25.5 millibarns.

Fig. 4.G.1 shows the multiplicity distributions. The bubble chamber events were corrected for the simulated stopping of protons in the target. The T1 events were corrected for the empty target interactions. (The corrected cross section for zero track T1 events was negative 2 mb. Photon conversions were not rejected in the T1 triggers, and were not counted in the bubble chamber data.) Although the average multiplicity was 4.9 in both cases, the T1 events contained a greater number of events with an odd number of tracks, indicating the existence of spurious tracks as well as losses.

The bubble chamber tracks were flagged as reconstructible if they were compatible with the geometrical requirements of the trackfinding program, including the corroboration requirement assuming measured chamber efficiencies. T1 tracks (without empty target correction) are compared with reconstructible bubble chamber tracks in fig. 4.G.2 through

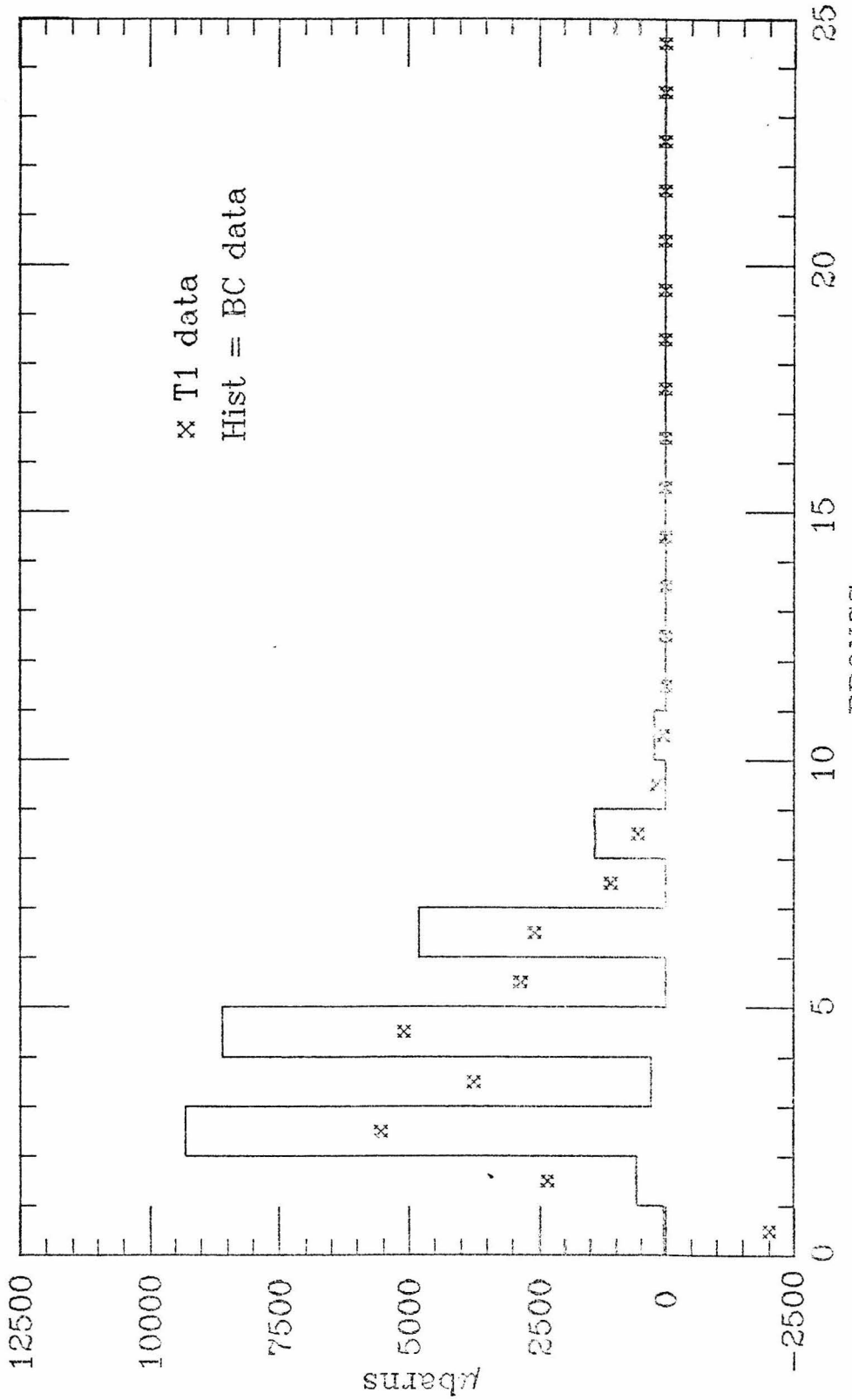

Figure 4.G.1: Comparison of multiplicity distributions:
T1 (full minus empty) and bubble chamber.

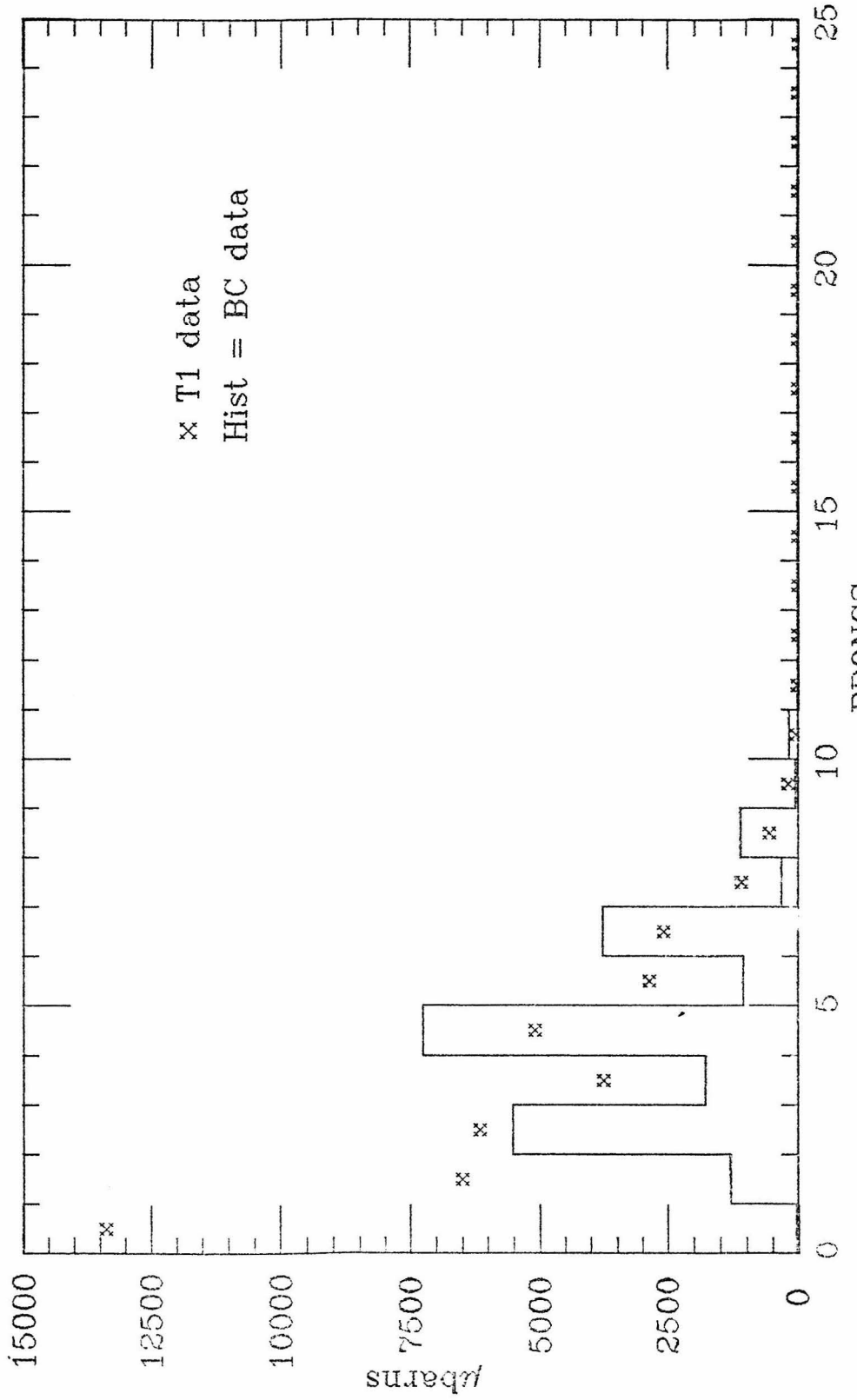

Figure 4.G.2: Comparison of multiplicity distributions:
T1 and "reconstructable" bubble chamber.

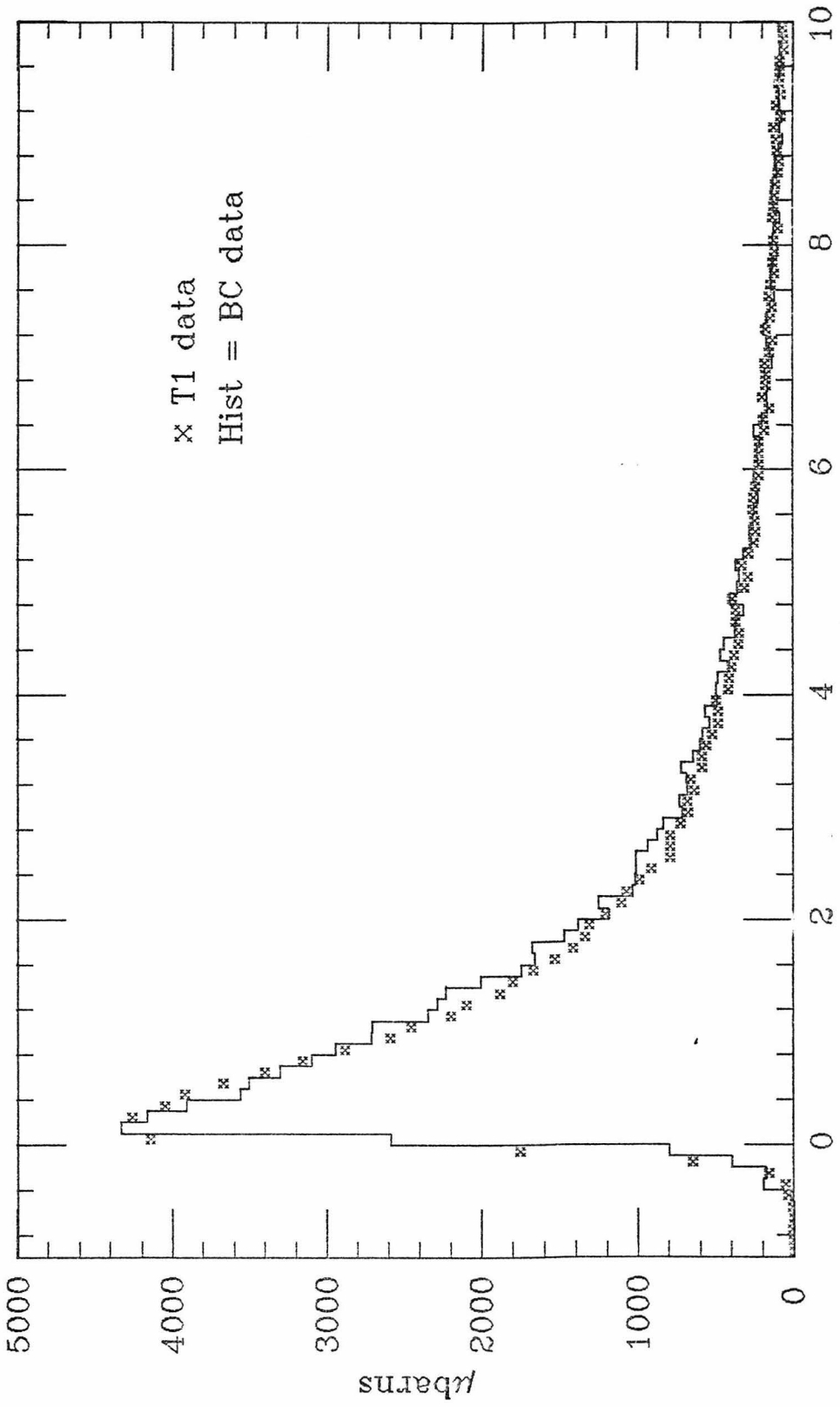

Figure 4.G.3: Comparison of P1 distributions of tracks from T1 and "reconstructable" bubble chamber.

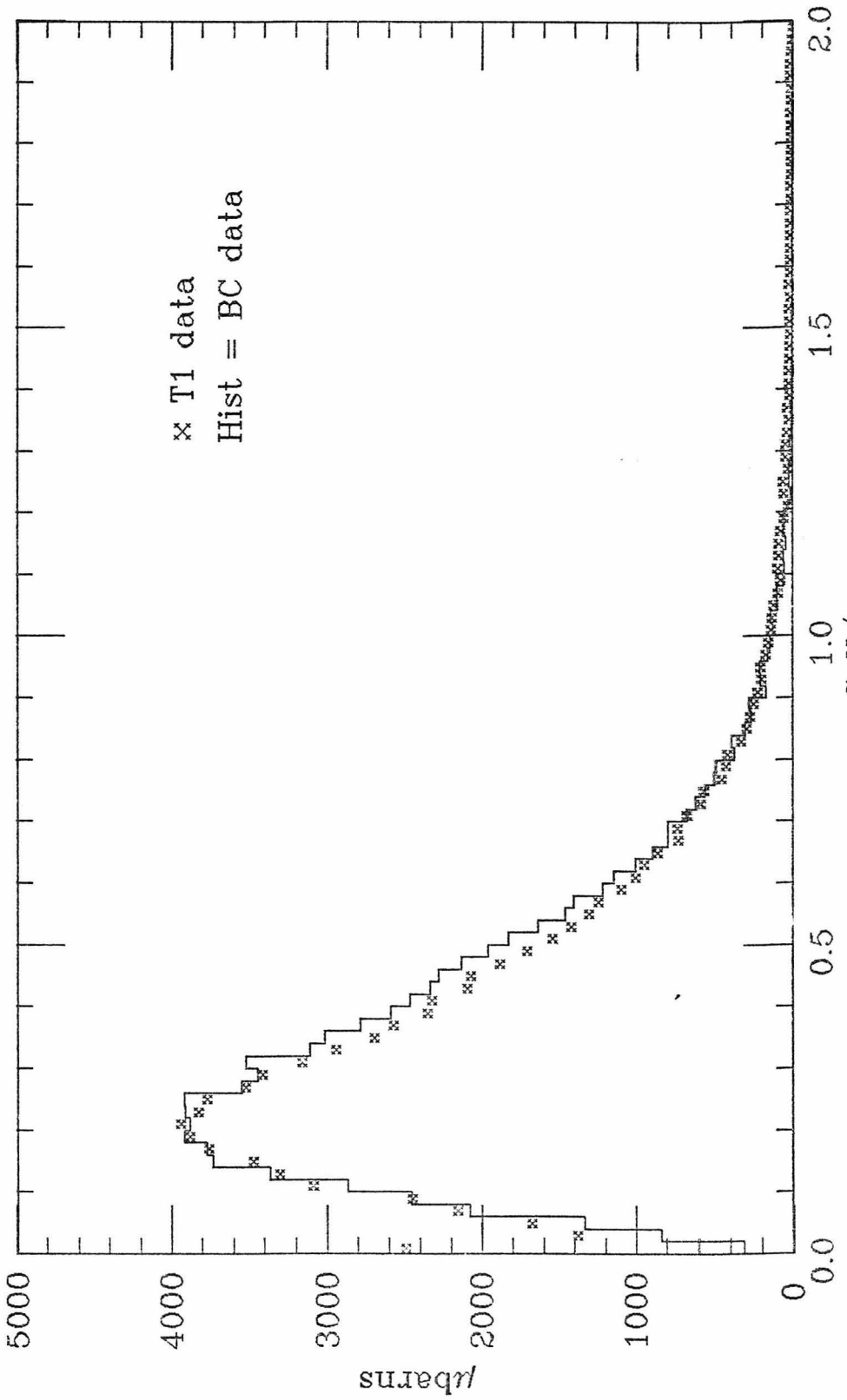

Figure 4.G.4: Comparison of Pt distributions of tracks from T1 and "reconstructable" bubble chamber.

4.G.4. The momentum distributions were in good agreement, but the multiplicity distributions were still quite different.

In order to understand the T1 multiplicity distribution, the bubble chamber multiplicity distribution was convoluted with a Poisson distribution simulating extra tracks. An additional trackfinding loss was applied independently to each track, and the normalization factor was allowed to float. The CHI-squared of the difference between the (empty target corrected) T1 and the adjusted bubble chamber distributions (for multiplicities one and above) was minimized as a function of the track loss probability, the extra track rate, and the normalization factor. The best fit occurred for a spurious track rate of 0.42±0.2 per event, a track efficiency of 97±5% per track, and a normalization of 1.06±0.15 (to increase the B.C. distribution). The multiplicity distributions are shown in fig. 4.G.5.

The comparison indicates that the reconstructible bubble chamber tracks corresponded rather well to the results of the trackfinding program. The reconstructibility tests were installed in the Monte Carlo program that estimated the trackfinding efficiency for electron pairs. The trackfinding efficiency determined in the Monte Carlo was believed to be correct within 5%, according to these

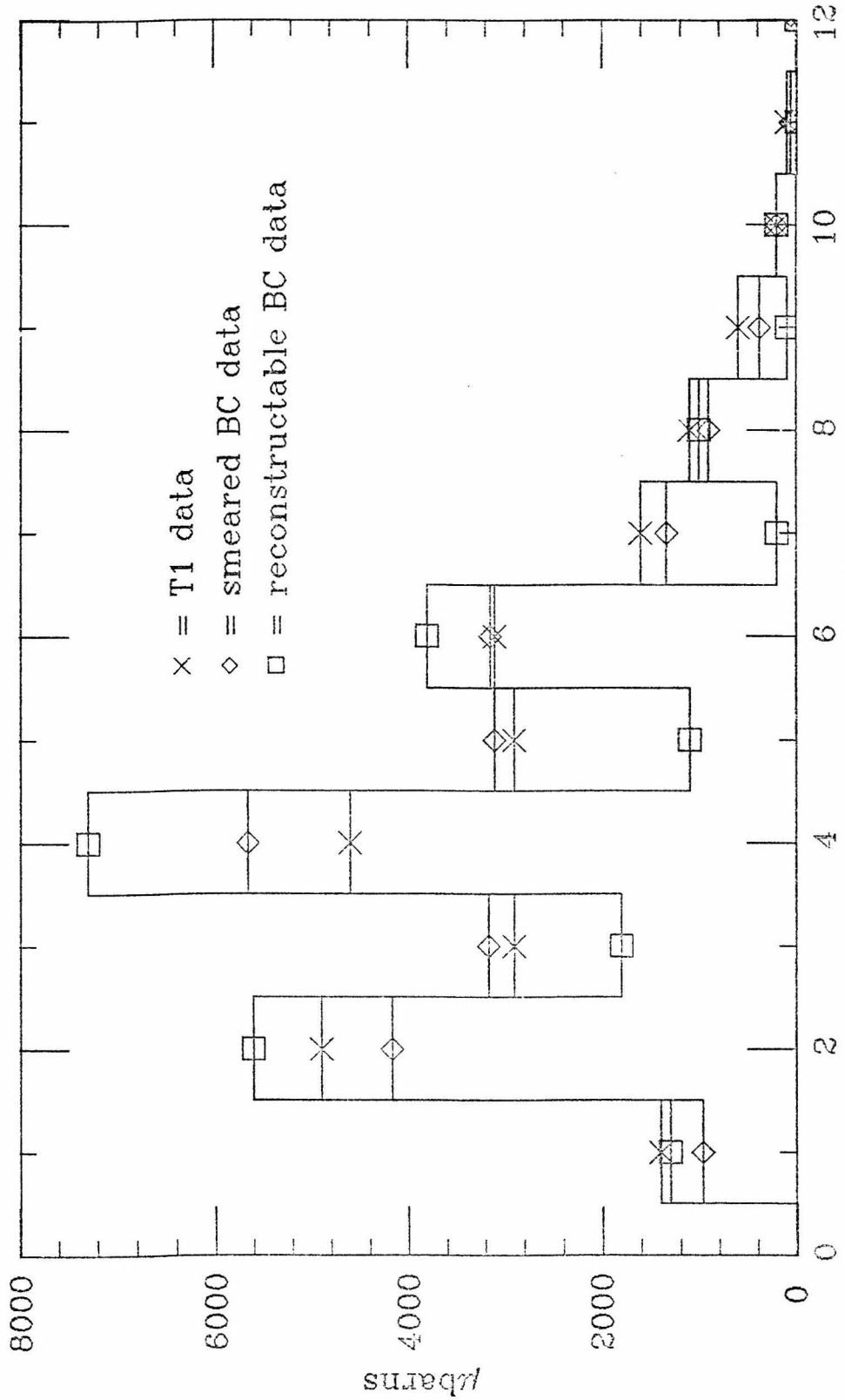

Figure 4.G.5: Comparison of multiplicity distributions: T1 (full minus empty), and bubble chamber before and after smearing.

results.

4.H -- Early Event Rejection

A pre-trackfinding cut "mask" on the possibility of finding a track satisfying the electron identification criteria is described below. Other cuts which were made in the process of trackfinding are described also. These cuts and the program flow are shown in the left half of fig. 5.A.1 (in the next chapter).

The "mask" selected 20% of the 5 million T0 triggers for trackfinding. The rejected events contained at least one registering C1 cell and one gamma-veto shower counter combination as required in the hardware trigger, but in a configuration that could not have been produced by a single track. These, and many that passed the mask, were due to separate spurious and uncorrelated counts in C1 and a shower counter. The presence of a track registering both in C1 and in a shower counter (a "triggering track") was required later, both in the trackfinding program, and again more rigorously in the data selection program.

A sample of tracks with momentum greater than 750 MeV/c (the lowest acceptable electron momentum) was used to produce the "mask". The mask was an array with entries for each pair of one of the 38 cells of C1 and one of the 13 shower counters.

Entries were flagged "possible" if any track in the sample hit both members of the pair. Events were rejected if none of the combinations of registering C1 cells and shower counters were possible.

After all combinations of pivotal plane chambers were searched for tracks, the event was rejected if none of the tracks satisfied the triggering track requirement. The computer time for trackfinding in the cylinders was thereby avoided. Other cuts made during the trackfinding process were the fatal unpack and match-point overflow (which have already been described), and the requirement of at least one track in the beam chambers.

Two cuts made immediately after the trackfinding program reduced the size of the DST's by a factor of two (to 120,000 events on 9 6250 BPI tapes): A second track identified as an electron, in C1 but not necessarily in a shower counter, was required. Events with multiple beam tracks were dropped in order to simplify a later cut involving the beam track. Finally, tracks with momentum below 750 MeV/c were extrapolated through the non-uniform field region as far as the end of C1. (This was done earlier for the high momentum tracks while searching for a triggering track.)

References for chapter 4

1. Comparison of E127 Total Cross Section Data with 16 GeV/c Pi-Minus Proton Bubble Chamber Data, C. L. Woody, SLAC Group B Internal Memo, October 5, 1979.

2. The bubble chamber experiment was reported in J. Bartke et. al., Nuclear Physics, B107, p.93 (1976).

CHAPTER 5 -- Data Processing: Cuts, Background, and Normalization

5.A -- Introduction and Summary

This chapter describes the cuts used to select the final sample of several hundred events from the 120,000 events that were reconstructed. It describes the procedure by which the background was estimated and subtracted, and the procedure by which the losses of signal were estimated and the final result was normalized.

"Low mass pair" will refer either to electron pairs produced by photon conversions and pi-zero Dalitz decays or pairs with a mass below 140 MeV/c^2, these classes being almost identical. "High mass pair" will always refer to electron pairs with a mass above 140 MeV/c^2, which are known to be almost free from pi-zero Dalitzes and photon conversions.

The material is presented in sections 5.B through 5.E in the same order as the corresponding cuts were made in the selection program. Section 5.B is concerned with electron identification and the cuts requiring two electron tracks in the event. Section 5.C describes two cuts made on the quality of the electron tracks. Section 5.D discusses low mass pairs which were erroneously reconstructed with large mass, and their removal by a cut on the association distance

of the electron tracks with the beam track. Section 5.E describes the geometrical properties of low mass pairs, a cut to remove events where the electrons originated as separate low mass pairs, and two cuts on the position of the pair vertex. The flow of the program and all the cuts described above are shown in the right half of fig. 5.A.1.

The various background processes which contaminated the direct electron pair signal are discussed in section 5.F. Most of these processes produced the same number of pairs where both electrons had the same charge as those with opposite charges. The same charge pairs were treated identically to the opposite, so that the former were a one for one estimate of the contamination in the latter. Misidentified hadrons pairs were not symmetric in this sense, and were treated separately.

Section 5.G describes the estimation of the acceptance and the normalization of the final result. The geometrical acceptance (for electron identification in the Cerenkov and shower counters) was estimated using track pairs generated by a Monte Carlo program. The usual trackfinding program was applied to simulated chamber measurements to estimate the trackfinding efficiency. Losses in the electron identification procedure and the beam association distance cut were reproduced in the Monte Carlo using values measured with real tracks. Losses are tabulated and used to

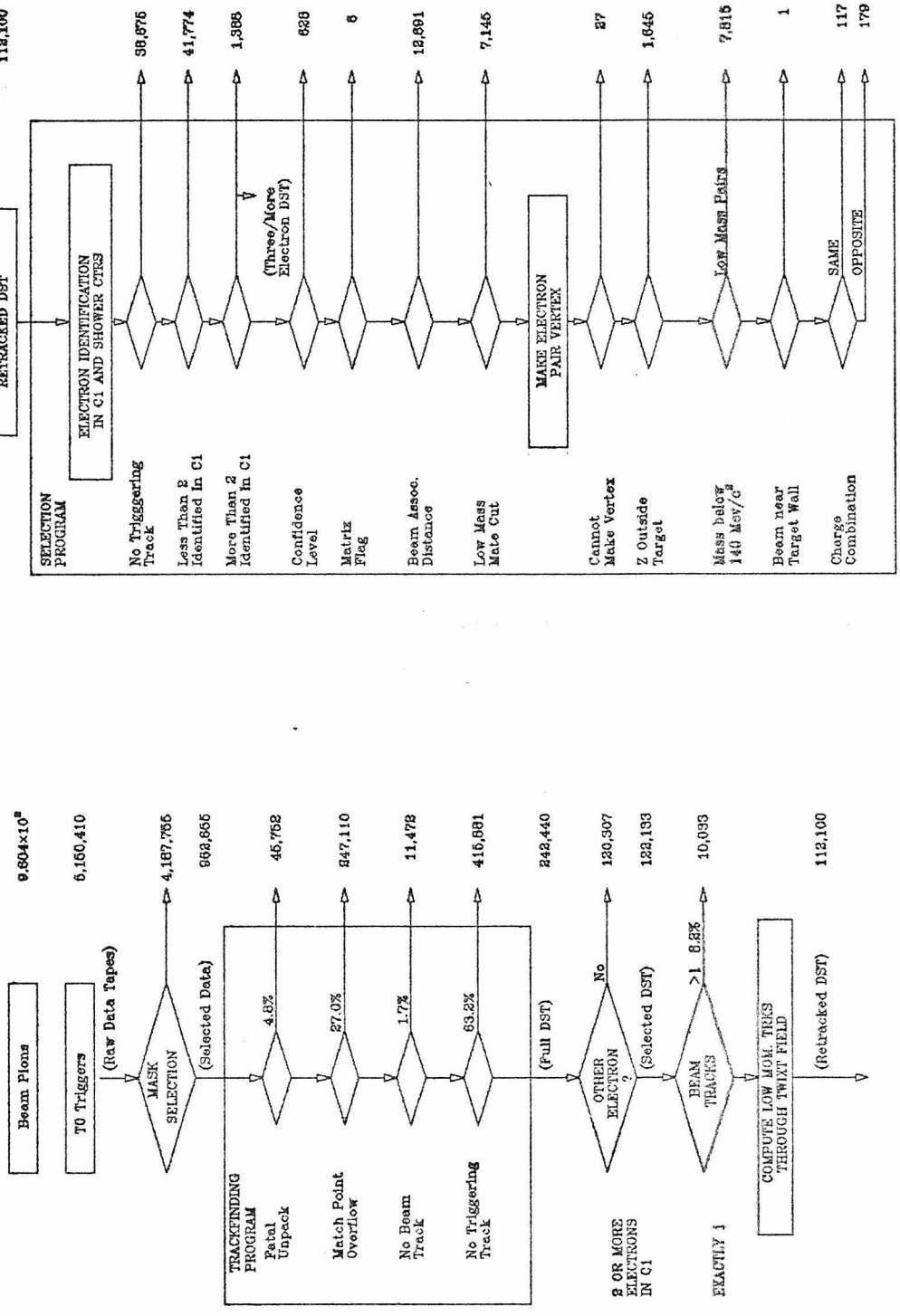

Figure 5.A.1: Program Flow and Event Selection

normalize the final result. The final differential cross section as a function of mass (valid for masses greater than 140 MeV/c^2) is presented in fig. 5.G.6. The total number of events with opposite charge pairs minus the number of same charge pairs (background estimate), with mass greater than 140 MeV/c^2 was 62±17. After subtracting the component of the hadron punch-through which was not charge-combination symmetric and correcting for the loss of real pairs due to the removal of low mass pairs, the result was 57±29 events.

5.B -- Electron Identification

This section describes the electron identification procedure using the C1 Cerenkov counter and the shower counters. The electron identification efficiency and the probability of misidentifying hadrons is estimated. The rejection of events with more than two electrons is discussed also.

All events presented to the selection program, i.e. the "candidate events" passing the C1-shower counter correlation mask, had been selected to have a so-called "triggering track". A triggering track must have traversed at least one C1 cell which registered light, and hit a shower counter which had a large pulse height (and was counted in the corresponding "gamma-veto" counter). The triggering electron identification requirement in the program was more stringent, as described below. The program also required a

second track to be identified as an electron in C1.

5.B.1 -- Shower Counters

If a track traversed any of the dipole-face shower counters, the pulse height of that shower counter (or of the one with greater path length, if two were traversed) was used to determine if it were an electron. The pulse height sum from all tubes on the shower counter was required to have fired the "buffer strobe" discriminator, corresponding to a sum of pedestal-subtracted ADC counts greater than approximately 600. A count was required in the corresponding gamma-veto counter in order to reject tracks that could not produce the hardware trigger. The identifying counter was required not to have been hit by any other track with momentum above 750 MeV/c. (To test for lower momentum tracks hitting the counter would have required a large extra computer effort.)

The pulse height cut of 600 accepted 50% of electron tracks with an energy of 750 MeV, determined before the run by placing the counters in a test beam. This measurement was verified later using "test tracks" from recorded T0 events. Acceptance versus pulse height cut for various energy test track electrons and pions is shown in fig. 5.B.1. (The test track electrons are described immediately below, and the pions are described in section 5.B.4.)

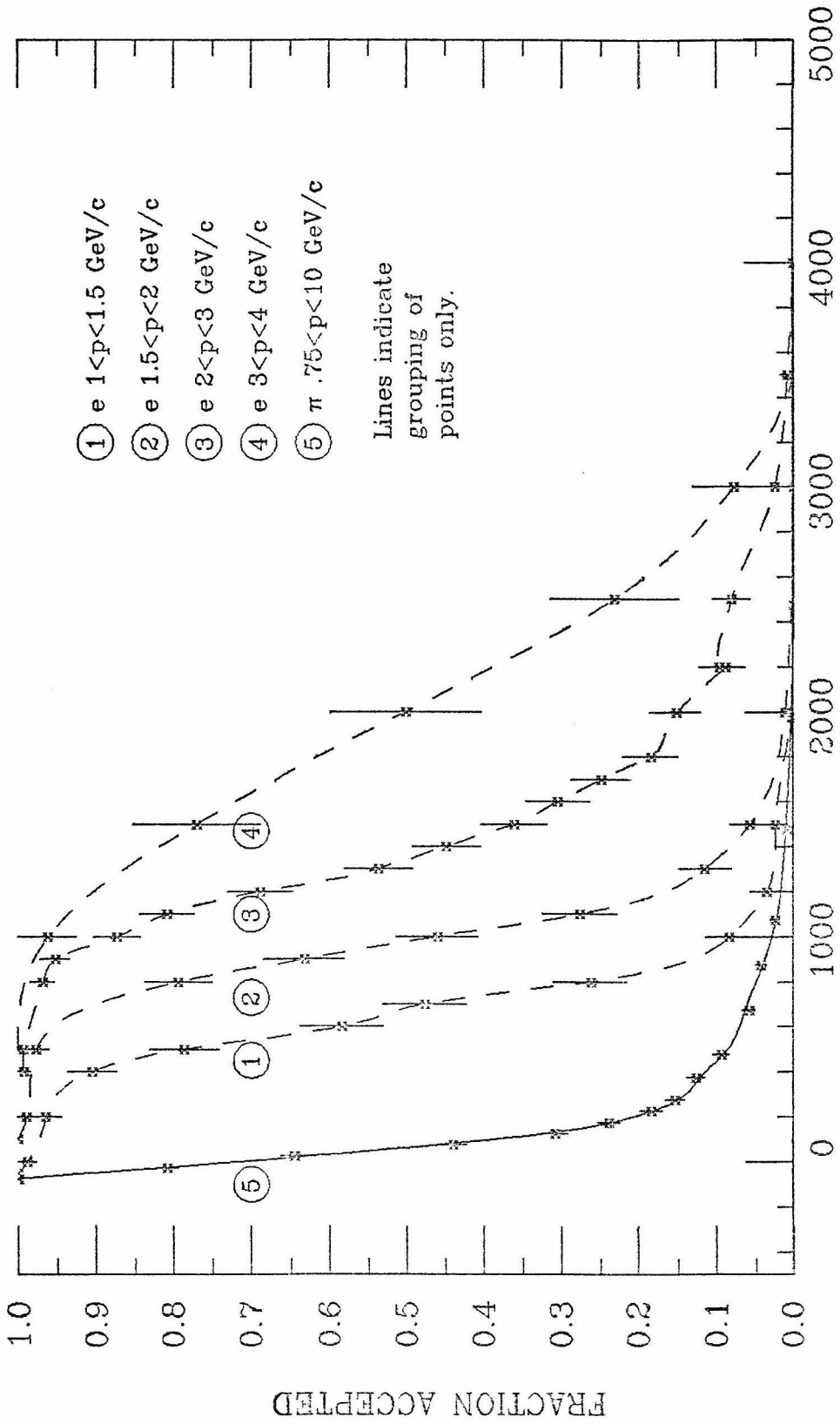

Figure 5.B.1a: Accepted fraction as a function of pulse height cut in GpE counters.

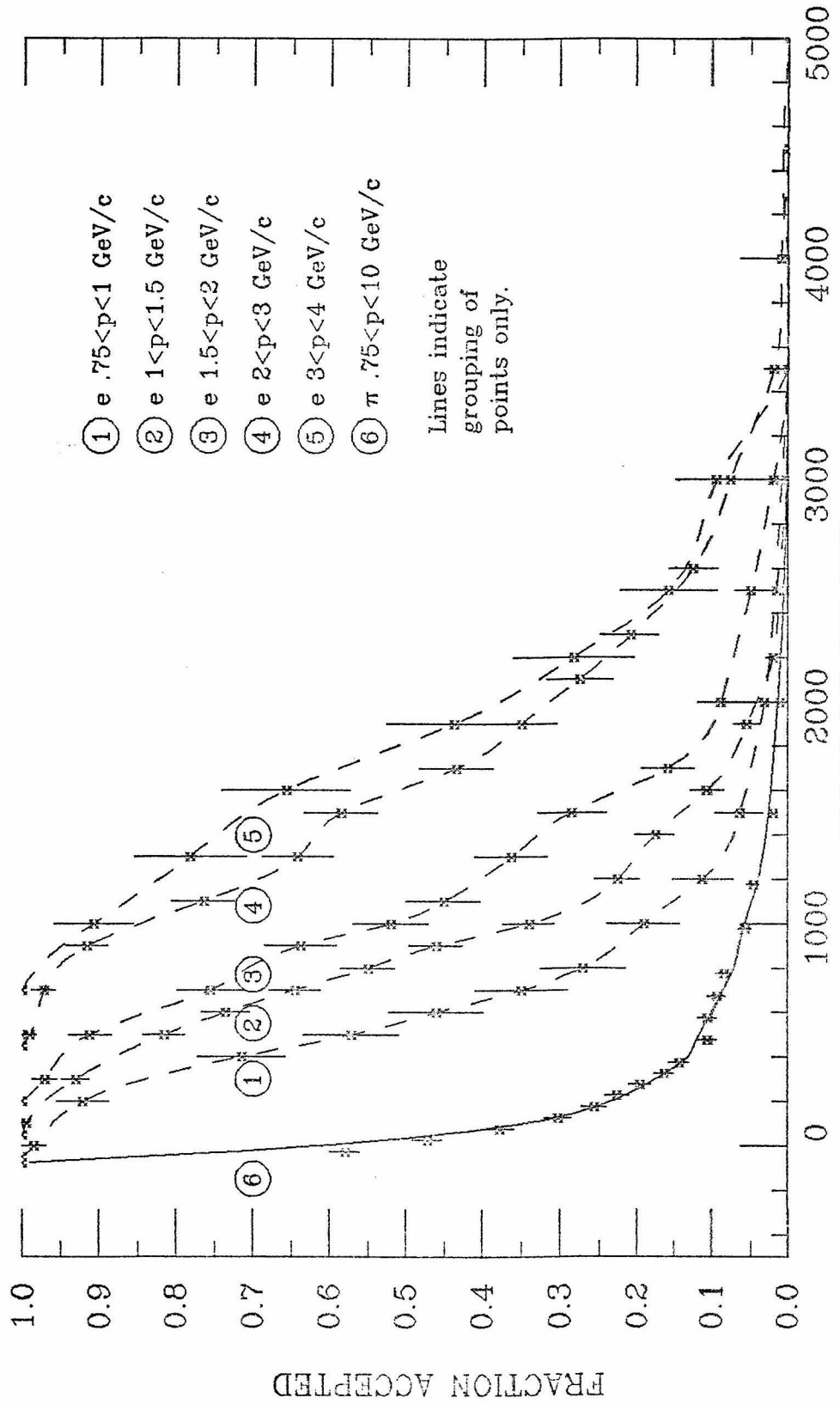

Figure 5.B.1b: Accepted fraction as a function of pulse height cut in CTT counters.

Test track electrons were used to determine the shower counter electron identification efficiency, which was necessary to correct for the loss of electron pairs in the identification step. These were tracks in T0 events which formed low mass ($m<50$ MeV/c^2) pairs with identified electrons of opposite charge. The test tracks were free from trigger bias since the events were selected with the identified mate satisfying the hardware trigger. The number of tracks making low mass pairs with electrons of the same charge was one per hundred opposite charge pairs. This is taken as an estimate of the probability of chance pairing of a hadron with the identified electron and therefore of the hadron contamination in the test tracks. The further requirement that the test track be identified by C1 reduced the contamination effectively to zero.

The acceptance was found with a Monte Carlo program assuming a constant average identification probability for all tracks associated with a shower counter. The area of association included spaces between the shower counter enclosure and active element, and low efficiency regions near the edges where part of the shower escaped. The area of association also included a 4 cm. band beyond the physical counter boundaries to allow for track uncertainties and counter misalignment. The Monte Carlo identification probability was taken as the identification efficiency averaged over the whole area of acceptance. The average was obtained by

taking all test tracks associated with a shower counter and computing the fraction which registered in the buffer-strobe discriminator and the gamma-veto counter. The true efficiency of the counters was measured separately, using only test tracks 2 cm. inside the area of the counters. Fig. 5.B.1 shows the accepted fraction as a function of pulse height cut where the test tracks were 2 cm. inside the counters. Fig. 5.B.2 shows efficiency for buffer-strobe and gamma-veto for tracks 2 cm. inside the counters. Fig. 5.B.3 shows the efficiency for buffer-strobe and gamma-veto for all associated tracks.

The validity of averaging over a fairly large insensitive area depends on the similarity of the angular distributions of the test tracks and the electron candidates. The test tracks had the angular distribution of the pi-zeros that produced them and the real electrons were distributed like the parent virtual photon. Since the pi-zeros and virtual photons were both produced in the primary hadronic interaction, it is reasonable to assume the angular distributions were not radically different.

The identification efficiency as a function of electron momentum is shown in fig. 5.B.4 in the form it was used in the Monte Carlo. The "O"s in the figure represent the estimated identification probability at each momentum value. The "X"s represent the one standard deviation limits, which

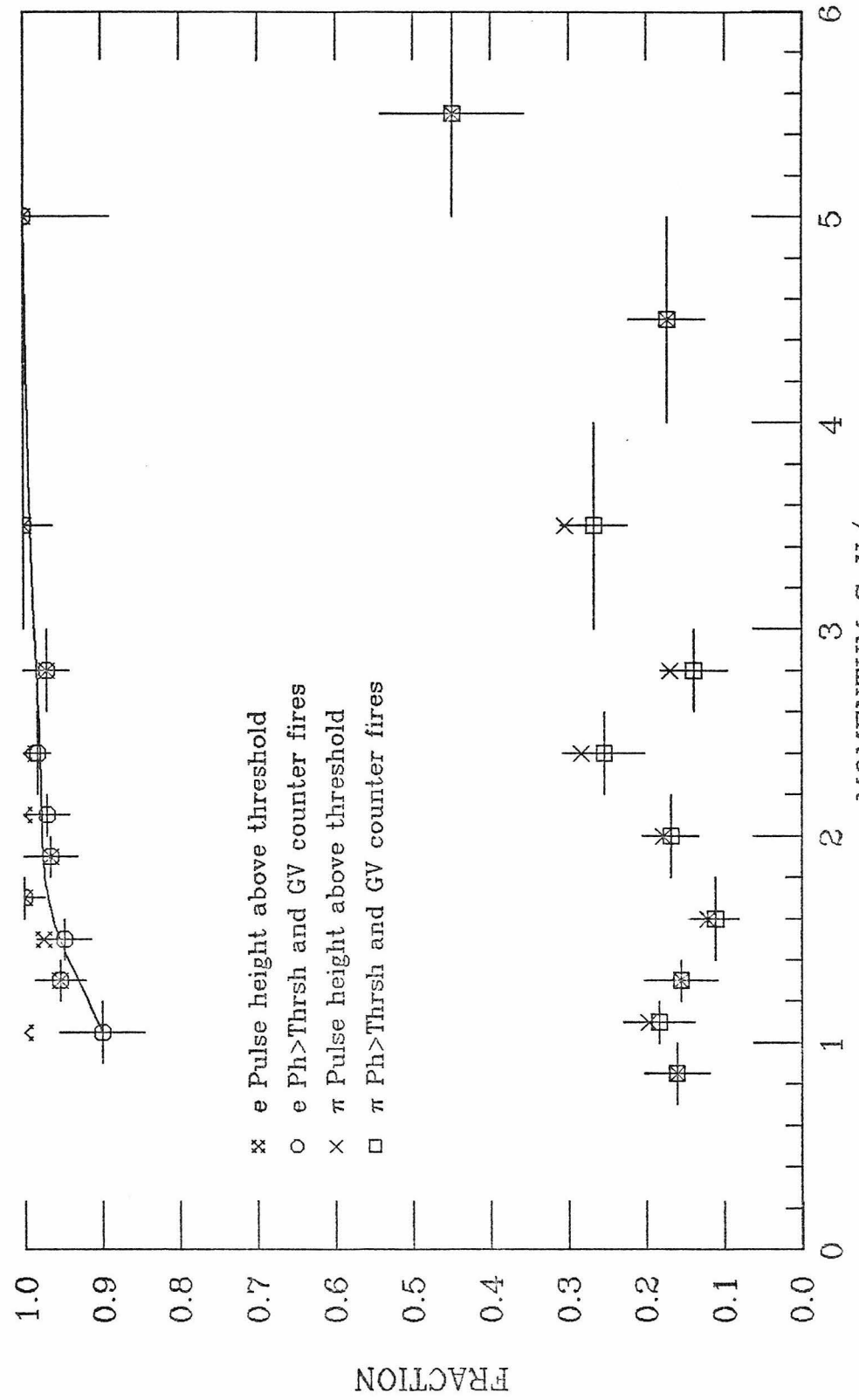

Figure 5.B.2a: Fraction producing hardware trigger inside active area of GpE counters.

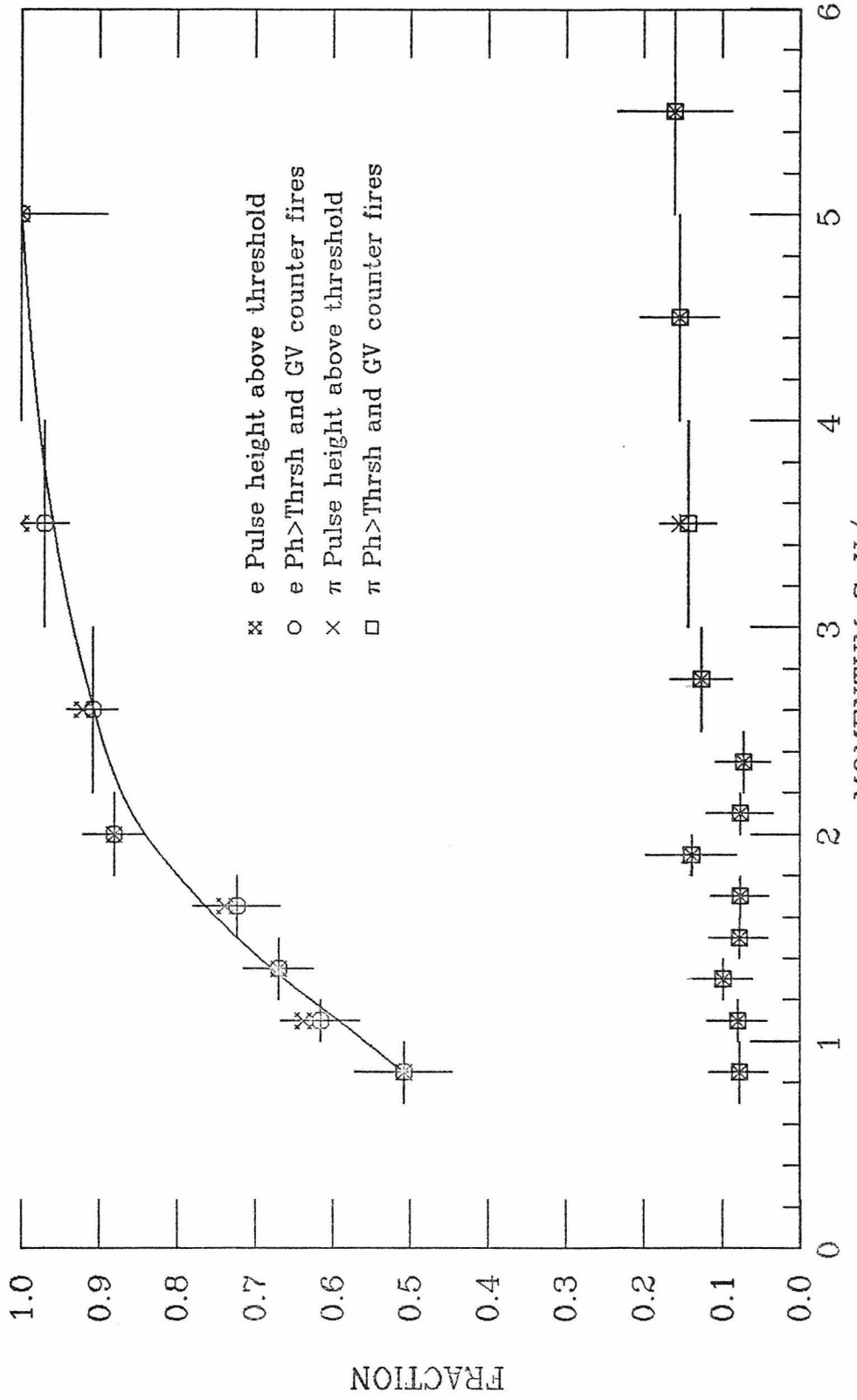

Figure 5.B.2b: Fraction producing hardware trigger inside active area of CIT counters.

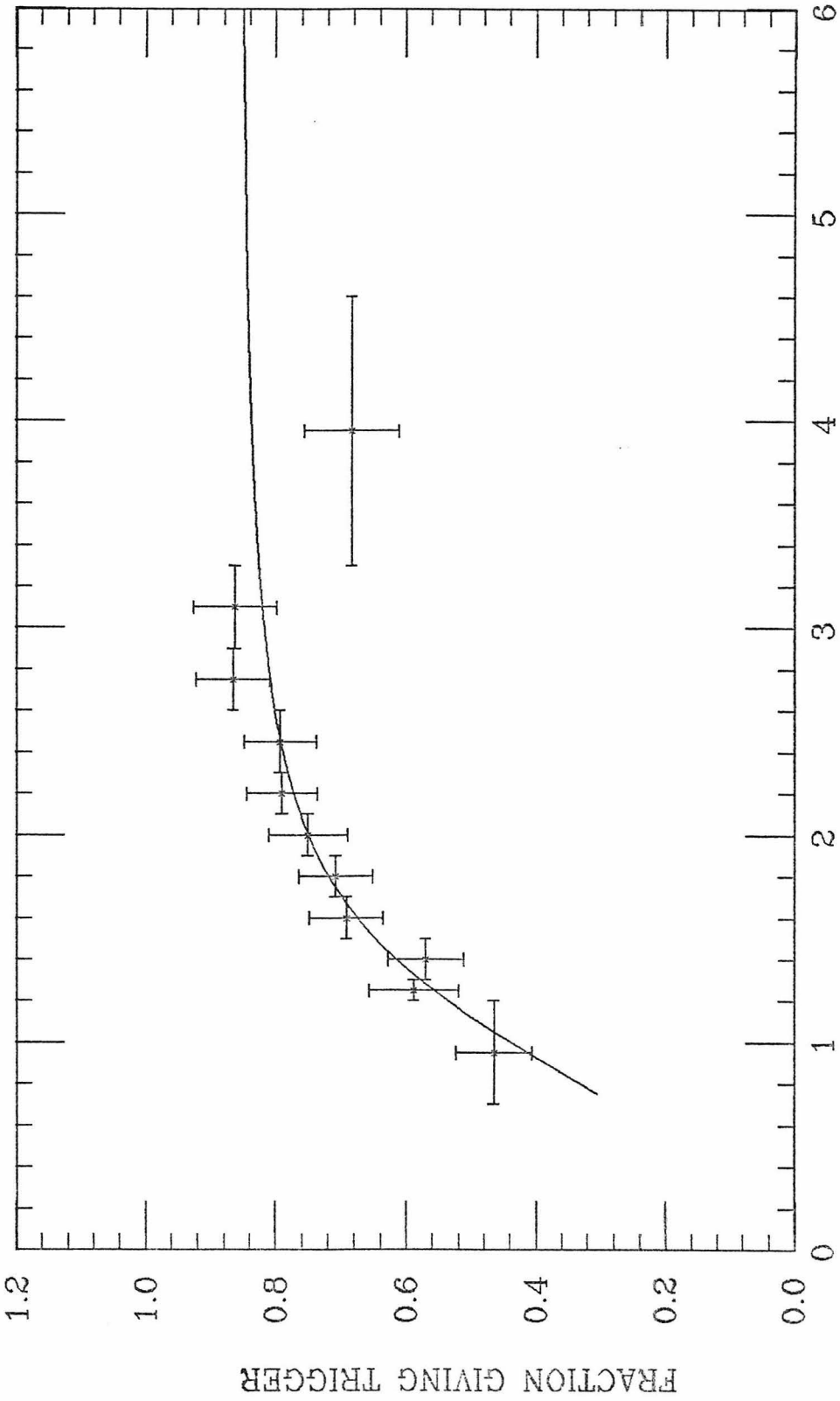

Figure 5.B.3a: Fiducial area efficiency in GpE counters.

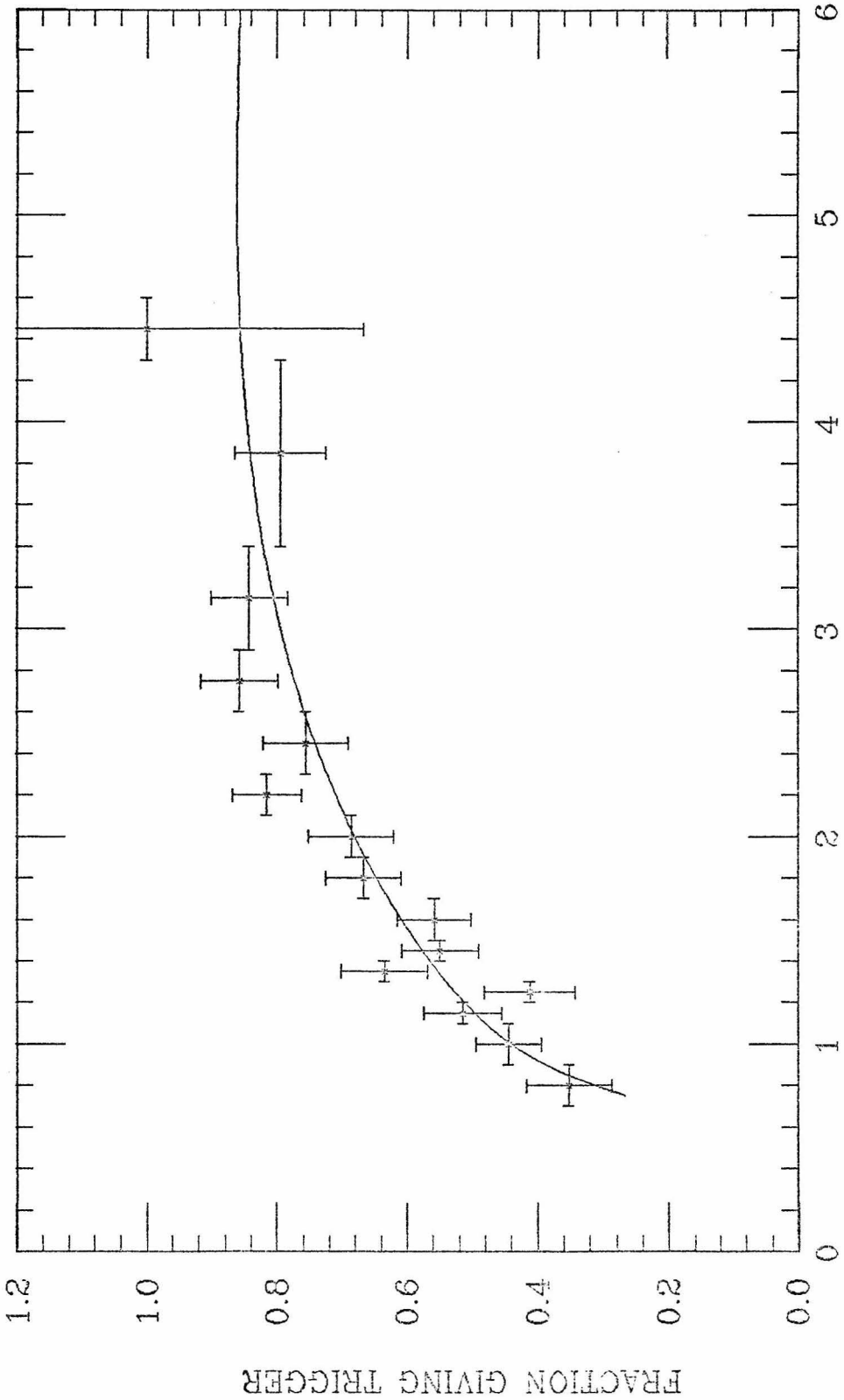

Figure 5.B.3b: Fiducial area efficiency in CIT counters.

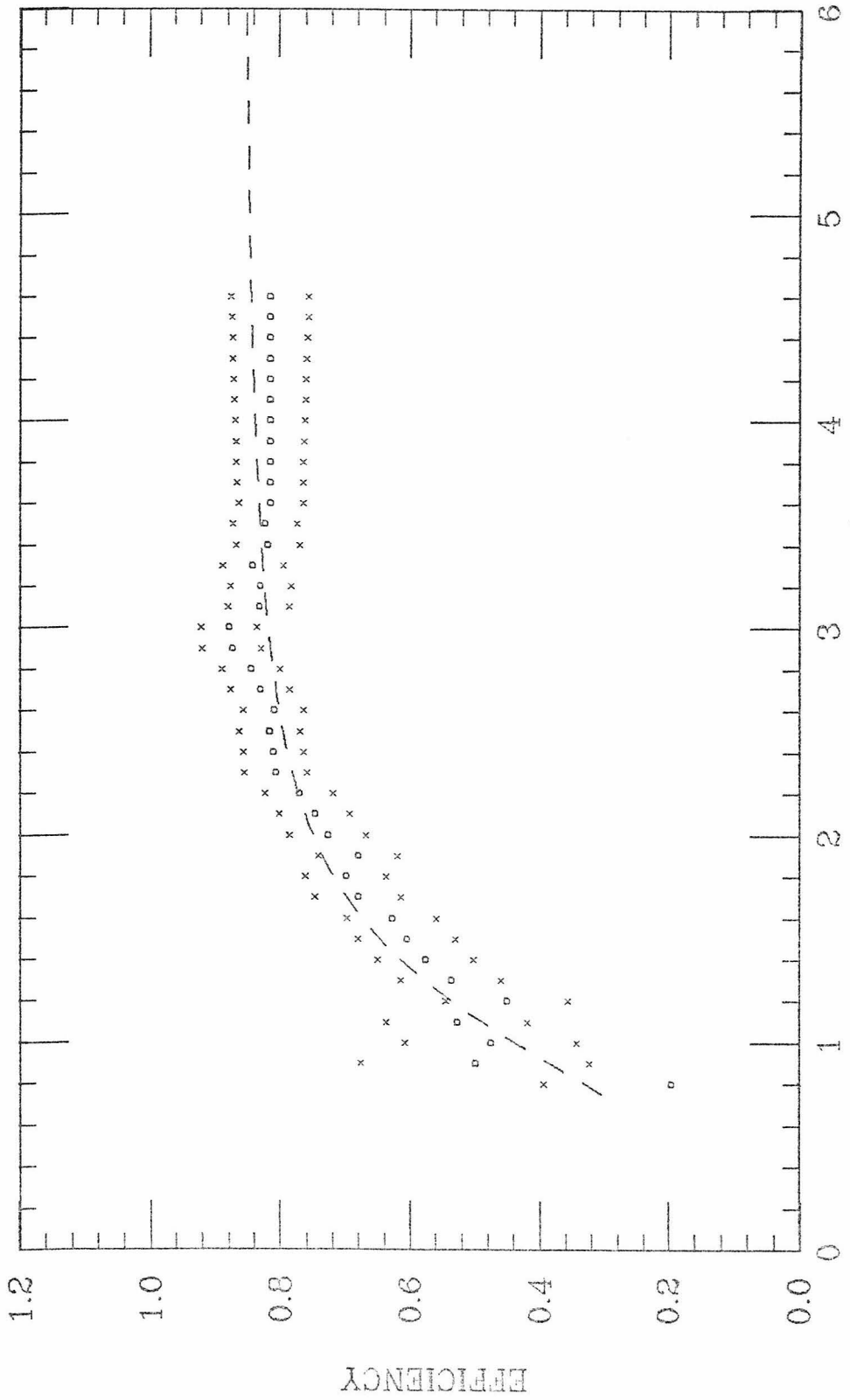

Figure 5.B.4a: Electron identification probability in GpE counters, one std. lower and upper limits, and polynomial fit.

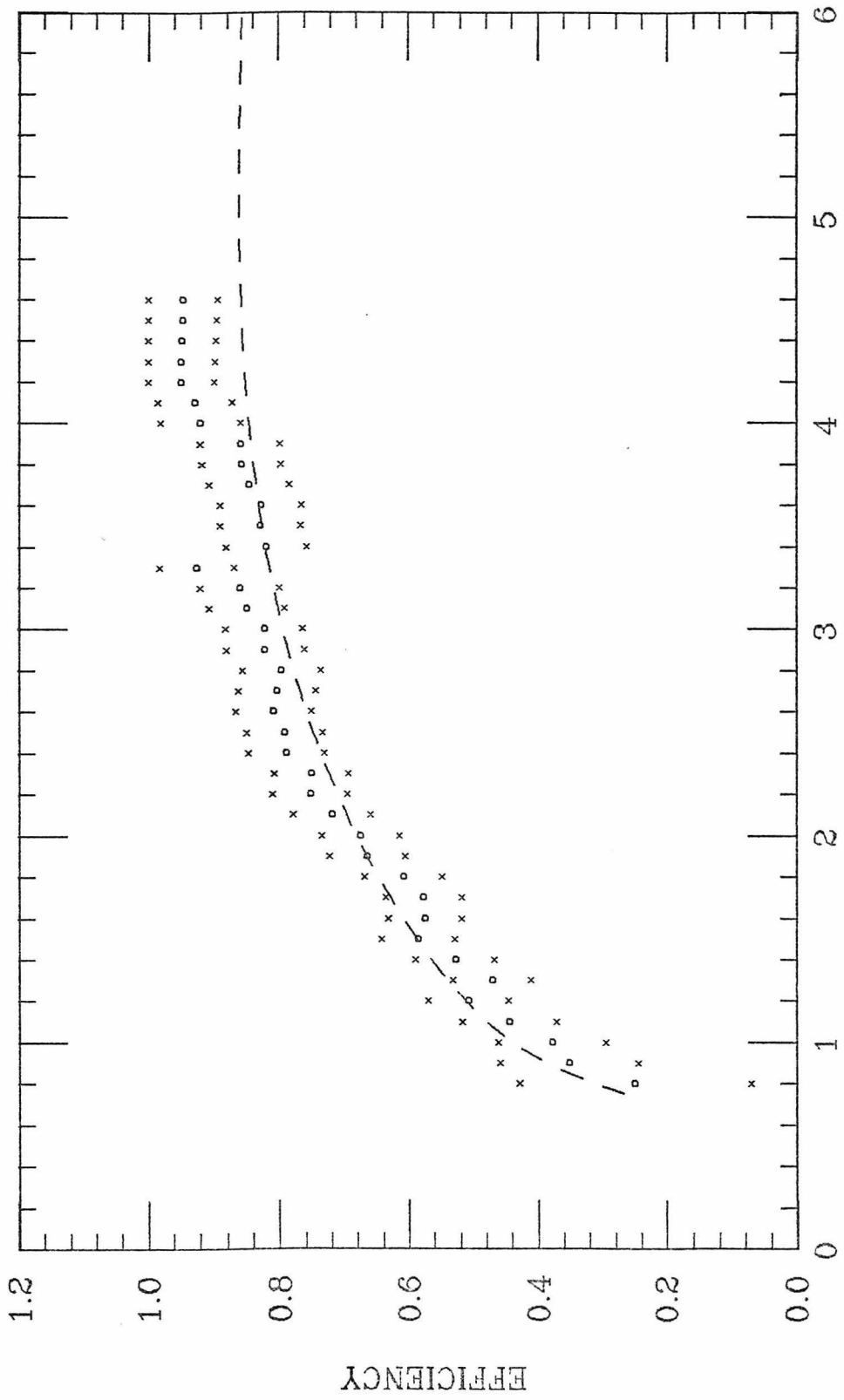

Figure 5.B.4b: Electron identification probability in CIT counters, one std. lower and upper limits, and polynomial fit.

were used to estimate the uncertainty of the final acceptance factor calculated by the Monte Carlo. The dashed line is a smooth 8 parameter fit to the measurement (of the form: $f(p)=C \cdot p + 1/Q(1/p)$, where C was a constant and Q(1./p) was a sixth-degree polynomial). This fit was used only to determine binning ranges as described below. (It would have been more straightforward to use the fit as the estimate rather than the Os. The final result would have been the same.)

The O's and X's were calculated at a large number of momentum values using test tracks within a variable range of momenta. These ranges generally overlapped, so that efficiencies measured at nearby momentum values were not statistically independent. The size of each bin was chosen depending on the rate of change of the parameterized efficiency in order to sum over a momentum range where the efficiency was fairly constant. The estimated uncertainty due to the range in momentum was combined with the statistical uncertainty to produce an overall uncertainty. The bin size was chosen to minimize this overall uncertainty. The O's are the fraction identified in the resulting bin and the X's correspond to the minimized overall uncertainty.

5.B.2 -- C1 Cerenkov Counter

The basic electron identification criterion in C1 was that the track produce light in one of the cells it crossed. Cells which were simultaneously crossed by another track were not counted. (Such cells will be referred to as "shared".) Every track produced by the trackfinding program was used to invalidate shared cells (including tracks which comprised about 20% of the total.)

Identification efficiency was measured using test tracks that made low mass pairs with "triggering" electron tracks of the opposite charge (i.e., identified in C1 and a shower counter). As mentioned above, the contamination was about one percent. (This was verified by making a cut in shower counter pulse height for the subsample of the test tracks hitting the shower counters.) The cells were grouped into outer, middle or inner ring, the unequipped cells being excluded. The two central "beam" cells were not measured.

Above pedestal, the pulse height distribution for cells containing electron tracks and cells without any apparent tracks overlapped to a large degree, as shown in fig. 5.B.5. (This may be because noise and electron tracks both corresponded to single photo-electrons.) The rate for pulse height above zero was 60% for electrons and 0.5% for empty cells. (The efficiency of cells with electrons appears low because the sample was dominated by low momentum tracks.) The empty cell rate was measured using interaction trigger

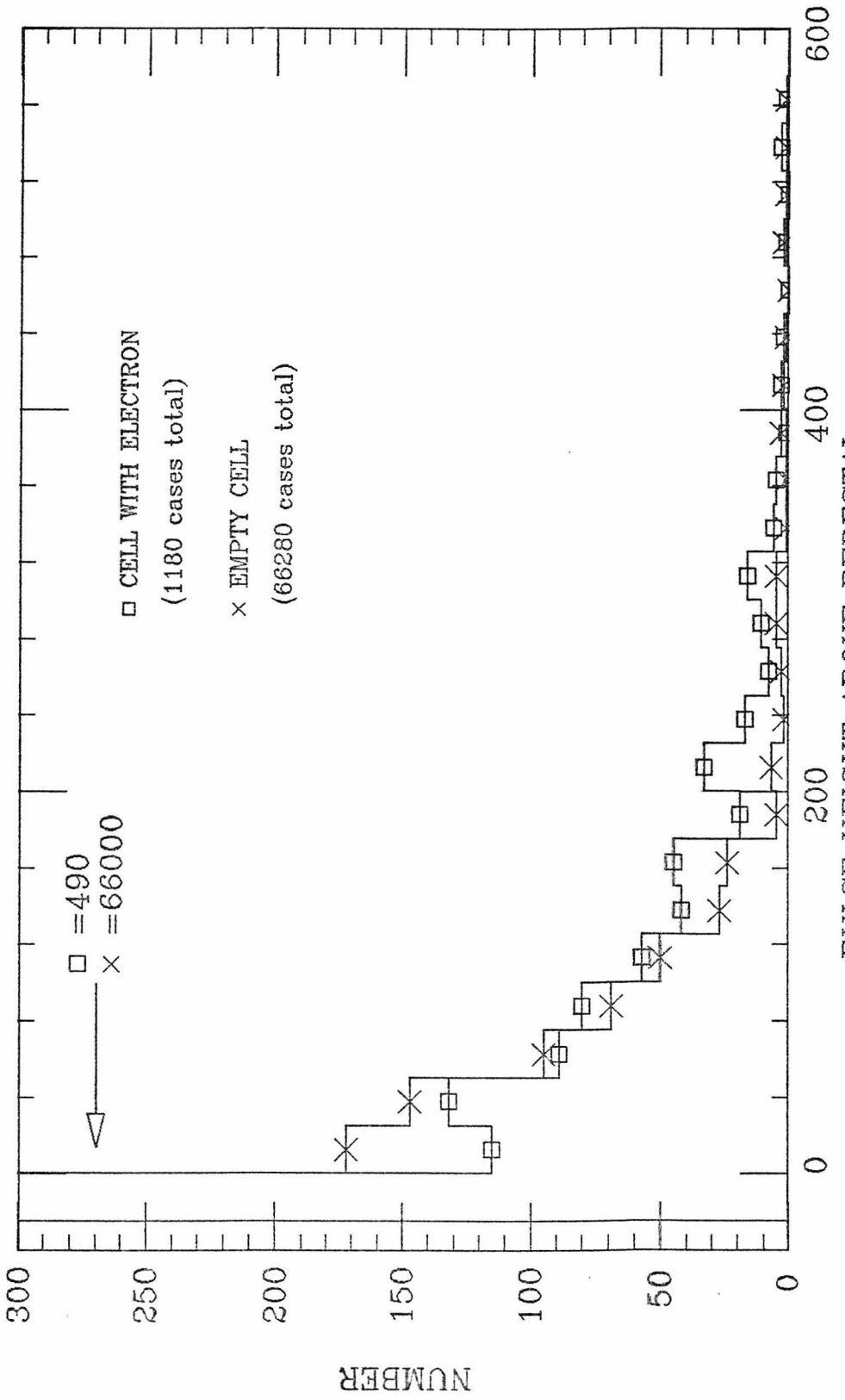

Figure 5.B.5: C1 pulse height for cells traversed by an electron and for cells traversed by no reconstructed track.

events and cells not traversed by any reconstructed track.

A pulse height cut just above the pedestal value for each C1 cell gave the best electron-hadron separation. Cells 15 and 33 were deadened in the program because of their high spurious count rate (counting when no track hit the cell) and cell 28 because it was inoperative (due to a detached mirror).

The detection efficiency depended on the position and angle of the track within the cell. Once an electron becomes extremely relativistic at about 100 MeV/c, the amount of light radiated and the Cerenkov angle are approximately constant. The momentum had therefore no direct effect on the cell efficiency. However, the light collection efficiency of the cell was low if the direction of the track was not parallel to the cell axis. The cells were built with the axis pointing toward the target, and so had good efficiency for high momentum tracks which followed a fairly straight path. Low momentum and large θ tracks made larger angles with the cell axes, and therefore had lower efficiencies. (Ψ, the angle, a track made with the cell axis may be approximated by the change in the angle of the track from where it left the target to where it enters C1, given by $\cos(\Psi) = 1 - \sin^2(\theta) \cdot \cos(\Delta\varphi)$, where $\Delta\varphi = (2\ \text{GeV/c})/B\chi$.) The constant, 2 GeV/c, is related to the magnetic field strength and the distance between the target

and C1. For small Ψ, Ψ was approximately TAN(θ)•(2 GeV/c)/P.) The efficiency was therefore measured as a function of momentum and whether the cell was in the inner, middle or outer ring. The ring selected a rough range of , so that these variables determined Ψ.) Measuring efficiency as a function of ring was also important because the cells of different rings differed in length.

Tracks sometimes went through several cells. Pulse height in any of the cells was considered sufficient for electron identification (providing the cell contained no other track). The identification probability therefore was sometimes higher than the efficiency of the individual cells. The individual cell efficiency was lower when a track went through several cells because the light from such tracks was directed at the inter-cell partitions. Separate measurements were made for tracks hitting only one cell and for those hitting more than one. The momentum bins used to determine the efficiencies were combined in varying numbers as described for the shower counters. Fig. 5.B.6 shows the one standard deviation lower and upper limits of the efficiencies and the parameterization (of the same form as was used for the shower counters).

The identification efficiency for a track (computed in the Monte Carlo) was calculated from the efficiency of the cell(s) it traversed and a constant representing the

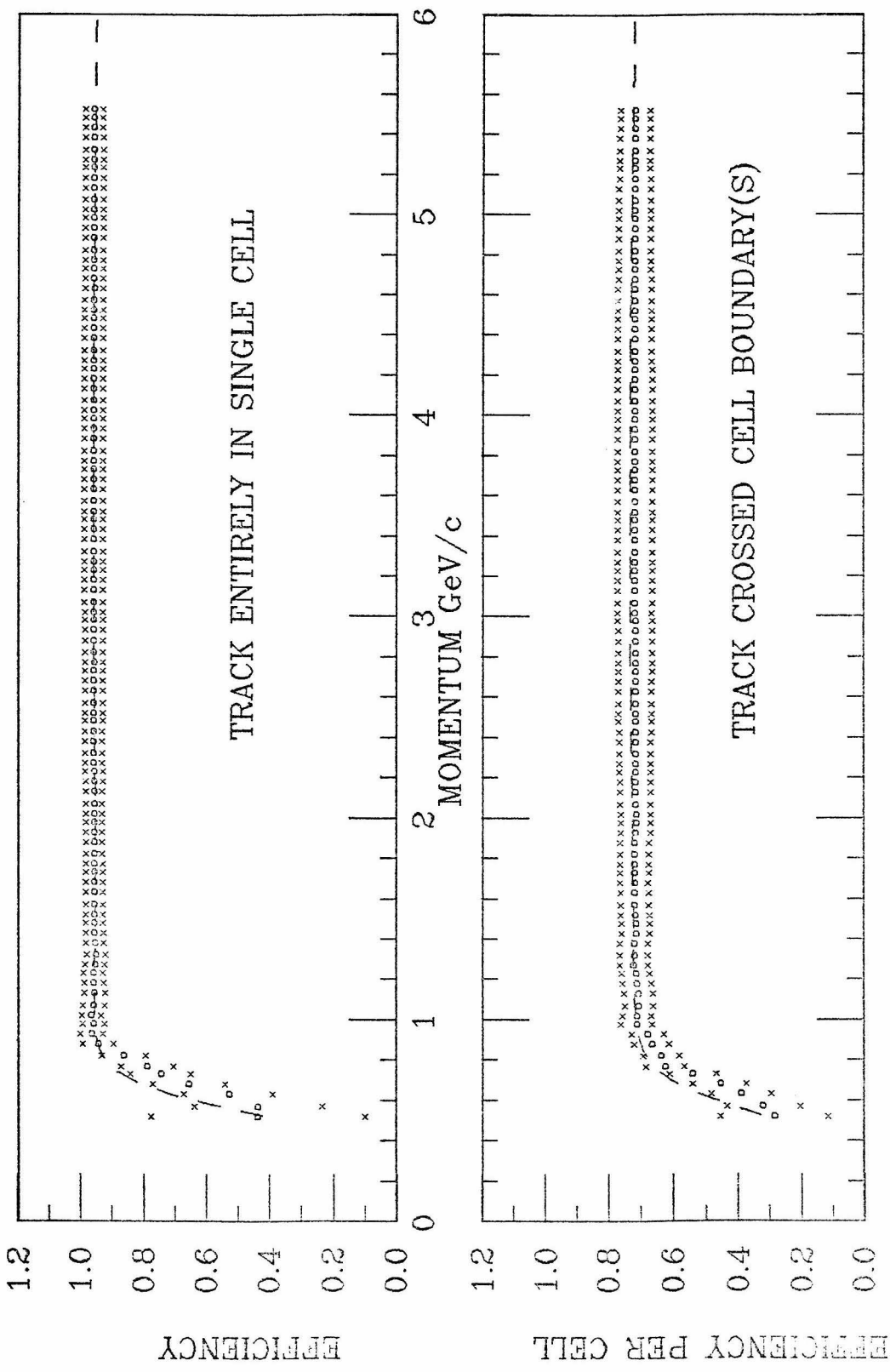

Figure 5.B.6a: Electron identification probability in the inner ring of C1, one std. lower and upper limits, and polynomial fit.

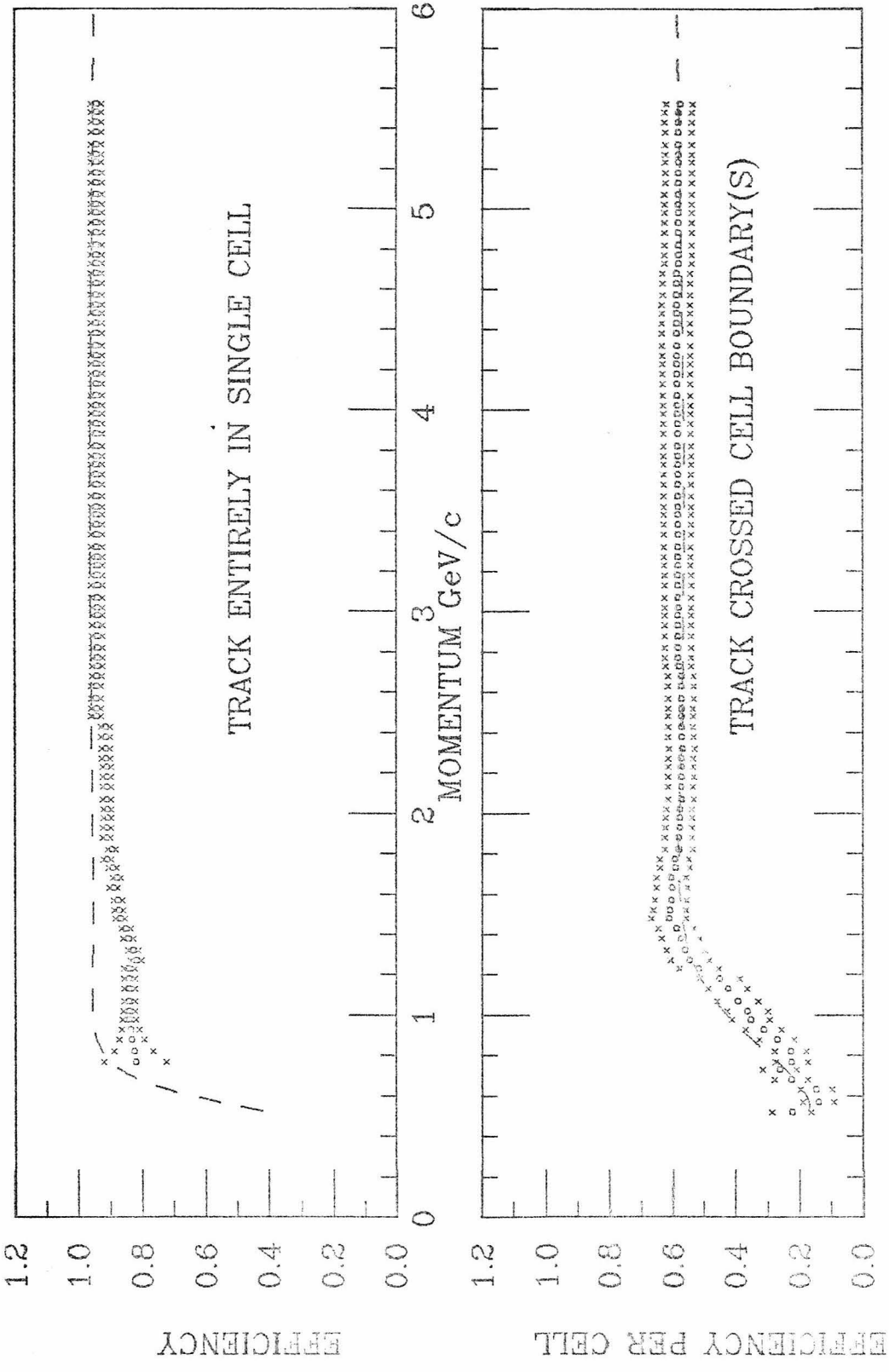

Figure 5.B.6b: Electron identification probability in the middle ring of C1, one std. lower and upper limits, and polynomial fit.

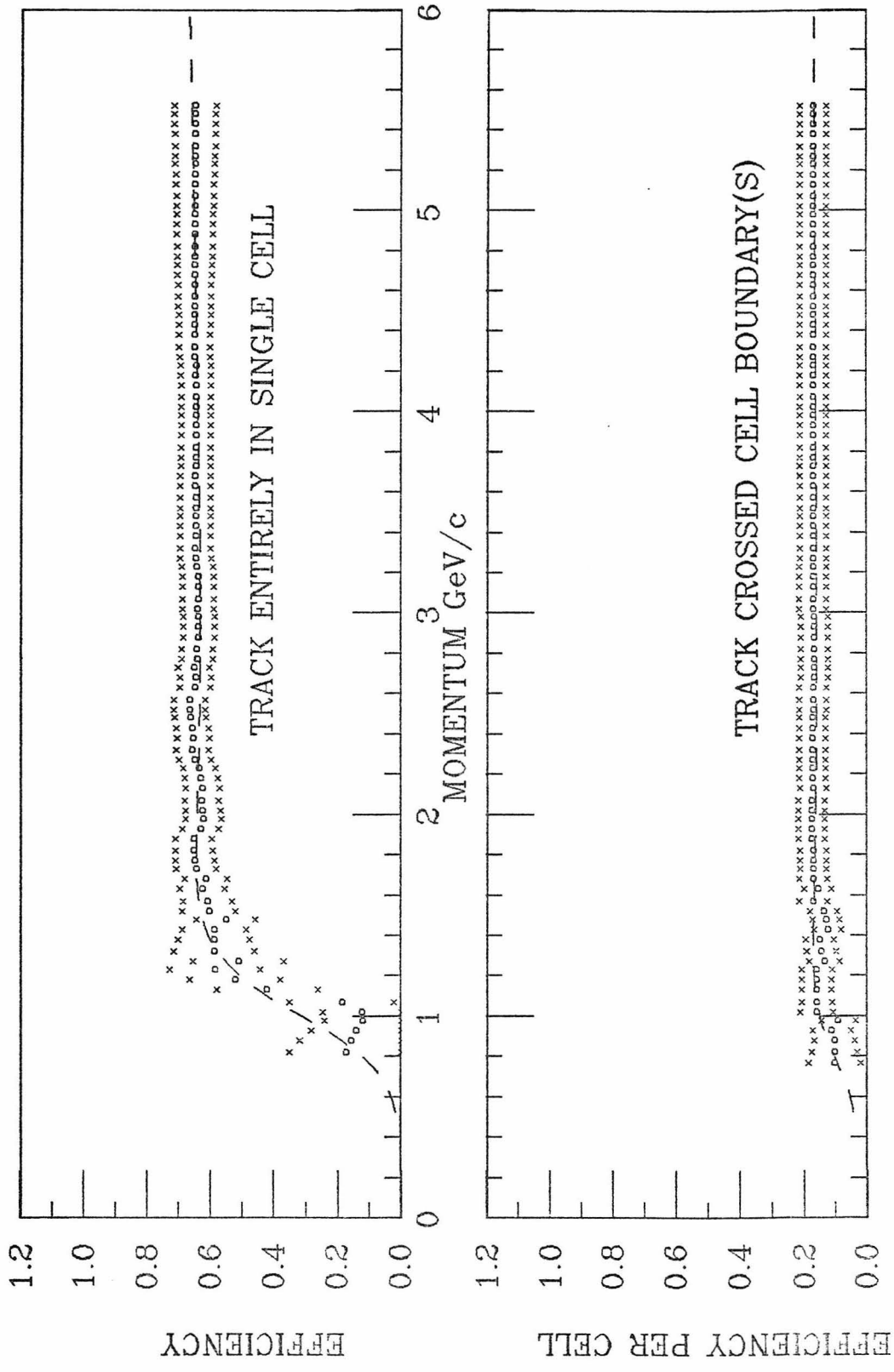

Figure 5.B.6c: Electron identification probability in the outer ring of C1, one std. lower and upper limits, and polynomial fit.

fraction of the events in which that cell was shared. This fraction was measured for interaction trigger events with two or more tracks. The interaction trigger events were chosen as a model for direct electron pair events rather than the electron trigger (T0) events, because the latter often contained electromagnetic showers, downstream photon conversions, and abnormally large multiplicities. It has been assumed that the interaction trigger events represented the direct pair events in terms of angular distribution and multiplicity. The noshare probabilities (per cell) were as follows: outer ring, 0.905; middle ring, 0.864; inner ring, 0.819.

The efficiency measured for each cell on the track (as in fig. 5.B.6 or zero for unequipped or dead cells) was multiplied by the probability that the cell was not shared. If the track hit several cells, these products were combined to get the probability that at least one cell identified the track as an electron. The Cerenkov identification efficiency calculated using the measured efficiencies and noshare probabilities (for electrons in the range 0.75 to 5.0 GeV/c from high mass pairs generated by the Monte Carlo) averaged 57% per track.

The lower momentum limit for electrons was chosen to be 750 MeV/c because the efficiency in C1 and shower counter dropped sharply there. Pions with momenta above 5.8 GeV/c

produced Cerenkov light. Fig. 5.B.7 shows the number of pion test tracks making light in C1. The detection probability was very low below 7 GeV/c since less light is radiated near the threshold. However, the momentum measurement errors were large (about 1 GeV/c) above 6 GeV/c, so there were pions registering in C1 as low as 5.8. The upper momentum limit for electron identification was chosen at 5.0 GeV/c, allowing a safety margin. (The selection of the pion test tracks is described below in the part of section 5.B.4 pertaining to hadron punch-through in C1.) The group in fig. 5.B.7 at the higher momenta corresponds to pions which produced Cerenkov light. The group at the lower momenta corresponds to a much smaller fraction of pions which were misidentified for other reasons, probably because a photon converted in the same cell. The number of punch-through tracks below threshold is however no greater than the estimated electron contamination as described in section 5.B.4.

5.B.3 -- Electron Detection Efficiency

In the Monte Carlo, the shower counter identification efficiency was read from a table of the efficiencies corresponding to fig. 5.B.4 and multiplied by the probability that it was not hit by another track above 750 MeV/c. As with C1, the noshare probability was taken as the frequency that the counter was not hit by a track in the

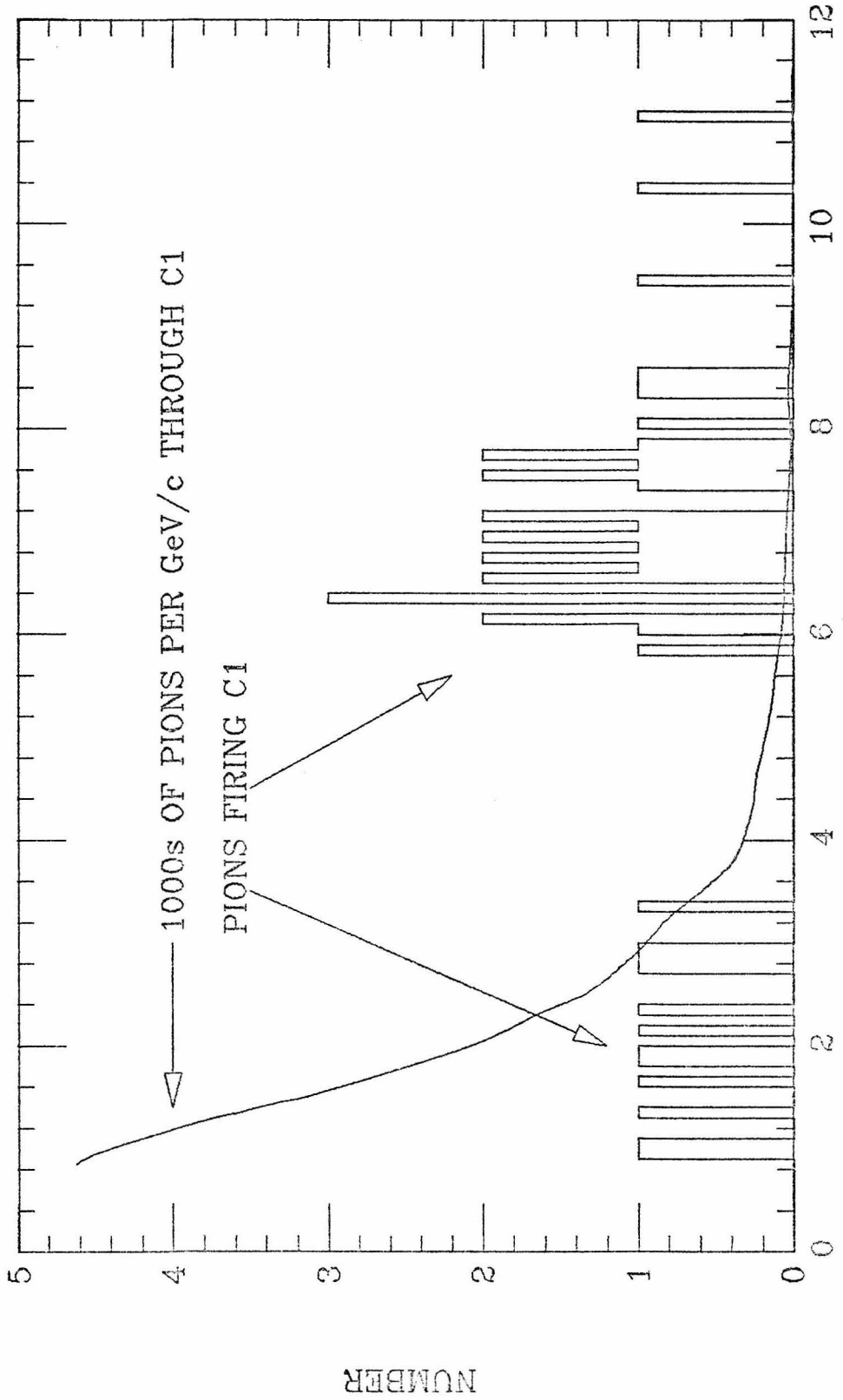

Figure 5.B.7: Pion test tracks in C1 cells: number registering light, and total number traversing, as a function of momentum.

interaction trigger data. The noshare probabilities are given in table T5.B.1 below.

When both electron tracks hit shower counters, the identification efficiency was calculated to reflect the fact that the event would have been rejected only if the identification failed for both tracks. For these events, the efficiency was the probability of identifying either, regardless of whether one or both actually registered. The shower counter identification probability calculated as described (for Monte Carlo high mass pair events) averaged 75% per event.

Table T5.B.1: PROBABILITY SHOWER COUNTER WAS NOT SHARED WITH ANOTHER TRACK

Group E

SC1	.889	SC6	.905
SC2	.917	SC7	.928
SC3	.973	SC8	.977
SC4	.974	SC9	.975
SC5	.982	SC10	.983

Cal Tech

SC11	.906
SC12	.851
SC13	.740

The total electron identification efficiency for an event was the product of the shower counter probability and the Cerenkov for each of the two electron tracks. This efficiency was evaluated in the Monte Carlo to estimate the electron identification correction factor. The total electron identification efficiency for Monte Carlo generated direct electron pairs averaged 22%. (This number includes the effects of cutting out shared cells.)

5.B.4 -- Hadron Punch-Through

The probability of calling a hadron an electron was needed to estimate the number of false electron pairs reaching the final sample. It was measured directly in the shower counters and inferred in C1.

Interaction trigger events were used as a source of hadrons. A sample of test tracks was chosen requiring that they go through equipped C1 cells and hit a shower counter well within the active area (to maximize the rejection of electrons). The sample was further cut as described below to give test hadrons for the shower counters or for C1. Tracks were not used if they made a low mass pair with any track of opposite charge.

To measure shower counter response, each test track was required to give no light while staying inside a single cell

of C1, starting well away from a partition. Events were used only if no pair of opposite charge tracks had a mass less than 150 MeV/c^2. 5% of the tracks in these events gave light in C1. Since C1 was about 90% efficient under these conditions, cutting out the tracks that made light left a maximum of 0.5% electron contamination.

The contribution to the shower counter punch-through rate from a photon hitting the counter simultaneously was assumed to be the same as the frequency of a photon hitting a counter without a track. This varied from 0.2% to 2% depending on the position of the counter and its area. The results are shown in fig. 5.B.8. The average punch-through probability was 13.3% (for buffer-strobe and gamma-veto). The dependence on the pulse height cut is shown earlier in fig. 5.B.1.

The punch-through in C1 was measured using a subsample of test tracks with a pulse height in the shower counter smaller than 150. The electron contamination in the subsample was calculated by comparing the pulse height distribution in the shower counters (before the pulse height cut) with the distribution for known hadrons. The frequency of pulse heights above 1000 was consistent with the test tracks being pure hadrons and with an upper limit of 1.3% contamination at the two standard deviation level. The fraction of the contaminating electrons surviving the pulse

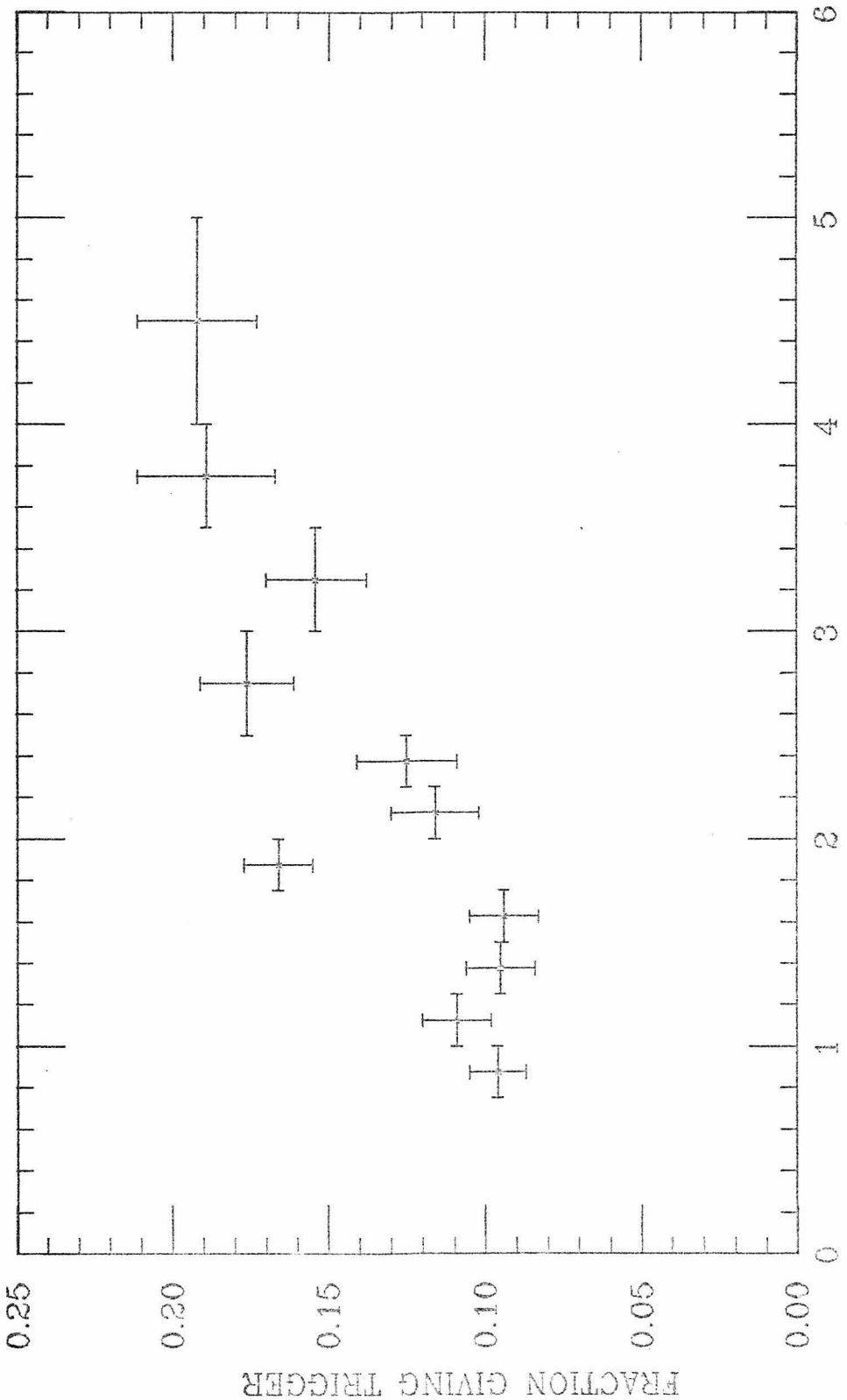

Figure 5.B.8: Punch through in shower counters (buffer strobe and gamma veto) for pion test tracks

height cut of 150 was estimated from the electron pulse height distribution as 1.4%. The contamination after the cut is estimated therefore as 0.02%.

The measurement was done for tracks in the middle and outer ring of C1 since tracks in the inner ring seldom hit a shower counter. The result is shown in fig. 5.B.7 (above). For momenta below 5.0 GeV/c the probability averaged 0.17%±.06% (7 tracks made light in the outer ring, 3 in the middle).

Table T5.B.2 below gives the frequency of each cell having light without any observed track. The average rates for the whole outer, middle, and inner rings (excluding unequipped

Table T5.B.2: PROBABILITY OF SPURIOUS COUNT IN C1 CELLS

Counts per 10**4 events

OUTER RING		MIDDLE RING		INNER RING		BEAM CELLS	
C1-01	10.3	C1-13	31.9	C1-25	82.8	C1-37	183.*
C1-02	6.0	C1-14	36.4	C1-26	90.1	C1-38	359.*
C1-03	7.1	C1-15	37.0*	C1-27	87.7		
C1-04	2.2	C1-16	13.7	C1-28	12.0*		
C1-05	U	C1-17	U	C1-29	U		
C1-06	U	C1-18	U	C1-30	U		
C1-07	U	C1-19	U	C1-31	U		
C1-08	7.6	C1-20	19.3	C1-32	90.7		
C1-09	2.2	C1-21	19.9	C1-33	291.*		
C1-10	9.2	C1-22	27.9	C1-34	64.2		
C1-11	21.1	C1-23	34.1	C1-35	75.1		
C1-12	13.0	C1-24	25.6	C1-36	9.9		

U=Unequipped Cell
*=Not Used (Deadened)

and deadened cells) were 0.09%, 0.27%, and 0.89% respectively. For the cells that registered light for hadrons below 5 GeV/c, the expected rate (weighted average of outer and middle ring) for registering without tracks would be 0.14%, as compared with 0.17 measured with tracks. The probability of a hadron registering in the absence of neutrals, undetected tracks, and phototube noise is taken as the difference in the rates, 0.03%±.06%. The punch-through rate using isolated pions was measured on a prototype C1 cell in a test beam as 0.02%. This rate was taken as zero, and the overall punch-through rates were therefore taken as the counting rates for trackless cells given above.

5.B.5 -- Two Electron Cut

After the detailed electron identification described above, more than half the original candidate events were left with less than two electrons. (These events were of the following types: events where a track was not found because it was too slow or for other reasons, where a track failed to go through the equipped part of C1, and where C1 cells failed to register or were shared.) These events were rejected.

Of the remaining 31651 events with two or more electrons, 1388 (four percent), had three or more electrons. The three and more electron events were rejected in the interest of

simplicity. In most cases, the extra electrons would have been removed later by the cuts designed to reject tracks which came from photon conversions. The loss of final pair events due to the cut was taken as 4% on the assumption that an extra electron was equally probable in the final pair events as any pair event.

5.C -- Track Quality Cuts

This section presents two cuts on track quality. The confidence level cut removed poorly measured tracks which caused poor mass resolution photon conversion pairs. The "matrix flag" cut removed tracks which could not be properly fitted.

5.C.1 -- Confidence Level Cut

The confidence level cut removed most false tracks and those real ones which were fitted with an incorrect match-point and therefore incorrectly measured. The cut was chosen at the 1% confidence level in order to make a small impact on the signal. A cut at 10% confidence level failed to increase the ratio of signal to background.

Fig. 5.C.1 shows the confidence level distribution of tracks identified as electrons in C1. If the resolution errors in

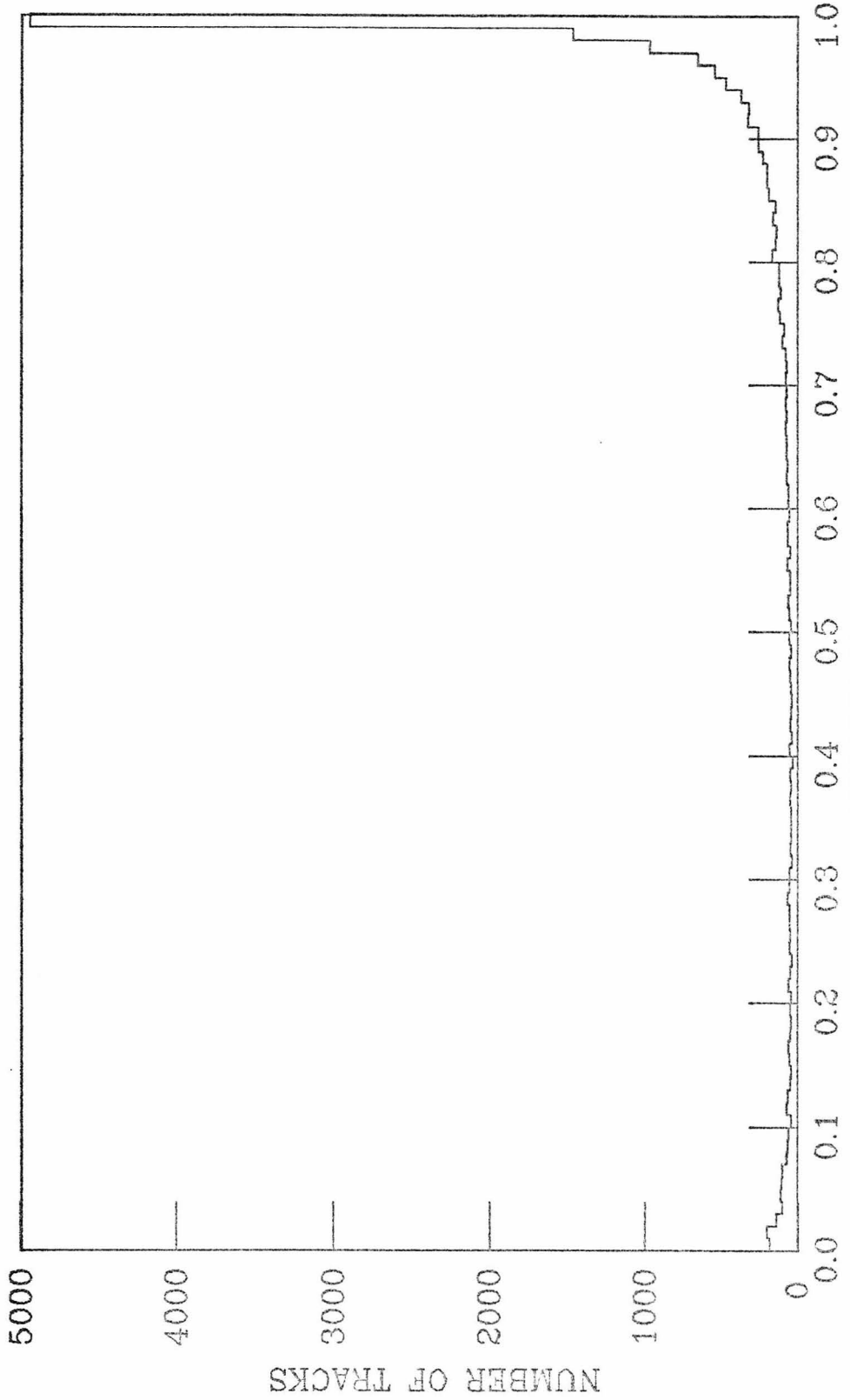

Figure 5.C.1: Confidence level distribution of electron tracks.

the chambers were distributed as a Gaussian with the width correctly specified in the program, the distribution of confidence level would be flat, and the cut would have removed exactly 1% of the real tracks. The excess of tracks with confidence level near one indicates that the resolution estimate was too large. The small increase near zero reflects the non-Gaussian tail of the measurement error distribution. The cut removed 2.08% of the pairs (1.04% of the tracks).

5.C.2 -- "Matrix Flag"

The chi-squared function used to fit the track parameters was unstable for high momentum tracks, low angle tracks, and in cases where the match-points did not fit a helix well. The "matrix flag" indicated when the fit failed to converge or when the approximate derivatives of chi-squared of the fit gave a non-positive-definite error matrix.

The cut eliminated the unfitted tracks and those with a bad error matrix. The error matrices were needed to fit the vertex pair, and the fit was needed to determine the mass.

Since electron tracks needed an angle of 30 milliradians to

hit the inner ring of C1, and were limited to a momentum below 5.0 GeV/c, most of the bad tracks were not electrons. Only 6 events in 71409 events (6 out of 142818 electron tracks) were cut.

5.D -- Pair Vertex Position and the Beam Association Cut

Below it is shown below how a measurement error on one of the tracks from a low mass pair, which were numerous because of photon conversions, could cause the reconstructed mass to be several hundred MeV/c^2. The beam association cut removed most poorly measured and erroneous tracks, thereby removing that source of false signal. The loss of signal due to the cut is estimated.

5.D.1 -- Mass, Geometry, and Conversion Pairs

Neglecting the electron mass, the parent mass of a pair is given by $m^2=2 \cdot P_1 \cdot P_2 \cdot (1-\cos(\psi))$ where P_1 and P_2 are the track momenta and ψ is the angle between them. Since the tracks were described by helices, ψ depended upon the position along the helices the tracks were believed to have originated. The point of origin, the pair vertex, was taken as the point giving the lowest combined chi-squared for both tracks, more or less the point of closest approach of the tracks. For photon conversions, in which the tracks started out parallel, the vertex position was especially uncertain.

This is analyzed in section 5.E.1, with the following results: The typical uncertainty along the beam direction of the reconstructed vertex for photons was 20 cm. The typical reconstructed mass for a low mass pair of well-measured tracks was 25 MeV/c^2 with many as high as 80. The reconstructed mass of photon conversion pairs where the parameters of one track were inaccurate by several centimeters could have masses as high as 300 MeV/c^2. Photon conversions which were produced far downstream of the primary vertex could not be separated from direct pairs because of the uncertainty on the vertex position of low mass pairs.

5.D.2 -- Photon Conversion Pairs at High Mass

Fig. 5.D.1 is a scatter plot showing the distance between the electron pair vertex (for opposite charge tracks, passing quality cuts, and not making a low mass pair with any other opposite charge track) and a primary vertex (consisting of three or more hadron tracks). The vertical scale shows the mass of the pair. Direct pairs comprise the narrow vertical band. The horizontal band at the bottom, corresponding to photon conversion pairs, shows several effects: The displacement towards the right (pair vertex downstream of main vertex) corresponds to the fact that photons converted downstream of the primary interaction. The points to the left show the extent of the vertex

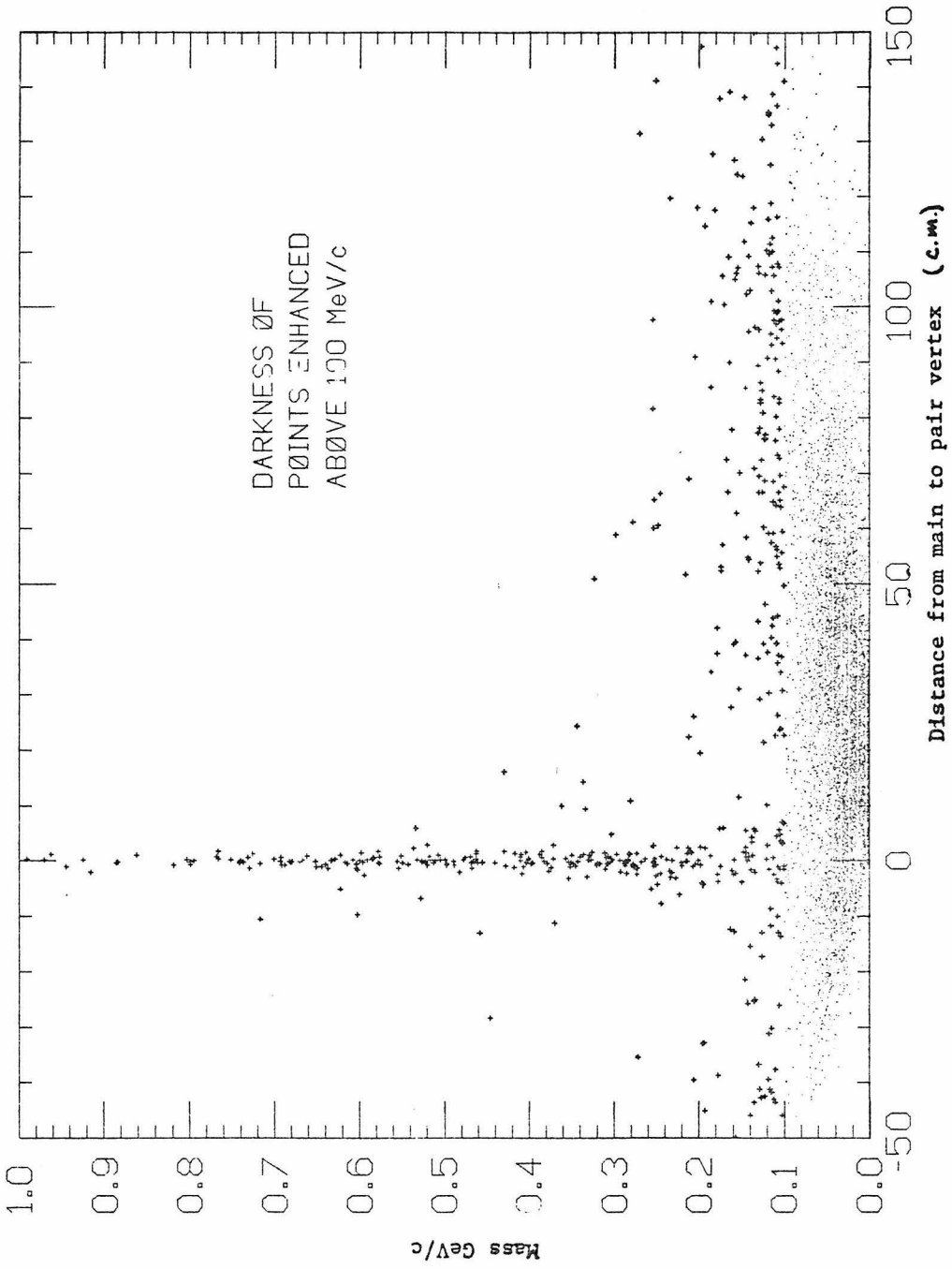

Figure 5.D.1: Separation of primary and electron pair vertex versus mass of pair, all opposite charge electron pairs.

position resolution error. The increase in mass to the left shows how the apparent mass increased with the error on the vertex position.

The occasional points at large mass and away from the primary vertex indicate the problem which necessitated the beam association cut. Above 140 MeV/c^2 in mass, the tracks must have crossed at an angle large enough that the resolution of the pair vertex position was better than 5 cm. Since no known long lived particle decays into electron pairs, one of the tracks must have been very badly measured or entirely fictitious.

The latter case is relatively benign, provided the fictitious tracks were distributed randomly in charge. The subtraction of the same-charge pairs cancels the effect. When both tracks corresponded to real electrons, the pair was almost certainly a photon conversion pair with a poorly resolved vertex, and would have appeared among the opposite charge pairs only. Even a small leakage of the photon into the high mass region would be a proportionally large effect. In fig. 5.D.2 the plot for same charge pairs corresponding to fig. 5.D.1 is shown. The photon conversion band is absent. (The narrow band of apparently direct same charge pairs is an example of the background processes that contributed to both opposite and same charge pairs, discussed below in section 5.F.) There were considerably

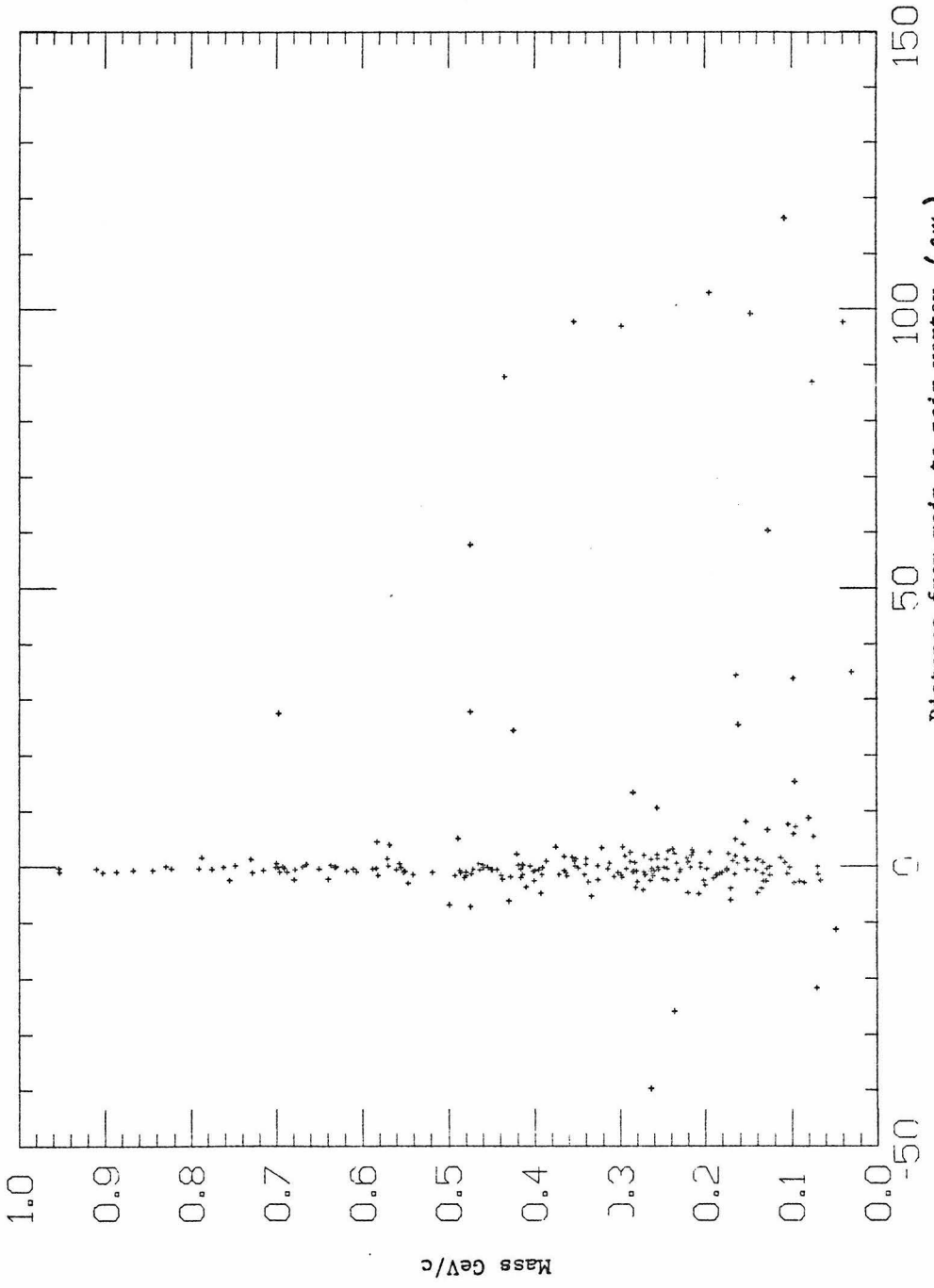

Figure 5.D.2: Separation of primary and electron pair vertex versus mass of pair, all same charge electron pairs.

fewer same charge high mass pairs far from the main vertex than opposite charge, indicating that many photon conversion pairs were present in the opposite-charge data at high masses. The beam association distance cut described below was designed to remove these spurious high mass pairs.

5.D.3 -- Beam Association Distance Cut

A cut requiring the pair vertex to be near the primary vertex was rejected for the following reasons. This cut would miss downstream conversions which coincidentally appeared to be near the primary vertex. Events without a primary vertex would have to be discarded. The same charge pair subtraction would no longer be valid for the following reasons. Opposite charge tracks bend in opposite directions in the field and so diverge more quickly than the same charge tracks which tend to follow each other. The vertex position resolution in the case of small opening angles was worse for same charge pairs than for opposite. Any cut involving a fit to the pair vertex would therefore complicate the matter of background subtraction.

Instead, cuts involving the tracks individually were considered, such as distance from the beam track, distance from the main vertex, or the sum of the distances to a common point along the beam track. The cut was made on the distance between the beam track and either of the electron

tracks at closest approach. The others were considered too complicated. This distance was required to be less than 4 mm. The cut removed 10% of a sample of test tracks (described below) chosen to resemble direct electrons.

Fig. 5.D.3 shows again the distance to the pair vertex plotted against the reconstructed mass where both tracks satisfy the 4 mm. cut. There were 2 faraway (>5 cm. from the main vertex) pairs above 140 MeV/c^2 out of a sample of 8453 events in which the hadronic vertex was accepted. (The background above 140 MeV/c^2 due to pairs inside the 5 cm. limit had to come from pairs whose "real" mass was above 120 MeV/c^2 since the maximum error on reconstructed mass was 4 MeV/c^2 per cm. error on the position. That background is treated in section 5.E.3.)

Not necessarily all faraway high mass pairs showed in fig. 5.D.3. There were cases in which no main vertex was made, and possibly cases of a downstream conversion wrongly reconstructed at high mass and near the main vertex. An upper limit for the number of cases of a high mass downstream photon conversion failing to be recognized in fig. 5.D.3, because it was reconstructed near the main vertex, was found by observing that less than 10% of the low mass pairs were reconstructed within 5 cm. of the main vertex. Using 10% as an estimate of the probability that a high mass faraway pair was too close to be detected in the

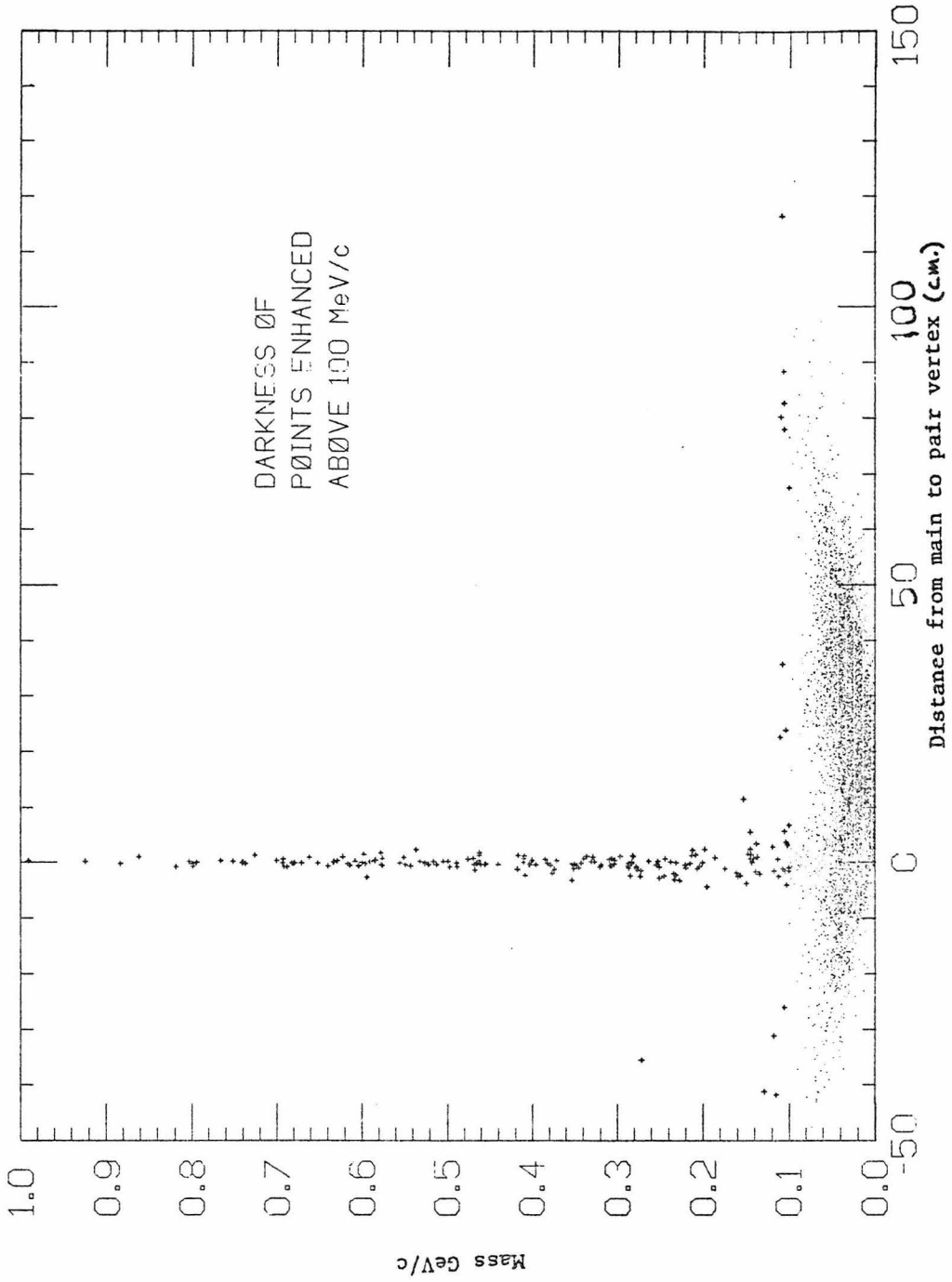

Figure 5.D.3: Separation of primary and electron pair vertex versus mass of pair, opposite charge tracks passing beam association cut.

8453 events, the additional contamination was 0.2 events. Another 0.7 false events are expected to have occurred where no main vertex was made (assuming the same rate). The two standard deviation upper limit on the expected 0.9 extra events is 2.0. The background from low mass pairs with poorly resolved vertices is estimated therefore as 2.9±0.5 events (quoting half the two std. upper limit), before correction for acceptance.

The loss of real pairs due to the cut was studied using the sample of test tracks. The test tracks were taken from interaction triggers. They were required to go through a single equipped C1 cell without making light. (Hadrons were expected to have geometricalproperties similar to the direct electrons, while most observed electrons, coming from downstream conversions, were farther from the beam when extrapolated back.) The test tracks were required to have registered in 80% of the spark and proportional chamber measuring stations they traversed. The last requirement removed most of the fictitious tracks which produced artificially large beam association distances. Fig. 5.D.4 shows the beam association distance distribution for the test tracks.

It is necessary to show that the 80% requirement did not significantly sharpen the track resolution (and thus artificially increase the fraction passing the cut). A

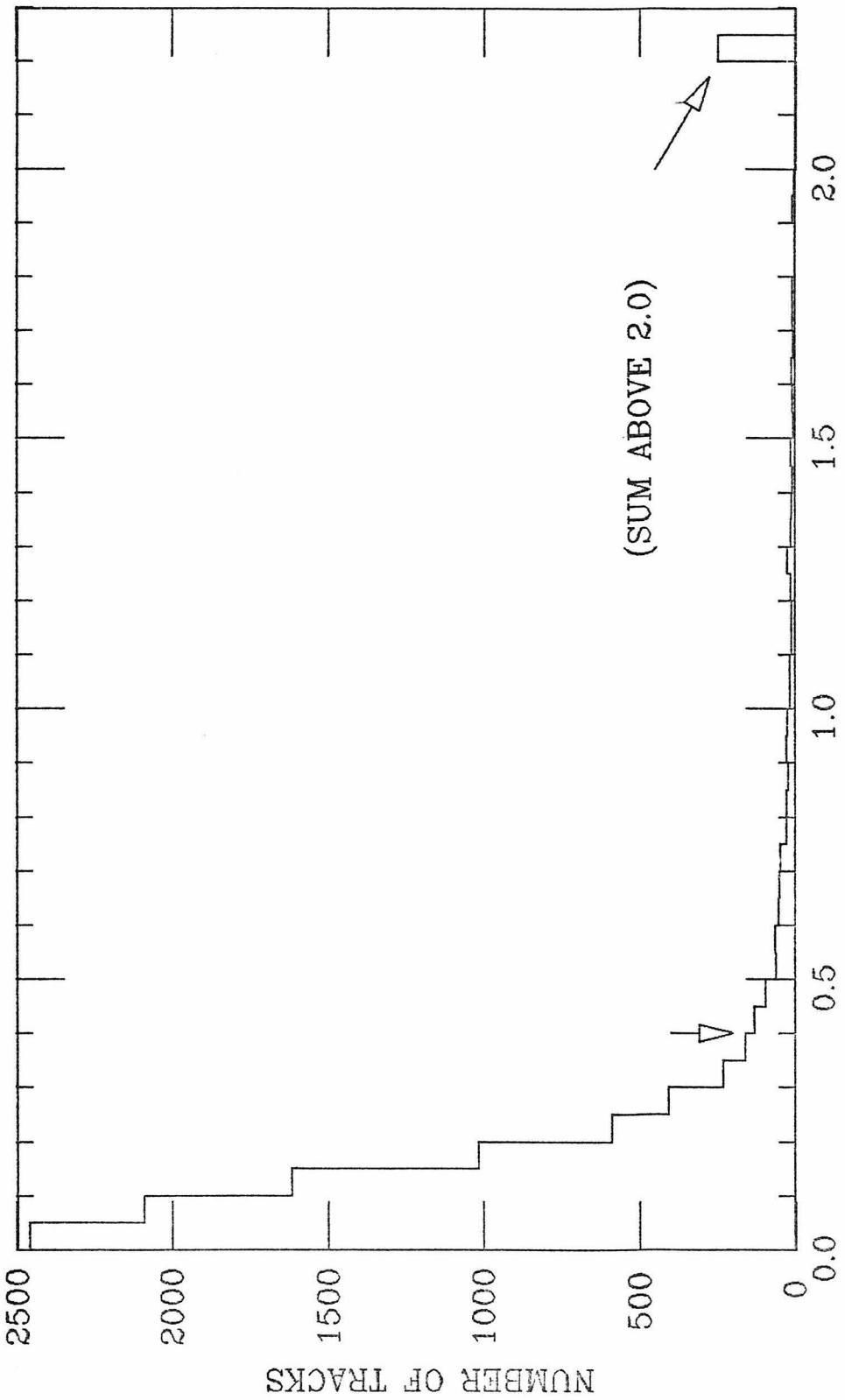

Figure 5.D.4: Beam association distance of test tracks.

subsample of the test tracks with moderately large angles and momenta was compared with and without the 80% coordinate requirement. There were few false tracks in this region of phase space. 91.7% of the unrestricted tracks passed, while of the good quality subsample, 93.4% passed. It is not known how much of this increase was due to the elimination of fictitious tracks, and how much due to sharpened resolution. The difference was treated as negligible.

The test tracks were separated into a two dimensional array of bins in momentum and Θ.) Bins were combined into rectangular groups in order to increase the statistical significance as described for the shower counter efficiencies in section 5.B.1. The additional uncertainty due to using data where the fraction of the tracks removed was different than at the nominal values, was estimated directly from the data (rather than using a fitted function as was done for C1 and the shower counters). The additional uncertainty was the sum of the magnitude of the difference between the efficiency for each of the four subsections and that for the whole rectangle. The rectangle was chosen to minimize the overall uncertainty (statistical plus that due to the spread). This procedure produced a two dimensional table of the fraction passing the cut and the uncertainty, as a function of momentum and angle. Fig. 5.D.5 shows one dimensional cross sections of this table. The average probability of passing the beam association cut (using the

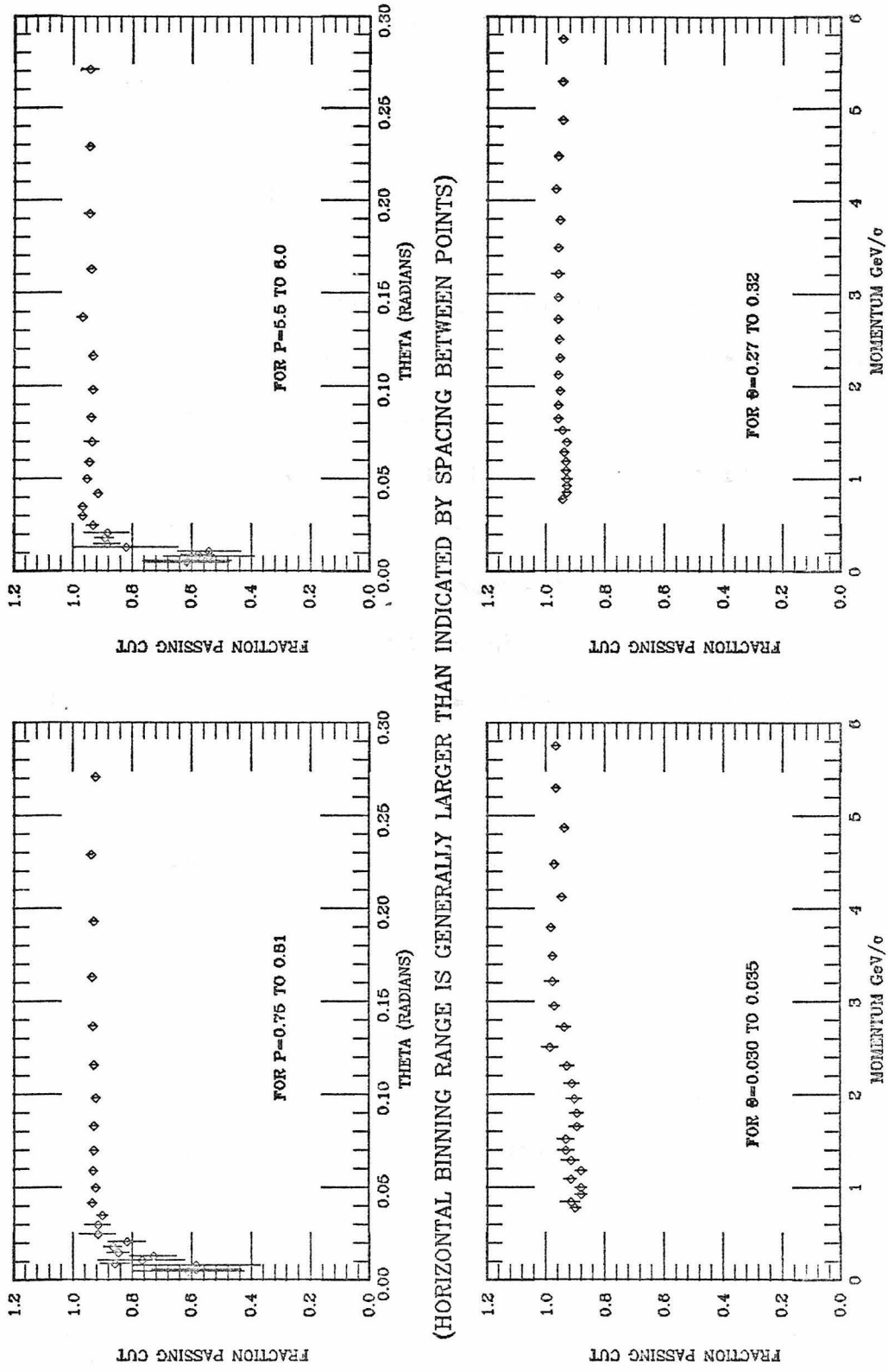

Figure 5.D.5: Result of beam association distance cut as a function of momentum and angle.

momenta and angles of Monte Carlo generated high mass electron pair tracks) was 93% per track.

5.E -- Low Mass Pairs

This section analyzes geometrically the low mass electron pairs: photon conversions and pi-zero Dalitz decays. Two sources of background are discussed: low mass pairs reconstructed at high mass and single electron tracks from photon conversions (referred to as "half-pairs"). The "low mass mate" cut, designed to remove half-pairs, is described. The contamination of the high mass signal with photon conversions and electron pairs from pi-zero Dalitz decays is estimated.

5.E.1 -- Geometry and Mass Resolution.

The mass of the electron pair (neglecting rest masses) is $m^2=P_1 \cdot P_2 \cdot 2 \cdot (1-\cos(\psi))$ where P_1 and P_2 are the momenta and ψ is the angle between them. For low mass pairs, the approximation, $m=\sqrt{(P_1 \cdot P_2)} \cdot \psi$, is used. The opening angle is given by $\cos(\psi)=\cos(\theta_1)\cdot\cos(\theta_2) + \sin(\theta_1)\cdot\sin(\theta_2)\cdot\cos(\varphi_1-\varphi_2)$, where $\tan(\theta) = P_t/P_l$ and $\tan(\varphi) = P_y/P_x$) Along the helical track, the direction of the momentum changed. The components P_x and P_y changed according to $d\varphi/dz=a/P_l$, while P_l, P_t, and θ remained fixed. For the 22.5 kG. field, a was 0.006735 (GeV/c)/cm.

Photon conversions and pi-zero Dalitz decays produced pairs with mass close to zero. The helices were therefore tangent to each other at the point of creation. Θ_1 and Θ_2 were equal everywhere and $\varphi_1 - \varphi_2$ was zero only at their common origin (recurring at isolated faraway points). Moving the helices closer (representing a small measurement error) resulted in a large shift in the position of closest approach of the tracks (the reconstructed vertex). Fig. 5.E.1 illustrates this point. The drawing on the left shows an end-on view of a photon conversion. The track helices appear as circles. The slope perpendicular to the page is 1/TAN( ) in units of Z distance per unit arc-length. The drawing on the right shows the result of moving one of the helices closer by a small distance e. The intersection point moves from V to V' by a distance h, given by $h^2=2 \cdot e \cdot r_1 \cdot r_2 / (r_1 + r_2)$. The Z positions of the tracks at V' are almost identical for the following reason: Θ_1 equals Θ_2 so that the Z change per arc-length is the same for both tracks. The arc-lengths from the beginning to V' are almost the same, because they are both approximately straight line segments. The fitted vertex is therefore near V'. (A measurement error in the opposite direction did not have this effect.)

The apparent mass calculated as a function of the distance e is $m^2=2 \cdot e \cdot c \cdot (P_{t1} + P_{t2})$, or in units of GeV/c, GeV/c^2, and

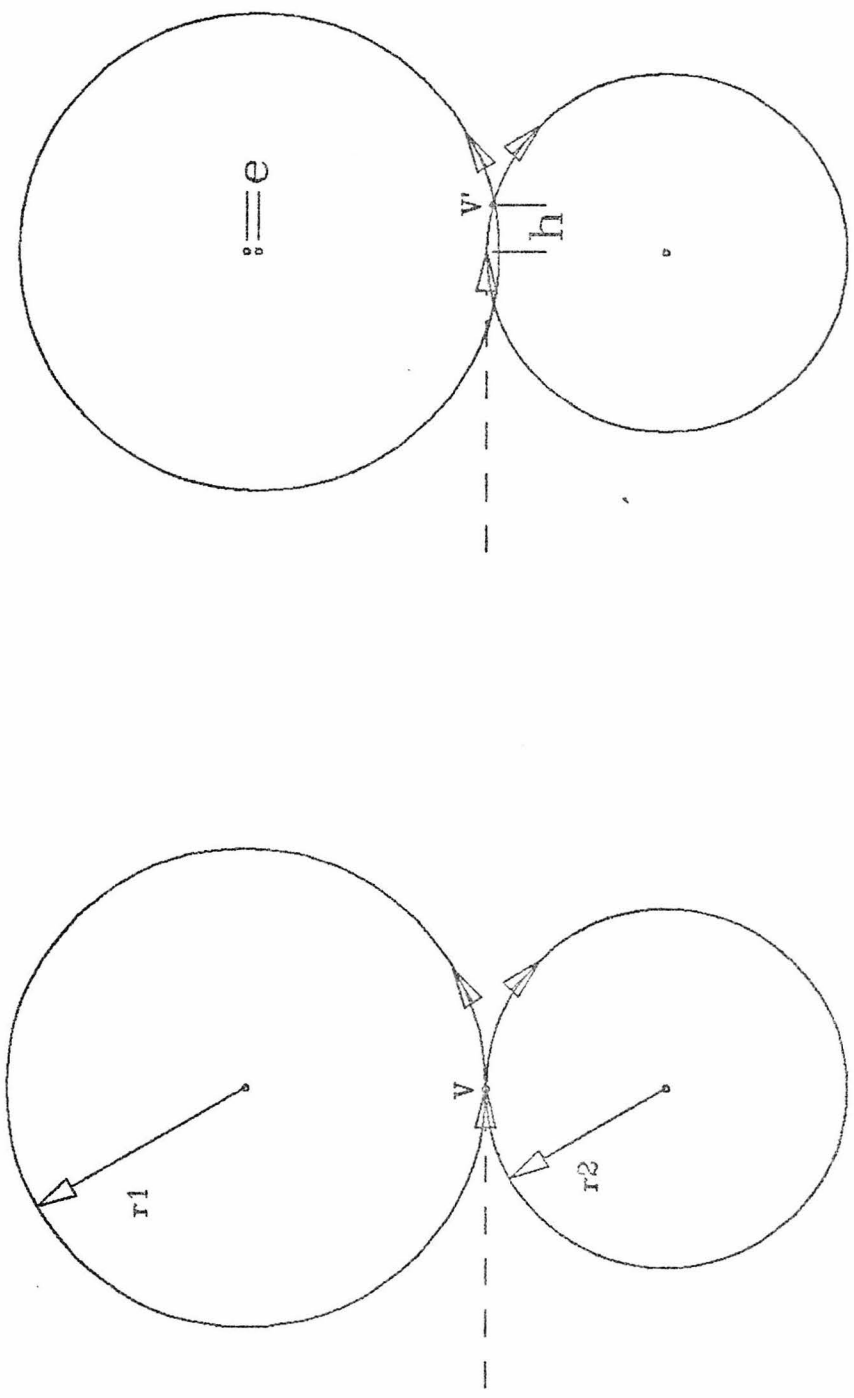

$h=\sqrt{2*e*r1*r2/(r1+r2)}$

Figure 5.E.1: Effect of a small shift of the center of a helix on the vertex position.

cm., $m=0.116\cdot\sqrt{(e\cdot(P_{t1}+P_{t2}))}$. The error on the vertex position is h/TAN(θ). This comes out as $z=17.2\cdot\sqrt{(e\cdot(P_1+P_2)/SIN(\theta))}/f$ in cm. and GeV/c. The number f = $(P_1+P_2)/\sqrt{(P_1\cdot P_2)}$ depends only on the ratio of the momenta and lies between 2 and 2.97 for momenta in the range 0.75 to 5.0. The rate of change of the mass with vertex error distance is $dm/dz=c\cdot f\cdot SIN(\theta)$. (This does not require a zero opening angle.) The angle θ was limited to the range 0.1 to 0.2 by the shower counter requirement for one of the tracks. (Fig. 5.E.2 shows the angular distribution of triggering tracks.) dm/dz therefore is expected to be in the range 1.3 to 4.0 (MeV/c^2)/cm. It is histogrammed in fig. 5.E.3 for values of P_1, P_2, and θ taken from opposite charge electron pairs. It fell between 1.1 and 3.5 in 99% of the cases.

The momenta were mostly low, averaging 2.2 GeV/c. The distribution of the reconstructed mass is calculated, assuming the distance e was the same as the beam association distance of the individual tracks in fig. 5.D.4. The beam association distance is well fit by the function dN/db proportional to EXP(-b/(.125 cm.)). These values predict a distribution for the mass of $dN/d(m^2)$ = constant • $EXP(-(m/(34\ MeV/c^2))^2)$. Fig. 5.E.4 shows a histogram of measured low mass opposite-charge pairs fit by dN/dm = constant • $m\cdot EXP(-(m/(34\ Mev/c^2)^2)$. The downward distortion of the pair masses at low masses is believed to be the result of the coordinates of each track being close enough

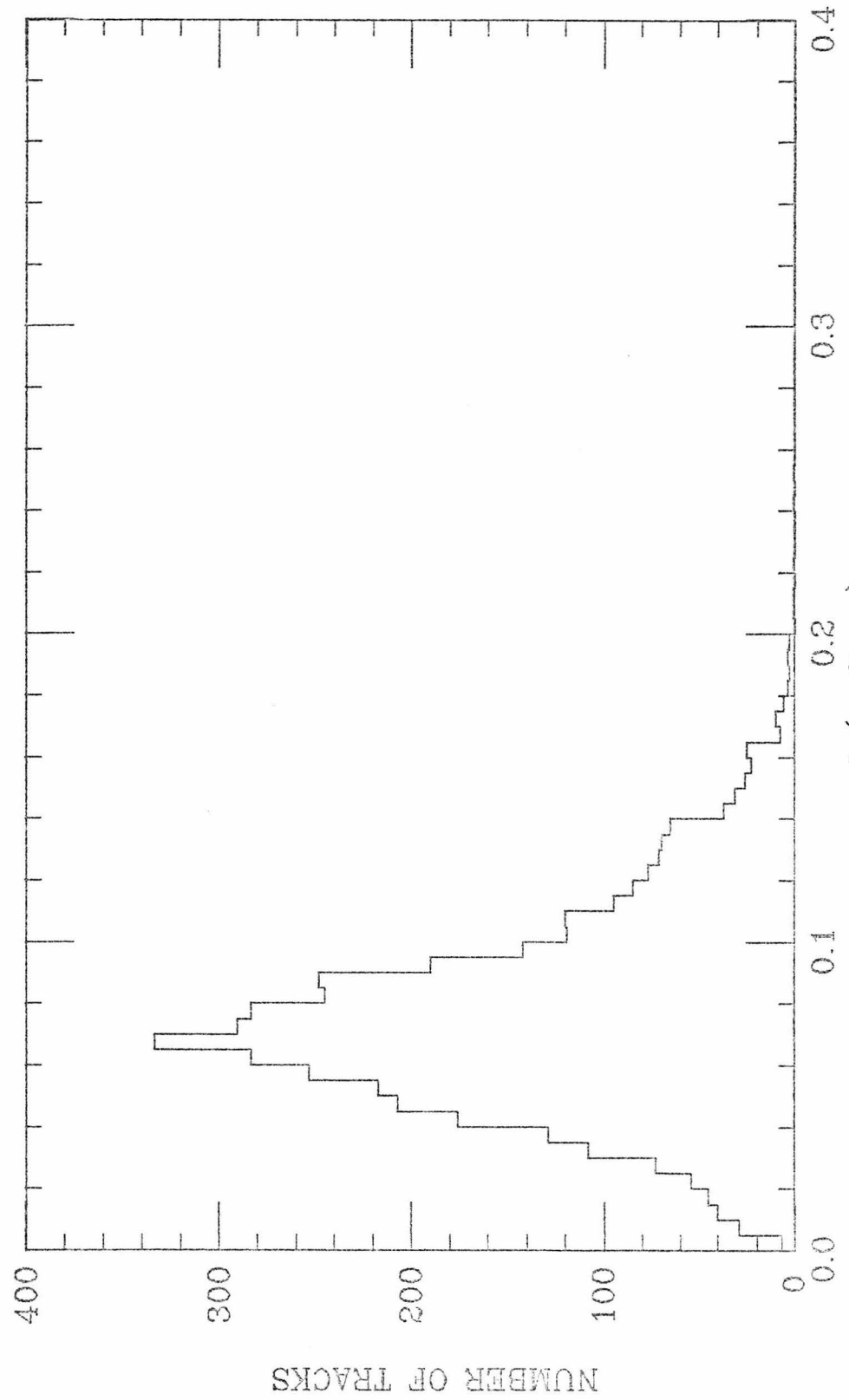

Figure 5.E.2: Θ angle of triggering tracks.

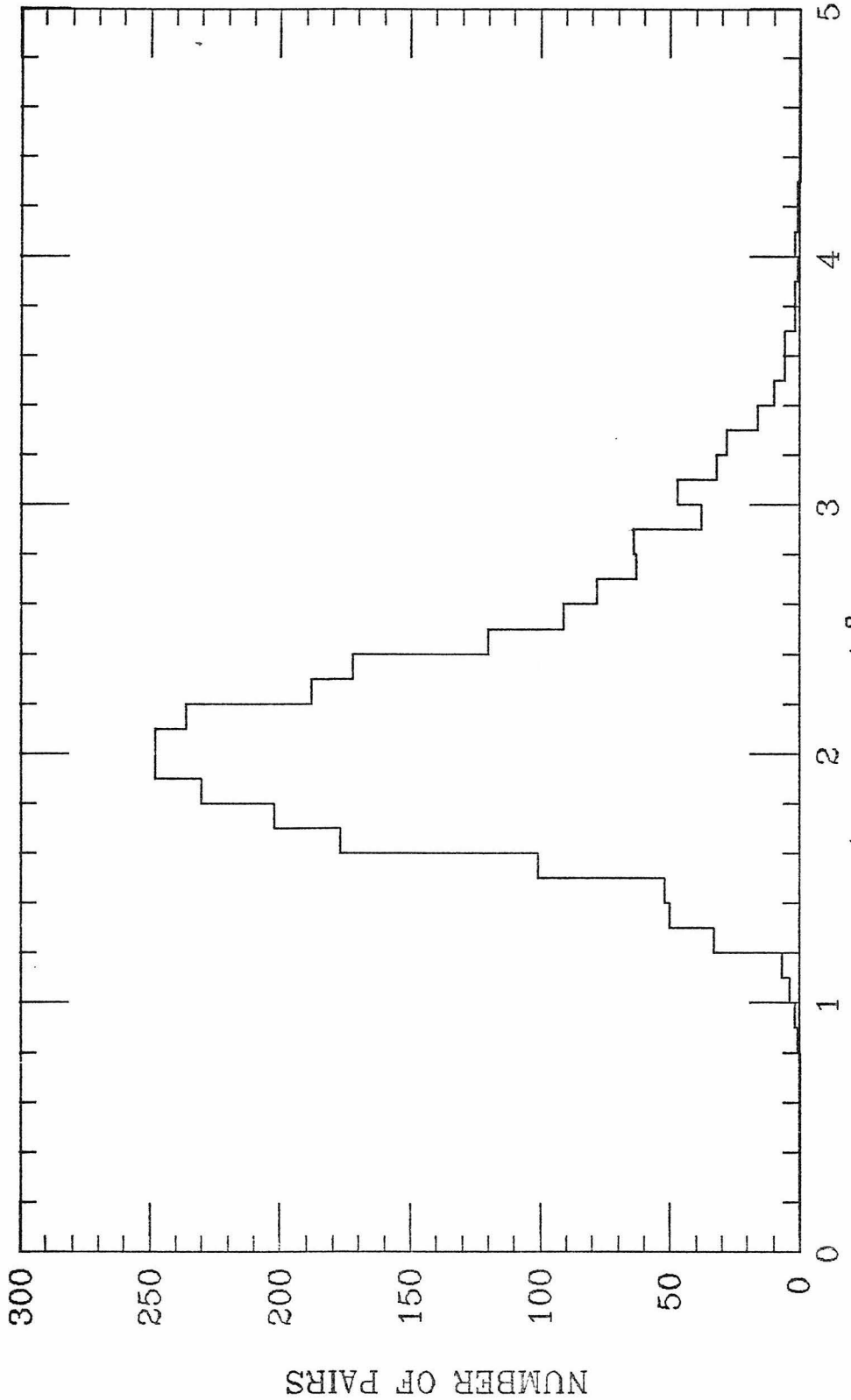

Figure 5.E.3: Distribution of dmass/dZ for electron pairs, where dmass/dZ=c*SIN(Θ)*(P1+P2)/√P1*P2.

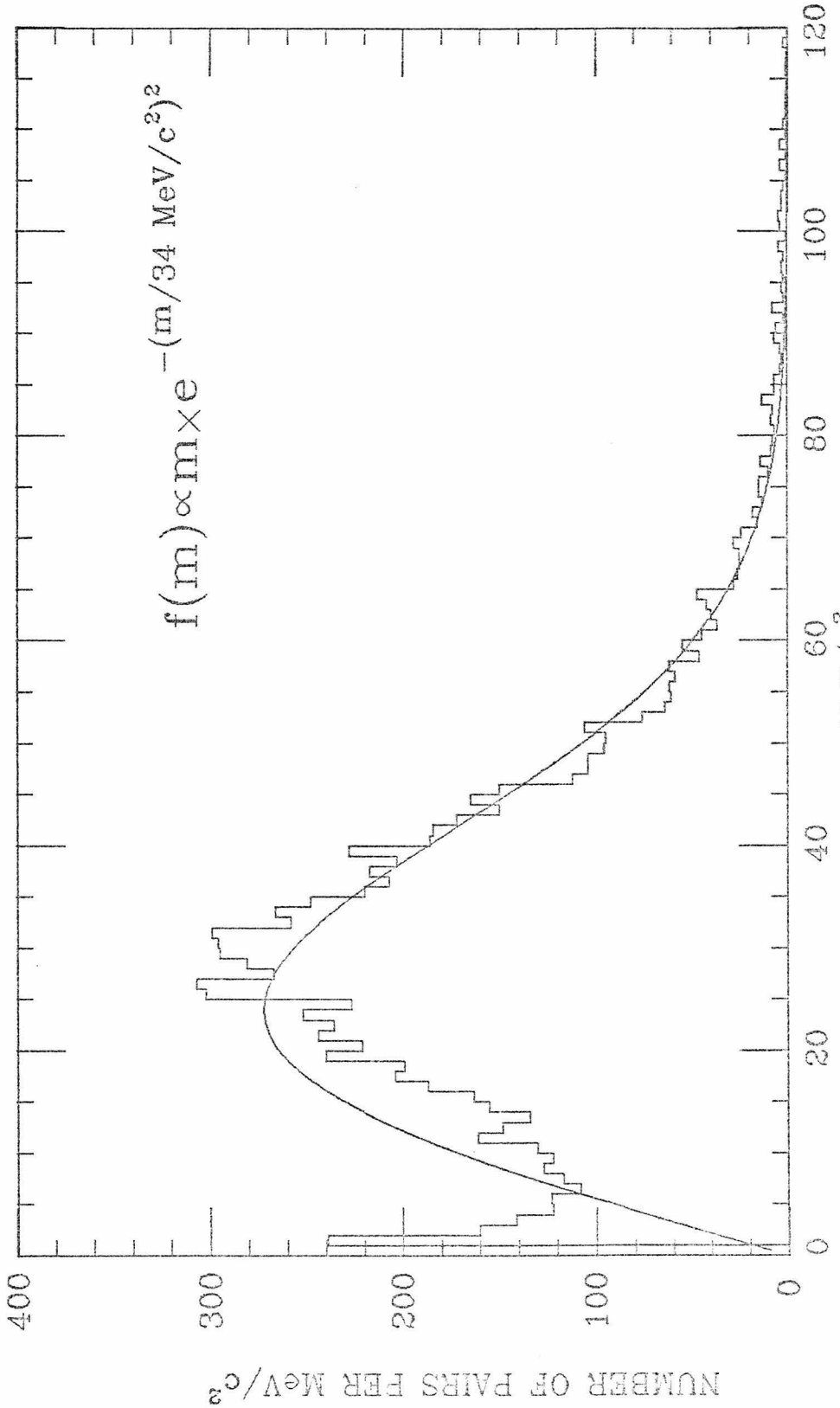

Figure 5.E.4: Distribution of electron pair mass, with fit.

together that they are combined into one point, in several of the planar chambers. Otherwise the agreement is striking.

5.E.2 -- Low Mass Mate Cut

Electron tracks from photon conversions would often mimic high mass pairs when the tracks were produced by two separate photons. The "mate" for each (coming from the same photon as the first electron and with which the pair mass was low) was often not identified as an electron because its momentum was below the cut-off or because it did not hit an equipped C1 cell. Such events were rejected by calculating the masses of all pairs consisting of one of the electrons and an opposite charge track not identified as an electron, and then requiring that none was less than 150 MeV/c^2 in mass. Pairs with tracks with bad matrix flags were not tested because the vertex could not be fitted.

Fig. 5.E.5 shows a scatter plot of the opening angle (Ψ) against the mean momentum ($\sqrt{(P_1 \cdot P_2)}$) for a test sample of opposite charge electron pairs. One electron was required to pass all the cuts described above, so that it corresponded to the candidate electron tracks. The other was required only to register in C1 in order to include as far as was possible mates which fell outside the momentum, confidence level, and beam association distance limits. The

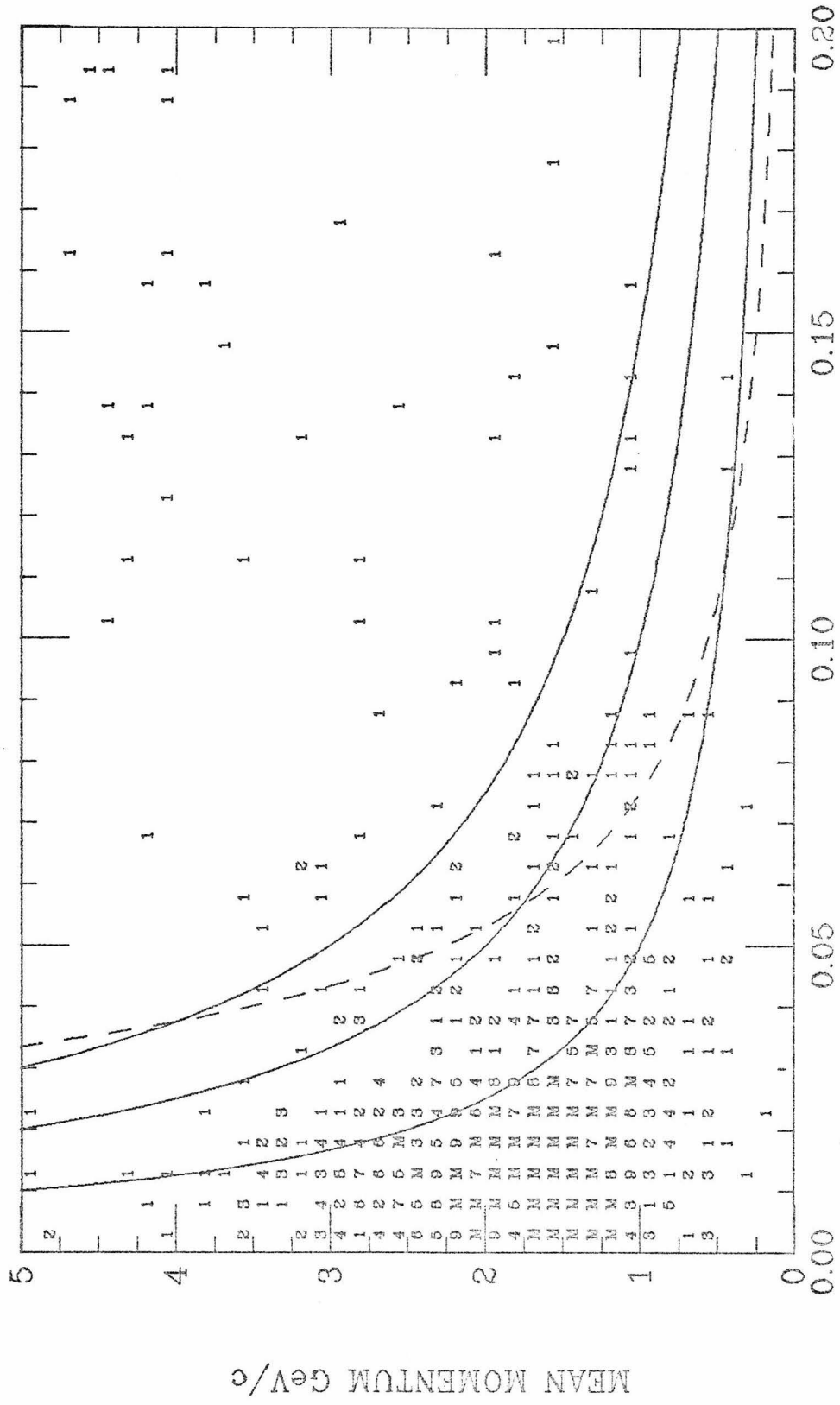

Figure 5.E.5: Scatterplot of opening angle versus mean momentum of electron test pairs, with curves of constant invariant mass.

C1 requirement cut out most very low momentum mates, but was necessary to eliminate electron-hadron pairs.

The solid curves correspond to $\sqrt{(P_1 \cdot P_2)} \cdot \psi$ = mass = 50, 100, 150 MeV/c². The dense region of conversion pairs covered a larger region of at lower momenta. The dense region is contained by the curve representing a mass of 100 MeV/c². The dashed curve is an example of $\psi \cdot ((P_1 \cdot P_2)**1/4)$ = constant, which is derived from the formula for the opening angle of zero mass pairs due to helix mismeasurement: $\psi^2 = 2 \cdot e \cdot c \cdot f \cdot TAN(\vartheta) / \sqrt{(P_1 \cdot P_2)}$, taking a constant upper limit for the separation, e, and the momentum partition, f. This curve does not seem to fit as well as the mass cutoff.

Fig. 5.E.6 shows the mass distribution of the test pairs described above. The test pairs at high masses were accidental combinations of electrons (coming from two separate conversions). They appeared as same charge pairs as well. A drop occurred in the distribution at both 80 and 150 MeV/c². A cutoff of 100 MeV/c² (rather than 150) passed many more same sign pairs, a measure of electrons coming from separate conversions. This indicates that there was a significant number of electron tracks having mates which formed masses between 100 and 150 MeV/c². The mass cutoff therefore was chosen as 150 MeV/c².

The loss of direct high mass electron pair events due to

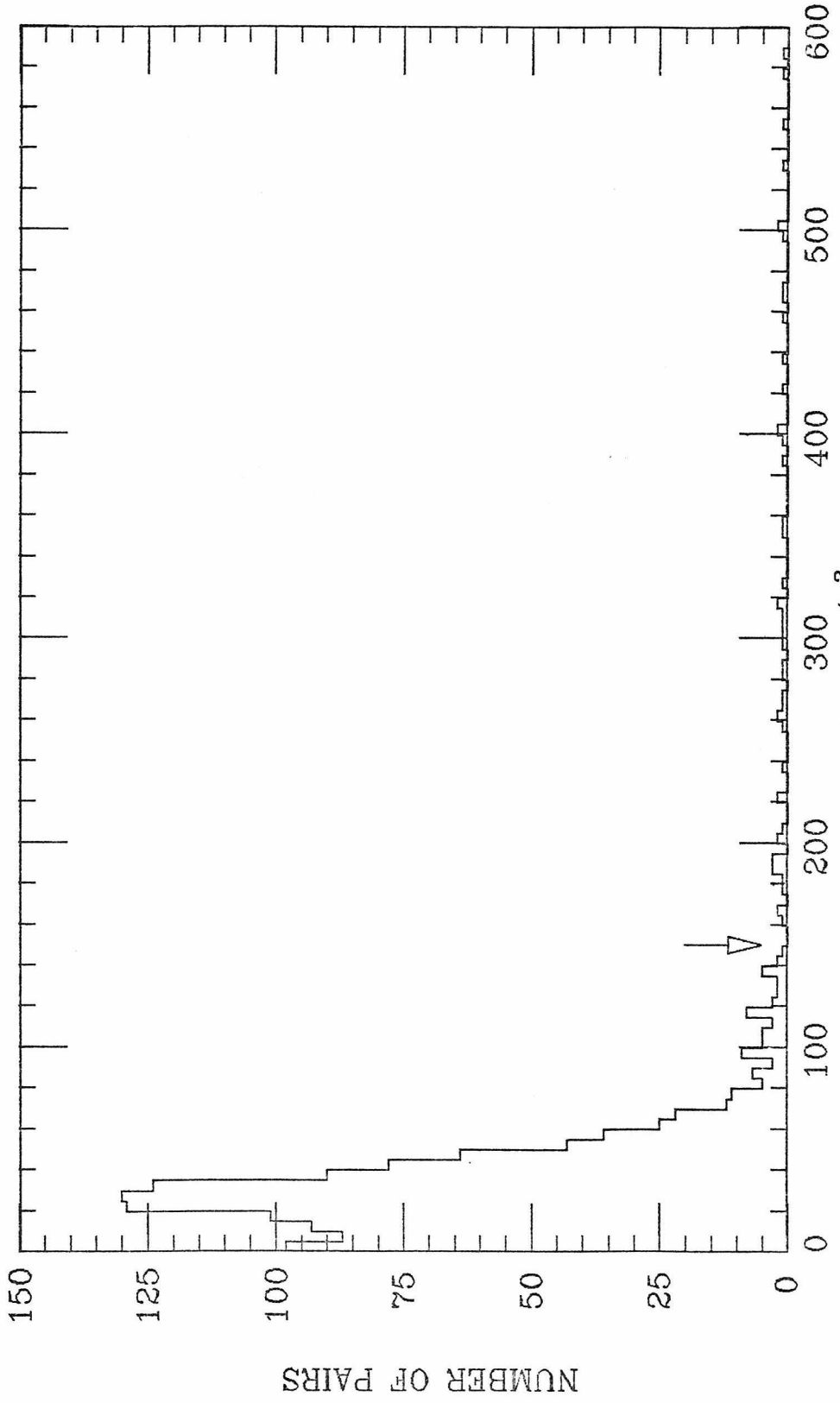

Figure 5.E.6: Invariant mass of electron test pairs.

chance low mass combinations with the other tracks in the event was compensated on an event by event basis by giving each event a weight equal to the reciprocal of the estimated probability of both electrons surviving the cut. The probability of avoiding a chance low mass pairing with one of the opposite charge tracks was read from a four dimensional table as a function of the electron charge, momentum and angle, and the number of opposite charge tracks in the event.

The table was computed using the T1 (interaction trigger) events and artificial electron tracks. The probability of an electron with a given momentum and θ making a low mass pair with one of the tracks of the event was taken as the fraction of the circle of φ values over which the mass was less than 150 MeV/c^2. For each T1 event, the probabilites of surviving the cut were calculated for electrons over a range of 32 momentum values, 32 θ values and both charges, and recorded as a function of these quantities and of the multiplicity of the opposite charge tracks against which it was tested. (The probability of making a low mass pair with none of the tracks was calculated assuming the individual probabilities were independent.) For each bin, the mean probability and the uncertainty on the mean were calculated to produce the table. Fig. 5.E.7 shows the probability of a single electron passing the cut for opposite charge track multiplicities of 1 through 8 as a function of electron

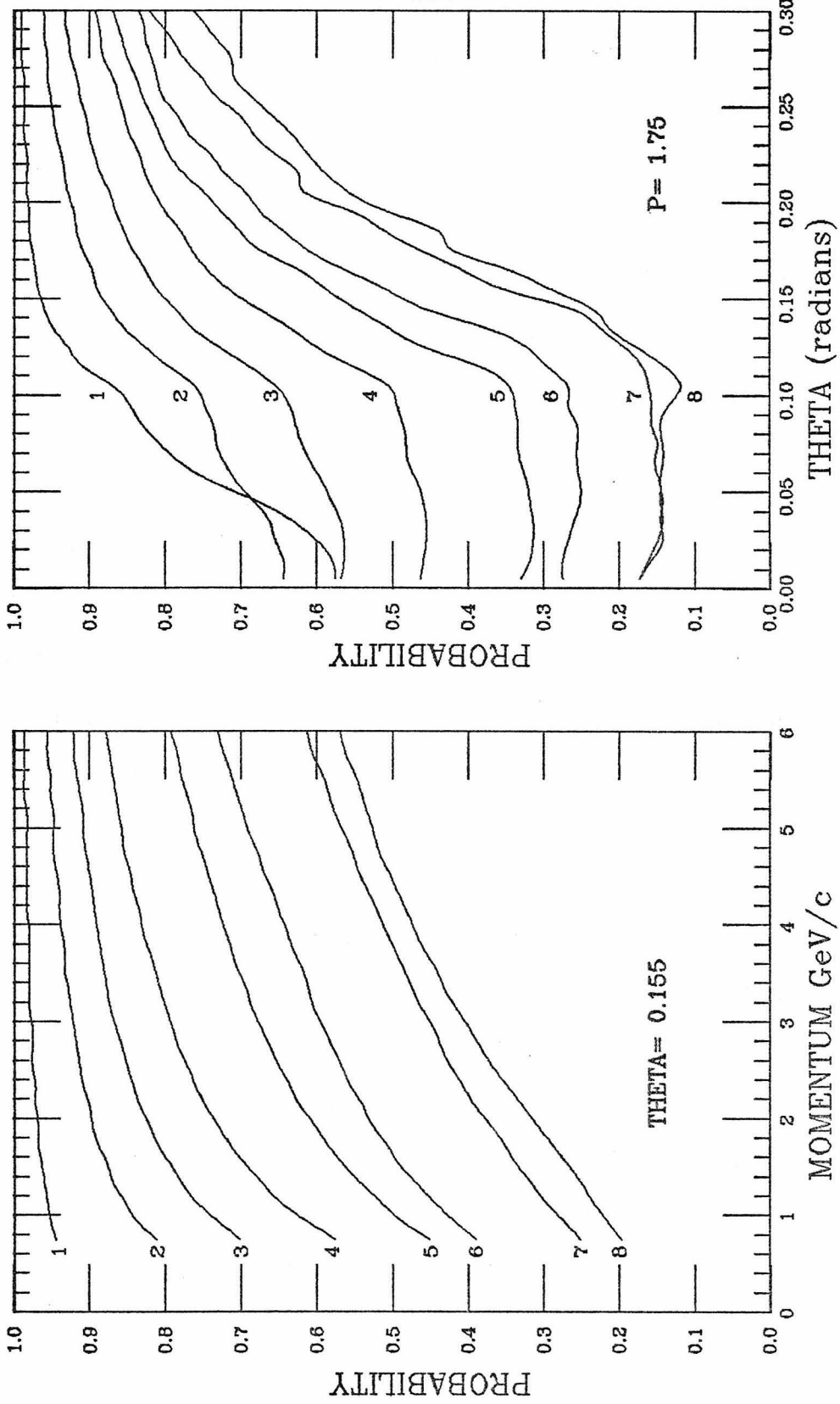

Figure 5.E.7: Probability of passing low mass pair cut as a function of momentum and angle (for 1 to 8 opposite charge track multiplicities).

momentum at a fixed angle, and of angle at a fixed momentum. The probability was one when there were no opposite charge tracks. (The values shown are for negative electron tracks. Those for positive tracks were only a few percent different.) The uncertainty of the probability estimate was recorded as a single value for each multiplicity (it depended mostly on the number of cases processed which fell as the multiplicity increased). The recorded uncertainties were an upper limit of the uncertainties for all values of momentum, Θ, and charge.

The distribution of the event weights (the reciprocal of the probability for both electrons passing the cut) is shown for the high mass electron pairs in fig. 5.E.8.

When binning the weighted events, a single large weight event added to a bin containing only small weight events greatly reduces the statistical significance. For example, a bin containing 9 events of weight 1 has a significance of 9±3. Adding an event of weight 4, i.e. 4±4, gives 13±5, a less significant indication of a signal. In order to avoid such a loss of significance, a ceiling was imposed on the event weights. A weight of 2 was assigned to all events in which the probability of passing the low mass pair cut was less than 0.5. The cutoff affected 49 out of a total of 325 events (with mass greater than 120 MeV/c^2). The cutoff reduced the average weight from 1.592 to 1.458. There was

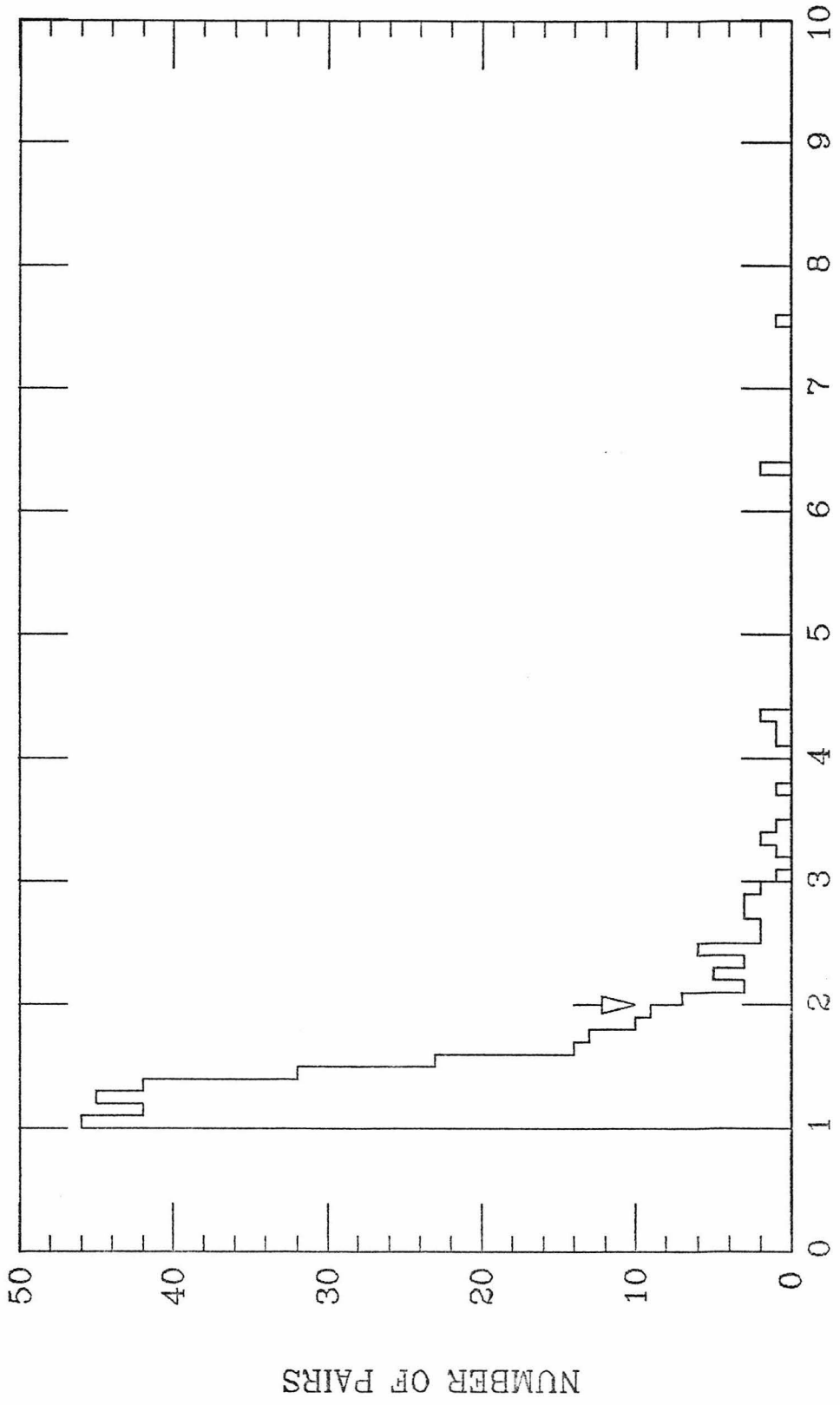

Figure 5.E.8: Low mass mate cut compensating weight for final sample of high mass electron pairs.

no apparent correlation between weights above 2.0 and the mass of the pair (scatter plot shown in fig. 5.E.9). A factor of 1.092 was included in the final acceptance correction to give the correct average weight.

5.E.3 -- Pair Vertex Related Cuts

Three cuts were concerned with the pair vertex: If the vertex fitting procedure failed to converge the event was dropped. Events were also dropped when the Z position of the fit was outside the target. Finally, events were cut if the X-Y position of the beam track at the Z of the fit was near the aluminum target jacket.

The vertex fit failed for 27 out of 9793 pair candidates. All were opposite charge and the difference in θ for the two tracks was always less than 14 milliradians. This indicates that they were low mass pairs. It is assumed that the cut had no effect on the high mass signal.

Fig. 5.E.10 shows the Z position of all the pairs. The liquid hydrogen extended from 23 to 114 cm. The material in Plug1/CD1 extended from 121 to 131 cm., and that of the 1.5 chambers from 165 to 167. (Not all low mass events seen in the Plug1 peak were created there. Tracks separated by less than one wire spacing were measured to have identical chamber coordinates. This distorted the fitted helices

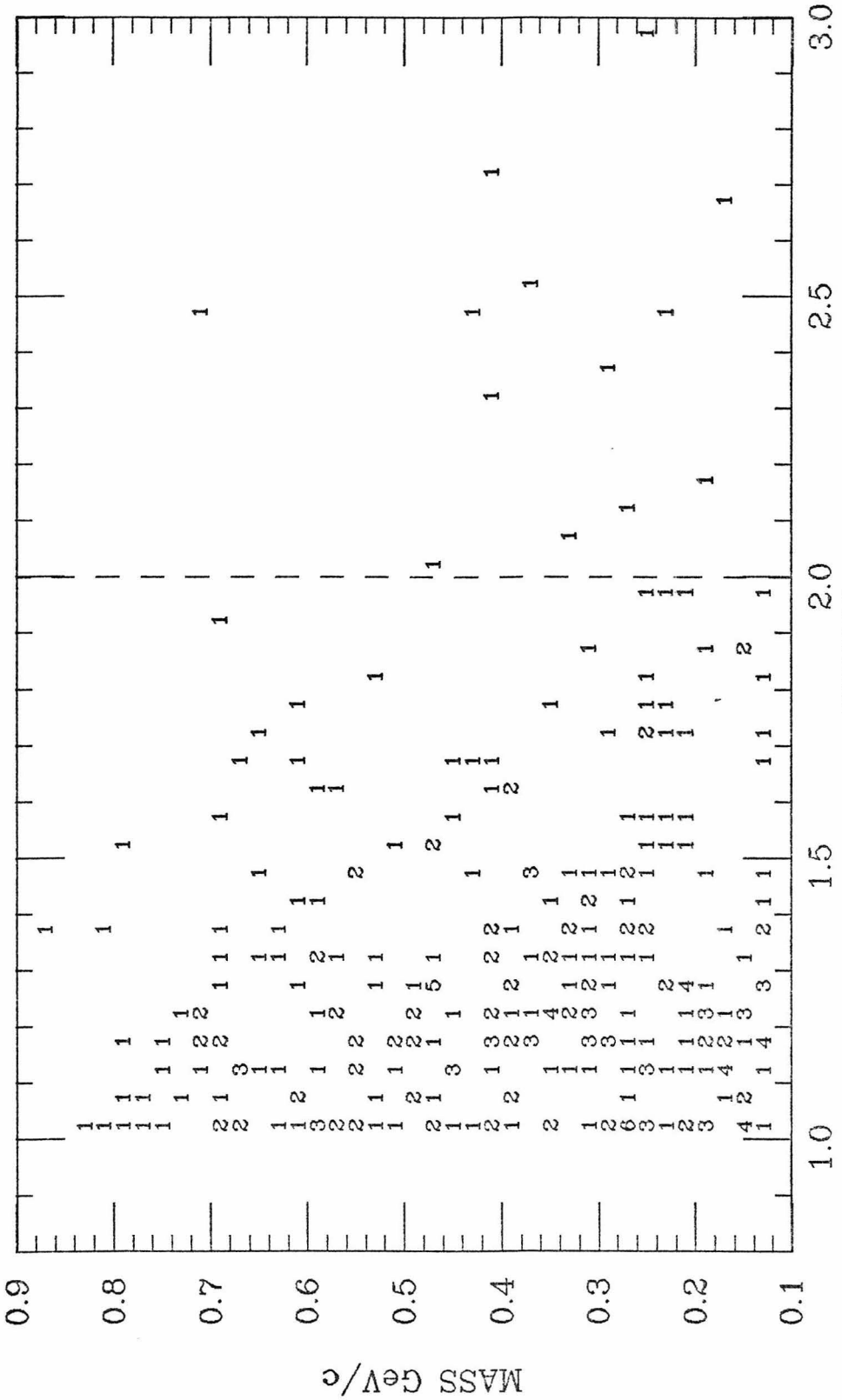

Figure 5.E.9: Scatterplot of the low mass mate cut compensating weight versus the mass of the pair.

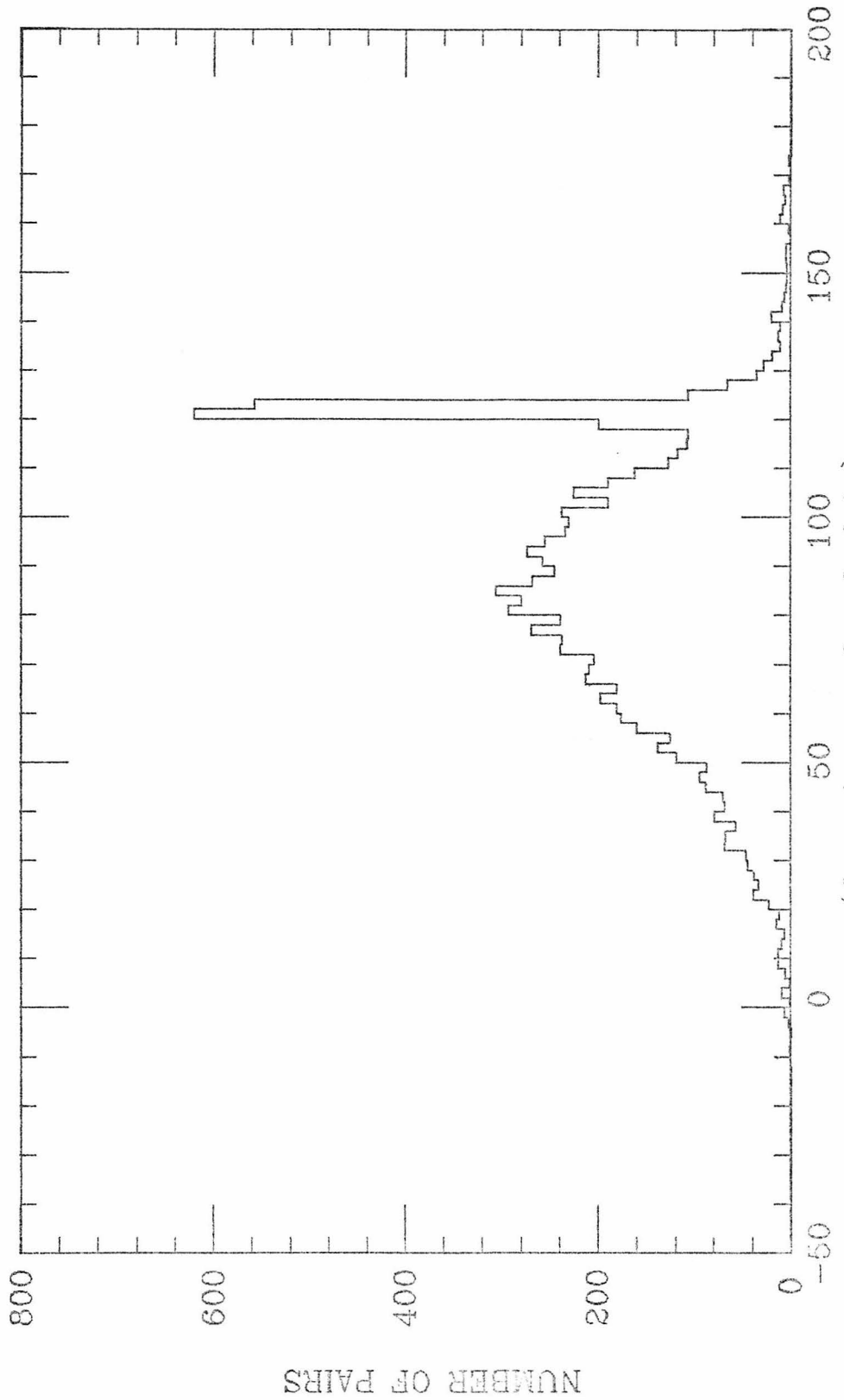

Figure 5.E.10: Z position distribution of all opposite chagre pair vertices.

enough that the vertex fitted best at the position of the chambers.) The linearly rising slope of the histogram containing the low mass pairs was a consequence of the increasing number of photons available for conversion at the downstream end of the target.

The Z position distribution for high mass pairs is shown in fig. 5.E.11. The histogram is level, indicating that most high mass pairs came from primary interactions.

The Z position was required to be no more than 5 cm. beyond the ends of the target. This insured that all pairs produced in the target were accepted even if smeared by the vertex resolution. With 5 cm. smearing, pairs produced in material outside the target could not fall within the cut, with the following exception. Pairs produced in the front of Plug1 could be smeared as far upstream as 116 cm. However, no pairs were observed between 116 and the cutoff of 119 cm., and thus background from material beyond the target was not significant.

Fig. 5.E.12 shows the distance from the center of the target to the beam track at the Z position of the pair. This was cut at 2.3 cm., 3 mm. from the aluminum jacket, in order to remove possible interactions in that material. The effect on the beam flux was negligible. One event was cut.

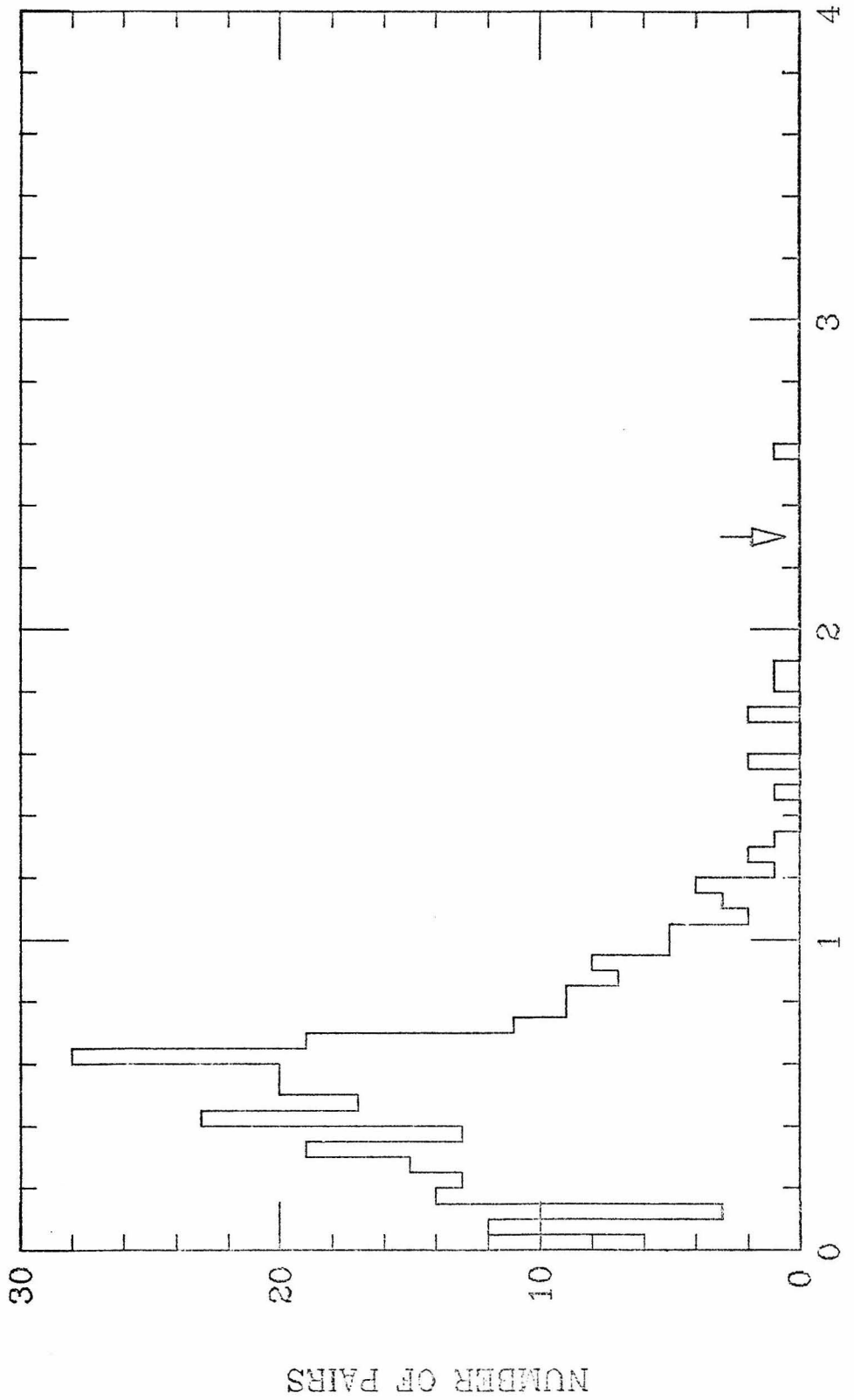

Figure 5.E.12: Distance from target axis to high mass pair vertices.

5.E.4 -- Low Mass Pairs Appearing at High Mass

The number of low mass pairs appearing at high mass due to very large errors in the reconstructed pair vertex position was estimated in section 5.D.3. The present section discusses the possibility of pairs from photon conversions and pi-zero Dalitz decays with a vertex reconstructed within 5 cm. of the correct position, being counted as the high mass signal. The number of low mass pairs is taken directly from the final mass spectrum. The relative number of Dalitz pairs and photon conversions is calculated assuming pions are the only significant source of photons. The mass resolution excluding the error on vertex position is calculated. The number of these pairs at high mass is estimated to be less than one.

The approximate ratio of photon conversion to pi-zero Dalitz decay pairs was obtained by computing the probability of a photon interacting with the material in the target. The amount of material in the path of the photon depended on its angle, increasing as $1/SIN(\theta)$. The angle of the photon was the same as that for the daughter electrons, and so an average value of the electron angle, 0.16, as shown in fig. 5.E.2 was used. (Photons originating in the last 18% of the target exitted through the mylar end window instead of the aluminum outer jacket. The estimate errs by about 15% by ignoring that effect. It errs by about 10% in the opposite

direction by ignoring the material in the CD1/Plug1 chambers.)

Tracks perpendicular to the target penetrated 2.6 cm. of hydrogen and 0.071 cm. of aluminum. This constituted 0.9% of a radiation length(1), or .7% probability of producing an electron pair (0.2% from the hydrogen and 0.5% from the aluminum). Correcting for the increased path length because of the angle, and counting both photons from the decay, each pi-zero produced 0.09 electron pairs on the average. The pi-zero Dalitz branching ratio is 0.0115 (2), leading to a prediction of 8 conversion pairs for each Dalitz. About 7815 pairs were detected below 140 MeV/c^2. An estimated 870 therefore came from pi-zero Dalitz decays.

The mass error on low mass pairs had three components. At the correct vertex position, mismeasurement of the track angles modified the opening angle of the pair. Mismeasurement of the momenta changed the factor $\sqrt{(P_1 \cdot P_2)}$ which multiplied the opening angle. Mismeasurement of the track position led to an incorrect reconstructed vertex position thereby changing the opening angle.

The contribution to the mass error from the vertex reconstruction was less than 20 MeV/c^2, for the events in question (vertex error < 5 cm.).

The error on the track momentum generally increased with increasing momentum. The error on the quantity $\sqrt{(P_1 \cdot P_2)}$, calculated from the track error matrices, was divided by $\sqrt{(P_1 \cdot P_2)}$, in order to better characterize it. Fig. 5.E.13 shows the histogram of $dLOG(P_1 \cdot P_2)/2 = d\sqrt{(P_1 \cdot P_2)}/\sqrt{(P_1 \cdot P_2)}$. Assuming this error was not correlated with the opening angle, dmass/mass (for the momentum errors only) had the same shape. Because of its proportional nature, this error was small for low masses.

The mass error due to mismeasurement of the opening angle was estimated by measuring the difference in the measured Θ angle of the electrons in opposite charge pairs. The error on Θ was independent of the vertex position.

A small opening angle, Ψ, may be resolved approximately into components parallel and perpendicular to the angle from the Z axis to the tracks. These components correspond respectively to the two terms in the approximation, $\Psi^2 = (\theta_1 - \theta_2)^2 + SIN(\theta_1) \cdot SIN(\theta_2) \cdot (\varphi_1 - \varphi_2)^2$. This is shown geometrically in fig. 5.E.14 where a region of the unit sphere is approximated by a plane. Ψ is the hypotenuse of a right triangle whose legs are the two terms mentioned above. Assuming that the direction of the error on the track direction was random, the distribution of reconstructed for zero opening angle pairs can be inferred.

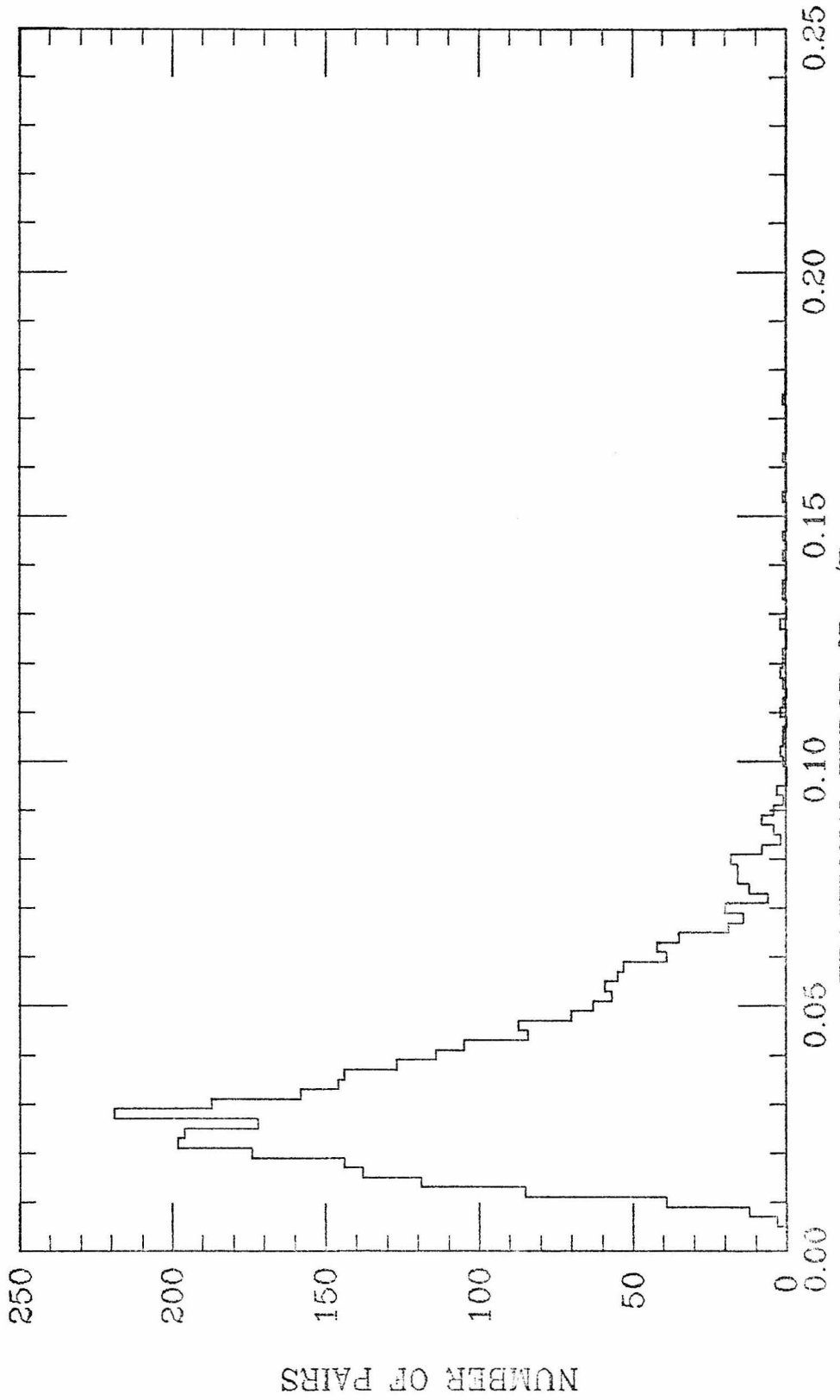

Figure 5.E.13: Fractional error on average momentum, $P_{AV}=\sqrt{P_1 \times P_2}$

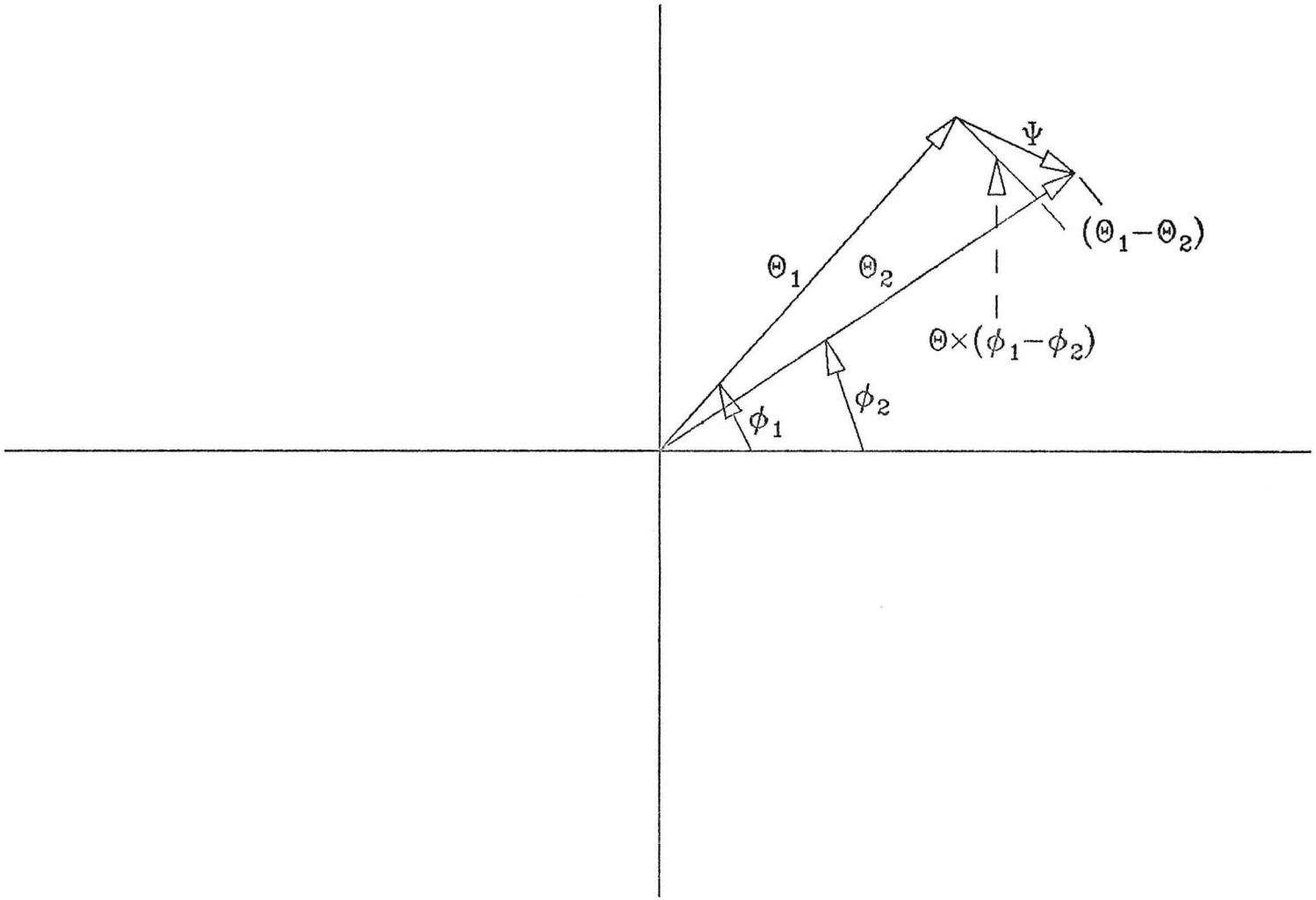

Figure 5.E.14: Illustrating the decomposition of the angle Ψ into components parallel and perpendicular to the angle of the pair relative to the Z axis.

If the distribution of the difference, $\Delta\theta = |\theta_1 - \theta_2|$, is Gaussian, i.e. $dn/d\Delta\theta = EXP(-(\Delta\theta/K)^2)$, and the distribution of the difference, $\Delta\varphi = SIN(\theta)\cdot|\varphi_1 - \varphi_2|$, is the same and independent, the distribution as a function of both is the product of the two similar distributions. Adding exponents, $dN/d\Omega$ equals $EXP(-(\Psi/K)^2)$, where $d\Omega$ is $d\Delta\theta \cdot d\Delta\varphi$, and equals $2\cdot\pi\cdot SIN(\Psi)\cdot d\Psi$.) $dN/d\Psi$ is therefore proportional to $\Psi\cdot EXP(-(\Psi/K)^2)$, (replacing $SIN(\Psi)$ by Ψ).

This procedure was applied to the quantity $m_\theta = \sqrt{(P_1 \cdot P_2)}\cdot\Delta\theta$) If $\sqrt{(P_1 \cdot P_2)}$ were constant and dN/dm_θ were Gaussian, the desired result would be dN/dmass proportional to $mass\cdot EXP(-(mass/K)^2)$. For real data with varying momenta, the distribution of m_θ might be the sum of many Gaussians. It was, in fact, fitted very well by the sum of two Gaussians, as shown in fig. 5.E.15. The predicted curve for the measured mass of photon conversions is also shown. For 10000 zero mass conversions, less than a tenth of an event is expected above 40 MeV/c^2. The above distribution is appropriate only for pairs of zero mass. It overestimates the mass error if the pair mass is greater than zero. When the mass is large, mass>> K, the mass resolution, ΔM, is distributed as $dN/d\Delta M = EXP(-(\Delta M/K)^2)$ around the central value. That distribution falls faster than $dN/dmass = mass\cdot EXP(-(mass/K)^2)$. Using the latter as an estimate for the mass increase, the number at higher masses was overestimated. (The similarity to the distribution of

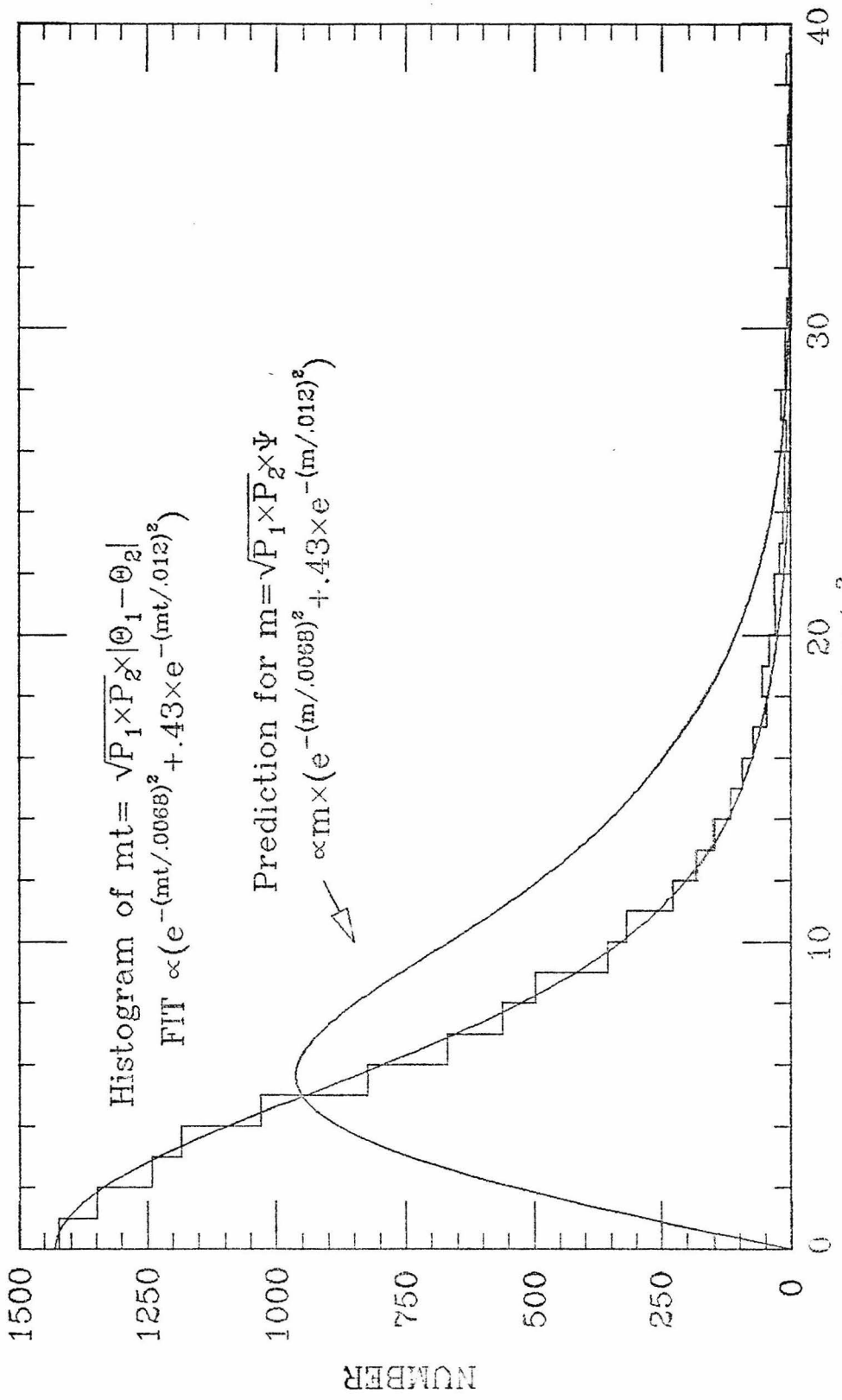

Figure 5.E.15: Mass resolution, m, excluding vertex position error, as predicted from mt, which corresponded to the Θ component of the opening angle

dN/dm_θ mentioned above is due to the fact that at large masses, the component of the angular error parallel to the opening angle changes the mass, whereas the perpendicular component does not, just as φ was ignored in calculating m_θ.)

The theoretical mass distribution of the electron pairs in pi-zero Dalitz decays was generated according to the paper by Kroll and Wada(3). This distribution was convoluted with the angular resolution mass increase distribution. The result was smeared according to the proportional momentum resolution. The final result is shown as the integrated fraction expected above a given mass, in fig. 5.E.16. Starting with 870, the background contribution from pi-zero Dalitz decays is expected to be less than 0.3 (less than one with 95% confidence) above 120 MeV/c^2. Counting the additional 20 MeV/c^2 possible from the vertex position uncertainty, the limit was 140 MeV/c^2, and the background at high mass from low mass pairs that had 5 cm. or less vertex resolution was less than 0.3 events (unweighted).

The mass of electron pairs produced in photon conversions (Bethe-Heitler process) is generally only a few electron masses since the q^2 of the virtual photon that couples to the charges in the matter is approximately proportional to the mass of the resulting pair. (q^2 is approximately $2 \cdot m \cdot k$, where k is the incoming photon momentum and m is the pair

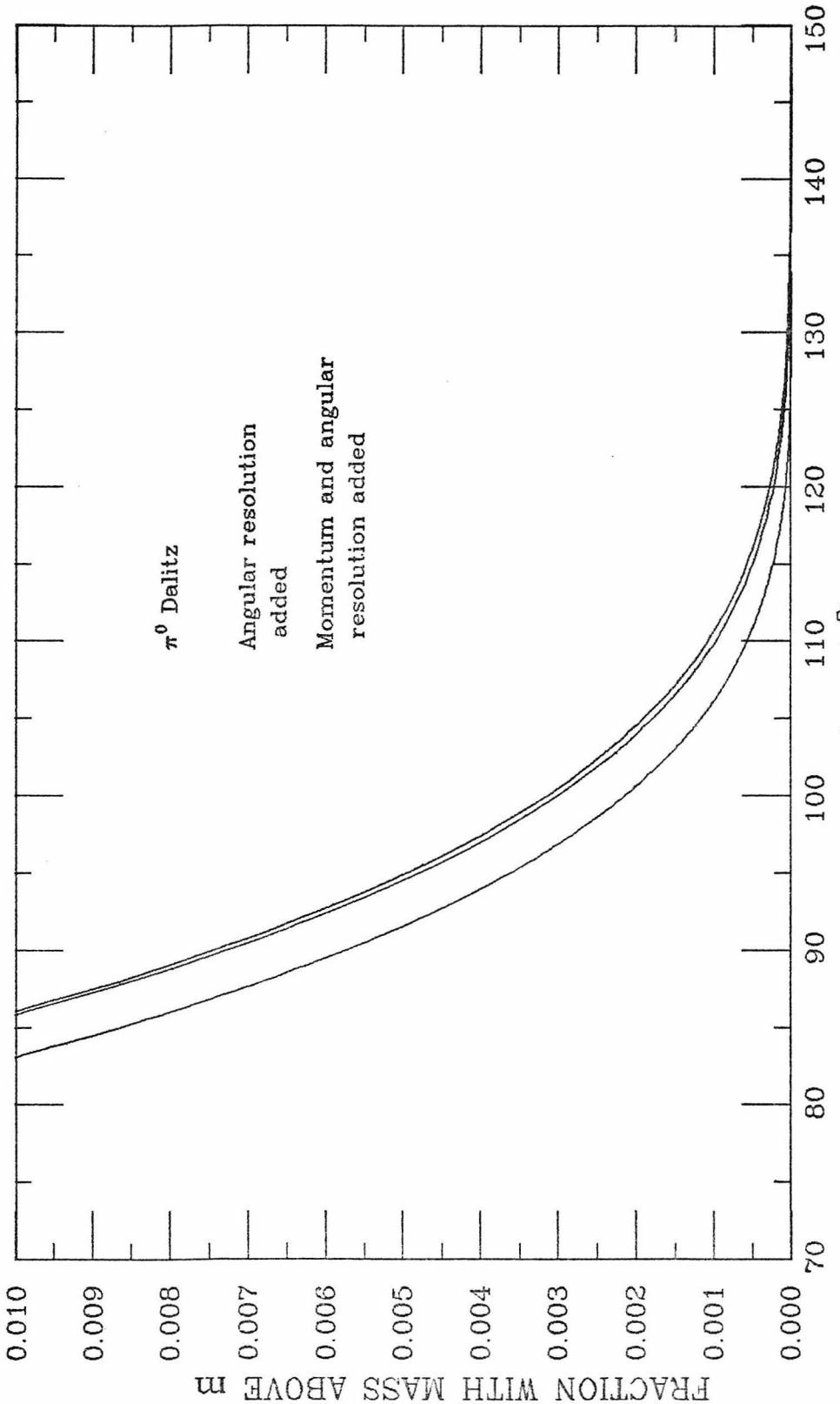

Figure 5.E.16: π^0 Dalitz decay contamination to high mass including resolution errors

mass.) Because there were about 10^4 conversions, even a small fraction at large masses could be a serious background problem. The high mass tail of the distribution is larger then predicted by the $1/q^4$ suppression of the photon propagator because small q^2 interactions are reduced by the screening effect of the atomic electrons. The tools for evaluating the mass distribution in different materials are given in the paper of Tsai(4), but the author has not attempted it because of the complexity. The assumption is made that including resolution effects, less than one in 10^4 occurred above 140 MeV/c^2, which was the case if the true mass did not exceed 100 MeV/c^2.

5.F -- Background Processes

This section discusses the various sources of background, their rates, and their subtraction. Much of the background was removed by subtracting the same charge pair events. The additional corrections are discussed below.

The mass of the final opposite charge pairs is histogrammed in fig. 5.F.1. Fig. 5.F.2 shows the histogram with the weighting that compensated for the low mass mate cut, along with the weighted same charge pairs. The difference is histogrammed in fig. 5.F.3. This difference was composed of "direct" electron pairs (counting the Dalitz decays of mesons other than the pions as "direct") and pairs of

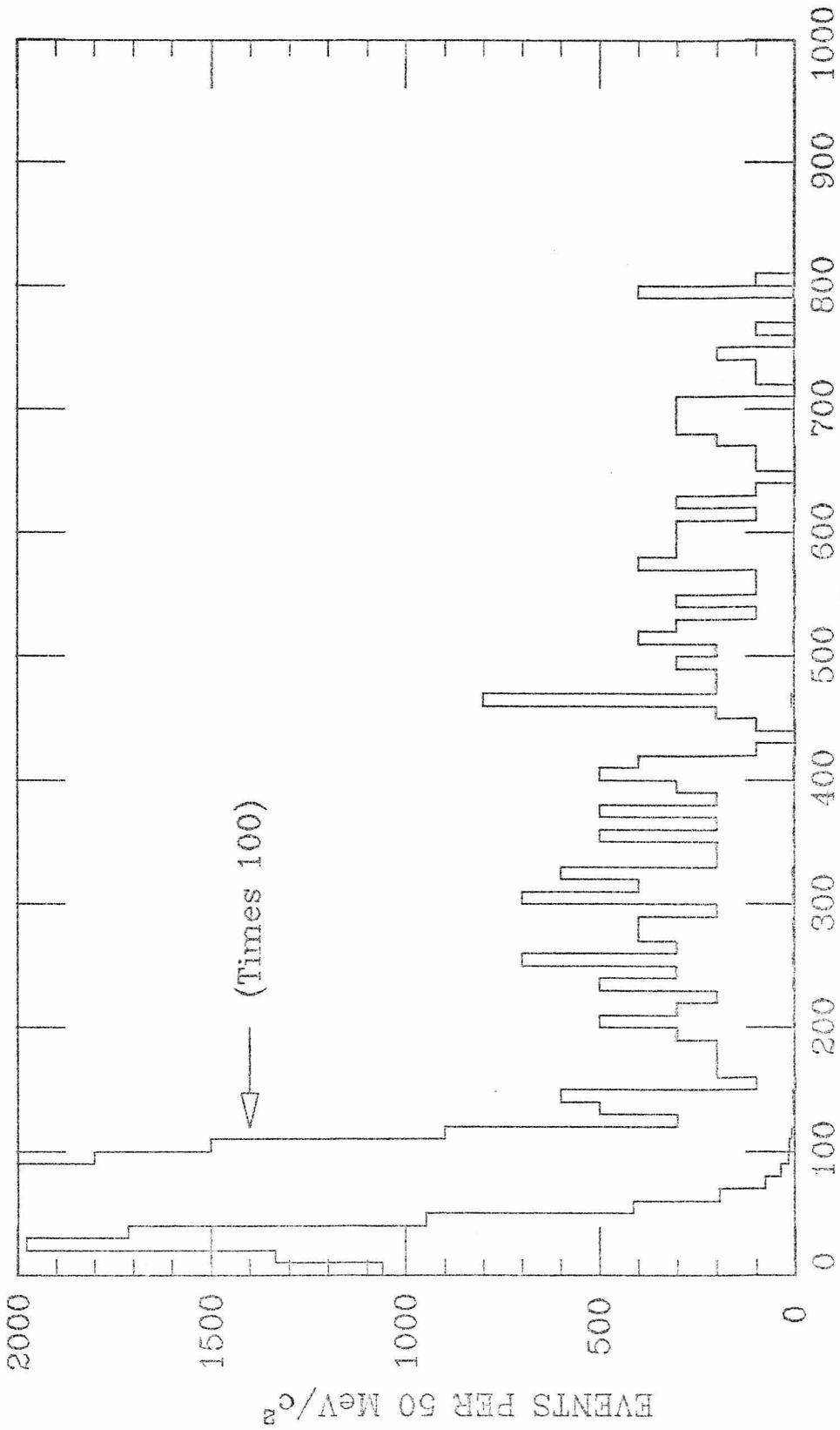

Figure 5.F.1: Mass of opposite charge pairs weighted for the low mass mate cut.

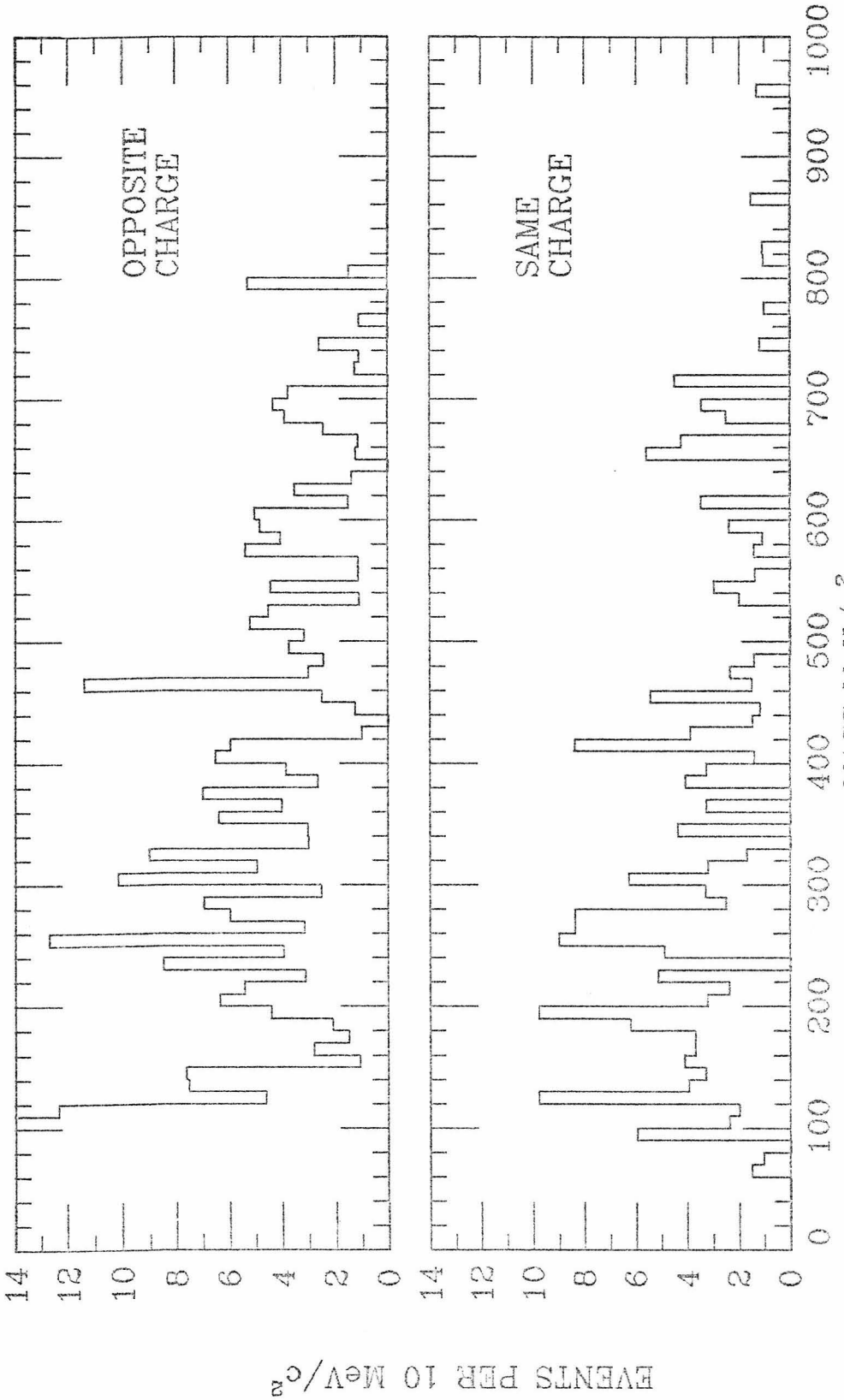

Figure 5.F.2: Mass of pairs -- weighted for the low mass mate cut.

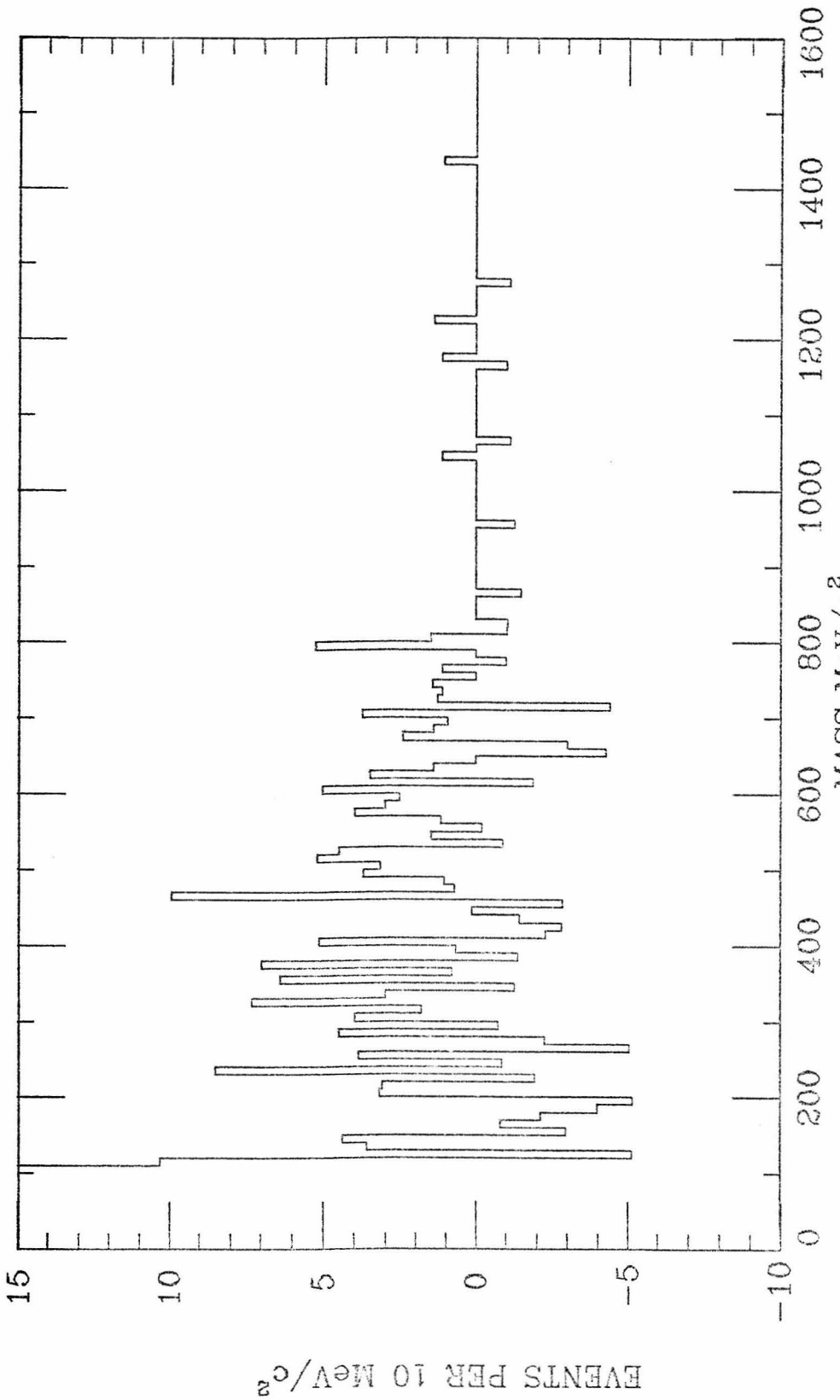

Figure 5.F.3a: Mass distribution after same charge subtraction.

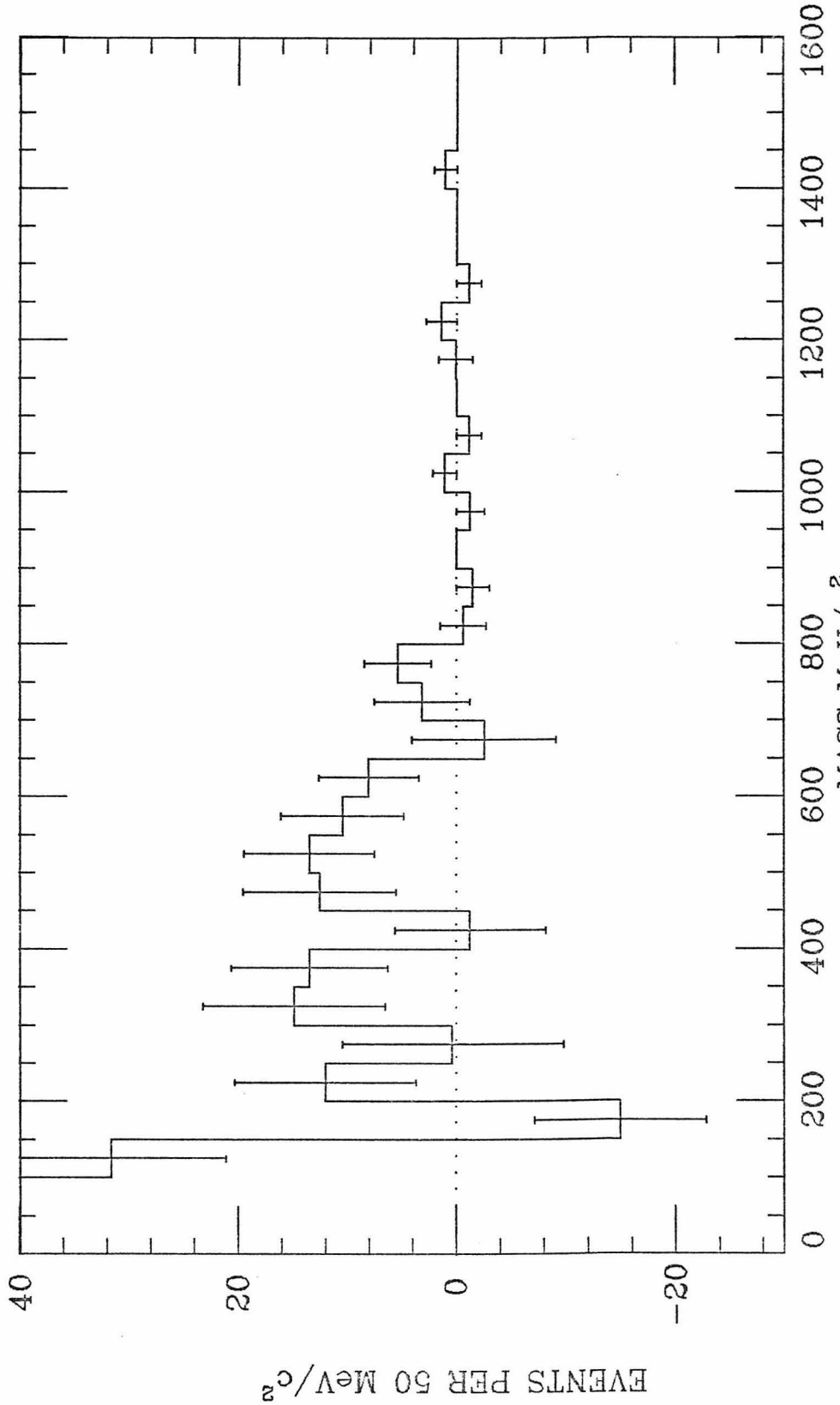

Figure 5.F.3b: Mass distribution after same charge subtraction.

misidentified hadrons (which are discussed in section 5.F.4).

5.F.1 -- Sources of Background

Opposite charge pair background occurred in two ways: Opposite charge pairs of low mass could be reconstructed above 140 MeV/c^2. There was no corresponding contribution to the same charge pairs. Opposite charge pair background also arose as two uncorrelated electron-identified tracks ("half-pairs" from conversions, Compton scattered atomic electrons, and misidentified hadrons). The uncorrelated pairs were roughly equally distributed as opposite-charge and same-charge pairs, so that a large part of this background was removed by the same-charge subtraction.

The background of the first type, pi-zero Dalitz and photon conversions, was treated above. The number of such pairs is estimated (in sections 5.D.3 and 5.E.4) as 2.9±0.5 due to poor vertex reconstruction, and 0±0.3 due to all other effects. The estimate must be increased by a factor of 1.6 to account for the low mass mate cut, giving 4.6±1.0. The rest of the background discussion concerns second-order corrections to the uncorrelated pair background due to differences in its distribution into opposite and same charge pairs.

5.F.2 -- Sources of Uncorrelated Electron Tracks

Electrons from "half-pairs" (photon conversion or pi-zero Dalitz low mass pairs where only one electron was found) were equally often positive and negative. Positive and negative misidentified hadrons differed by only a few percent. Compton scattered electrons, however, were always negative, giving an overall excess of negative electron tracks.

In the data the final number of high mass pairs, after correcting for the low mass mate cut was: opposite charge, 250.2; double negative, 106.0; double positive, 70.4. The excess of double negative pairs implies the ratio of negative to positive electron candidates was 1.23±0.17.

This charge asymmetry caused a much smaller asymmetry in the same to opposite ratio as follows: Assuming no correlation, and a negative to positive electron ratio of a to b, the same to opposite ratio was (a^2+b^2) to $2 \cdot a \cdot b$. In this case it was 1.021 (-0.019 +0.036). Since the same charge events were believed to originate in an uncorrelated way, their weights were increased by a factor of 1.021 before subtraction. The negative excess is analyzed in detail in section 5.F.3.

There was one more necessary correction, due to charge correlation between the hadrons. Although the sources of real electrons (half-pairs and Comptons) were totally uncorrelated with each other and with the hadrons, charge conservation in the hadronic interaction introduced a difference between the rates for same and opposite charge hadron pairs. For example, an event with three each positive and negative tracks has nine opposite-charge and only six same-charge pair combinations, all of which have a chance of being misidentified as electron pairs.

The number of pairs of misidentified hadrons was estimated using the measured punch-through rate and a Monte Carlo program for hadron tracks. (Pairs made up of one misidentified hadron and one real electron were completely removed by the subtraction of the same-charge pairs.) The prediction was 42 opposite-charge and 26 same-charge hadron pairs. The 16 pair difference was the estimated background beyond the correction by same-charge subtraction, and was subtracted from the opposite-charge result as a function of mass. The hadron pair calculation is described in Section 5.F.4.

5.F.3 -- Sources of Negative Electrons

Compton scattering, high energy knock-on electrons, and electrons in the beam were investigated as sources of

negative electrons. Of these possible sources, only Compton scattering was significant. Knock-on electrons with a momentum greater than 750 MeV/c were much less likely to be produced than Compton electrons with the same momentum. A knock-on of momentum greater than 750 MeV/c cannot be produced by a pion with a momentum less than 4.0 GeV/c. Such pions were rare compared to photons which needed have only 750 MeV/c. Electron contamination in the beam was estimated as one per million, far too small to compete with the other processes.

The following paragraph describes a rough estimate of rate for Compton electrons relative to half pairs in order to show that Compton scattering was a plausible source for the excess negative electrons. First, the probability was calculated for a photon conversion to produce a half pair, i.e. for one track not to be found and the other to have a momentum greater than 750 MeV/c. (Geometric acceptance and identification efficiency of C1 are assumed to have an equal effect in the two processes.) Photons were generated according to a momentum distribution calculated in a Monte Carlo study of pi-zero production and decay. The distribution of the momentum fraction going into each electron was taken as flat(5). The probability of losing a track was assumed to be 5% for momenta above 100 MeV/c and 50% for those below. (The assumed efficiencies may be correct only within a factor of two. The goal was an order

of magnitude estimate only.) Multiplying by the pair production cross section(6) gave a cross section of 530 microbarns for a photon producing a half pair in hydrogen. Using photons with the same momentum distribution the cross section for a Compton scatter(7) with electron momentum above 750 MeV/c was 170 microbarns. Accounting for the different Z dependence of the processes (Z for Compton, Z•(Z+1) for pair production)(8) and the known ratio of hydrogen to aluminum in the path of a photon exiting the target wall, half pairs are predicted to occur ten times more frequently than Compton scatters, i.e. negative electrons were 20% more frequent than positive, assuming no dilution by hadrons. This is in agreement with the measured ratio.

5.F.4 -- Two Hadron Punch-Through

This section describes the estimation of the number of misidentified hadron pairs using the measured C1 punch-through probabilities. The predicted excess of punch-through pairs, opposite charge minus same, was subtracted from the electron pair excess to give the background corrected result.

The input hadron events came from a DST produced by the trackfinding program starting with artificial chamber coordinates generated according to tracks measured in the

bubble chamber experiment (Bartke et. al.)(9). 3200 events were used.

Pairs of tracks were selected where one of the tracks went through a sensitive C1 cell and hit a shower counter and the other went through a sensitive C1 cell. About half a pair per event was used. There were about 50% more opposite charge pairs than same. The pair was assigned a weight equal to the product of the punch-through probabilities of the tracks, which depended on which ring of C1 was traversed. 0.13 was used as the probability of shower counter punch-through.

The pair punch-through was determined in two cases. The nominal values of C1 punch-through described in section 5.B.4 gave the nominal hadron pair punch-through. In the second case, the two standard deviation upper limit was calculated by increasing the single cell C1 punch-through rate according to the uncertainty due to the possibility that the presence of a hadron in a cell increased the punch-through over the counting rate for empty cells. (The increase was measured as consistent with zero having an upper limit of 0.15% as described in section 5.B.4.)

The expected number of punch-through pairs using the nominal values for the C1 misidentification rate is shown in fig. 5.F.4 for opposite and same charge combinations. The

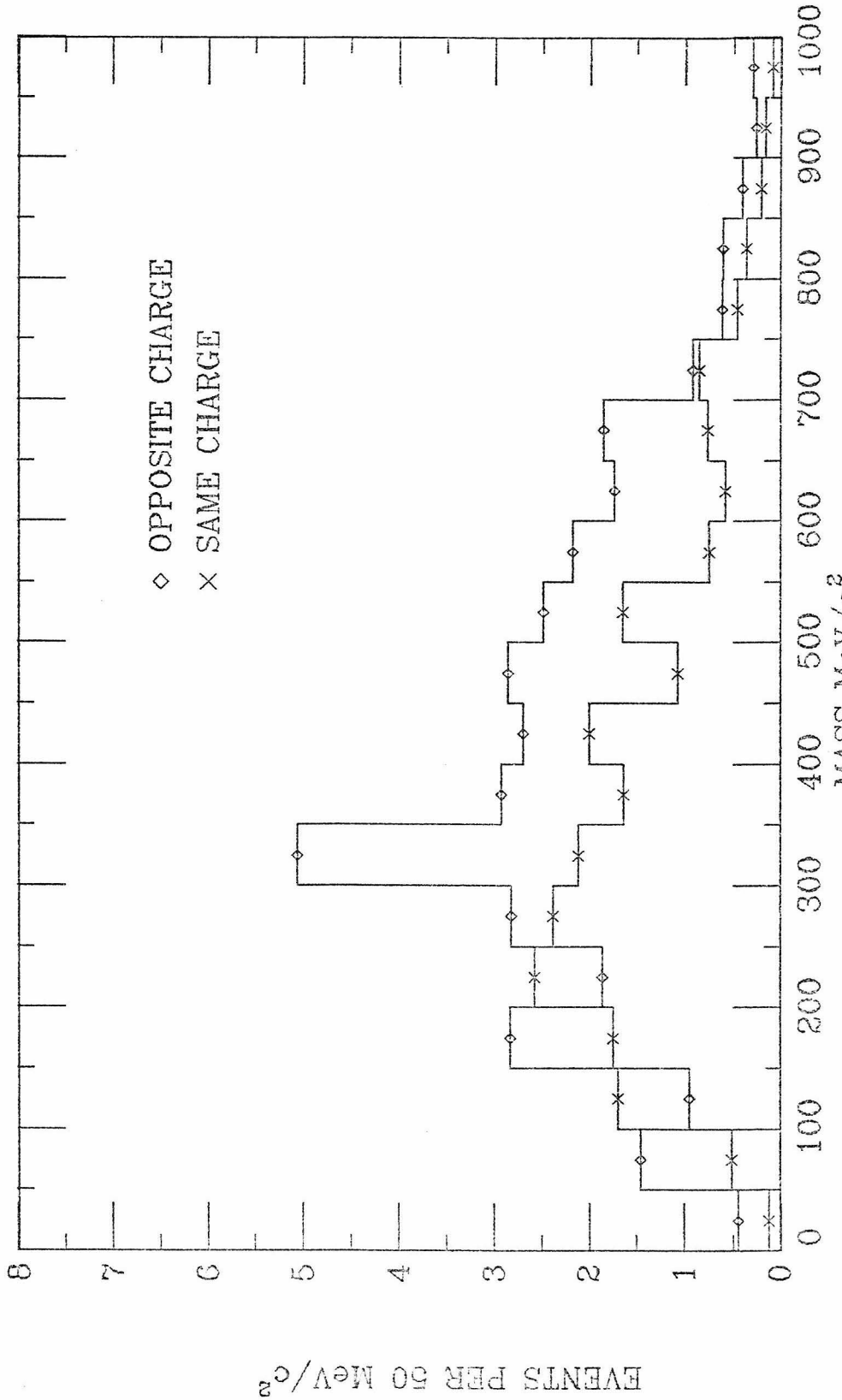

Figure 5.F.4: Mass of two misidentified hadrons predicted from bubble chamber data.

difference, opposite minus same, is histogrammed in fig. 5.F.5 for the nominal and the upper-limit probabilities of C1 punch-through. The total difference for masses above 140 MeV/c^2 was 16 in the nominal case, and 42 assuming the two standard deviation upper limit. The one standard deviation error was taken as half the difference: The background was taken as 16±13 events.

5.F.5 -- Empty Target Background

The cuts on the position of the pair vertex were designed to remove all interactions in matter other than the liquid hydrogen (and the mylar windows). The empty target correction was taken as the ratio of the interaction rate for the 0.026 cm. of mylar compared to the hydrogen, 0.4%.

The analysis of empty target runs with an integrated beam flux equal to 2% of the normal runs, yielded two pairs, both opposite charge with mass less than 30 MeV/c^2. The null result for high mass pairs implies a two standard deviation upper limit of 150 high-mass pairs in the normal runs, a useless result.

5.F.6 -- Background Subtracted Result

The final weighted electron pair sample was 250.2±19.2 opposite charge pairs, and 176.3±16.7 same charge pairs.

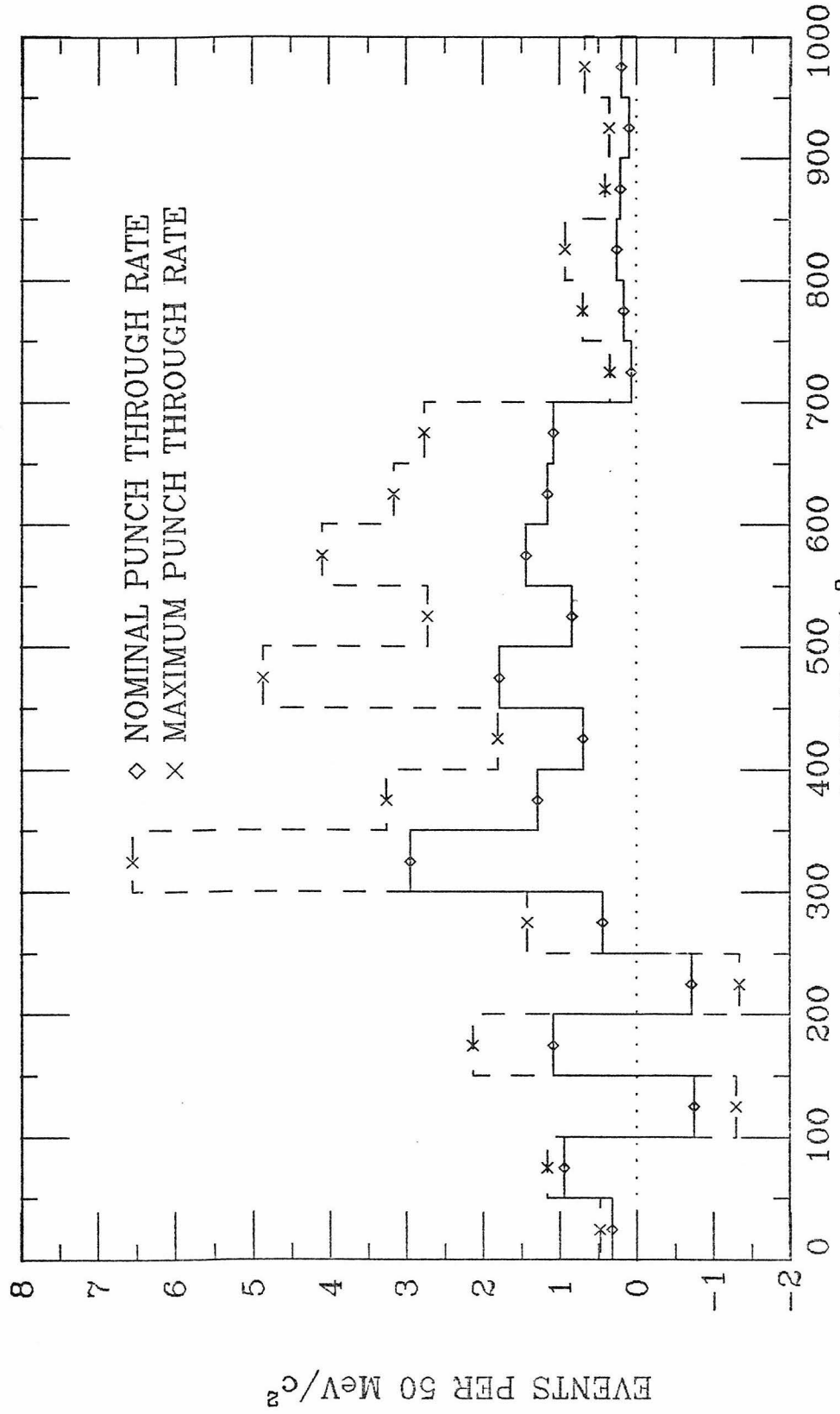

Figure 5.F.5: Predicted hadron punch through, opposite minus same charge.

Subtraction of type one background (poorly resolved photon conversions) left 245.6±19.3 events. Subtraction of same-charge pairs weighted by 1.021 left 72.9±25.5. After removing the hadron pairs in excess of the same charge correction, the estimated number of direct electron pairs with masses above 140 MeV/c^2 was 57±29, a two standard deviation signal. The empty target correction was negligible.

The corrected mass spectrum (not corrected for the 4.6 event expected background due to poorly resolved low mass pairs, whose mass distribution was unknown) is presented in fig. 5.F.6.

5.G -- Monte Carlo and Acceptance Correction

This section describes the Monte Carlo calculation of geometric acceptance, trackfinding efficiency, electron identification losses, and the loss due to the beam association cut, as a function of the mass of the pair. The background subtracted mass spectrum was corrected for the losses listed in table T5.G.1. The normalized mass spectrum (differential cross section for pi minus + proton --> electron pair + anything) is presented.

5.G.1 -- Monte Carlo Track Generation

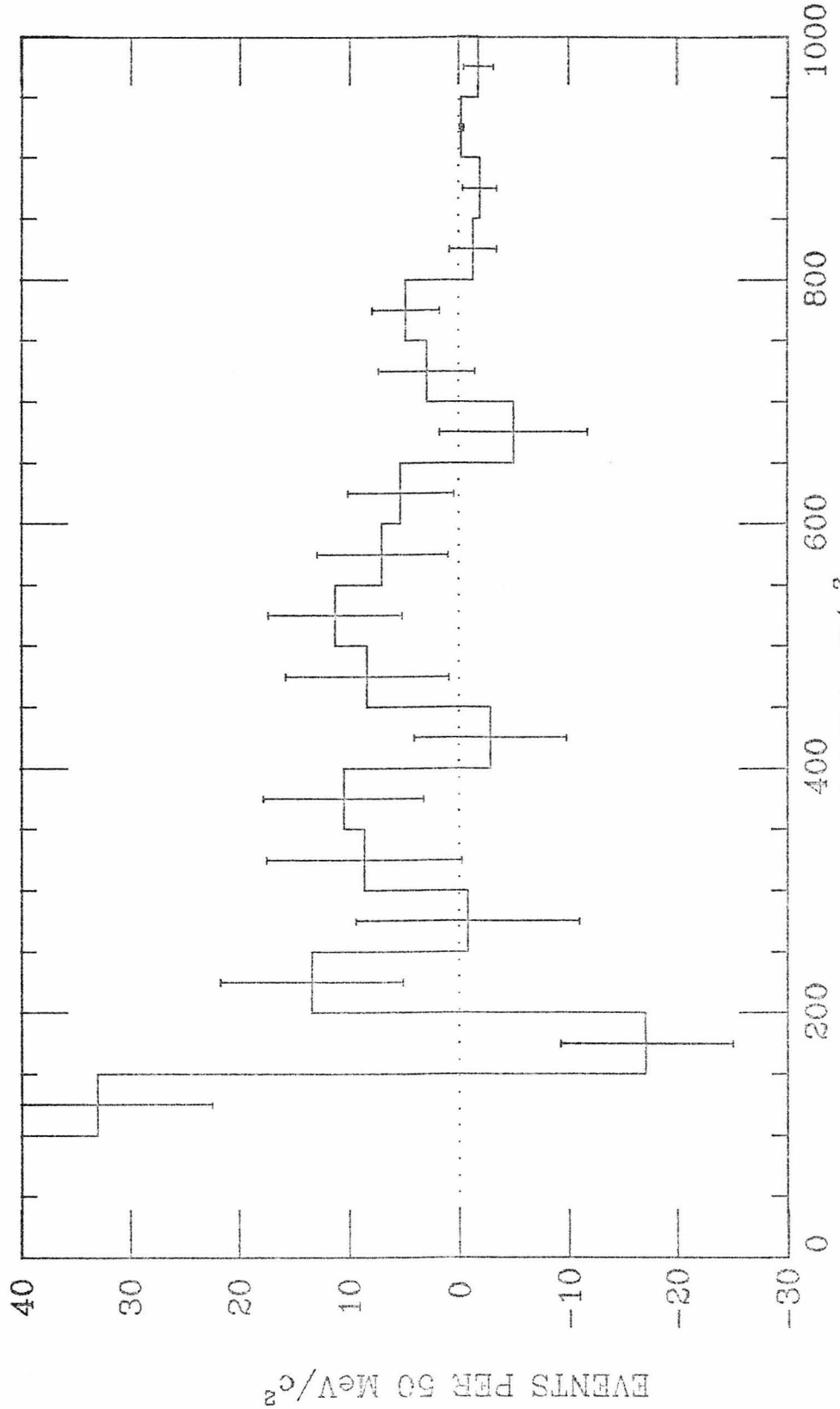

Figure 5.F.6: Mass after same charge and hadron subtraction

The X and P distribution for pi minus + proton --> rho zero + anything at 16 GeV/c measured by Bartke et. al.(10) was parameterized and used to generate momentum values for an electron pair center of mass system(11). In the center of mass, electron momenta were generated corresponding to a given invariant mass with an isotropic distribution. (Distributions according to $1+SIN^2(\theta)$ and $1+COS^2(\theta)$ with respect to the center of mass momentum direction were investigated also, for pairs with the mass of the rho only.) The electron momenta were transformed to the lab frame, and used to calculate track trajectories with a starting point distributed randomly along the length of the target. Chamber intersections were generated at the nearest wire, dropped according to the measured chamber efficiencies, and passed on to the standard trackfinding program. Only events where both tracks went through equipped C1 cells and one hit a shower counter, were reconstructed. The fraction of such events was called the geometric acceptance. It ranged from 6% to 10% depending on the mass of the pair, as shown in fig. 5.G.1.

The trackfinding efficiency was taken as the fraction of these events where both tracks were successfully reconstructed. It was about 92% independent of the mass of the pair (96% per track). The difference between the reconstructed and the initial mass was a measure of the mass resolution. This is shown for several masses in fig. 5.G.2.

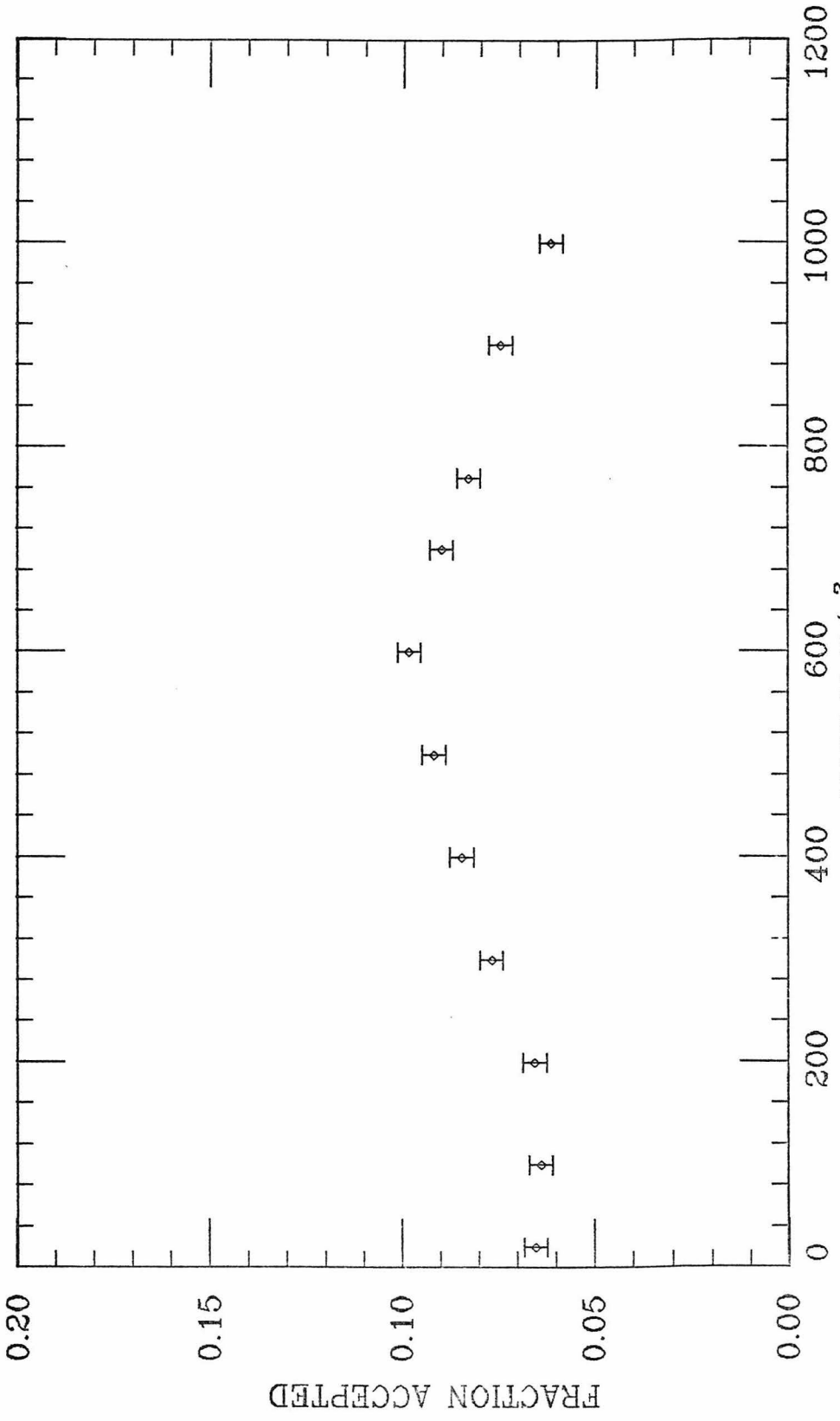

Figure 5.G.1: Geometric acceptance from Monte Carlo.

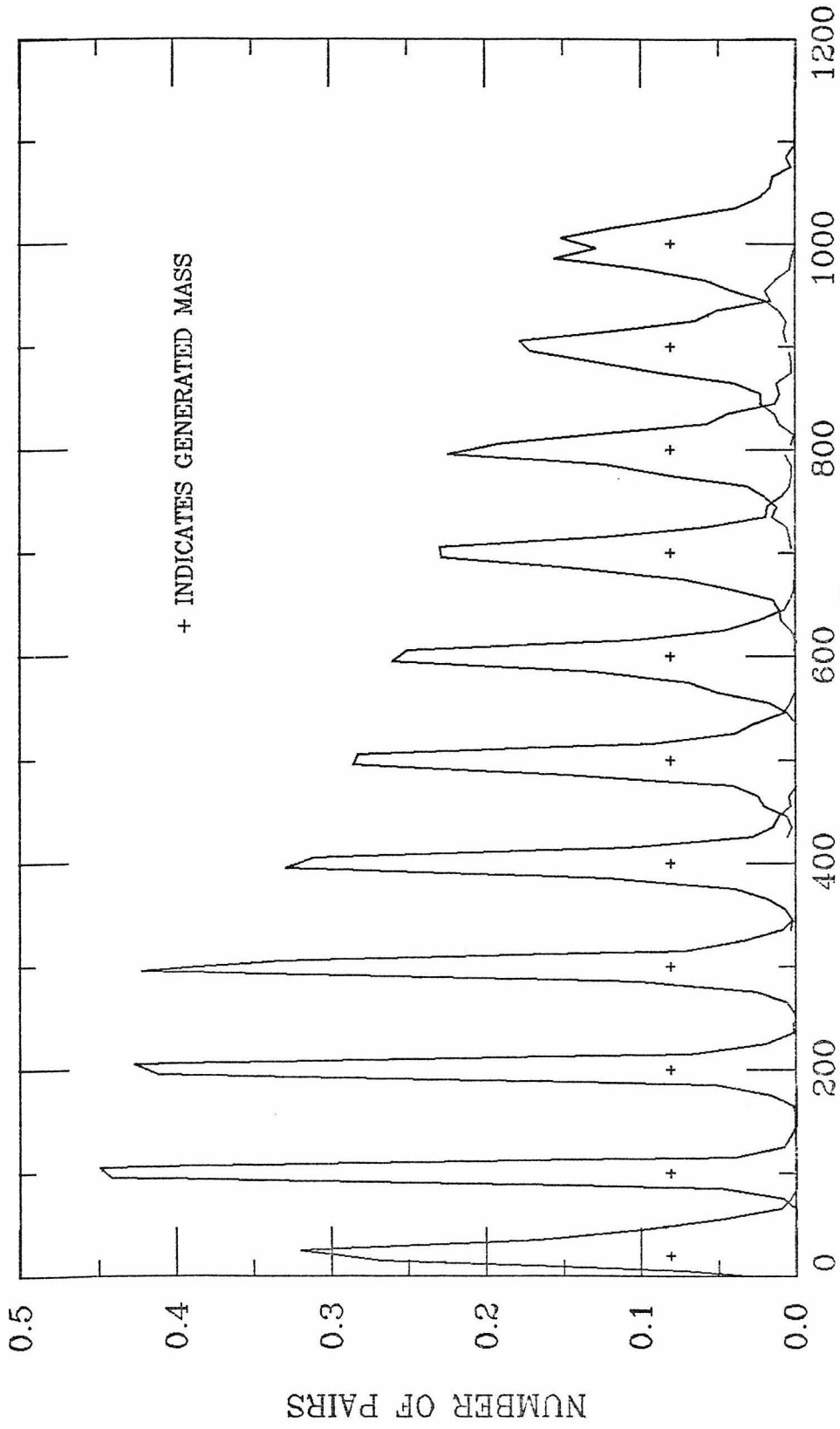

Figure 5.G.2: Pair mass resolution in Monte Carlo.

5.G.2 -- Electron Identification and Beam Association Acceptance

The Cerenkov and shower counter identification probabilities were calculated for each track in the Monte Carlo according to its momentum and which cell(s) and shower counter it hit, using the efficiencies and methods described in sections 5.B.2 and 5.B.3. The probability of passing the beam association distance cut was calculated from the momentum and Θ of the track using the table described in section 5.D.3. It was about 93.5% per track, almost independent of the mass of the pair.

These acceptances were multiplied together to form a combined acceptance probability for electron identification and beam association for the pair. This is shown in fig. 5.G.3 as a function of the mass of the pair. Uncertainties on the measured efficiencies led to an overall uncertainty of 20% on the combined acceptance probabilities. The uncertainties shown in the figures are statistical only.

The product of all acceptances determined by the Monte Carlo, geometric, track finding, electron identification, and beam association is shown as a function of mass in fig. 5.G.4. The 20% systematic uncertainty applies. At the mass of the rho, the acceptance was 18% lower for a $1+\cos^2$

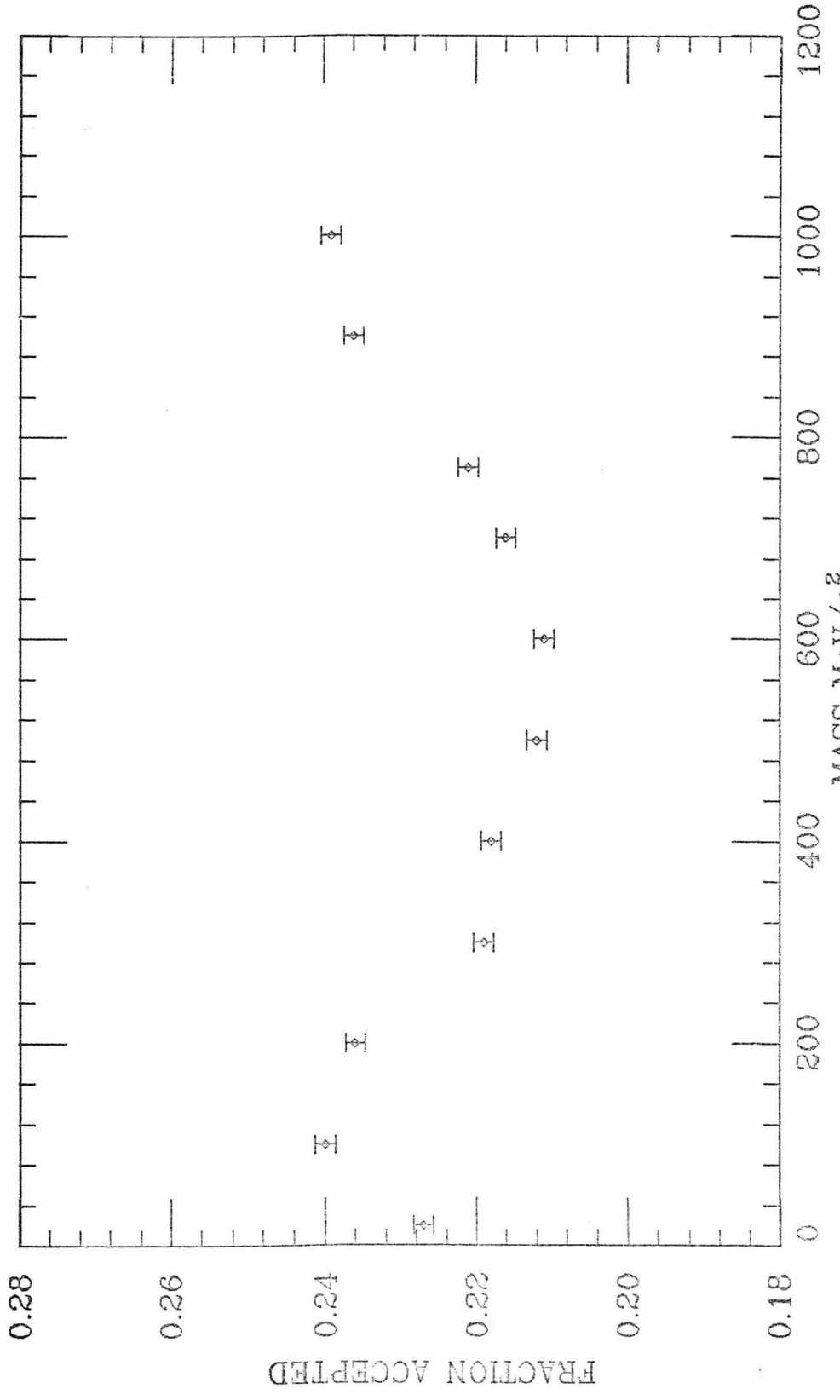

Figure 5.G.3: Electron identification and beam association acceptance calculated in the Monte Carlo for different masses.

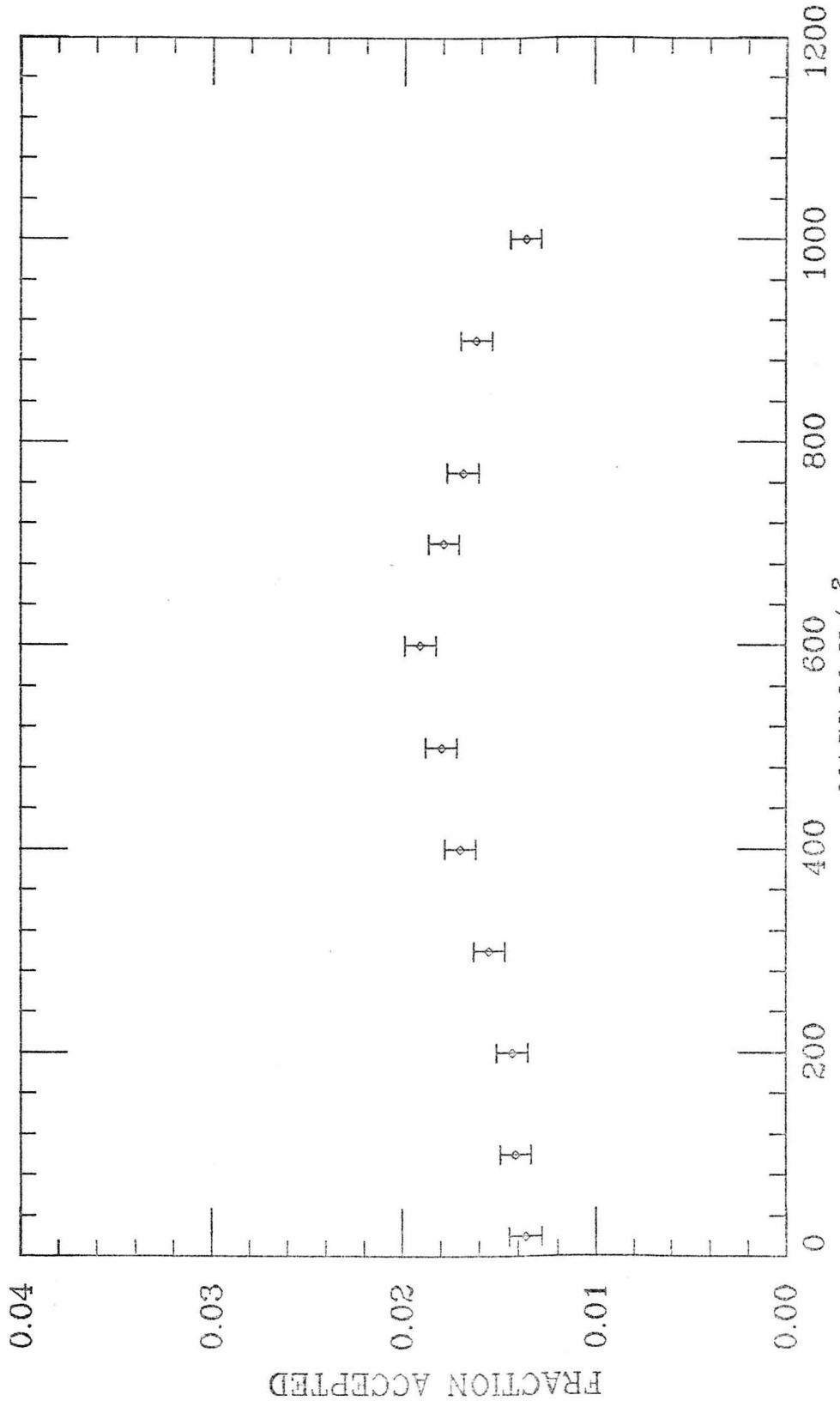

Figure 5.G.4: Acceptance due to all losses calculated in Monte Carlo.

distribution, and 12% higher for a $1+SIN^2$ distribution.

5.G.3 -- Final Acceptance Correction and Normalization

Table 5.G.1 lists all the stages where data could have been lost along with the estimated fraction kept. Where the loss depended on the pair mass, the value shown is for the rho mass. The loss due to match-point overflow is taken as the fraction of overflow events out of the total number of pion interactions, on the assumption that they produced the hardware trigger and were not correlated with direct pairs. (They are believed to be electron showers, following the field lines, producing large numbers of hits in the

Table T5.G.1: FRACTION OF SIGNAL PASSED

Geometric Acceptance	0.0830*
Mask Correlation Test	1.000
Unpack Okay	0.953
One or More Beam Tracks	0.982
No Match Point Overflow	0.997
Trackfinding Efficiency	0.920*
Exactly One Beam Track	0.918
Electron Identification	0.253*
Two Electron Cut	0.960
Confidence Level Cut	0.979
Matrix Flag Cut	1.000
Beam Association Cut	0.874*
Low Mass Mate Cut Wt Ceiling	0.916
Vertex Cuts	1.000
Overall Acceptance	=0.0121

* = Mass Dependent -- Value Shown is for Rho Mass

chambers, and triggering in C1 and a shower counter.) This gave a factor of 0.9974, one minus the fraction of overflows per interacting pion. (If the overflows were not responsible for the triggers, they disguised the fraction of direct electron pairs normally present at that stage of the selection, and the fraction lost of the direct pairs was the fraction of overflows in the data presented to the trackfinding program, making the factor 0.63.) Other event related losses, garbled data from the detectors (fatal unpack), no beam track, and more than one beam track, were assumed to be uncorrelated with the signal.

The factor shown for the low mass mate cut compensated only for the event weight ceiling, most of the loss (it averaged 0.67) was corrected by weighting the individual events. As seen in the table, the acceptance at the rho mass was about 1 in 80. The corrected mass spectrum is shown in fig. 5.G.5.

$9.604 \cdot 10^8$ pions entered the target during the sensitive time of the trigger. With a 91 cm. target, and correcting for attenuation along the target, the sensitivity was 3.343 events per nanobarn. The final cross section for producing "direct" pairs with mass greater then 140 MeV/c^2 (eta Dalitz, etc. included) was 1.14±0.68 microbarns. The differential cross section in shown in fig. 5.G.6. The cross section in the rho-omega mass region, 700 to 860

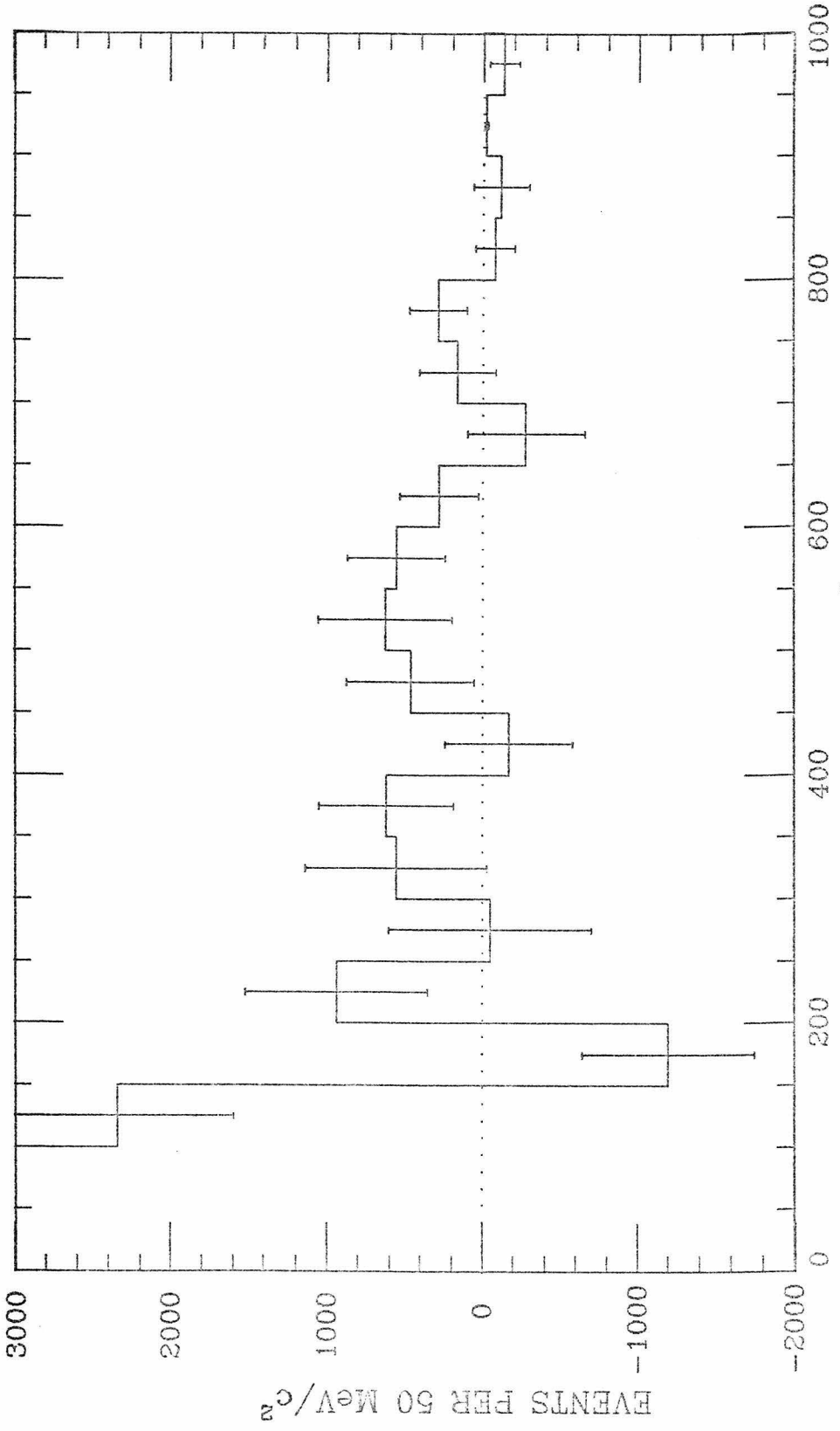

Figure 5.G.5: Acceptance corrected and background subtracted mass spectrum.

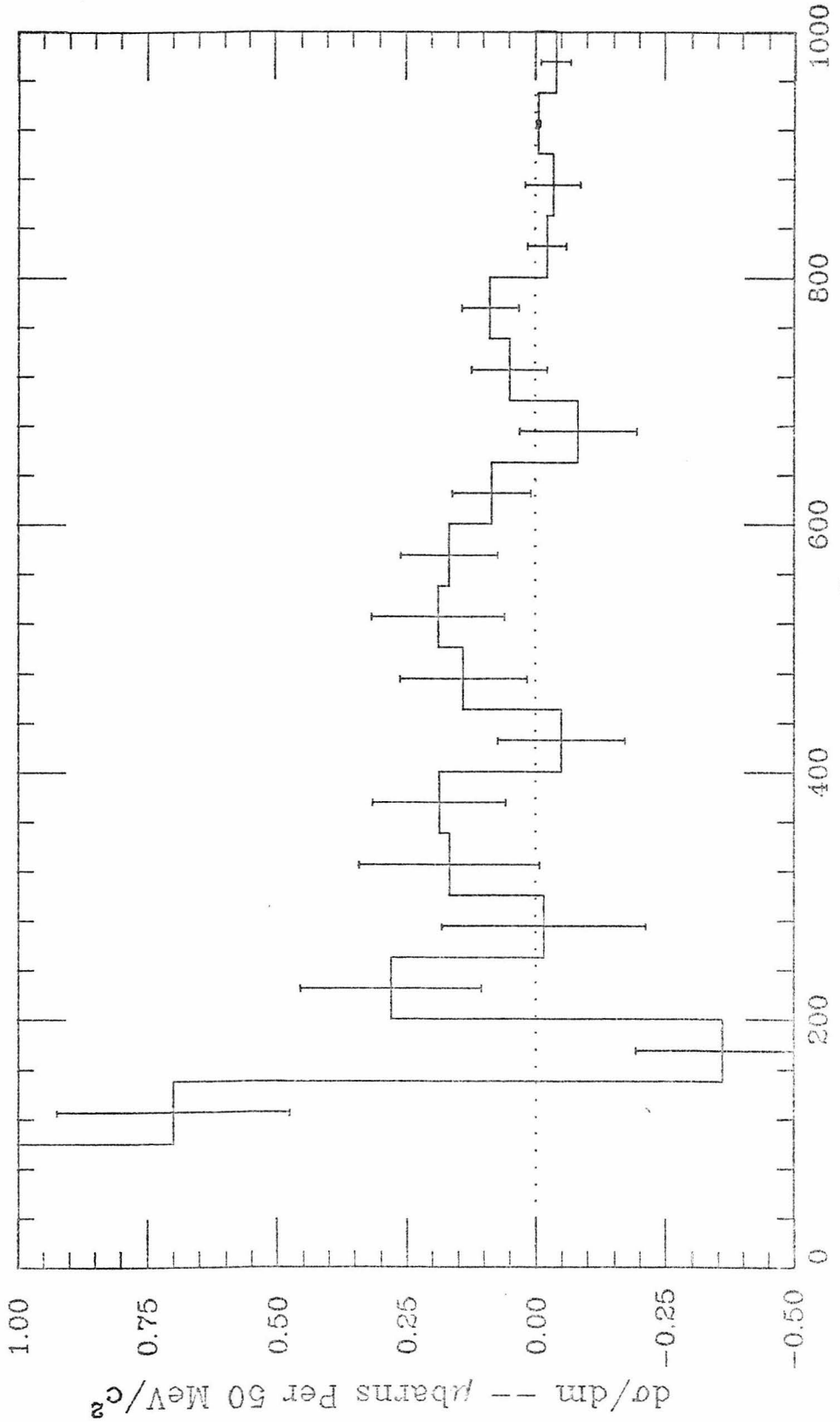

Figure 5.G.6: Normalized differential cross section, $d\sigma/dm$, for $\pi^- + P \longrightarrow e^+ + e^- + X$.

MeV/c^2, was 0.16±0.13 microbarns.

The normalization of the final sample is uncertain to a level of 20% due to electron identification efficiency, 10% due to the uncertainty of the center of mass decay angular distribution, and possibly 30% or more due to the difference between the real X distribution of the events and that of the rho which was assumed in the acceptance calculation. The X distribution uncertainty is treated in the next chapter.

References for chapter 5

1. Radiation length in aluminum and hydrogen taken from Review of Particle Properties, Phys. Letters 50B, No.1, (1974) which was revised from CERN NP Internal Report 74-1.
Pair production constituting 7/9 of the "radiation length" interaction cross section is reported in B. B. Rossi, High Energy Particles, Prentice-Hall, (1952).

2. Branching ratio reported in Review of Particle Properties, op. cit., as taken from Budagov et. al., J.E.T.P. 11, 755 (1960) and Samios et. al., Phys. Rev. 121, 275 (1961).

3. N. Kroll and W. Wada, Internal Pair Production Associated with the Emission of High-Energy Gamma Rays, Phys. Rev. 98, 1355 (1955).

4. Y.-S. Tsai, Pair Production and Bremsstrahlung of Charged Leptons, Rev. Mod. Phys., 46, No. 4 (1974).

5. The distribution is nearly flat. It is given in Rossi, op. cit.

6. Rossi, op. cit.

7. J. D. Bjorken and S. D. Drell, Relativistic Quantum Mechanics, McGraw-Hill (1964).

8. Rossi, op. cit.

9. Bartke et. al., Nucl. Phys. B107, 93 (1976).

10. Ibid.

11. D. L. Blockus, Johns Hopkins University, Ph.D. thesis, to be published.

CHAPTER 6 -- Results

6.A -- Introduction

This chapter discusses the direct electron pair result of the previous chapter. The limited region of geometrical acceptance is discussed first since assumptions were made in order to extrapolate beyond that region. The signal due to the known cross section for the decay of the rho and omega mesons decaying is used to check the results. The measured rho/omega cross section is consistent both with the prediction and with zero.

The results of this experiment are compared with two other experiments at similar energies: a bubble chamber experiment with full solid angle electron detection; and a hybrid streamer chamber experiment which identified muons only in the forward direction. The overall lepton pair cross section is consistent with these experiments for masses above 200 MeV/c^2. There is evidence for a source of pairs other than vector mesons and Dalitz decays.

The signal between the pi-zero and rho mass is compared with the prediction of a pion annihilation model which includes features of several earlier models. The results are consistent with the model above 200 MeV/c^2. The data point for 150 - 200 MeV/c^2 is not in agreement with the steep rise

predicted by the model.

6.B -- Geometrical Acceptance and Rho-Omega Signal

In order to obtain the cross section presented in the previous chapter, it was necessary to estimate the number of pairs outside the region of acceptance. The final cross section therefore is quite model dependent. The correction factor was computed in the Monte Carlo assuming the Feynman X and P_t distributions measured for rho and omega mesons, with the result that pairs originating as these mesons were correctly normalized. At lower masses, where the production mechanism is not known, the calculated result could be different from the actual cross section. For the particular model discussed below, a larger fraction of these pairs were produced in the region of acceptance than those due to the rhos, in which case the cross section was overestimated by a factor of 1.34.

In this section, the observed distributions and the Monte Carlo predictions for production and acceptance of the rho in X and P_t are presented. Since the signal in the rho region is weak, a mass plot showing a strong pi-zero signal is presented as evidence that the reconstruction and electron identification worked. Finally, the smallness of the final sample of events is reconciled with the size predicted before the experiment was run.

The X and P distributions were generated in the Monte Carlo according to the measurements of Bartke et. al. for rho-zeros produced inclusively in 16 GeV/c pi-minus proton interactions(1). (Omegas have been observed to be distributed similarly in the one constraint channels and assumed to have the same behavior in the multi-neutral final states(2).) The P_t was generated first, and then the X, since X was distributed differently in different ranges of P_t.) At low P_t, X peaked near one, whereas at high P_t it was centered around zero. The projected distributions are shown for X and P_t in figs. 6.B.1 and 6.B.2 respectively.

The geometrical acceptance was defined by requiring both daughter tracks to pass through the equipped part of C1 and one to hit a shower counter. The acceptance is shown in bins of X and P_t in table T6.B. There was little interplay between X and P_t, i.e. the acceptance was approximately the product of functions of each separately. The acceptance as a function of X integrated over P_t, and as a function of P_t integrated over X is shown in figs. 6.B.3 and 6.B.4 respectively. As a function of P, it is almost uniform, falling to zero below 80 and above 1400 MeV/c. As a function of X it is a window centered at X=0.27 and about 0.2 in width. These acceptance functions were calculated using pairs with the mass of the rho. The acceptance was fairly constant as a function of mass, but at low masses the

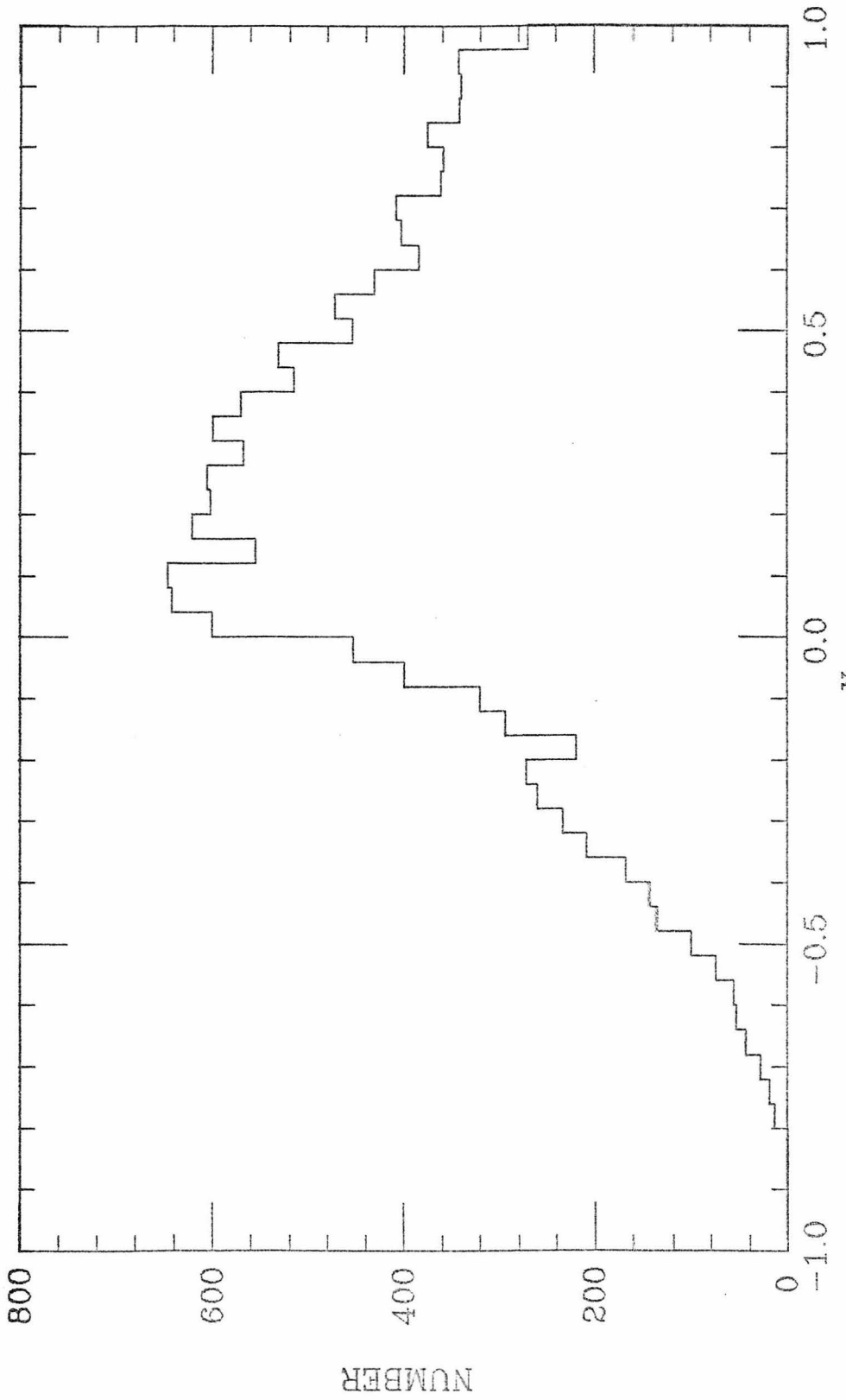

Figure 6.B.1: X distribution of p's from Monte Carlo

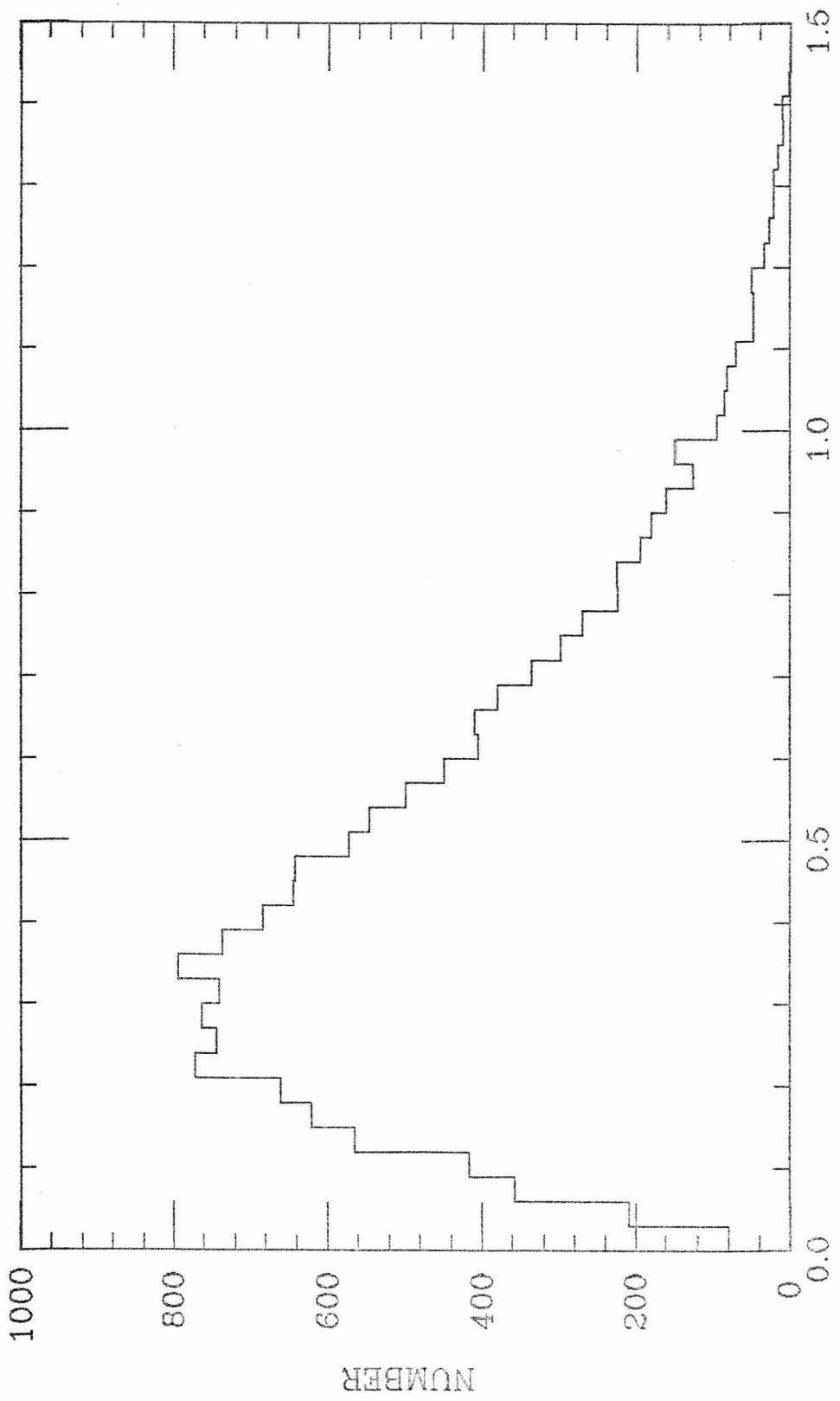

Figure 6.B.2: P_t distribution of ρ's from Monte Carlo

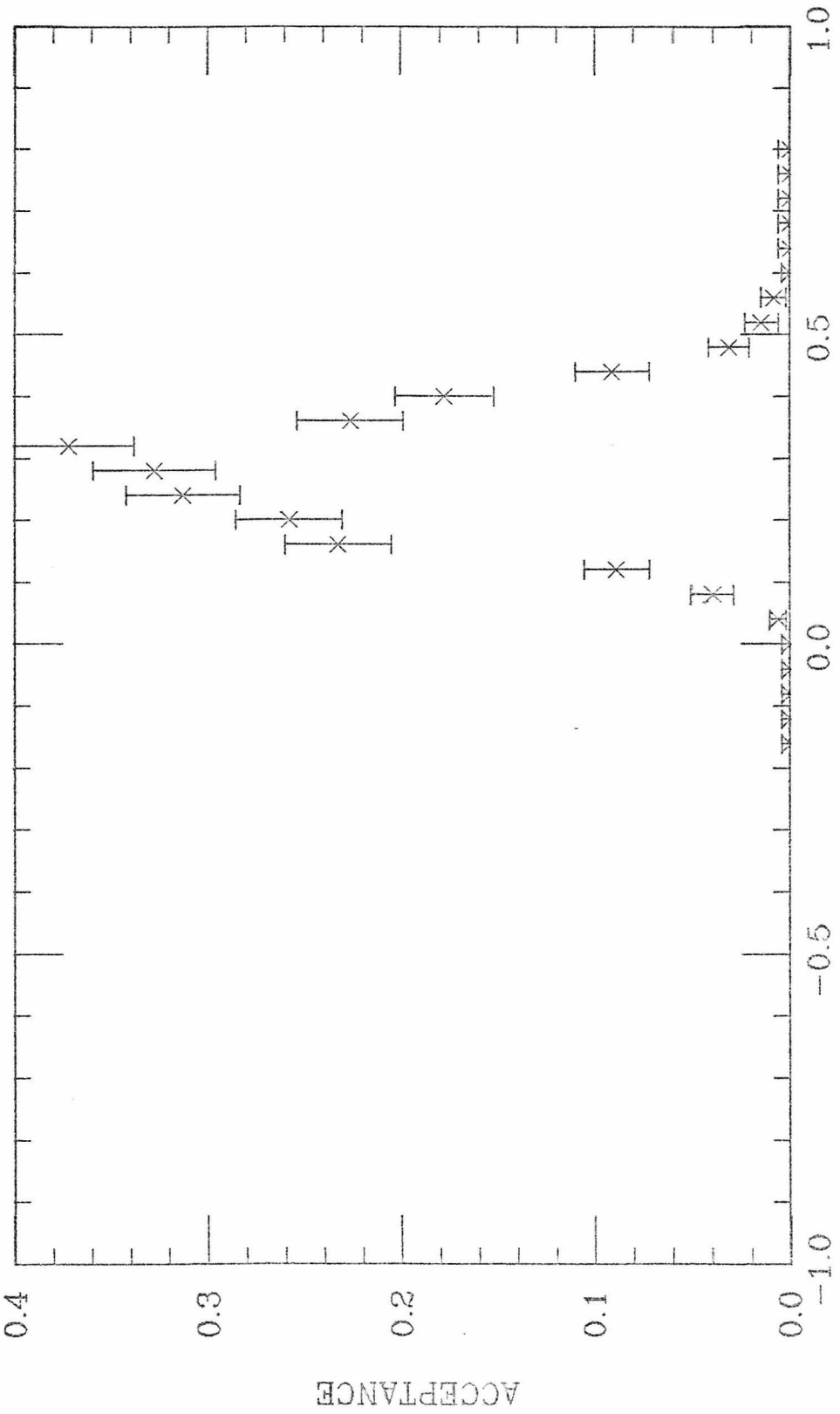

Figure 6.B.3: Acceptance as a function of Feynman X

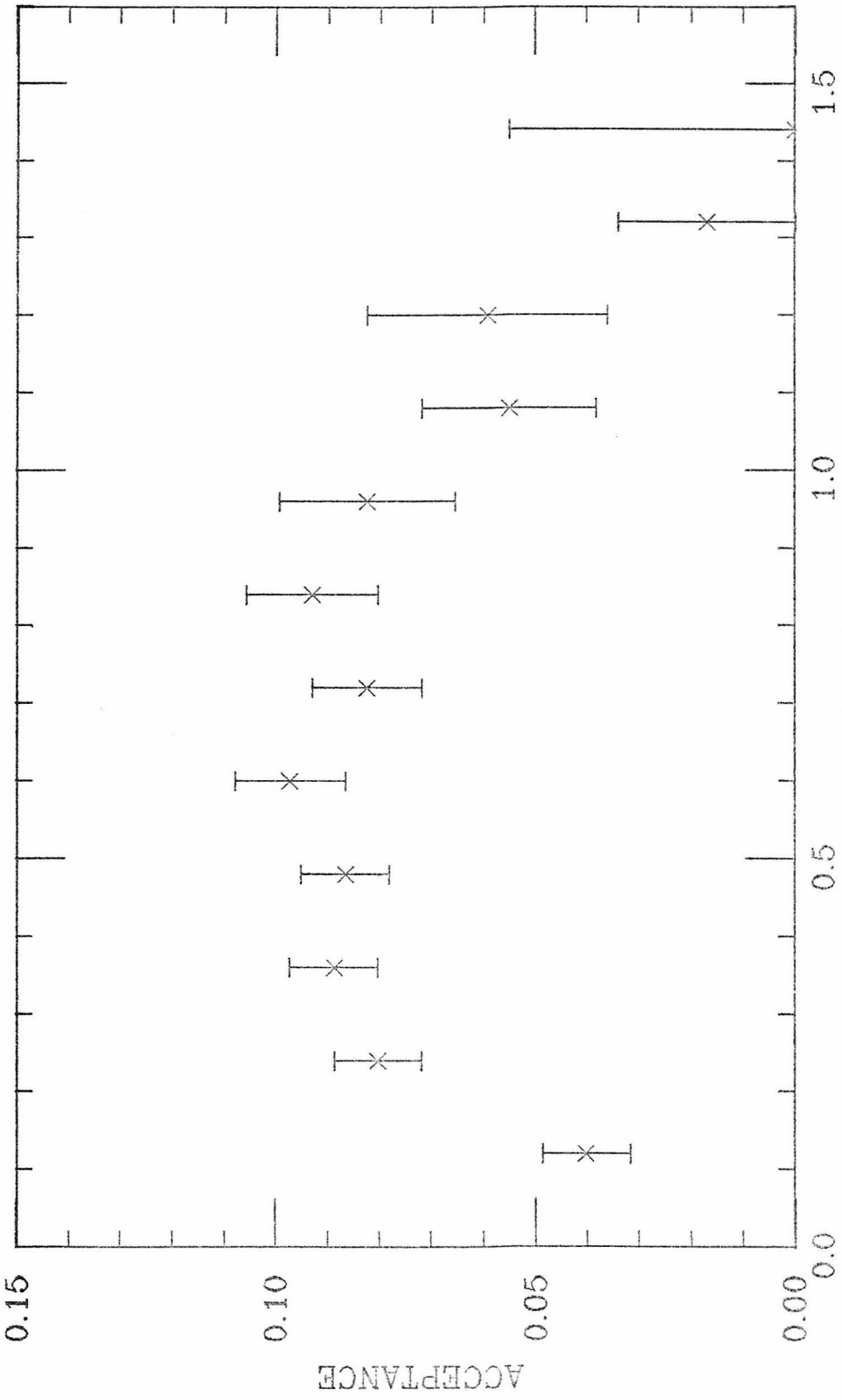

Figure 6.B.4: Acceptance as a function of transeverse momentum

pair needed more P_t for an electron to hit a shower counter.

The X and P_t distributions of the observed events with mass greater than 140 MeV/c^2 are shown in figs. 6.B.5 and 6.B.6. Same charge pairs were subtracted, but no correction was made for charge-combination correlated hadron punch-through. The P_t distribution is quite consistent with that of the

Table T6.B: ACCEPTANCE AS A FUNCTION OF Xf AND Pt IN PERCENT

	<-- Xf -->							
Pt	-.1	0.0	.1	.2	.3	.4	.5	.6	.7
0.	0±8	0±6	11±8	17±8	13±7	3±4	0±3	0±2
.1	0±3	14±5	21±5	33±6	33±6	5±3	0±1	0±1
.2	0±2	3±2	35±5	34±5	19±4	4±2	0±1	0±1
.3	0±2	4±2	25±5	33±5	29±5	1±1	0±1	0±1
.4	0±1	2±1	23±4	29±5	21±4	2±2	1±1	0±2
.5	0±2	6±2	17±4	34±6	21±4	6±3	0±2	0±3
.6	0±3	1±2	20±6	39±7	26±6	6±3	0±2	0±4
.7	0±3	0±2	18±6	46±9	18±6	11±5	2±3	0±8
.8	0±3	0±2	12±5	25±8	15±10	3±4	0±6	0±21
.9	0±5	0±3	7±5	20±7	28±12	18±13	0±13	---
1.0	0±6	0±4	5±5	35±12	16±15	---	---	---
1.1	0±15	0±6	17±12	10±11	---	---	---	---
1.2	0±21	0±10	0±23	---	---	---	---	---
1.3								

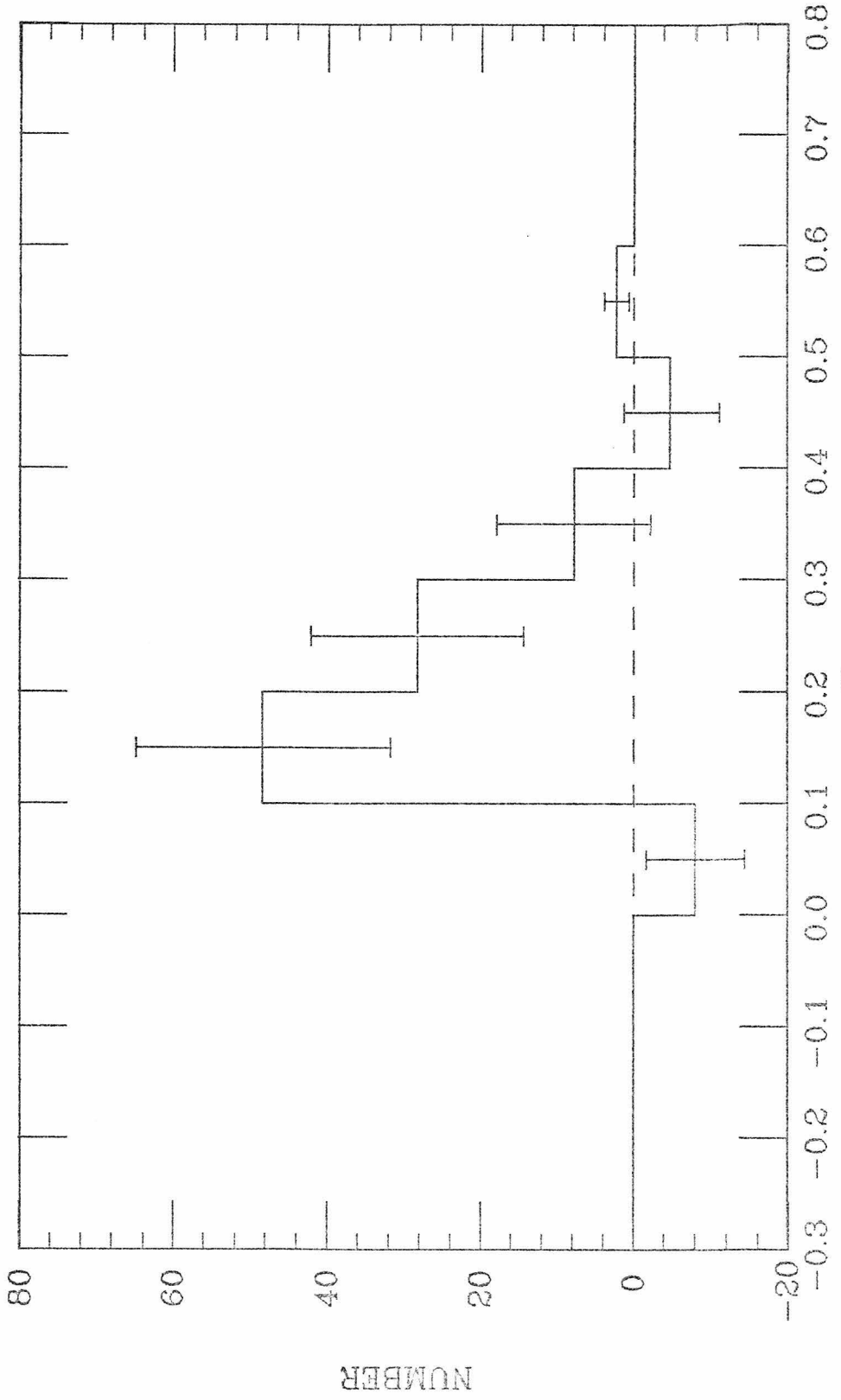

Figure 6.B.5: X distribution of events (same charge subtracted)

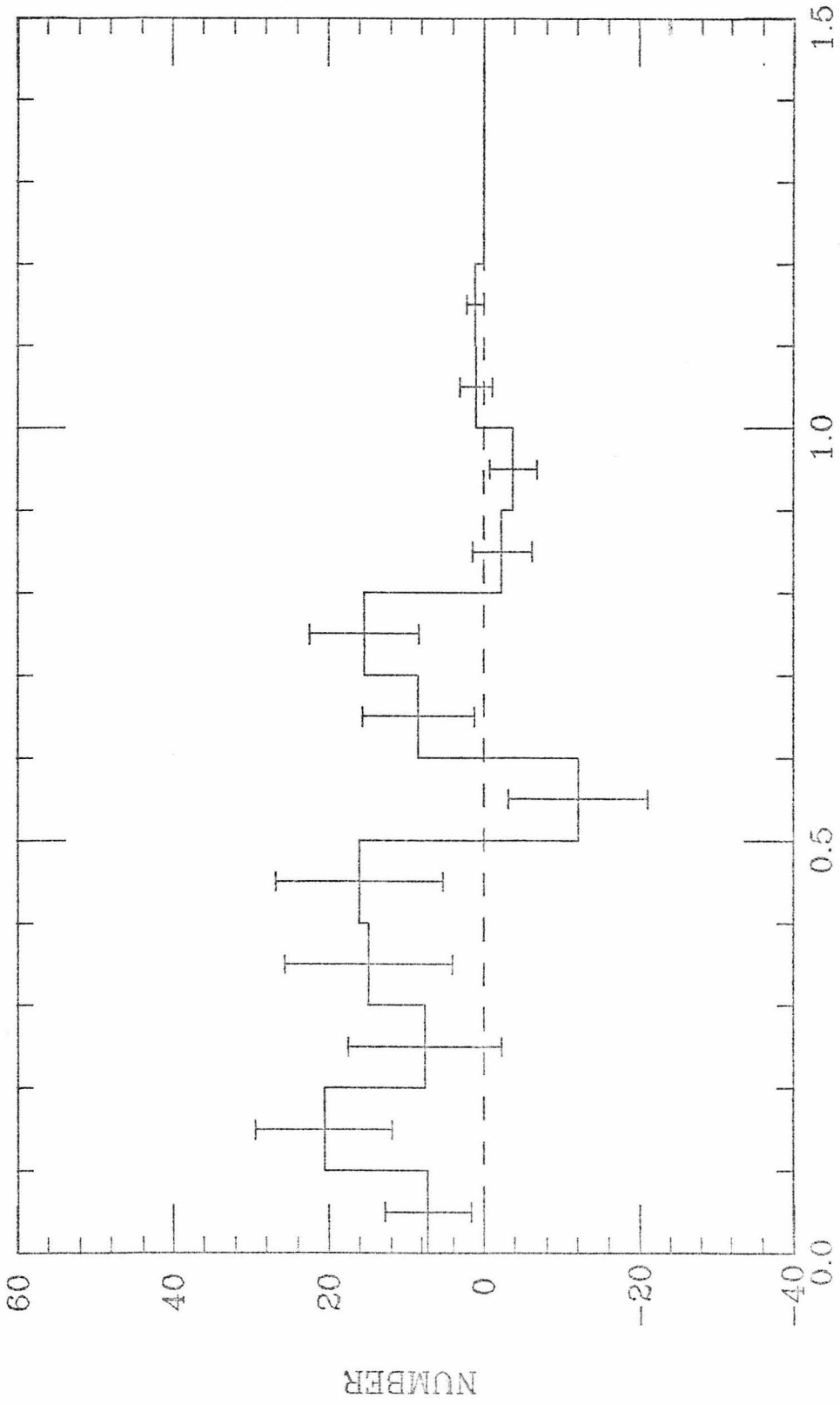

Figure 6.3.6: P_t distribution of events (same charge subtracted)

rho. The X distribution shows the possibility of a much greater cross section for pairs with X between 0.1 and 0.2 than 0.2 and 0.4. The statistical accuracy of the data does not however allow a definitive statement.

4.4±3.6 events occurred in the rho-omega region, 700 to 860 MeV/c^2, after background subtraction. The cross section corresponding to these events was 0.16±0.13 microbarn. Although correctly normalized in terms of X and P_t, this signal is uncertain by 20% due to uncertainty of the electron identification efficiency and 10% more due to the possible polarization of the vector mesons. The rho total cross section was measured as 4.8±0.4 millibarns and the omega 4.0±0.7 (3). The branching ratio exclusively into electron pairs is 0.043%±0.005% and 0.076%±0.017% respectively(4). All the omega and 63% of the rho signal are expected to occur within the mass range. This yields an expectation of 0.43±0.09 microbarns. The difference was 0.27 ± 0.19, 1.4 standard deviations from the prediction, and 1.2 standard deviations from zero.

Since the observation of direct rho and omega electron pairs was questionable, the functioning of the reconstruction and electron identification procedures was verified by reconstructing pi-zeros from two photons which were seen as conversion pairs. Each oppositely charged track pair with mass below 50 MeV/c^2, in which at least one track was

identified as an electron, was interpreted as a photon whose momentum was the sum of the momenta of the tracks at their vertex position. The invariant mass of all pairs of such photons is shown in fig. 6.B.7. Pi-zeros were clearly present near the correct mass of 135 MeV/c^2.

A signal of 3500 pairs with negligible hadron punch-through was expected when the experiment was planned, (assuming a down time of 50%). The flux was reduced a factor of two because of spark chamber latency problems. The geometrical acceptance was down by a factor of two because the downstream shower counter and Cerenkov counter were not used. Electron identification inefficiency for the two tracks and the low mass mate cut yielded another factor of five. Finally, the measured cross section was five times lower than anticipated. The hadron punch-through was underestimated by a factor of ten in C1 and in the shower counters, making the rate a thousand times higher than anticipated for pairs with one doubly and one singly identified track. As a result, the punch-through caused a background subtraction of about 20%.

6.C -- Comparison with Other Experiments

Two other experiments have measured direct lepton pair production by pi-minus near 16 GeV/c: a bubble chamber

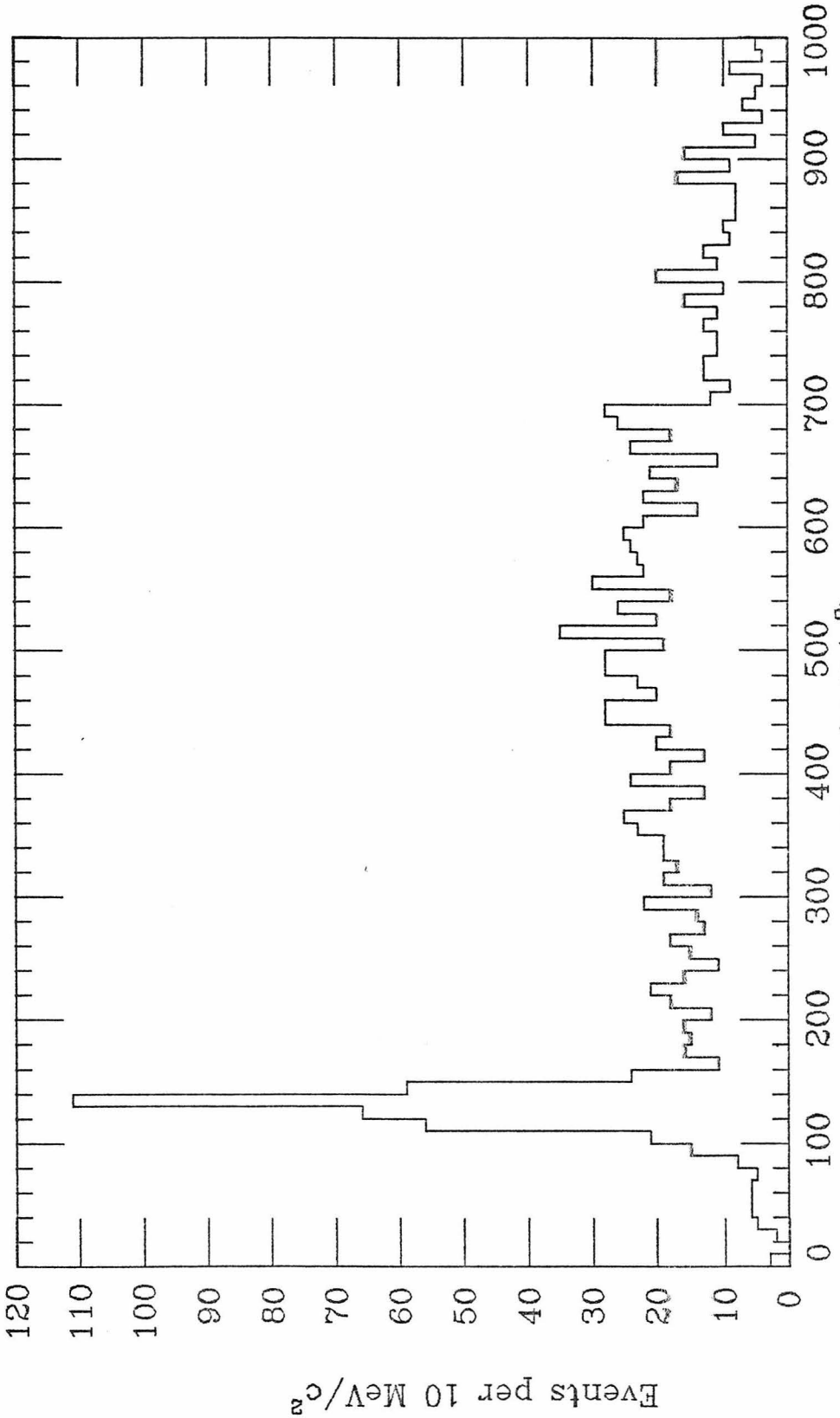

Figure 6.B.7: Invariant mass of two photons

experiment(5) which detected electron pairs at all angles with a final sensitivity one ninth that of this experiment; and a hybrid streamer chamber experiment(6) which identified muon pairs in the forward direction with a final sensitivity twenty-four times that of this experiment. Both these experiments ran also with an equal amount of pi-plus beam.

In the bubble chamber, about 90% of the electrons were identified, using several methods including shower production in metal plates installed inside the chamber. The data consisted of pairs where both electrons were positively identified. (No correction was made for the variation of identification efficiency with angle.) The contamination from pi-zero Dalitz decays was believed to occur completely below 130 MeV/c^2 in mass.

In the mass region between 130 and 1000 MeV/c^2, 22 events were observed in pi-minus interactions and only 7 in pi-plus. Most of this difference occurred below 250 MeV/c^2, where there were 15 in pi-minus and 3 in pi-plus. This low mass enhancement was not seen in the LASS data. All but three of the low mass events occurred with an X less than 0.15, below the LASS region of acceptance.

The results are compared in three mass regions in table T6.C. The 140-300 MeV/c^2 region contains the low mass enhancement. The 300-700 region contains the rest of the

non-resonant cross section, and the 700-860 region is dominated by decays of the rho and omega vector mesons. The combined rho and omega cross section for making electron pairs is expected to be 430 nanobarns (and somewhat higher for muons). (The observed cross section was 160±130 nb.) The pi-minus bubble chamber data are presented both as observed, and as would pass the LASS acceptance (normalized according to the rho). This acceptance restriction did not change the cross section; however, it removed most of the events so that the disagreement was no longer statistically significant.

Table T6.C: COMPARISON OF EXPERIMENTS

Cross sections in nanobarns.

Mass Range (MeV/c^2)	140-300	300-700	700-860
This experiment (LASS) accept. corr. assuming rho	40±540	1100±400	160±130
Bubble chamber (pi-plus)	490 (2)	490 (2)	250 (1)
Bubble chamber (pi-minus)	3400 (16)	1300 (6)	0
Bubble chamber (pi-minus) passing LASS acceptance	3500 (3)	620 (4)	0
Streamer chamber (pi-minus) accept. corr. assuming rho	124±14	445±27	250±20

Numbers in parentheses indicate the number of events. (After weighting by acceptance, events do not contribute equally, and the statistical uncertainty corresponds to the number of events in parentheses.)

The authors of the bubble chamber paper estimated the possible contamination from the Dalitz decays of the eta and omega mesons as less than 750 nanobarns in the 140-300 region and less than 100 nanobarns in the 300-700 region. This estimate is applicable to the LASS data with the caution that Dalitz pairs occurred at lower X than the rho and were therefore overestimated.

In the streamer chamber experiment, both muons were required to pass through ten interaction lengths of absorber. The minimum muon momentum was therefore 2.4 GeV/c, which limited the acceptance to greater than 0.3 for the X of the pair. The acceptance was fairly uniform above 0.3 in X and at all masses. The pi-plus and pi-minus mass distributions were similar in shape and the pi-plus cross section was about two-thirds as large as pi-minus overall. The rho and omega contribution was about one-fourth of the total and was about half as large as expected from the X distribution, cross section and branching ratio of the rho and omega.

The regions of acceptance of LASS and of the streamer chamber overlapped only slightly. The larger proportion of events in the rho region in the streamer chamber is consistent with the expectation that the rho and omega are produced at higher X than the non-resonant pairs and Dalitz decays. The streamer chamber cross sections in table T6.C

have been normalized assuming that 55% of the cross section has X greater than 0.3 as is the case for the rho.

6.D -- A Model for Lepton Pair Production

In this section, the pion annihilation model of Goldman, Duong-van, and Blankenbecler(7) is described and evaluated for the conditions of this experiment. The model was chosen because it is numerically explicit and predicts a cross section of the right magnitude, and because it involves interesting physics.

The original and most basic model for lepton pair production by the interaction of constituents of colliding hadrons is the Drell-Yan model(8) which treats the case of the annihilation of a free quark and anti-quark contained in the incoming hadrons. The weakness of the Drell-Yan model is the treatment of the constituent quarks as free, i.e. neglecting the interaction between the binding forces and the electromagnetic annihilation process. Important processes that are ignored are: hadronic interaction of the annihilating quarks, hadronic bremsstrahlung, large momentum transfer interactions with spectator quarks, and annihilations involving quarks produced in the collision(9). Feynman diagrams for these processes are shown in fig. 6.D.1. The predicted cross section is too low by up to two orders of magnitude, and too few pairs are predicted at

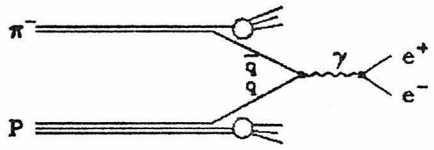

a) Free quark annihilation
Drell–Yan model

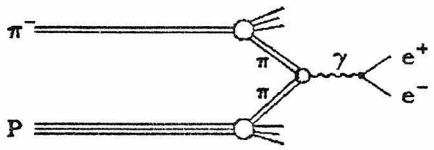

b) Pion–pion annihilation
GDB model

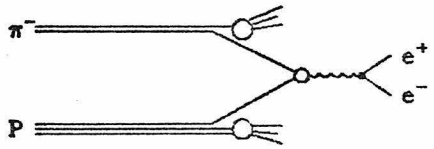

c) Hadronic interaction
of annihilating quarks

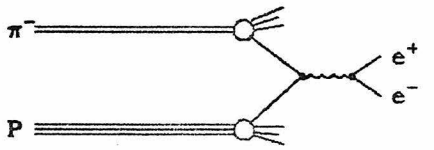

d) Annihilation of quarks
produced in the interaction

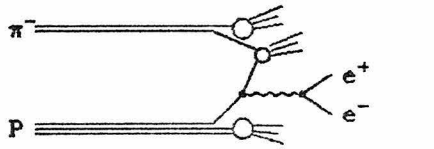

e) Electromagnetic bremsstrahlung
by interacting quark

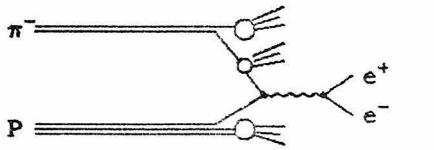

f) hadronic bremsstrahlung
by annihilating quark

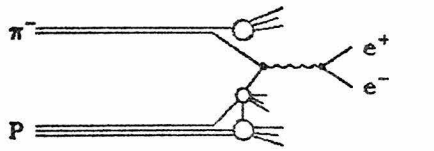

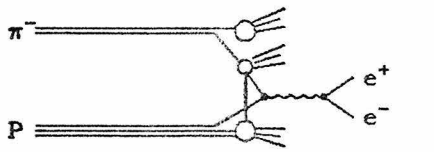

g) Large momentum transfer interactions with spectator quarks

Figure 6.D.1: Feynman diagrams for lepton pair production

large transverse momenta.

The GDB model is an analog of the Drell-Yan model where the meson rather than the quark constituents of the incoming hadrons annihilate. Meson-meson annihilations are believed to be more important than bare quark annihilations at masses below 1 GeV/c^2. Charged pion annihilation is the largest contribution, and that process alone is considered. The effect of strong-interaction coupling between the annihilating mesons is included by using the pion form-factor measured in the formation of pion pairs in electron-positron colliding beams. This form-factor includes the effect of the rho resonance, but not the omega (because it does not couple to two pions). Effects involving a third particle, such as hadronic bremsstrahlung and large momentum transfer to spectators, are not included because the form-factor refers only to exclusive pion pair production.

The lepton pair cross section is given by:

$$\frac{d\sigma}{dm\,dX} = \frac{8\pi\alpha^2}{3m^3}\int dy\,dz\,\delta(X-z+y)\,\delta\left(yz-\frac{m^2}{s}\right)\,y\,P_p(y)\,z\,P_\pi(z)\,|F_{\pi\pi}(m)|^2$$

$P_\pi(z)$ is the distribution function for a pion of momentum fraction z occurring in the incoming pion and is given by $z \cdot P_\pi(z) = \{(1-z) + C_\pi \cdot (1-z)^3$ for $z>z_0$ and $C_\pi \cdot (1-z_0)^3$ for $z<z_0$, where $z_0=0.4$ and $C_\pi=2.8$. $P_p(y)$ is for a pion of momentum fraction y occurring in the incoming proton and is

given by $y*P_p(y) = C_p*(1-y)^5$ for $y>y_o$ and $C_p*(1-y_o)^5$ for $y<y_o$, where $y_o=0.3$ and $C_p=0.4$. The constants C_π and C_p were not independently measured. They were adjusted to give the cross section for the rho measured in the streamer chamber experiment, and the correct ratio for X below and above 0.3. The pion form-factor was parametrized as a P-wave Breit-Wigner function measured at Orsay(10):

$$|F_{\pi\pi}(m)|^2 = (F_o m_\rho \Gamma_\rho)^2 / [(m_\rho^2 - m^2)^2 + m_\rho^2 \Gamma_\rho^2 (m_\rho/m)^2 (p/p_o)^6]$$

where $M_\rho=0.775$ GeV/c², $\Gamma_\rho=0.15$ GeV/c², $F_o=5.83$, $p_o=0.36$ GeV/c, and p is the c.m. momentum of the pions. (p was taken as 0 for pair masses below two pion masses.)

The differential cross section, $d\sigma/dmdX$ is shown as a function of X at the two pion threshold and at the rho mass in fig. 6.D.2. The large contribution near X of 1 comes from the delta function for a pion constituent having the full momentum of the incoming pion, corresponding to diffractive production. If the exchanged four momentum were allowed off mass shell in the space-like direction, this peak could be smeared downwards to correspond to the observed X distribution of the rho (fig. 6.B.1). The high X component is larger at higher pair masses.

The model was evaluated using the acceptance for the LASS experiment ($0.36*EXP(-(X-0.27)^2/(2*(0.11)^2)$), and using that of the streamer chamber experiment (zero for X below 0.3 and 30% for X greater than 0.3). The results of the

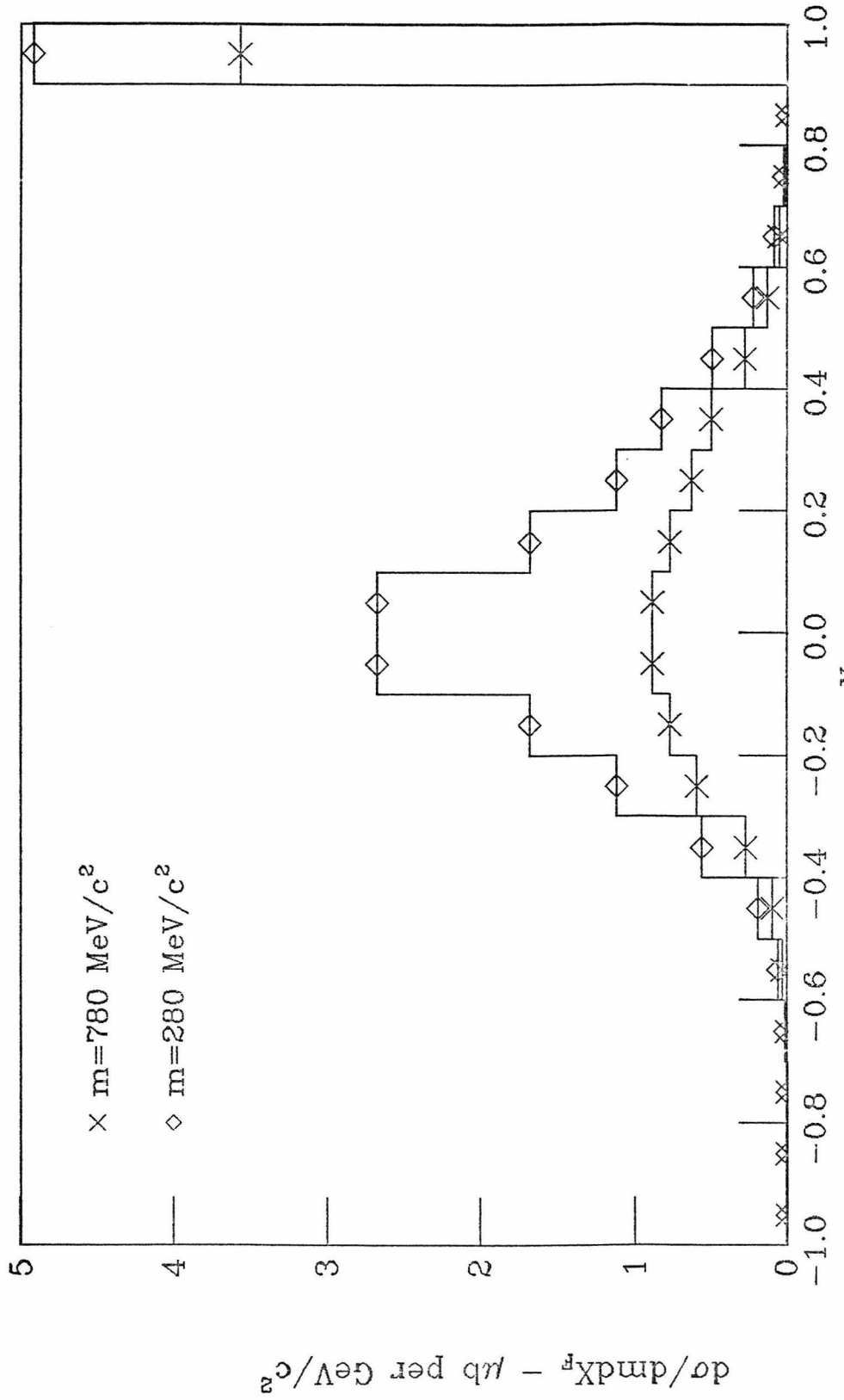

Figure 6.D.2: Predicted X distrution in GDB model

model are compared with the streamer chamber measurement in fig. 6.D.3, and the LASS measurement in fig. 6.D.4. In the muon case, the cross section has been multiplied by a factor $(1 - (2 \cdot M_\mu/m)^2)$ to account for the lepton pair phase space. The curve has been normalized to the rho peak (excluding the omega), and the agreement is good at lower masses. The corresponding prediction for LASS used the same normalization above 700MeV/c^2. Below, the production is increased by a factor of 1.34 to reflect the possible overestimation of the measured result due to assuming an X distribution like that of the rho. The prediction is well within the experimental upper limit for masses above 200 MeV/c^2. The 150 - 200 MeV/c^2 data point was not in agreement with the predicted steep rise of the model. The 100 - 150 MeV/c^2 data point contains pi-zero Dalitz decay events and is therefore not valid.

6.E -- Summary

An overall cross section for pi-minus - proton going to an electron pair with mass greater than 140 MeV/c^2 inclusive was measured as 1.1 ± 0.7 microbarns, corresponding to a single lepton to pion ratio of 2.6 x 10^{-5}. The cross section in the rho mass region is consistent both with zero and the known cross section for rho and omega.

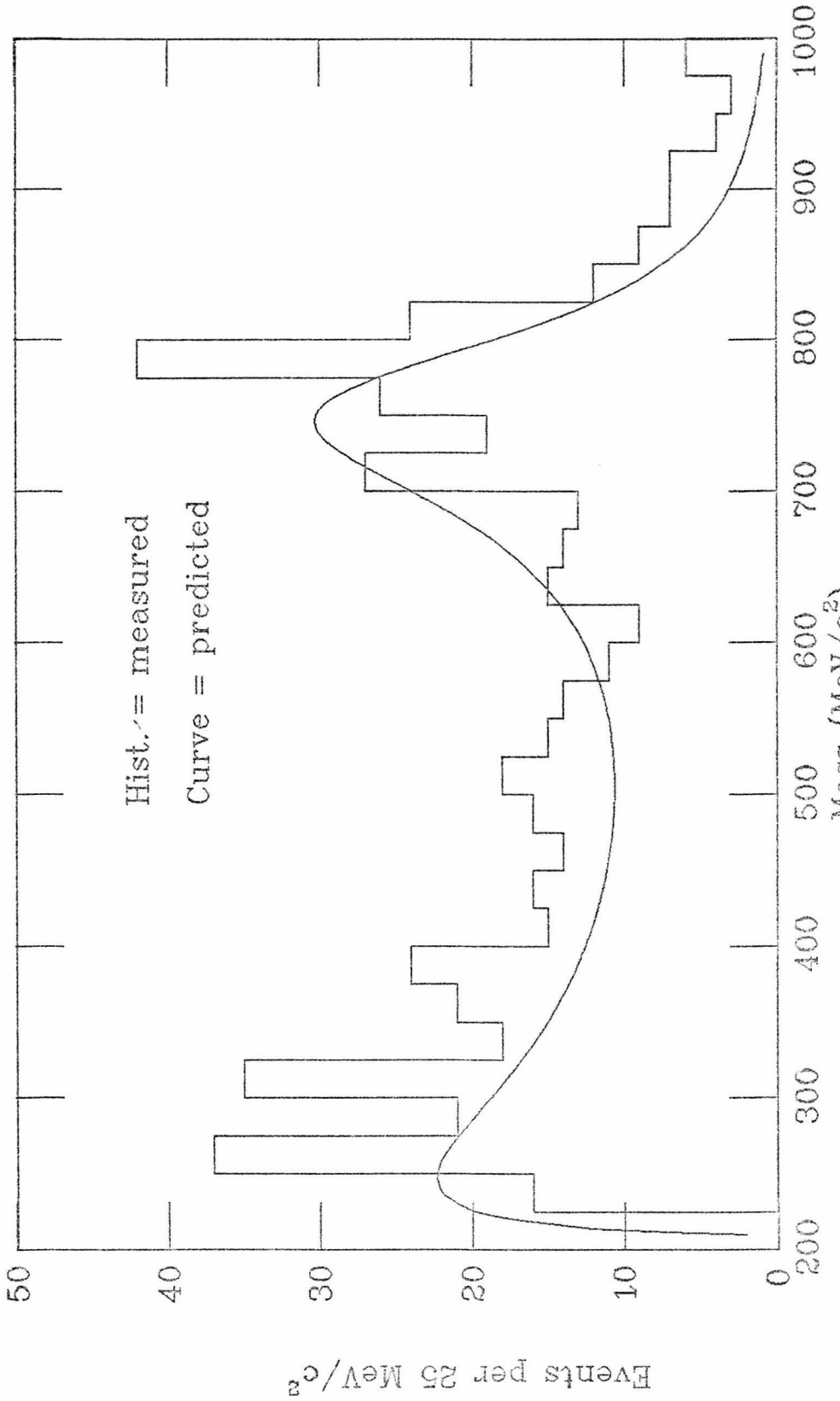

Figure 6.D.3: Prediction for streamer chamber - GDB model

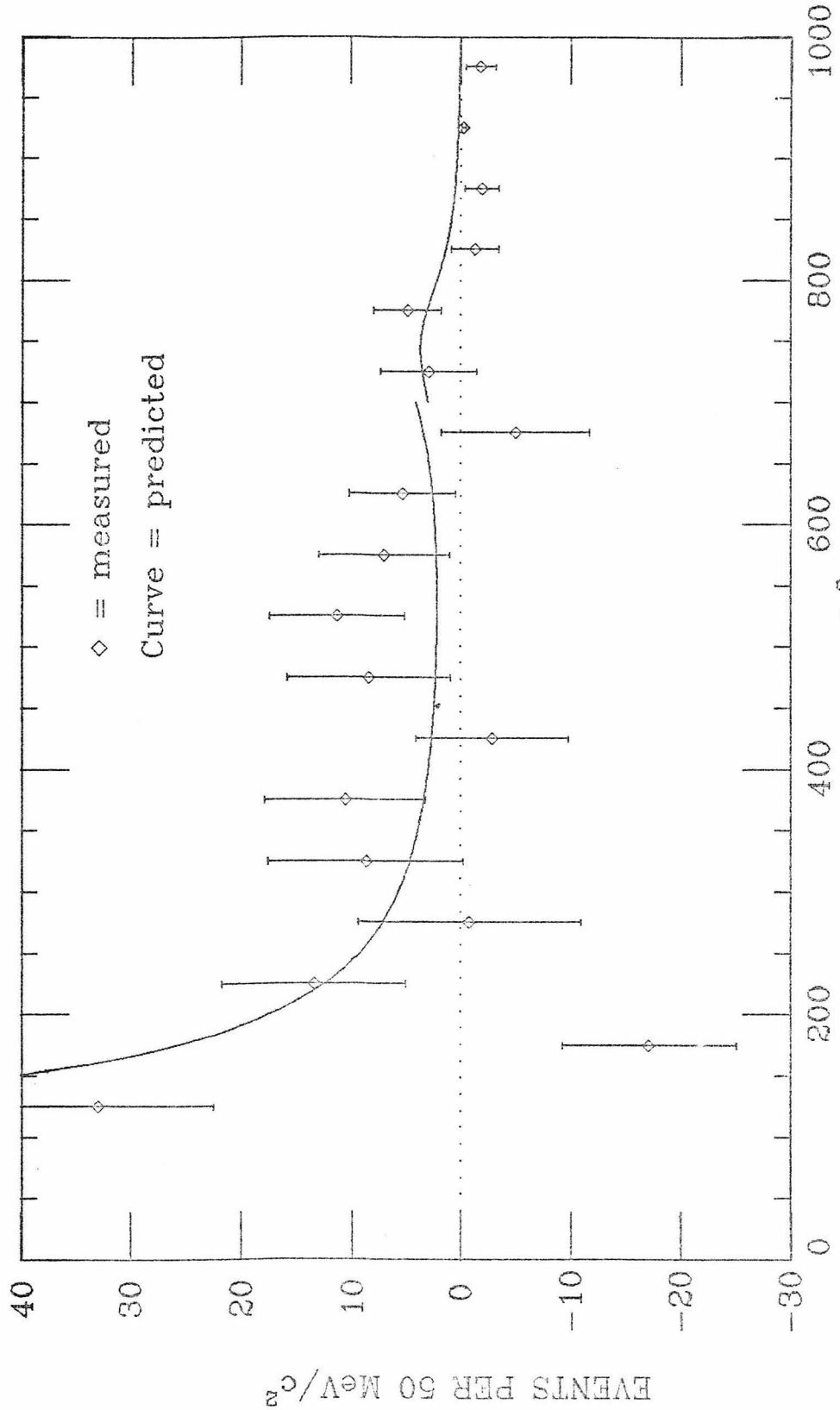

Figure 6.D.4: Prediction for LASS experiment – GDB model

The signal in the 200 - 700 MeV/c^2 mass range, not entirely due to Dalitz decays and vector mesons, is consistent with the two experiments of similar energies. This experiment complements the streamer chamber by observing a different region of X and masses below the two muon threshold. It has better statistics than the bubble chamber experiment in a limited region of X.

The lowest mass data point is not consistent with the steep rise at low mass predicted by the model. Such a rise was observed in the bubble chamber in pi-minus but not in pi-plus.

References for chapter 6

1. J. Bartke et. al., Nucl. Phys. B107, 93 (1976).

2. J. Bartke et. al., Nucl. Phys. B118, 360 (1977).

3. Ibid. and op. cit., refs 1 and 2.

4. Branching ratio of rho and omega into electrons from Review of Particle Properties, Phys. Lett. 50B, No. 1 (1974) and references therein.

5. J. Ballam et. al., PRL 41, 1207 (1978).

6. R. E. Cassell, Ph.D. Thesis, Vanderbilt University, (1979), also K. Bunnell et. al., PRL 40, 136 (1978).

7. T. Goldman et. al., Phys. Rev. D20, 619 (1970).

8. S. Drell and T.-M. Yan, PRL 25, 316 (1970).

9. For example:
J. Bjorken and H. Weisberg, P.R. D13, 1405 (1976);
C. Sachrajda and R. Blankenbecler, P.R. D12. 3642 (1975);
N. Cragie and D. Schildknecht, Nucl. Phys. B118, 311 (1977).

10. D. Benaksas et. al., Phys. Lett. 39B, 289 (1922).

APPENDIX 1 -- Cylindrical Spark Chamber System

A1.A -- Introduction

The layout of the solenoid and its detectors dictated the physical and electrical characteristics of the cylindrical spark chamber package: good resolution of the curvature of large angle tracks; good detection efficiency for several tracks in a small area; low mass in the downbeam end to minimize scattering; and compact electronics inside the solenoid able to operate in the field. Better resolution was necessary in the PHI direction than in the Z direction since the PHI angles were used to calculate a curvature whereas only a slope was calculated from the Z measurements. The curvature was to be measured for tracks with P_t in the range from about 100 to 1500 MeV/c. 100 MeV/c P_t tracks had a maximum excursion of only 30 cm., while 1.5 GeV/c P_t tracks deviated only 1.5 cm. from a straight line inside the 50 cm. radius of the package. The following sections describe how the constraints were met and the problems that arose. It is assumed that the description in chapter 2 section F has been read.

A1.B -- Physical Description

The amount of matter past the beginning of the target was minimized by utilizing the strength of styrofoam and of

cylindrical tubes of mylar. The spark occurred between 0.125 mm. dia. copper clad-aluminum wires glued onto thin sheets of mylar. These sheets were rolled into cylindrical tubes. The cylindrical shape was maintained by clamping between rings at each end. The cylinder package was a set of concentric mylar cylinders, between concentric support rings at each end. The target and cylindrical proportional chamber fit inside the hole formed by the inner gas-bag cylinder. The upbeam support rings were 0.25 inch lucite. Some downbeam rings were styrofoam wrapped with Saran Wrap, others were hollow lucite. A tubular aluminum frame surrounded the package, supporting each end by the outermost ring.

The mylar tubes were quite rigid once the ends were fixed; the narrow ones were able to support many times their weight hung from the end. The outer ones, whose diameters were comparable to the length, had a tendency to buckle, and had to be thicker. A problem due to the glued seams required much work and was never completely eliminated. The edges were overlapped 0.25 inches and glued with Scotchcast 221 epoxy. The extra rigidity of the seam caused a region of less curvature near the middle of the tube. This resulted in a flat spot and a variation in the gap spacing so that the electric field strength was not uniform over the chamber. It was therefore difficult to find a suitable operating voltage.

A first set of chambers (the inner 3 of the 5 eventual pairs) could be made to operate only in PHI-bands, roughly half of the area would not operate at voltages that did not cause spontaneous breakdowns elsewhere. A new, final, set was made stiffer with thicker mylar. This set (except for one cylinder) was made reasonably efficient by using a large amount of alcohol in the gas to widen the operating voltage plateau.

Two types of chambers made up the package. In the first type the wires were glued onto the mylar at an angle so that the PHI angle changed with Z. The wires on the inside of the gap pitched left (counterclockwise with increasing distance), those outside pitched right. The PHI difference measured at the upbeam end gave the Z position of the spark. The wires in the second type went parallel to the axis, only the outer wires were read out. The sparks in the axial chambers were used to eliminate ghosts in the pitched wire match-points.

In the original inner three chambers, the unread inner surface of the axial wire chambers was the 0.5 mil aluminum layer of aluminized mylar. The outer wires of the pitched wire chambers were glued on the inside of the same mylar sheet. The close proximity necessitated connecting these surfaces electrically (which made the high voltage system

more complicated). For the final inner chamber pairs, the downbeam support rings were changed from styrofoam to hollow lucite. The unread plane was changed to glued wires (the aluminum developed visible pits), and the outer chambers were enlarged to separate the previously shared surfaces. (The outer two chamber pairs were built without the separation although using wires on both sides instead of aluminum, so that these surfaces still had to be electrically connected.) The separation allowed the seams to be staggered so that the trouble areas did not coincide in PHI. Since the axial chambers were then too far from the pitched chambers to use for corroboration of match-points, they were treated as separate chambers.

Table TA1.B lists the chamber surfaces. The spark gap was 1 cm. in all chambers. The active length was 91 cm. Each wire was attached to an individual readout circuit. These were located on a printed circuit board bent in the shape of a hoop. The p.c. boards were glued between the upbeam support rings on the outer chambers. Those on the inner chambers were plugged into a connector so that pieces could be removed for repair. Even so, the six inch space between the chamber and the steel plate to which it was bolted was filled so completely that replacing a diode would have taken hours. No such repairs were done except to disconnect wires in small regions of two chambers where breakdown interfered with the operation of the whole chamber.

Table TA1.B: CYLINDRICAL SPARK CHAMBER PARAMETERS

CYL. name	radius cm.	# of wires	spacing mm.	pitch	pol-arity	side of gap
inner gas bag						
A1	10.19	320	2.	L	-	inner
A2	11.20	352	2.	R	+	outer
--	12.22	384	2.	-	+	inner
A3	13.24	416	2.	-	-	outer
B1	15.28	480	2.	L	-	inner
B2	16.30	512	2.	R	+	outer
--	17.32	544	2.	-	+	inner
B3	18.33	576	2.	-	-	outer
C1	20.37	640	2.	L	-	inner
C2	21.39	672	2.	R	+	outer
--	22.41	704	2.	-	+	inner
C3	23.43	736	2.	-	-	outer
intermediate gas bag						
D1	30.56	960	2.	L	-	inner
D2	31.58	992	2.	R	+	outer
--	31.58	-------solid-------			+	inner
D3	32.59	1024	2.	-	-	outer
E1	56.02	880	4.	L	-	inner
E2	57.04	896	4.	R	+	outer
--	57.04	-------solid-------			+	inner
E3	58.06	912	4.	-	-	outer
outer gas bag						

The high voltage pulse was brought in on RG58 coax cable, whose conductors attached to a bus on the p.c. boards (or to a copper strip in the case of the unread surface). Several cables supplied each chamber in parallel, the number depending on its size. A low voltage signal indicating the presence of a spark was formed at the far end of the p.c. board. These signals were connected to a rack outside the solenoid by 8 meter unshielded ribbon cables (spectra-strip), using one conductor per spark wire (the wires weighed two hundred pounds). Gas entered on the upbeam end through the lucite spacer between the inner gas bag and the first spark cylinder. It left through the ring between the outer cylinder and the outer gas bag. The gas was led through the entire volume by punching small holes between the wires at alternating ends of consecutive cylinders. An intermediate gas bag was added to put the outlet on the same end as the inlet. Gas tubing, coax and signal cables were threaded through holes in the iron end cap.

In the original inner chambers, sparks induced by ultraviolet photoionization were observed near where a spurious spark occurred in an adjacent chamber. This was remedied in the final inner chambers by painting the back of the mylar sheets black.

A description of the construction and testing of the original inner three chambers has been published(1).

A1.C -- Electrical Description

The system is divided into the following sections for description: the high voltage pulser system; the clearing field voltage system; the chambers, with the attached capacitor diode circuitry; the shift register system; and the automatic electronics tester. The chamber circuitry and the shift register systems associated with the cathode (ground) and anode (high voltage pulsed) wires were electrically separate. There were a number of voltage levels which acted as "floating grounds" for different systems. These levels are given names to reduce references between the systems. GND refers to real lab ground.

The clearing field was a continuous field used to sweep and collect ions from old tracks and previous sparks. The polarity was made opposite to the pulsed voltage so that the slow beginning rise of the high voltage pulse was canceled and did not clear out the fresh tracks. The voltage was -40V (negative on the anode surface), it was increased to -250V for one millisecond one beginning millisecond after the spark pulse. This reduced the time needed to clear the remnants of the spark, increasing the allowable pulse rate. It was discovered that a field above 80V/cm. would sustain

the arc started by the spark. At 40V, tracks remained capable of producing sparks for 1 microsec.

A "rectangular" high voltage pulse of about 4 kV was produced by switching coax cables charged to 8 kV across the chambers with thyratron tubes. The chambers were equipped with terminating resistors to minimize reflections. The pulse was delivered from the thyratrons through 50 ohm coax. The cathode wires were connected to the coax shields and the anode wires to the center conductor. The center conductors which came from the thyratron cathodes were connected also through an inductor to the clearing field voltage level, so that while the anode voltage averaged to the c.f. voltage, it could be pulsed for the spark. The clearing voltage was thereby applied through the HV cables from the thyratrons. Since the terminating resistors were also connected across the gap, series diodes were inserted to prevent them from shorting out the clearing voltage. Figs. A1.C.1 through A1.C.4 are schematic diagrams of the chamber electronics.

The cathode wire readout system is described first. The anode system was slightly more complex. The basis for the capacitor diode readout system was the resistor diode and capacitor, R1, C1, and diode shown in fig. A1.C.4. The R1-C1 time constant (5 nsec.) was so short that the voltage across R1 essentially tracked the chamber current. C1 was charged during the spark. D1 prevented it from discharging

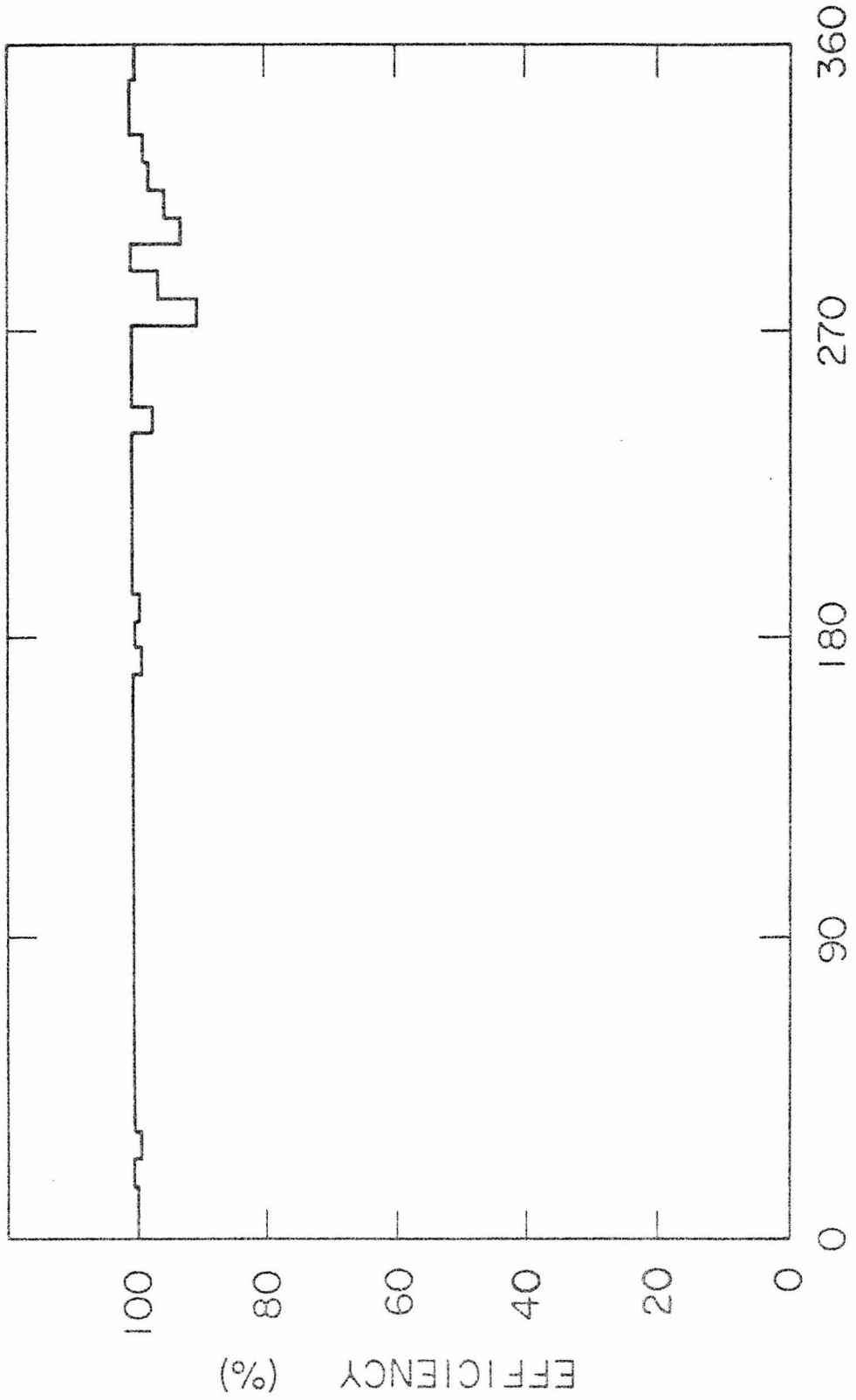

11-79 Figure A1.G.3: Efficiency as a function of Φ for cylinder surface B3.

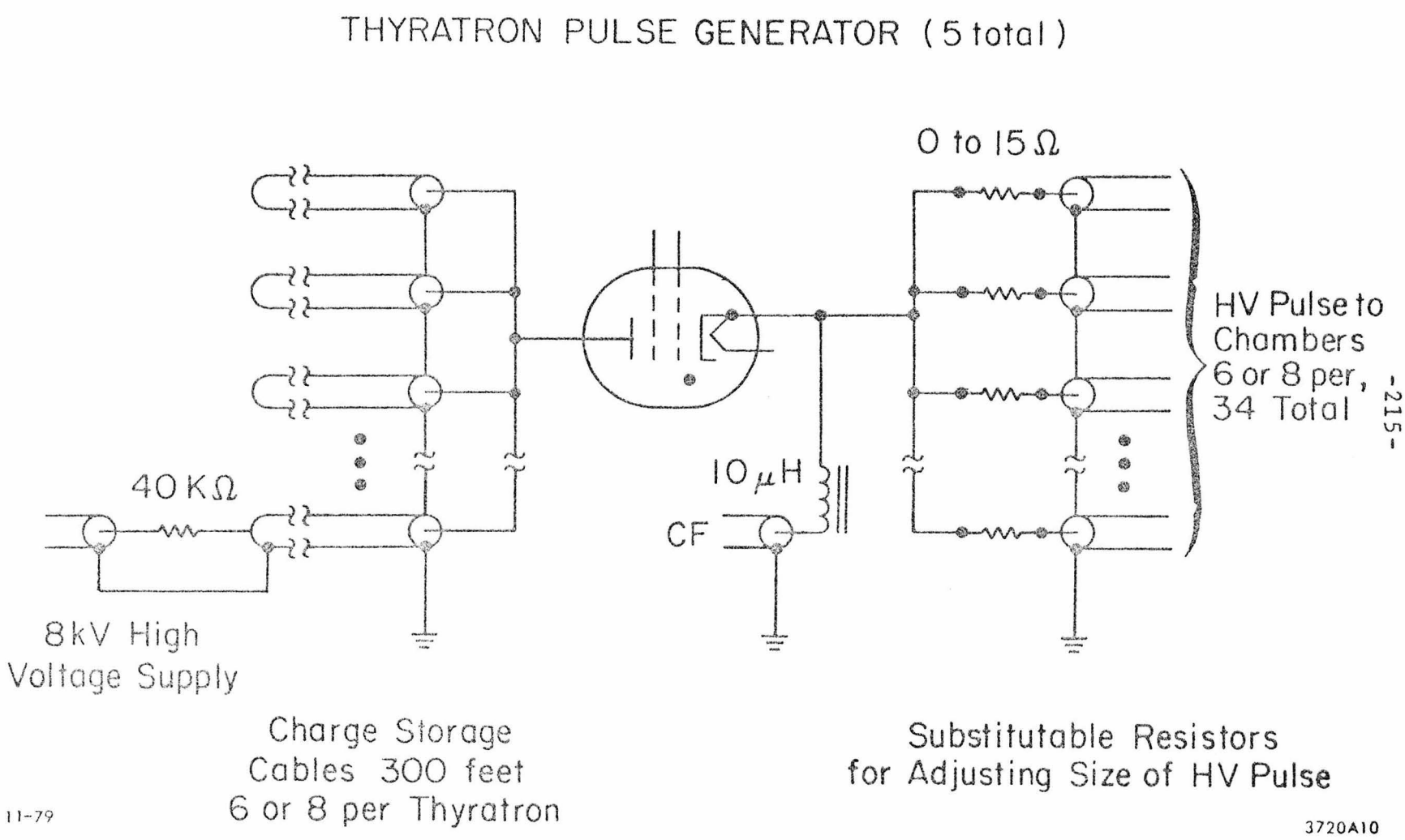

Figure A1.C.2a: High voltage pulse generation system: charge storage cables, thyratron, voltage adjustment resistors.

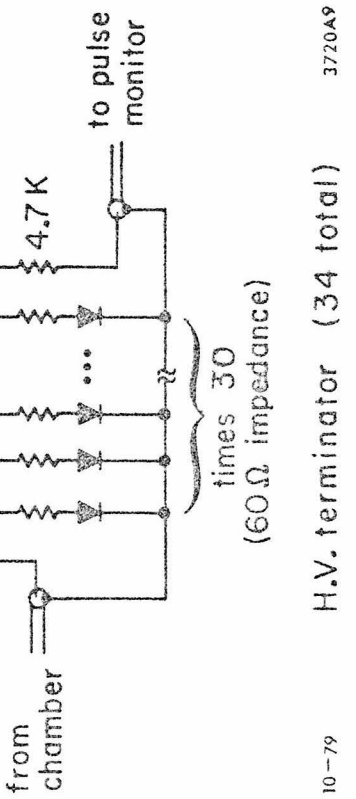

Figure A1.C.2b: High voltage pulse terminator: CF isolation diodes and pulse monitor.

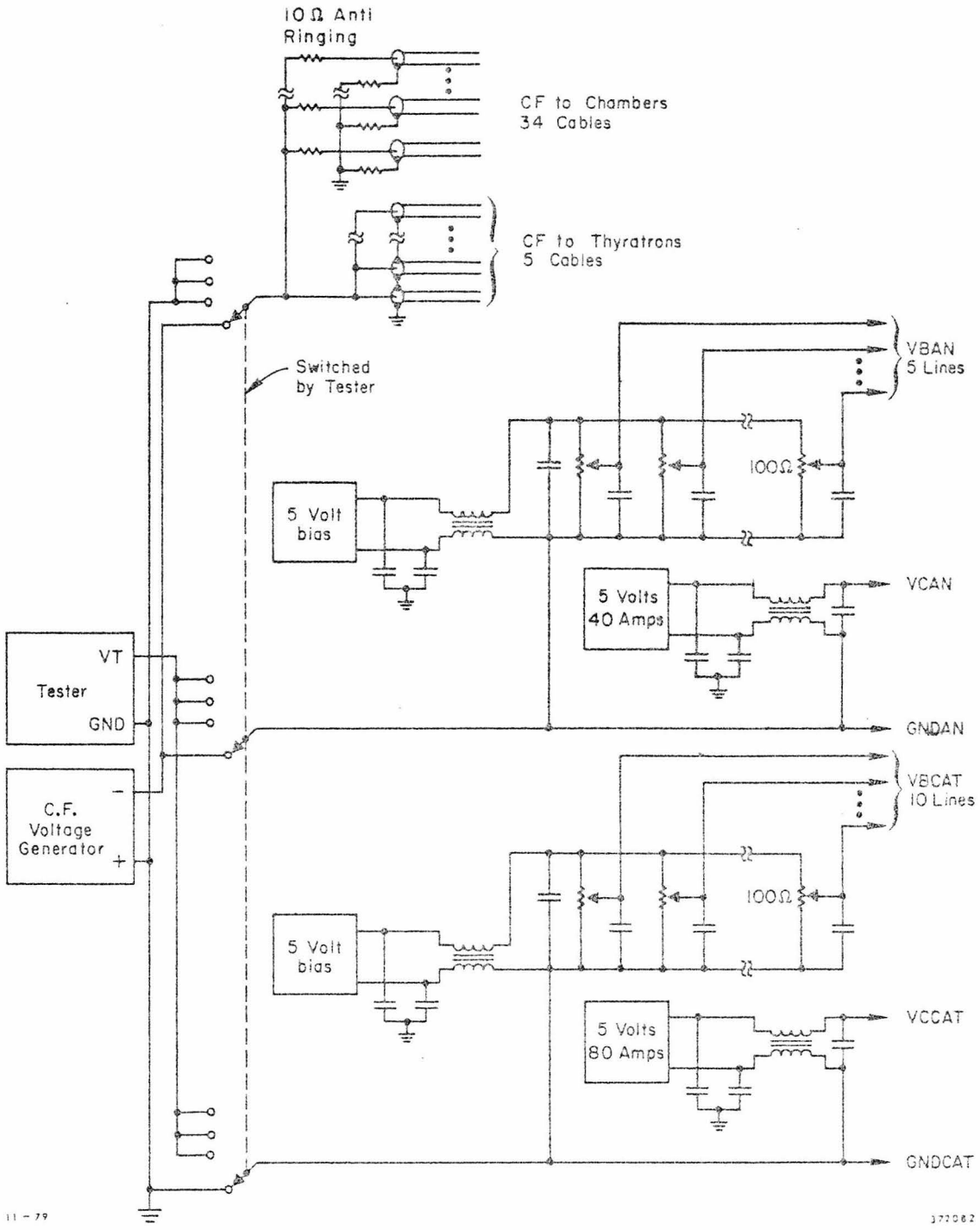

Figure A1.C.3: Low voltage supplies: 5V power to IC's, bias voltage, clearing field, and tester.

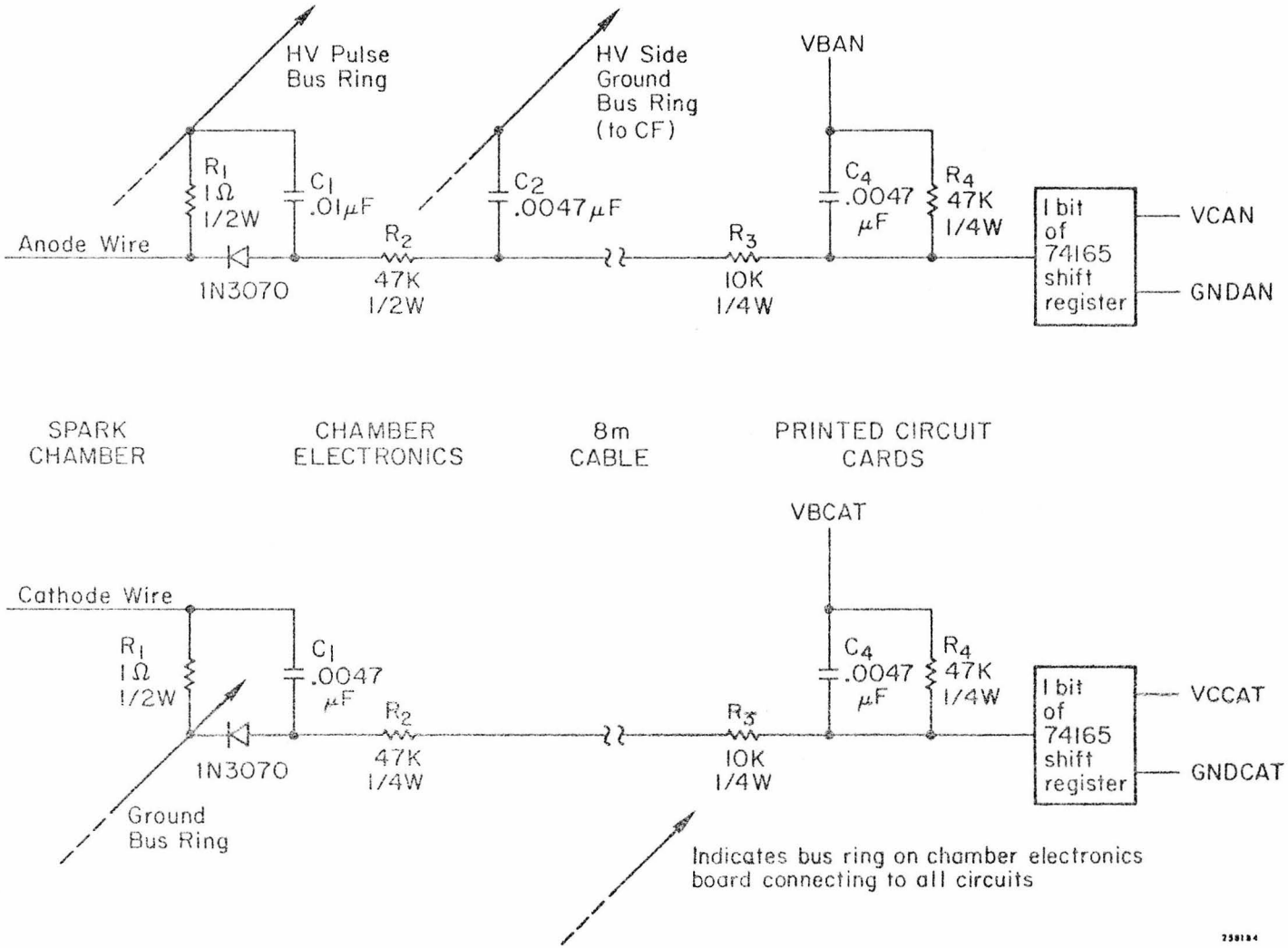

Figure A1.C.4: Electronics: chamber-mounted, and discriminator/shift-register cards.

through R1 afterwards. The resistor and diode solved two problems with the system using a capacitor only: The resistor limited the voltage difference between adjacent wires, so that the spark did not spread. The diode prevented inductive ringing from discharging the capacitor.

The rest of the circuitry converted the charge in C1 into a voltage compatible with the 74165 TTL integrated circuit. This IC discriminated the voltage into hit or no-hit, stored this information, and acted as a shift register for readout to the computer. Before the spark pulse a small current flowed from the bias voltage bus, VBCAT, through R4, R3, R2, and the diode. VBCAT was about 3.5V positive of the floating ground, GNDCAT, which was connected to real ground, GND, except when the tester operated. Therefore the input to the shift register chip sat at about 2.0V relative to GNDCAT. When a spark hit the wire, C1 was charged. Immediately afterward, the junction of C1 and R2 was at about -40V relative to GND. Current in R2, R3 caused this voltage to decay and the voltage at the input of the shift register to fall. A diode inside the shift register chip kept this voltage from falling below -.7V. The voltage on C1 decayed with a characteristic time of 250 microsec. and the voltage on C4 reached a minimum at about this time. The shift registers were strobed 250 microsec. after the HV pulse, causing a bit to be set if the voltage was less than the threshold, about 1.4V. The shift register input drew

current only when the strobe was enabled, and C4 kept this momentary current from changing the voltage. It was necessary to split R2 and R3 to damp out ringing involving the spectra strip and ground cables. (Ringing from the HV pulse had been rectified, and charged C1 as a spark would.)

On the anode side, the capacitor diode circuit was connected to HV, delivered through the center conductor of the high voltage feed cables. The floating ground for the part of the circuit in the outside rack was GNDAN (connected to the clearing field bus except when the tester operated). Therefore these busses were at the same voltage except during and immediately after the spark pulse (when HV was about 4 kV more positive). During this time 0.1 amp flowed through R2 for each wire. This amounted to about 300 amps total, rising in tens of nsec. This current would have destroyed the shift registers if it had been allowed to reach them. The purpose of C2 and R3 was to shunt the current and isolate the sensitive electronics. C2 passed this current into the CF bus, and if no spark occurred, was charged 6 V positive in the process.

The extra RC filter on the anode side delayed the voltage peak at C4 to 450 microsec. after the spark. The bias voltage on VBAN was set lower, about 2.0V, since the 6V on C2 increased the voltage at C4 to 1 Volt above the static equilibrium point. The voltage at C4 was again about 2.0V

providing the high voltage pulse came and no spark occurred. If a spark occurred, C1 was charged to -40V and C4 hit a low 450 microsec. after the pulse, the time of the anode side strobe.

Most of the busses were common to all chambers. The exceptions were HV and the bias voltage busses (VBCAT and VBAN). It was desirable to fine tune the size of the spark pulse for each chamber. Better sensitivity was achieved by adjusting the biases independently since different HV pulses produced different no-hit voltages at the shift registers.

A1.D -- Electronics Fabrication and Testing

The 10000 diodes and 1000 shift register IC's were individually tested and rated. The diodes were tested for short, open, correct labeling of polarity, and sorted according to the reverse breakdown voltage. Extra diodes were purchased so that only those able to withstand 250V were used.

The IC tester was interfaced to a PDP-8 computer which selected any of the eight inputs, applied a voltage, sensed the input current and read the shift register bits. Those IC's with extreme values of threshold voltage or a large input leakage current were not used.

The chamber p.c. boards were tested by the computer under conditions similar to chamber operation. A high voltage pulser system capable of delivering 300 nsec. pulses of 0 to 100 amps was connected to each of the 64 circuits of the system of the p.c. board, spectra-strip, and the shift register. A 10 kV pulse from a thyratron in series with a 100 ohm resistor simulated the spark. This, having a longer rise time , did not stress the components as much as a real spark. The test consisted of determining the current at which each circuit registered a hit, pulsing each 1000 times at maximum current while checking that none of the others registered, and rechecking the threshold. This test uncovered many bad connections, solder bridges, and arc-over problems, as well as causing early failures in several diodes.

When the inner chambers were rebuilt, the p.c. boards were refurbished. They were tested by applying a 10V triangular waveform to the spectra-strip end and displaying current versus voltage on an oscilloscope. Faults or changes in component values were easily noticeable in the pattern. After 2000 sparks per wire average, approximately 1% of the circuits had gone bad. These were approximately equal numbers of shorted diodes and leaky capacitors C1. In many more cases the capacitor was only leaky enough to reduce the sensitivity. About 10% of the C1 capacitors had a resistance of less than 50 k ohms and were replaced at that

time. The C1 capacitors were chosen for their extremely small size even though they were rated at 50V maximum. In retrospect, a larger operating voltage at the expense of size would have been chosen.

A1.E -- Digital Readout

The shift register IC's were chained to form two extremely long shift registers. The IC's for the cathode readouts of all chambers were chained together amounting to 7000 bits. The anode side IC's formed a shift register of 3500 bits (only pitched wire chambers being read). An extra (8 bit) shift register was inserted in the chain between the end of one chamber and the beginning of the next. These 8 bit "fiducials" were hard wired to read no-hit, six hits, no-hit. They allowed the computer to check that the shift registers counted correctly.

These long shift registers needed only three connections besides the floating power supplies: the LOAD (strobe) pulse; the CLOCK (shift) pulse; and the DATA output from the first stage. These signals, two coming from and one going to the digital "control box" passed through level shifters which electrically isolated the output from the input. Using a schottky clamped optical isolator, even with impedance matching, inverting, and buffering, they delayed the signal by only 125 nsec., allowing a 4 MHz shift rate.

The control box received a trigger coincident with the HV pulse to the chambers. It produced the LOAD pulse for the cathode side after 250 microsec. and for the anode side at 450 microsec. It produced the signal which drove the 250V clearing field pulse. Following the second LOAD pulse, it sent 3500 CLOCK pulses to the anode side shift register reading the DATA signal after each. Then it switched to the cathode side and did likewise for 7000 pulses. It transmitted to the PDP-11 only when it encountered a hit, giving the number corresponding to the first wire hit along with the number of contiguous hits following it: clockwise-most (facing the electronics end, i.e. downstream) edge and width minus one for each cluster. Sparks hitting the "last" and "first" wires of the cylinder, of course, were not combined by the control box. This information was transferred to the computer when the end of a cluster was detected. The next CLOCK pulse was delayed until the transfer was finished. Four one bit shift registers were inserted in the long CLOCK and DATA cables between the control room and the chambers. The cable delay between them was less than 125 nsec., so that no data were lost when the control box paused. The shift rate was reduced to 2 MHz because of timing problems that were never located. The resulting scan time of 5 millisec. was acceptable since 25 millisec. deadtime was required to allow the spark chambers to clear.

A1.E -- Automatic Tester

The tester applied voltages to the floating grounds in such a way as to test all of the circuits in parallel. It was controlled by the PDP-11: all electrical switching was automatic. The C.D. electronics and the shift register system were tested simply by running a program on the PDP-11.

When enabled, the tester cycled through eight states, each lasting about 0.5 sec., coming to rest again in state 0. Separate tests were performed in states 1 through 5. States 6 and 7 were dummies, identical to state 0. During states 1-5, CF was switched from the clearing field generator to GND. GNDCAT and GNDAN were switched to VT, a voltage generated by the tester. Halfway through each state, after the relays had settled, the control box was triggered, loading and reading in the shift registers.

In state 1, VT was +20V relative to GND (i.e. to the wires in the spark chamber). Current through the diode, R2, and R3 produced a low input to the 74165, unless one of these was open. In state 2, VT was -20V and the bias voltages were zero. All shift register inputs were low unless C1, C2, or the diode leaked current.

In state 3 VT was at -20V with the bias back on. At the same time the readout was triggered, an SCR pulled VT to zero, making conditions as for normal operation. If a circuit worked properly, C1 was charged at -20V which caused a low input to the shift registers after the proper delay of 250 or 450 microsec., when the LOAD pulses came.

In states 4 and 5 VT was zero. In 4 the bias was switched off to test the ability of the shift register to read hits. In 5, it was back on, testing the ability to read no-hits.

The results of all five tests were stored and collated in the computer memory. The location and nature of incorrect responses were printed. The hard wired patterns from the fiducials were also verified, localizing breaks in the chain.

A display showed whether the relays failed to reconnect things properly after the test.

A1.F -- Gas System

Neon (with 10% helium) gas was circulated to all the spark chambers through an LBL gas cart which used activated charcoal and a liquid nitrogen bath to remove alcohol, water vapor, air and other impurities. 1% ethyl alcohol was added by bubbling the gas through liquid at -3 degrees C. (The

temperature range of the system was capable of varying the concentration from 0.05% to 5%.) Good regulation of the concentration was achieved with the following techniques: All the gas went through alcohol at low temperature, rather than trying to divert a fixed proportion through alcohol at high temperature. The gas was broken into many small bubbles using an aquarium aerator stone. The gas was precooled in the same bath that cooled the alcohol. The temperature of the bath was controlled electronically to a fraction of a degree.

The gas was circulated at about 10 cu. feet per hour. At this rate, the pressure drop in the tubing was about 0.5 inch of water: the necessary pressure at the beginning of the inlet was considered unsafe for the chamber, and the negative pressure at the end of the outlet would collapse it. The pressure drop inside the chamber was quite small. The inlet and outlet pressures were adjusted to give the desired flow rate with about 0.15 inch (water) pressure at the chamber. If the chamber pressure fell below 0.1 the outflow was interrupted by an electric valve. If it exceeded 0.25 the inflow was interrupted. Oil filled bubblers kept the pressure within ± 0.5 inch if the electrical system failed. The gas flow was interrupted if the alcohol cooler failed in order to prevent a large concentration of alcohol from entering the chamber. The pressure regulation system was inadequate in that there was

no sensitive backup protection. (The oil filled bubblers operated only at relatively large pressures.)

A1.G -- Cosmic Ray Tests

After the experience with the first set of chambers, the second set was tested at Caltech with cosmic rays to determine whether the chambers were sensitive over their entire area. Four 1 meter by 6 inch scintillation counters were arranged as a square tube inside the center hole in chamber package. A coincidence between either set of opposite sides triggered the spark and readout. (This occurred about once per second.) Events were read into a PDP-11/45 with 28K words of core and a disk. The PDP-11 program divided the cylinders into regions of PHI and Z and counted whether a track went through the region, whether there was a hit near the track, and whether there were hits not attributable to the track. The width of the sparks was recorded. Two thirds of the sparks covered only one wire. Of the rest most hit two, the number falling by a factor of four for each additional wire.

The program had two basic pieces: a foreground piece which read in events (either online or from tape), found tracks, and accumulated counts in the region histograms; and a background piece which accepted and executed commands from a terminal. Commands controlled the definition of regions;

displayed statistics, single events, histograms, and tables; and controlled reading, writing, or updating disk files containing the accumulated counts.

For this section, the chambers will be designated as follows: innermost crossed wire cathode surface - A1; anode surface - A2; next chamber (axial wire) cathode surface - A3; similarly through E1, E2, and E3 for the other four chamber pairs.

One chamber pair was designated to find tracks, and was not tested. In practice the outer (E) pair was used. (Another run using the D pair determined the efficiency for the E pair.) Tracks were defined as two match-points in the PHI-Z chamber at approximately opposite PHI angles, both corroborated in the PHI only cylinder. Tracks were required to intersect the outer cylinder within the active Z range.

Fig. A1.G.1 shows the PHI distribution of hits in the innermost axial-wire chamber (A3). Since tracks were required to go through the center, this is reflection of the cosmic ray distribution which goes approximately like cosine squared of the angle from the vertical. The four dips are the shadows of two aluminum poles that ran the length of the chamber at ± 45 degrees. Also visible are regions of inefficiency and narrow dips in the efficiency due to dead wires or readouts. Sometimes the adjacent bins are

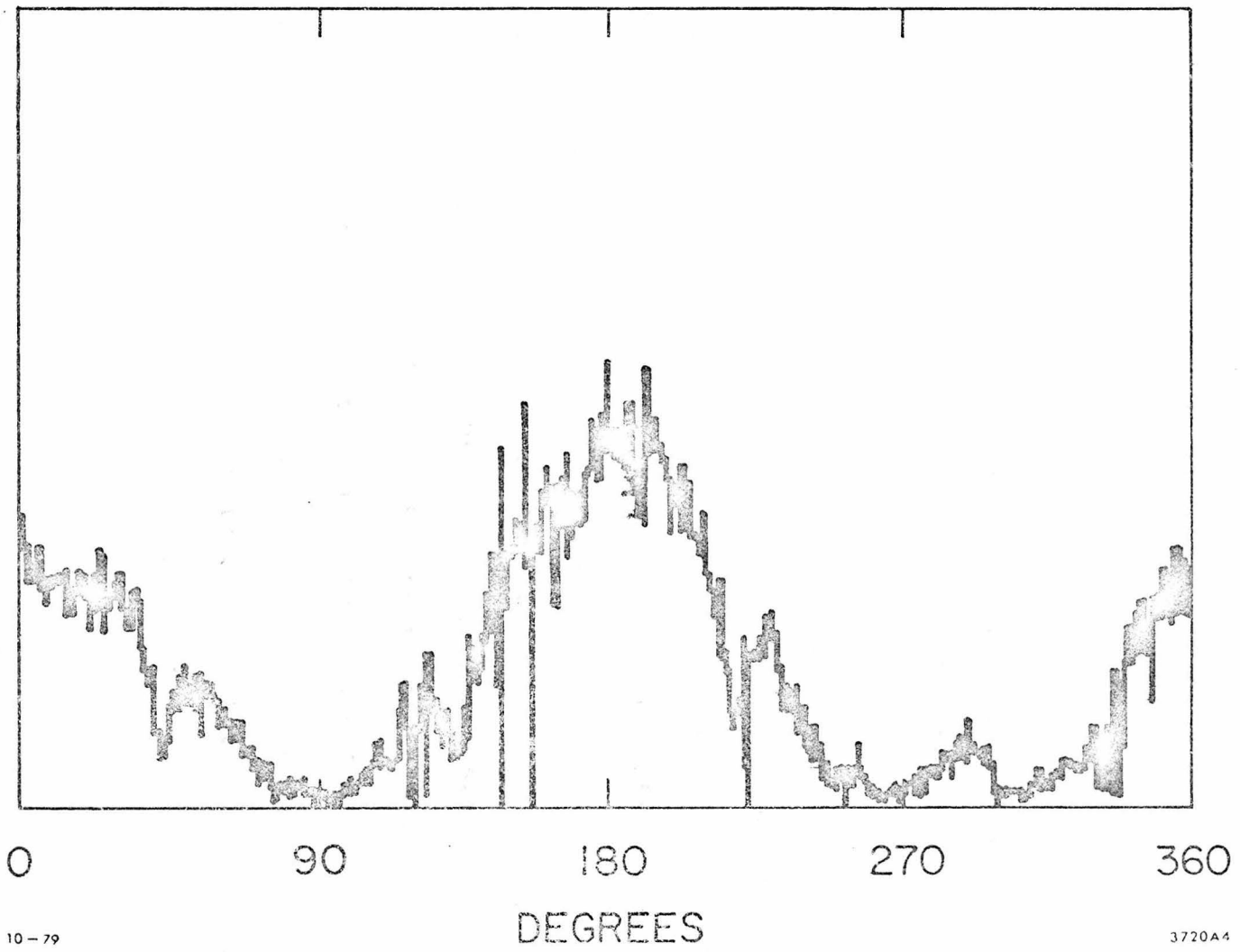

Figure A1.G.1: φ distribution of hits in cylinder A3 showing cosmic ray angular distribution.

abnormally high, indicating the spark was pulled, perhaps because the proper voltage was not present at the dead spot.

A typical event is shown in fig. A1.G.2. The hits are plotted at the PHI of the wire at the front of the chamber. Hits in pitched wire cylinders appear to be rotated by a distance proportional to the distance from the front end.

Fig. A1.G.3 and A1.G.4 shows plots of efficiency for all Z as a function of PHI for the best and worst chamber surfaces (bins of about 1.5 cm. of circumference). The average efficiency for all chambers was 90%. All inefficiencies were limited to regions rather than being uniform over the cylinder. The consistently lower efficiency of the anode (or "2") surfaces was a result of the lower sensitivity of the anode readout and the need to ignore certain wires that permanently registered hits. (The fact that sparks have two ends leads to the expectation of equal efficiency in the "1" and "2" surfaces.) Efficiency versus PHI for an inefficient chamber is shown in 20 cm. Z slices in fig. A1.G.5. One dip was worst in the middle. The other was worst at the back.

C3 had a breakdown region which became worse over the weeks as the chamber was sparked. The deterioration is thought to be due to the roughening of the spark wires leading to electron emission in the field. Eventually a spark occurred in this region every trigger. It became so bad that the

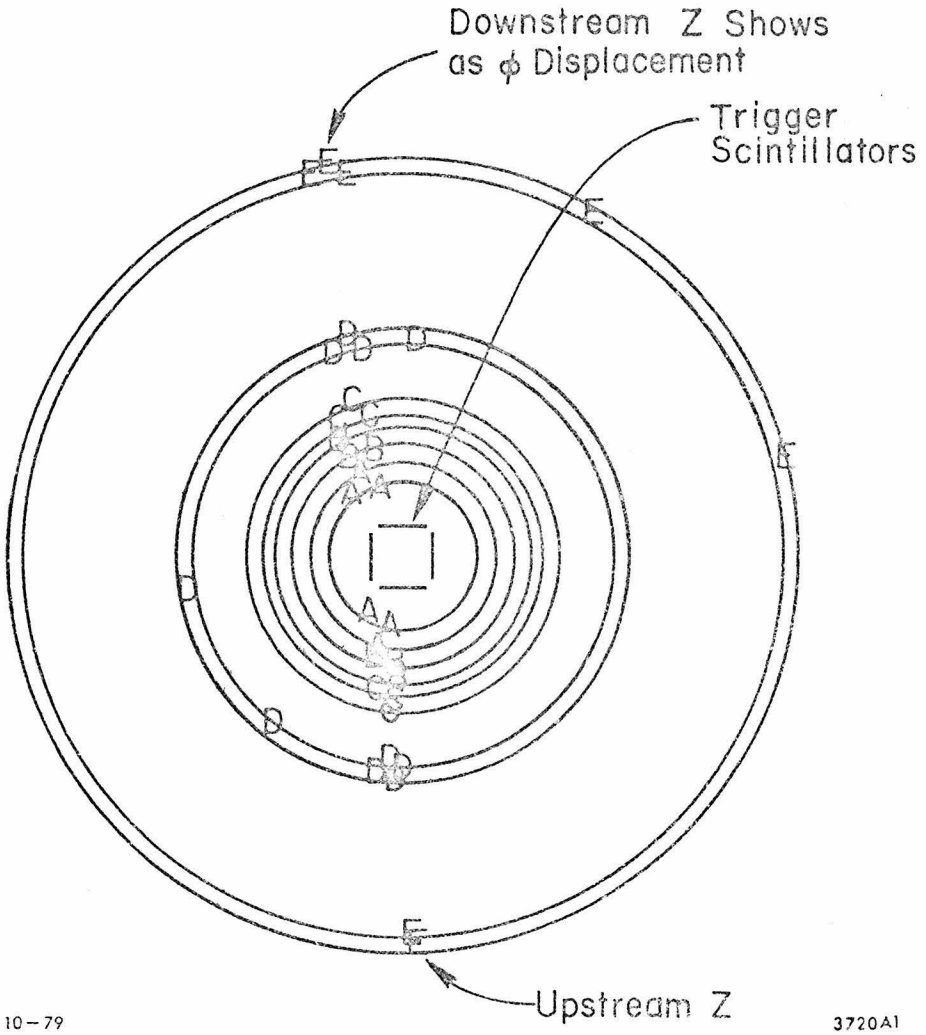

Figure A1.G.2: A cosmic ray event: letters indicate φ position of upstream end of wires.

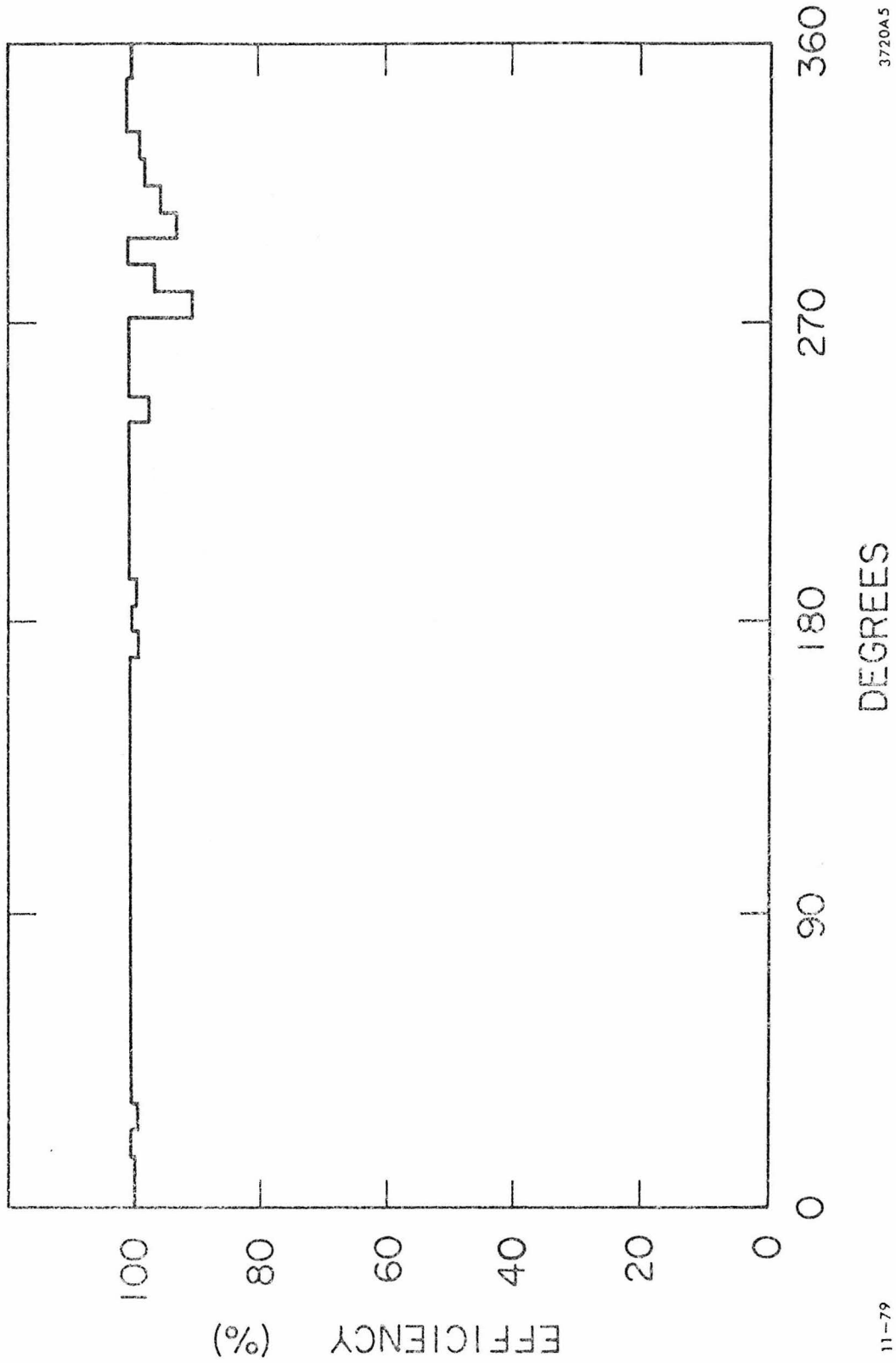

Figure A1.G.3: Efficiency as a function of ϕ for for cylinder surfaces B3.

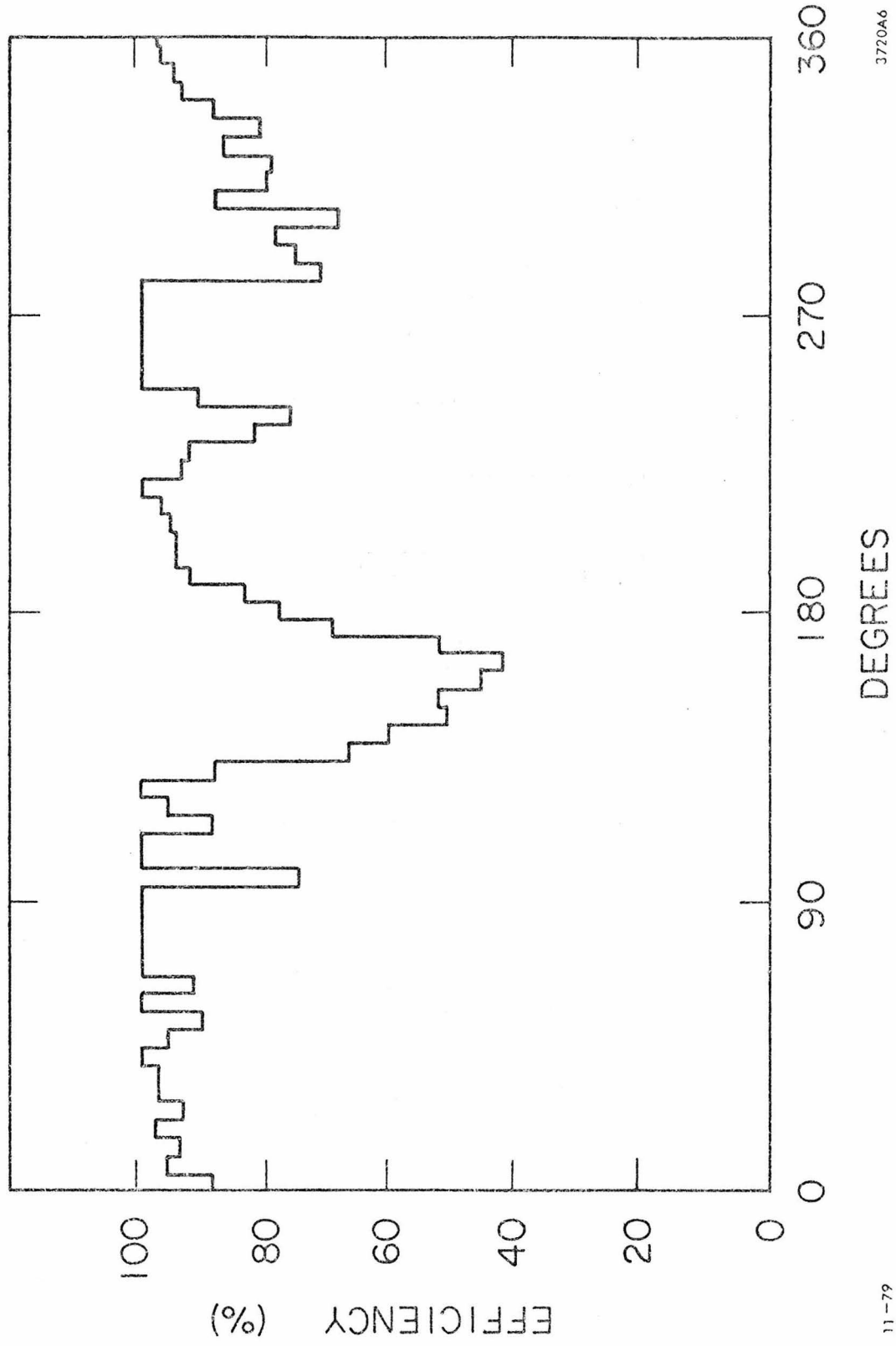

Figure A1.G.4: Efficiency as a function of φ for cylinder surface B2.

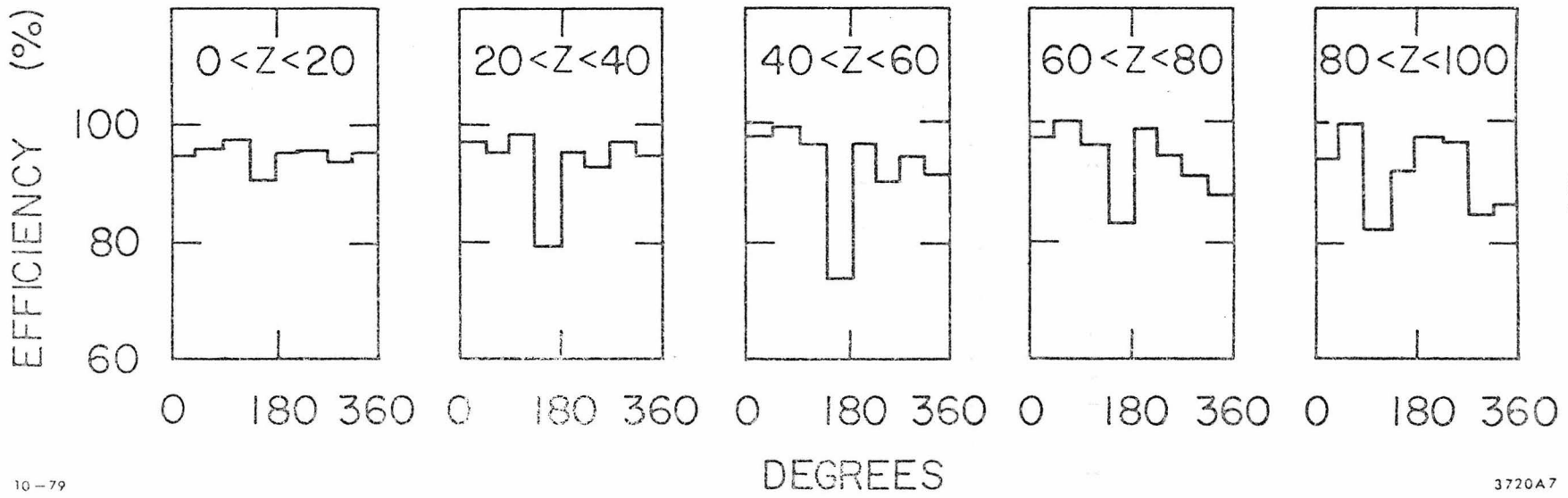

Figure A1.G.5: Efficiency as a function of φ in bins of Z for surface B2.

breakdown sparks prevented the voltage on the chamber from reaching the value necessary to produce sparks elsewhere in this chamber. The wires in this 2 cm. region were disconnected allowing the rest of the chamber to operate. Breakdown occurred frequently at the edges of this region which became worse until again the chamber was dead. More wires were cut. The breakdown began again after the package was installed at SLAC. During the experiment, this chamber was run at lower voltage giving about 50% efficiency. Fig. A1.G.6 shows a plot of spurious sparks vs. PHI for this chamber after the surgery. A small region was cut in E3 also, with satisfactory results.

Reference for appendix 1

1. H. B. Jensen et. al., A New Single Wire Readout System for Spark Chambers, Nucl. Inst. Meth. 125, 25 (1975).

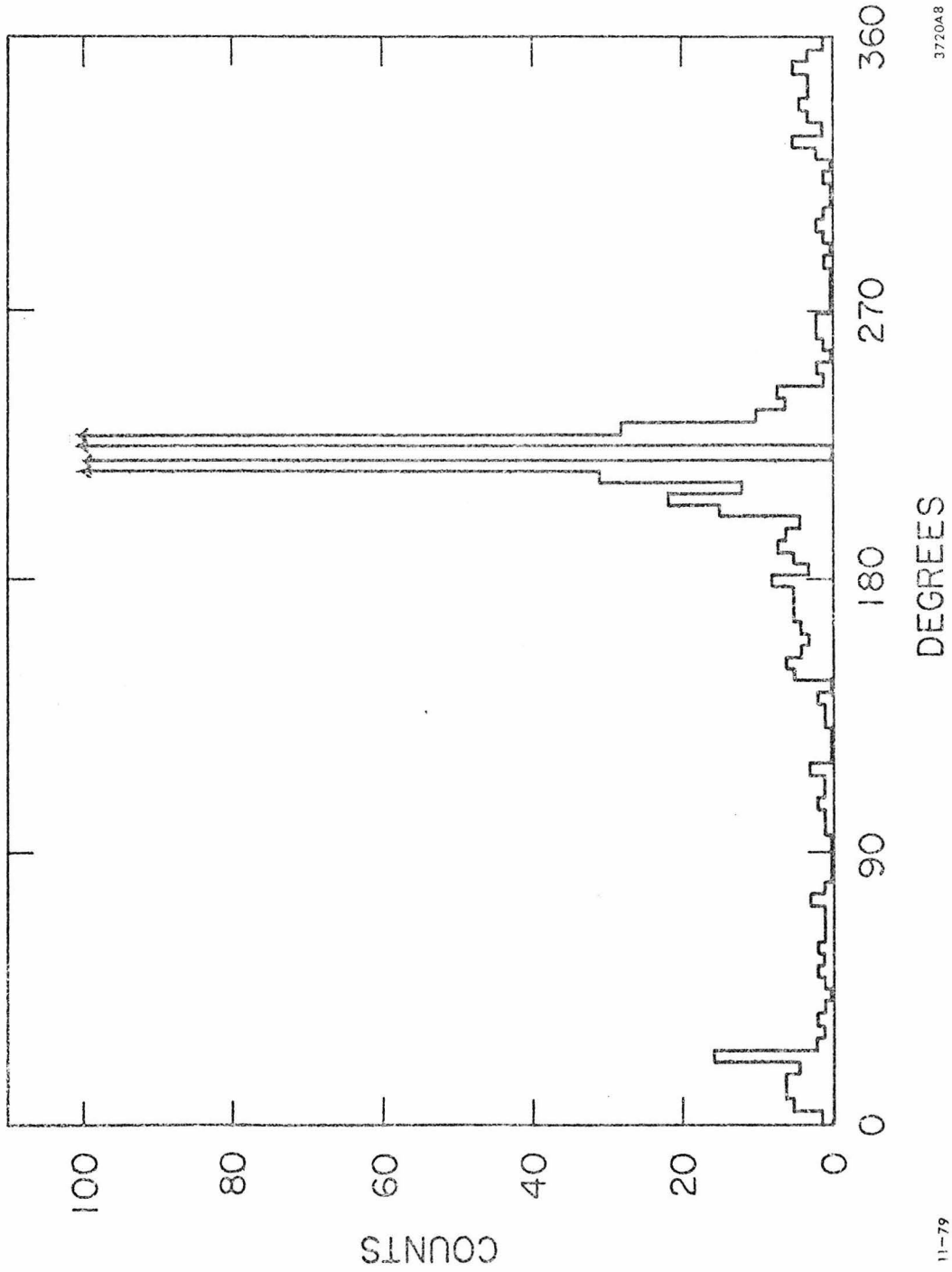

Figure A1.G.6: Spurious sparks in C3 gap showing breakdown. Two bins are truncated.